Universidad de La Laguna
Oficina de Sede Electrónica
Entrada
Nº registro: 2019/67752
Nº reg. oficina: OF002/2019/65034
Fecha: 03/09/2019 00:01:47

DEPARTAMENTO DE ASTROFÍSICA

Universidad de La Laguna

Optical Characterisation of the Planck PSZ1 Galaxy Cluster Catalogue: Building a Reference Sample for Cosmology

Memoria que presenta
D. Antonio Ferragamo
para optar al grado de
Doctor por la Universidad de La Laguna.

INSTITUTO Ð ASTROFISICA Ð CANARIAS
octubre de 2019

Examination date: octubre de 2019
Thesis supervisors: Dr. José Alberto Rubiño Martín and Dr. Rafael Barrena Delgado

Alla mia famiglia,
a Carmela ed a Nonna Lella.

Abstract

This thesis has been dedicated to the study of Galaxy Clusters as Cosmological tools. The work is divided into two main parts; the first is purely observational, whereas the second is dedicated to the preparation of tools for cosmological analyses.

The observational section has been developed within the frame of the optical validation program Sunyaev-Zeldovich (SZ) sources, observed by the *Planck* satellite in the northern hemisphere, and included in the PSZ1 catalogue. The 212 targets were observed during a two-year International Time Project (ITP) at the Roque de Los Muchachos Observatory (ORM) facilities on La Palma Island.

During the observational programme, each target underwent a validation process in two phases: photometric and spectroscopic. In the first phase, we performed imaging in g', r' and i'-bands at INT/WFC and WHT/ACAM. We obtained a deep photometry for the majority of the targets, reaching a magnitude in r'-band of about 23.2 and 23.8 for WFC/INT and ACAM/WHT, respectively. This allowed us to estimate their photometric redshift up to $z_{phot} \sim 0.8$ cluster richness. In the second phase, we performed the spectroscopy of the photometrically-confirmed clusters. We used TNG/DOLORES and GTC/OSIRIS spectrographs in order to observe clusters at $z_{phot} \leq 0.4$ and $z_{phot} > 0.4$, respectively. The aim of the spectroscopic follow-up is to confirm clusters and to characterise their physical properties, such as velocity dispersion and mass. We used the Multi-Object Spectroscopy (MOS) technique in order to observe as many cluster members as possible. Due to the large sample of SZ effect sources, we were able to use, on average, only one mask per cluster, so we retrieved a median number of cluster members of $N_{gal} \sim 14$. Due to this low number of galaxy members we could not use sophisticated membership techniques. Therefore, we assigned the cluster membership according to the galaxy radial velocity and distance from the cluster centre. At the end of the follow-up programme we were able to validate for the first time a total of 88 new galaxy clusters.

The second part of this thesis is focused in the cosmology, with the main aim of estimating the mass bias parameter $(1-b)$ through the characterisation of the scaling relation between the cluster masses calculated from dynamical and SZ proxies. The *Planck* Collaboration demonstrated that the mass bias is crucial to determine the cosmological parameters Ω_m and σ_8 by using the cluster number counts formalism. The *Planck* Collaboration showed that the latter are in tension with the parameters derived from CMB primary anisotropies, and that, by varying the mass bias parameter, this tension could be alleviated.

Since the $(1-b)$ should be a measure of the bias of the SZ mass estimation, it is extremely important to understand the possible biases in the dynamical mass estimate. It is impossible to obtain an accurate dynamical mass estimate if the velocity dispersion is biased. The nature of the biases may be statistical or physical, and in this thesis we studied both kinds of biases by using hydrodynamic simulations.

We tested three velocity dispersion estimators, namely biweight, gapper and standard deviation, and observed that they present a statistical bias in the low galaxy numbers regime. In order to correct this effect, we designed a receipt to obtain unbiased velocity dispersions in the whole N_{gal} regime.

Physical biases are mainly related to the cluster members sampling. For instance, due to the velocity dispersion radial profile a 5% bias is introduced when clusters are sampled in their cores only. We also observed that the velocity dispersion estimate obtained by using only the most massive galaxy members is biased by about 2%. However, the most important source of bias is the interlopers contamination, which overestimates the velocity dispersion by about 10%.

Furthermore, we demonstrated that even an unbiased velocity dispersion could lead to a biased estimate of the cluster mass. We defined new mass estimator, which takes into account this statistical effect.

In order to perform the cosmological analysis, we selected all clusters within the ITP sample with reliable velocity dispersion estimation (more than 7 members and no multiple detections). On the other hand, in order to improve the statistical significance of our study, we applied the cluster identification procedure to the PSZ1 clusters within the SDSS footprint as well. This way, we built a sample of 207 galaxy clusters. This sample is the largest catalogue of clusters for which both the SZ and dynamic masses have been estimated. Based on it and after applying all corrections, we found that the mass bias parameters is $(1-B) = 0.78 \pm 0.02$.

The compatibility of this result with the one obtained by the *Planck* Collaboration ensures that we are not able to alleviate the tension on the cosmological parameters. However, we were able to reduce the uncertainty on the mass bias down to $\sim 2\%$ for the first time, based on velocity dispersion mass estimators. Therefore, although the parameter estimates will not vary, our result will allow us to reduce the uncertainty on the combination of Ω_m and σ_8 by about a factor ~ 2 with respect to previous studies. Other solutions are discussed.

Resumen

Este trabajo de tesis está dedicado al estudio de los Cúmulos de Galaxias como herramientas fundametales en Cosmología. El trabajo está dividido en dos partes principales: la primera puramente observacional, mientras que la segunda está orientada a la preparación de herramientas para análisis cosmológicos.

Las observaciones se han desarrollado en el marco de la validación de contrapartidas ópticas de las fuentes de efecto Sunyaev-Zeldovich (SZ), observadas por el satélite *Planck* en el hemisferio norte e incluidos en el catalogo PSZ1. Estos 212 candidatos a cúmulos se han observado durante un International Time Project (ITP) de dos años, usando instalaciones del Observatorio del Roque de los Muchachos (ORM) en la isla de La Palma.

Durante el programa observacional, cada objeto ha pasado por un proceso de validación de dos fases: una fotométrica y una espectroscópica. En la primera fase, hemos realizado imágenes en los filtros g', r' and i' con los instrumentos WFC/INT y ACAM/WHT. De esta forma, hemos obtenido fotometría profunda de la mayoría de los candidatos, alcanzando magnitudes límite en el filtro r' de 23.2 y 23.8, para las cámaras WFC/INT y ACAM/WHT, respectivamente. Esto nos ha permitido de estimar sus corrimientos al rojo fotométricos hasta $z_{phot} \sim 0.8$ y sus riquezas. En la segunda fase, se han realizado observaciones espectroscópicas de los cúmulos previamente confirmados durante la primera fase, usando los espectrógrafos DOLORES/TNG y OSIRIS/GTC para observar los cúmulos a $z_{phot} \leq 0.4$ y $z_{phot} > 0.4$, respectivamente. El objetivo del seguimiento espectroscópico es confirmar dichos cúmulos y caracterizar sus propiedades físicas, como la dispersión de velocidad y la masa. Con el fin de observar el mayor número posible de miembros del cúmulo, se ha utilizado la técnica de Espectrosopía Multi-Objetos (MOS). Debido al alto numero de candidatos sólo se ha podido observar una máscara por cúmulo, obteniendo así un número mediano de miembros $N_{gal} \sim 14$. Un número tan bajo de galaxias miembro no permite el uso de técnicas sofisticadas de asignación de pertenencia al cúmulo. Por lo tanto, se han seleccionado los miembros de los cúmulos de acuerdo con las velocidades radiales y distancia desde el centro.Al final del programa de seguimiento hemos sido capaces de validar 88 nuevos cúmulos de galaxias.

La segunda parte de este trabajo tiene como objeto evaluar el sesgo en la estimación de la masa de los cúmulos, $(1 - b)$. Esto se ha realizado en base a la caracterización de la relación de escala entre las masas dinámica y SZ. La Colaboración *Planck* ha demostrado que el valor del sesgo es un parámetro crucial para determinar los parámetros cosmológicos Ω_m y σ_8 usando el formalismo de cuentas de cúmulos. Además, estos parámetros están en tensión con los

calculados usando las anisotropías primarias del Fondo Cósmico de Microondas (CMB) y que esta tensión puede ser atenuada variando el valor del sesgo.

Considerando que el parámetro $(1-b)$ es una medida del sesgo en la estimación de la masa SZ del los cúmulos, es muy importante comprender los posibles sesgos en la estimación de la masa dinámica. Es imposible obtener una correcta medida de la masa dinámica si la dispersión de velocidad está sesgada. La naturaleza de estos sesgos puede ser tanto estadística como física, aquí se estudian ambos tipos de sesgos haciendo uso de simulaciones hidro-dinámicas.

Se han comparado tres diferentes estimadores de la dispersión de velocidad (biweight, gapper y desviación típica) y se ha observado la presencia de un sesgo estadístico en el régimen de bajo número de galaxias miembro, que se ha corregido definiendo nuevos estimadores no sesgados.

Los sesgos físicos están relacionados principalmente con el muestreo de los miembros. Debido al perfil radial de la dispersión de velocidad, muestrear únicamente el centro de cúmulo introduce un sesgo de aproximadamente 5%. Se ha observado que el valor de la dispersión está sesgado aproximadamente un 2% cuando se utilizan solo las galaxias más masivas para calcularlo. Sin embargo, la mayor fuente de sesgo es la contaminación por galaxias no ligadas al cúmulo, que tienden a sobreestimar la dispersión de velocidad aproximadamente un 10%.

Hemos demostrado que incluso una dispersión de velocidad no sesgada podría llevar a una estimación sesgada de la masa. Por ello, hemos definido nuevos estimadores de la masa de los cúmulos teniendo en cuenta este efecto estadístico.

Para llevar a cabo el análisis cosmológico, se han seleccionado los cúmulos más fiables de la muestra del ITP y para mejorar el poder estadístico de la muestra, se ha aplicado el procedimiento de identificación de cúmulos también a aquellos pertenecientes al catálogo PSZ1 y que están incluidos en el archivo SDSS. De esta forma se ha construido un catalogo de 207 objetos, que resulta ser el más extenso con medidas tanto de la masa SZ como de la dinámica. Usando este catálogo, hemos encontrado un valor del sesgo entre estas masas de $(1-B) = 0.78 \pm 0.02$. Aunque la compatibilidad de este resultado con aquel obtenido por la Colaboración *Planck* no permite disminuir la tensión en la estimación de los parámetros cosmológicos, es la primera vez que se reduce el error en el sesgo a aproximadamente el 2% usando estimadores de masa basados en la dispersión de velocidad. Por lo tanto, aunque los valores de los parámetros cosmológicos no cambien, nuestro resultado permite disminuir la incertidumbre en la combinación de Ω_m y σ_8 en un factor 2, aproximadamente, con respecto a estudios previos.

Sinossi

Questa tesi è rivolta allo studio degli Ammassi di Galassie come strumenti d?indagine per la cosmologia. Il lavoro è diviso in due parti; la prima è puramente osservativa, mentre la seconda è dedicata alla predisposizione degli strumenti per le analisi cosmologiche.

La sezione osservativa è stata sviluppata nella cornice della conferma delle controparti ottiche delle sorgenti dell'effetto Sunyaev-Zeldovich (SZ), osservate dal satellite *Planck* nell'emisfero nord ed incluse nel catalogo PSZ1. Durante un International Time Project (ITP), 212 target sono stati osservati con le apparecchiature dell'Osservatorio del Roque de Los Muchachos (ORM), sull'isola di La Palma.

Durante il programma osservativo ogni target è stato sottoposto ad un processo di validazione in due fasi, una fotometrica ed una spettroscopica. Nella prima fase sono state acquisite immagini nei g', r' and i', con gli strumenti INT/WFC ed WHT/ACAM. Tramite questo approccio abbiamo ottenuto una fotometria profonda per la maggior parte degli oggetti, raggiungendo magnitudini nel filtro r' di circa 23.2 e 23.8, rispettivamente per la WFC/INT e ACAM/WHT, permettendoci di stimarne il redshift fotometrico fino a $z_{phot} \sim 0.8$. Inoltre, utilizzando queste informazioni fotometriche, è stato possibile stimare la ricchezza degli ammassi, confermando quegli oggetti con $R \geq 15$.

Nella seconda fase è stata eseguita la spettroscopia degli ammassi precedentemente confermati attraverso la fotometria. Usando gli spettrografi TNG/DOLORES e GTC/OSIRIS sono stati osservati gli ammassi a $z_{phot} \leq 0.4$ e $z_{phot} > 0.4$, rispettivamente. L'obiettivo della verifica spettroscopica è di confermare e caratterizzare le proprietà fisiche degli ammassi di galassie quali la dispersione di velocità e la massa. Al fine di osservare il maggior numero possibile di membri dell'ammasso, è stata usata la tecnica della Spettroscopia Multi-Oggetto (MOS). A causa del numero elevato di candidati si è potuto osservare ogni cumulo con solo una maschera, ottenendo così un numero mediano di membri $N_{gal} \sim 14$. Un numero così basso di galassie membri non permette l'uso di tecniche sofisticate per assegnare l'appartenenza all'ammasso, per cui i membri degli ammassi sono stati invece selezionati secondo la loro velocità radiale e distanza dal centro, applicando un taglio in velocità a 2.5σ dalla velocità media e di 2.5 Mpc in distanza radiale. Una volta che è stata stimata la dispersione di velocità, si confermano quegli ammassi che presentano $\sigma \geq 500\,\mathrm{km\,s^{-1}}$ e $\sigma \geq 650\,\mathrm{km\,s^{-1}}$ a $z \leq 0.2$ y $z > 0.2$, rispettivamente. Alla fine del programma osservativo siamo stati capaci di confermare 88 nuovi ammassi di galassie.

La seconda parte di questo lavoro è stata orientata alla cosmologia, con l?obiettivo di stimare l'errore nella stima della massa degli ammassi $(1 - b)$

grazie alla caratterizzazione della relazione di scala tra la massa dinamica e quella SZ. La Collaborazione *Planck* ha dimostrato che il valore dell'errore è un parametro cruciale per determinare i parametri cosmologici Ω_m e σ_8 usando il formalismo del conteggio degli ammassi. Per di più, questi parametri sono in contrasto con quelli calcolati usando le anisotropie primarie del Fondo Cosmico a Microonde (CMB) e questa tensione può essere attenuata cambiando il valore di questo errore.

Considerando che il parametro $(1-b)$ è una misura dell'errore nella stima della massa SZ degli ammassi, è molto importante indagare i possibili errori nella stima della massa dinamica. È impossibile ottenere una misura corretta della massa dinamica se la dispersione di velocità stimata è non corretta. La natura di questi errori può essere sia statistica che fisica, qui sono stati analizzati entrambi i tipi di errori facendo uso di simulazioni idrodinamiche. Sono stati confrontati tre differenti stimatori della dispersione di velocità (biweight, gapper e deviazione standard) ed è stata osservata la presenza di un errore statistico nel regime di un basso numero di galassie membri, che abbiamo corretto definendo nuovi stimatori corretti.

Gli errori fisici sono principalmente relativi al campionamento dei membri. A causa della forma del profilo radiale della dispersione di velocità, il campionamento del solo centro dell'ammasso introduce un errore approssimativamente del 5%. Si è inoltre osservato che il valore della dispersione di velocità presenta un errore di circa il 2% quando si usano solo le galassie più massicce per calcolala. Tuttavia, la fonte principale di errore è la contaminazione dovuta a galassie non legate all'ammasso, che tendono a sovrastimare la dispersione di velocità approssimativamente del 10%.

Abbiamo dimostrato che finanche una dispersione di velocità corretta può portare ad una errata stima della massa. Per questo, abbiamo definito nuovi stimatori della massa degli ammassi tenendo conto di questo effetto statistico.

Al fine di eseguire l'analisi cosmologica abbiamo selezionato gli ammassi più affidabili del campione ITP e, per migliorare il potere statistico del campione, abbiamo applicato il procedimento di identificazione degli ammassi anche a quelle sorgenti del PSZ1 incluse nell'archivio SDSS. In questo modo abbiamo costruito un catalogo di 207 oggetti, che risulta essere il più grande catalogo di ammassi per cui sono state misurate sia la massa SZ che quella dinamica. Usando questo catalogo, e dopo aver applicato tutte le correzioni, abbiamo trovato che il parametro dell'errore sulla massa è $(1-B) = 0.78 \pm 0.02$. Sebbene la compatibilità di questo risultato con quello ottenuto dalla Collaborazione *Planck* non permetta di ridurre l?incopatibilità nella stima dei parametri cosmologici, questa è la prima volta che si riduce l'incertezza di questo errore a circa il 2% usando stimatori di massa basati sulla dispersione di velocità. Conseguentemente, nonostante il valore dei paramenti cosmologici non cambi, il nostro risultato permette di ridurre l'incertezza della combinazione di Ω_m e σ_8 di un fattore circa 2 rispetto agli studi precedenti.

Contents

List of Acronyms

2MASS	Two Micron All-Sky Survey
160SD	160 square degree ROSAT Survey
400SD	400 square degree ROSAT Cluster Survey
ACAM	Auxiliary-port CAMera
ACO	Abell et al. (1989) cluster Catalog
ACT	Atacama Cosmology Telescope
ACTPol	Atacama Cosmology Telescope Polarimeter experiment
AGN	active galactic nuclei
AMF	Adaptive Matched Filter
BAO	Baryon acoustic oscillations
BBN	Big Bang nucleosynthesis
BCES	bivariate correlated errors and intrinsic scatter
BCG	Bright Central Galaxy
BCS	ROSAT brightest cluster sample
BPZ	Bayesian Photometric Redshifts
BWT	Biweight
CCCP	Canadian Cluster Comparison Project
CCD	Charge-Coupled Device

CDM	cold dark matter
CFHT	Canada France Hawaii Telescope
CFHTLS	Canada France Hawaii Telescope Legacy Survey
CFHTLenS	Canada France Hawaii Telescope Lensing Survey
CIZA	Clusters in the Zone of Avoidance
CLASH	Cluster Lensing And Supernova survey with Hubble
CMB	Cosmic Microwave Background
CMBLens	CMB lensing
CMD	colour-magnitude diagram
CNB	Cosmic Neutrinos Background
COBE	Cosmic Background Explorer
COBRAS	Cosmic Background Radiation Anisotropy Satellite
CS82	Canada-France-Hawaii Telescope Stripe 82 Survey
DDT	Director's discretionary time
DE	Dark energy
DM	Dark matter
DOLORES	Device Optimized for the LOw RESolution
DR	Data Release
DRM	Differential Microwave Radiometer
DSS	Digitized Sky Survey
eBCS	Extended ROSAT Bright Cluster Sample
EFOSC	ESO Faint Object Spectrograph and Camera
EMSS	Einstein Extended Medium Sensitivity Survey
ESA	European Space Agency

ESO	European Southern Observatory
ESZ	*Planck* Early SZ catalogue
EXOSAT	European X-Ray Observatory Satellite
FRWL	Friedman-Robertson-Walker-Lemaître
FWHM	Full width at half maximum
FoF	Friend-of-Friend
FoV	Field-of-view
GAP	gapper
GC	Galaxy Cluster
GL	Gravitational lensing
GMBCG	Gaussian Mixture Brightest Cluster Galaxy
GMOS	Gemini Multi-Object Spectrograph
GNFW	Generalized Navarro–Frenk–White profile
GR	General Relativity
GTC	Gran Telescopio Canarias
GUI	graphical user interface
HEAO	High Energy Astronomy Observatory Program
HEMT	High-electron-mobility transistor
HFI	High Frequency Instrument
HSC-SSP	Hyper Suprime-Cam Subaru Strategic Program
IAC	Instituto de Astrofísica de Canarias
ICM	Intra-cluster medium
IMDI	Interactive Mask Design Interface
INAF	Istituto Nazionale di Astrofisica

ING	Isaac Newton Group
INT	Isaac Newton Telescope
IR	Infra-red
IRAM	Institut de Radioastronomie Millimétrique
ITP	International Time Project
InP	indium phosphide
KID	kinetic inductance detector
LFI	Low Frequency Instrument
LIFU	Large fixed Integral-Field Unit
LP15	long-time programme 128-MULTIPLE-16/15B
LR	Low Resolution
LS	Long-Slit
LSS	Large Scale Structure
LoCuSS	Local Cluster Substructure Survey
LoS	line-of-sigh
MACHOs	Massive Compact Halo Objects
MACS	MAssive Cluster Survey
MAMBO	Max *Planck* MillimeterBolometer Array
MCMC	Monte Carlo Markov Chain
MCXC	Meta-Catalog of the compiled properties of X-ray detected Clusters of galaxies
MD	MaskDesigner tool
MMF	matched multi-filter
MOS	Multi-Object Spectroscopy
MPG	Max *Planck* Gesellschaft

NASA	National Aeronautics and Space Administration
NAT	narrow-tail radio sources
NED	NASA/IPAC Extragalactic Database
NEP	North Ecliptic Pole Deep survey
NFW	Navarro–Frenk–White profile
NIKA	Neel-IRAM-KID-Array
NORAS	Northern ROSAT All-Sky
NOT	Nordic Optical Telescope
NTT	New Technology Telescope
odr	Orthogonal distance regression
ORM	Roque de Los Muchachos Observatory
OSIRIS	Optical System for Imaging and low-Intermediate-Resolution Integrated Spectroscopy
OVRO	Owens Valley Radio Observatory
PLA	*Planck* Legacy Archive
PSF	Point Spread Function
PSM	*Planck* Sky Model Simulation
PSZ	*Planck* Sunyaev-Zeldovich sources catalogue
PlCS	*Planck* cosmological sample
PwS	Powell Snakes
RASS	ROSAT All-Sky Survey
RCSLenS	Red Cluster Sequence Lensing Survey
REFLEX	ROSAT-ESO Flux-Limited X-Ray
REXCESS	Representative XMM-Newton Cluster Structure Survey
RGB	Red-Green-Blue

RS	red sequence
RSS	Robert Stobie Spectrograph
RTT150	Russian Turkish 1.5 m Telescope
SALT	Southern African Large Telescope
SAMBA	Satellite for Measurement of Background Anisotropies
SDSS	Sloan Digital Sky Survey
SGP	south Galactic pole
SHARC	Serendipitous High-Redshift Archival ROSAT Cluster
SN	supernova
SNeIa	supernovae type Ia
SNR	Signal to noise ratio
SPT	South Pole Telescope
STScI	Space Telescope Science Institute
SZ	Sunyaev-Zeldovich
SZE	Sunyaev-Zeldovich effect
TFOSC	TÜBİTAK Faint Object Spectrograph and Camera
TNG	Telescopio Nazionale Galileo
UCO	University of California Observatories
UPP	Universal Pressure Profile
USNO	United States Naval Observatory
WARPS	Wide Angle ROSAT Pointed Survey
WCC	WEAVE Cosmological Cluster Survey
WEAVE	WHT Enhanced Area Velocity Explorer
WFC	Wide Field Camera

WFI	Wide-Field Imager
WHL12	Wen et al. (2012) cluster catalogue
WHT	William Herschel Telescope
WIMPs	Weakly Interacting Massive Particles
WISE	Wide-field Infrared Survey Explorer
WL	Weak Lensing
WMAP	Wilkinson Microwave Anisotropy Probe
WtG	Weighing the Giants
XMM-Newton	X-ray Multi-Mirror-Newton Telescope
ZwCl	Zwicky Cluster

1

Introduction: Galaxy Clusters as Cosmological tools

This thesis is dedicated to the study of Galaxy Clusters (hereafter GCs) as cosmological tools. For instance, their abundance as a function of mass and redshift, namely the Cluster Number Counts, is a powerful probe (e.g. Carlstrom et al. 2002; Allen et al. 2011), allowing us to set constraints on cosmological parameters such as Dark Matter density or the amplitude of the primordial density fluctuations (e.g. Vikhlinin et al. 2009; Mantz et al. 2010). The work carried out during this thesis was focused on the analysis of the first *Planck* all-sky catalogues of Sunyaev-Zeldovich (SZ) sources, PSZ1 (Planck Collaboration XXIX 2014; Planck Collaboration XXXII 2015), and on the use of this catalogue as a reference sample for further Cosmological analyses. In this chapter, we review the theoretical and observational framework of GCs. We will briefly describe the theory of GC formation and then outline the principal observational methods to detect GCs and their use in Cosmological analyses. Finally, we will introduce the motivations and objectives of this work.

1.1 Galaxy Clusters formation: from the homogenous to the inhomogeneous Universe

In this section we introduce the theoretical background describing the formation of GCs as building blocks of the Large Scale Structure (LSS) of the Universe. Throughout the following sections, we use units where the speed-of-light is

$c = 1$. For a detailed description of the subject treated in this section see Weinberg (1972); Peebles (1980); Padmanabhan (1993); Liddle & Lyth (2000); Dodelson (2003).

1.1.1 Background

General Relativity (GR) is the underlying theory behind cosmological model. Formulated by Albert Einstein (Einstein 1916), it describes of gravity as a local distortion of space-time due to the presence of matter and energy through a set of non-linear differential equations:

$$R_{\mu\nu} - \frac{1}{2} g_{\mu\nu} R + \Lambda g_{\mu\nu} = 8\pi G \, T_{\mu\nu}, \tag{1.1}$$

where $R_{\mu\nu}$ and R are the Ricci curvature tensor and the Ricci's scalar (or curvature scalar), respectively, $g_{\mu\nu}$ is the metric tensor and $T_{\mu\nu}$ is the energy-momentum tensor

$$T_{\mu\nu} = (P + \rho)\, u_\mu u_\nu + P \, g_{\mu\nu}, \tag{1.2}$$

where ρ and P are the energy density and the pressure of the perfect fluid, respectively. Under the assumption of the *cosmological principle* (i.e an homogeneous and isotropic Universe) the solution of these equations is the Friedman-Robertson-Walker-Lemaître (FRWL) metric

$$ds^2 = -dt^2 + a(t)^2 \left[\frac{dr^2}{1 - kr^2} + r^2 \left(d\theta^2 + \sin^2 \theta d\phi^2 \right) \right], \tag{1.3}$$

where $a(t)$ is the scale factor, which takes into account the spatial expansion and k is a parameter that accounts for the spatial curvature taking values $0, -1, 1$ for a flat (no curvature), open (negative curvature) or closed (positive curvature) Universe, respectively. This metric defines an expanding, homogeneous and isotropic Universe. The dynamic of the expansion is described by the Friedmann equations, a set of differential equations obtained by solving Einstein's equations using the FRWL metric and the energy-momentum tensor of a perfect fluid

$$\left(\frac{\dot{a}}{a} \right)^2 = \frac{8\pi G}{3} \rho + \frac{\Lambda}{3} - \frac{k}{a^2}, \tag{1.4}$$

$$\frac{\ddot{a}}{a} = -\frac{4\pi G}{3} \left(\rho + 3P \right) + \frac{\Lambda}{3}, \tag{1.5}$$

1.1.1.1 Cosmic inventory

The combination of equations 1.4 and 1.5 lead to the formulation of the continuity equation of the cosmic fluid

$$\dot{\rho} = -3\frac{\dot{a}}{a}\left(\rho + P\right). \tag{1.6}$$

In order to solve Einstein's equations, we assume an energy-momentum tensor of a perfect fluid that is characterised by a constant equation of state

$$P = \omega\rho. \tag{1.7}$$

where the ω parameter accounts for the different nature of the cosmic fluid components. This relation allows us to solve equation 1.6 as a function of the scale factor and the ω parameter

$$\rho \propto a(t)^{-3(1+\omega)}. \tag{1.8}$$

This equation displays how different components of the cosmic fluid evolve with cosmic time. The cosmic fluid consists of three macro components: matter, radiation and Dark Energy (DE).

Dust

The term dust is referred to all the pressure-less matter, $\omega = 0$. This matter is divided into two different subcomponents:

- *Baryonic matter*: the ordinary matter made of protons, neutrons and electrons. It constitutes almost the 20% of the entire dust energy density;
- *Cold dark matter*: constitutes 80% of the dust budget and $\sim 25\%$ of the total energy density of the Universe. According to the *Standard Cosmological Model*, Cold Dark Matter (CDM) is a non-relativistic collisionless fluid that interacts only gravitationally with ordinary matter. The first evidence of the presence of CDM dates back to the early 1930s with the study of velocity dispersion of the Coma cluster (Zwicky 1933). Further evidence of the necessity of CDM came from the study of the rotational curves of spiral galaxies (Rubin & Ford 1970), strong and weak gravitational lensing analysis (Adelman-McCarthy et al. 2006) and the amplitude of the primordial perturbations (Peebles 1982). Although the nature of CDM remains extremely elusive, a plethora of hypotheses about it have

been proposed over the past decades. A part of the CDM consists of ordinary matter that we are not successful in observing, such as Massive Compact Halo Objects (MACHOs). However, the amount of this matter is not sufficient to explain the observational evidence. For this reason, a non-baryonic (i.e. made up of non-standard particles) Dark Matter (DM) has been theorized. Some examples of these particles are WIMPs (Weakly Interacting Massive Particles) and the axions.

Radiation

All relativistic species are catalogued under the name of radiation. This fluid has a non-zero pressure with $\omega = 1/3$. The principal relativistic species today are:

- *Photons*: the relativistic species par excellence. As a result of the expansion and cooling of the Universe, they decoupled from the heavier components during recombination, and reached us in the form of isotropic radiation, called *Cosmic Microwave Background* (CMB), with a temperature of ~ 2.7 K. The possibility of associating this radiation with that emitted by a black body allows us to calculate the energy density of photons independently of the cosmological model in $\sim 0.005\%$ of the total energy budget of the Universe.

- *Neutrinos*: Although the thermal history of the Universe suggests the presence of a Cosmic Neutrinos Background (CNB), this relic radiation is far from being directly detected. However, CMB and LSS analyses support indirect evidence of the presence of a CNB. (Planck Collaboration VI 2018a). Under the assumption of massless neutrinos, their energy density is calculated to be a fraction that of photons. Nevertheless, particle physicists had to introduce massive neutrinos to explain the oscillation between its three different flavours. Therefore, the density of neutrinos will also depend on the sum of their masses, which is considered one of the free parameters of cosmological models.

Dark Energy

At the end of the 1990s, with the use of SNeIa, the expansion of the Universe was found to be accelerating (Riess et al. 1998; Perlmutter et al. 1999). In order to explain this effect, the concept of *Cosmological Constant*, originally introduced by Einstein in his equations to obtain a static and stationary

Universe, was recovered. This constant, called Λ, is the simplest model of DE having $\omega = -1$. More complex DE models such as Quintessence, or DE models with evolving ω, were introduced in order to solve the coincidence (Steinhardt 1997) and the fine-tuning problem. Moreover, during recent decades, DE was also theorised as a scalar field or as a proof for a modification of the GR, such $f(R)$ (De Felice & Tsujikawa 2010). However, SNeIa, CMB and Baryon-Acoustic Oscillations (BAO) joint analysis favours the ΛCDM model (Planck Collaboration VI 2018a). For a more detailed description of DE models see Yoo & Watanabe (2012) and references therein. The DE is the most abundant component accounting for $\sim 70\%$ of the total energy density of the Universe today.

According to equation 1.8, the three macro component of the cosmic fluid evolve with scale factor as

$$\begin{aligned} \rho_m &\propto a^{-3}, \\ \rho_r &\propto a^{-4}, \\ \rho_\Lambda &= \text{const}, \end{aligned} \tag{1.9}$$

where ρ_m, ρ_r, ρ_Λ are the density of dust, radiation and DE, respectively.

1.1.1.2 Cosmic Evolution

The first of Friedman's equations, equation 1.4, relates the evolution of the Universe with its content. In order to quantify how the scale factor evolves with time, it is convenient to define the *Hubble* parameter as

$$H \equiv \frac{\dot{a}}{a}. \tag{1.10}$$

In other words, the Hubble parameter represents the expansion rate of the Universe. Lemaître (1927) connected the expansion rate to the Doppler effect observed in distant extra-galactic sources formulating the Hubble-Lemaître law (Lemaître 1927; Hubble 1929)

$$v = Hd, \tag{1.11}$$

where v is the *recessional velocity* and d is the distance of the source. A moving object that emits light in a certain wavelength λ is observed in a different wavelength λ_0. The measure of how much the wavelength is changed is a quantity called redshift

$$z \equiv \frac{\lambda_0 - \lambda}{\lambda}. \tag{1.12}$$

According to the Hubble-Lemaître law, the variation of wavelength is due to the expansion of the Universe, which is reflected in the different values of the scale factor today, a_0, and at the moment of the emission, $a(t)$

$$z = \frac{a_0}{a(t)} - 1. \tag{1.13}$$

Therefore, Equation 1.4 can be rewritten as a function of the redshift in the form

$$H(z)^2 = \frac{8\pi G}{3}\rho(z) - k\,(1+z)^2 + \frac{\Lambda}{3} \tag{1.14}$$

It is useful to define *critical density* as the density of a spatially flat Universe

$$\rho_c = \frac{3H^2}{8\pi G}, \tag{1.15}$$

and the *density parameter* as the density of cosmic fluid components ρ_i in units of critical density,

$$\Omega_i = \frac{\rho_i}{\rho_c}, \tag{1.16}$$

where the subscript i indicates each one of the cosmic fluid components. Consequently, assuming the evolution of the cosmic fluid components, equation 1.9, equation 1.14 can be recast as

$$H(z)^2 = H_0^2 \left[\Omega_m\,(1+z)^3 + \Omega_r\,(1+z)^4 + \Omega_\Lambda + \Omega_k\,(1+z)^2\right], \tag{1.17}$$

where H_0 is the *Hubble constant* at redshift $z = 0$.

Through this equation, we can infer the evolution of the Universe across cosmic time. The different evolution of cosmic fluid components allows us to divide the redshift story of the Universe into three epochs dominated by one single component. As discussed above, today DE is the dominant component. Going backwards across cosmic history, according to equation 1.9, the Universe falls into the matter-dominated era and then a smaller and hotter Universe radiation starts to rule, as shown in fig. 1.1.

1.1.2 Perturbations

The cosmological principle is a condition for solving Einstein's equations. At a very large scale, $\gtrsim$ 100 Mpc, the homogeneity and isotropy of the Universe are well proven. Nonetheless, a quick look at our neighbourhood tells us that, at a small scale, the Universe is evidently neither homogeneous nor isotropic. The filamentary structure observed nowadays is the consequence of

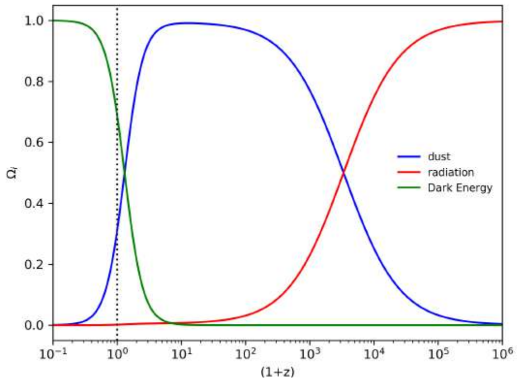

Figure 1.1: Redshift evolution of the density parameter of cosmic fluid components according to Planck Collaboration XIII (2016) cosmological parameters: $\Omega_m = 0.3075$, $\Omega_\Lambda = 0.6925$ and $\Omega_r = 5.389 \times 10^{-5}$.

the evolution of small inhomogeneities in the primaeval density field (Peebles 1980). The inflationary model (Guth 1981) states that perturbations arise from quantum fluctuations of the inflaton field (Liddle & Lyth 2000). According to the simplest single component inflaton model, the primaeval inhomogeneities field is Gaussian and adiabatic (Gordon et al. 2001), which means that the perturbation of a field can be expressed in terms of a time shift of the background, $\delta(t, \mathbf{x}) = \delta\rho/\dot{\rho}(t)$. Therefore, all components of the cosmic fluid have the same shift in time implying that $\delta_r = 4/3\delta_m$.

In this section, we show how small perturbations in the homogeneous background density field evolve in the LSS as described by the Newtonian perturbation theory. Although the Newtonian perturbation theory is only an approximation of the more general treatment in GR, it is an adequate approach in our case study of non-relativistic, sub-horizon perturbations in a matter-dominated Universe.

1.1.2.1 Linear theory

Let us assume a flat Universe filled by a non-relativistic, homogenous and isotropic fluid. Its dynamic is described by the continuity equation, the Euler equation and the Poisson equation solutions ρ_b, $\mathbf{v}_b$, p_b, ϕ_b are the density, velocity, pressure, and self-gravitatational potential of the fluid, respectively.

Let us consider an overdense region, whose dimensions are smaller than the Hubble radius, characterised by

$$\begin{aligned}
\rho(\mathbf{r},t) &= \rho_b(t) + \delta\rho(\mathbf{r},t),\\
p(\mathbf{r},t) &= p_b(t) + \delta p(\mathbf{r},t),\\
\mathbf{v}(\mathbf{r},t) &= \mathbf{v}_b(t) + \delta\mathbf{v}(\mathbf{r},t),\\
\phi(\mathbf{r},t) &= \phi_b(t) + \delta\phi(\mathbf{r},t),
\end{aligned} \tag{1.18}$$

where $\mathbf{r} = \mathbf{x}/a(t)$ and $\mathbf{v}$ are the comoving coordinates and velocity, respectively. The evolution of the perturbation is defined by

$$\frac{\mathrm{d}\rho(\mathbf{r},t)}{\mathrm{d}t} = -\frac{\rho(\mathbf{r},t)}{a(t)}\nabla\cdot\mathbf{v}(\mathbf{r},\mathbf{t}) = 0, \tag{1.19}$$

$$\frac{\mathrm{d}\mathbf{v}(\mathbf{r},\mathbf{t})}{\mathrm{d}t} = -\frac{\nabla p(\mathbf{r},t)}{\rho(\mathbf{r},t)a(t)} - \frac{\nabla\phi(\mathbf{r},t)}{a(t)}, \tag{1.20}$$

$$\frac{1}{a(t)^2}\nabla^2\phi(\mathbf{r},t) = 4\pi G\rho(\mathbf{r},t). \tag{1.21}$$

Defining the density contrast as $\Delta = \delta\rho/\rho_b$ allows us to determine if the problem can be studied in linear, $\Delta \ll 1$, or non-linear, $\Delta \geq 1$, regime.

If $\Delta \ll 1$, by combining the perturbed equations with those for the background, taking only the linear terms, and by recalling that the total temporal derivative is

$$\frac{\mathrm{d}}{\mathrm{d}t} = \frac{\partial}{\partial t} + \left(\mathbf{v}\cdot\frac{1}{a}\nabla\right), \tag{1.22}$$

one obtains the equation that depicts the behavior of the density contrast

$$\frac{\mathrm{d}^2\Delta(\mathbf{r},t)}{\mathrm{d}t^2} + 2\,\frac{\dot{a}}{a}\frac{\mathrm{d}\Delta(\mathbf{r},t)}{\mathrm{d}t} = \frac{c_s^2}{a^2}\nabla^2\Delta + 4\pi G\rho_b\Delta(\mathbf{r},t), \tag{1.23}$$

where $c_s^2 = \delta p/\delta\rho$ is the sound speed of the fluid. This equation is the one for a damped harmonic oscillator where the damping term comes from the expansion of the Universe. If one considers non-relativistic perturbations in a matter-dominated Universe, the term $c_s^2/a^2\ \nabla^2\Delta$ can be ignored. Therefore, the equation 1.23 becomes an equation depending on the time component only. Then, the density contrast can be considered as the product of two components, one purely spatial, and the other one only time-dependent

$$\Delta(\mathbf{r},t) = \Delta(\mathbf{r},0)\ \delta(t). \tag{1.24}$$

Equation 1.23 can be rewritten only taking into account the temporal part of the density contrast, as follows:

$$\ddot{\delta}(t) + 2\ H\dot{\delta}(t) = 4\pi G\rho_b\delta(t), \tag{1.25}$$

where the dot denotes the derivative with respect to cosmic time. Since in a matter-dominated Universe $a \propto t^{2/3}$, and consequently $H = \dot{a}/a = 2/3\ t$, the equation 1.25 becomes

$$\ddot{\delta}(t) + \frac{4}{3t}\dot{\delta}(t) - \frac{2}{3t^2}\rho_b\delta(t) = 0, \tag{1.26}$$

where, according to equation 1.14, $4\pi G\rho_b = 3/2H^2$. This equation admits solutions of the form $\delta = \delta_0\ t^n$. Therefore, equation 1.26 has two solutions for $n = -1$ and $n = 2/3$ corresponding to a decaying and a growing mode, respectively. The growing mode is responsible for the growth of the perturbations having

$$\delta(t) = \frac{\delta\rho}{\rho_b} \propto t^{2/3} \propto a. \tag{1.27}$$

This means that in a matter-dominated Universe, the perturbation growth is proportional to the scale factor. This behavior is followed until matter is the dominant component of the Universe. When the dominant component becomes the DE, the accelerated expansion of the Universe tends to hold down the growth of perturbations until it stops completely for $a >> 1$, with $a = 1$ today.

1.1.2.2 Non-linear theory

The linear perturbation theory we depicted in the previous section is valid until the density contrast is $\Delta \ll 1$. When $\Delta \lesssim 1$ this theory of the evolution of inhomogeneities loses its power to describe the structure formation and the LSS we observe today. For this task, a complete formulation of a non-linear theory is needed; one whose equations are effectively integrated numerically by N-body simulations. However, with some approximations, it is possible to obtain analytic solutions for simple models.

1.1.2.2.1 Spherical collapse model

The simplest model of non-linear evolution describes the collapse of a spherical overdensity of radius R and mean density contrast $\bar{\Delta}(r,t)$, in a homogenous background with density ρ_b. The simplicity and usefulness of this model consists in the fact that evolution of an overdense region can be reduced to that of a closed Universe. This evolution is characterised by an expansion followed by a collapse, and is led by simple energetic assumptions. Assuming that the overdensity follows the Hubble flow with negligible peculiar velocities, the kinetic and potential terms at $t = t_i$ are

$$K_i = \frac{H_i^2 r_i^2}{2}, \qquad U_i = -\frac{1}{2}H_i^2 r_i^2 \Omega_i \left(1 + \bar{\Delta}_i\right) = K_i\Omega_i \left(1 + \bar{\Delta}_i\right), \tag{1.28}$$

where $\Omega_i = \rho_b/\rho_{cr} = 1$ is the initial density parameter of the flat background Universe. The equation of motion can be solved in the parametric form

$$r = A\,(1-\cos\theta)\,, \qquad t = B\,(\theta-\sin\theta)\,, \tag{1.29}$$

where A and B are constants that can be determined studying the system at the *turn-around*, when $r = r_m$. At this moment, the kinetic energy goes to zero. The parameter θ leads the expected growth of r, until it reaches a maximum value r_m, and then it decreases. By following the evolution of a spherical overdensity, it is possible to understand how different the results are in linear and non-linear theory. The density contrast of a spherical overdensity is given by

$$\Delta_L = \frac{3}{5}\left(\frac{3}{4}\right)^{2/3}(\theta-\sin\theta)^{2/3} \tag{1.30}$$

$$\Delta = \frac{9}{2}\frac{(\theta-\sin\theta)^2}{(1-\cos\theta)^3} - 1 \tag{1.31}$$

in linear and non-linear theory, respectively. The main steps of the evolution of the overdensity are:

$\boldsymbol{\theta \to 0}$: in this case the linear perturbation theory has not yet broken down, hence

$$\Delta \sim \Delta_L. \tag{1.32}$$

$\boldsymbol{\theta = 2/3\pi}$: this θ corresponds to the transition to non-linearity, with

$$\Delta = 1{,}01, \qquad \Delta_L = 0.568. \tag{1.33}$$

$\boldsymbol{\theta = \pi}$: this is the turn-around, the moment of maximum expansion

$$\Delta \sim 4.6, \qquad \Delta_L \sim 1.06. \tag{1.34}$$

From this moment onwards, the overdensity starts to collapse.

$\boldsymbol{\theta = 2\pi}$: This is the moment in which the overdensity should be collapsed into a single point of infinite density. However, during the collapse the inhomogeneity undergoes the process called *violent relaxation*, in which it reachs a virial equilibrium and the collapse ends. Since the total energy has to be conserved, by applying the viral theorem, $|U_{vir}| = 2K_{vir}$, one can derive that $r_{vir} = 1/2r_m$, then

$$\Delta \sim 178, \qquad \Delta_L \sim 1.69. \tag{1.35}$$

Using the virial theorem we can also derive the scaling relations which relate the physical parameters of the overdensity with its mass. Once the sphere is collapsed, we have

$$|U_{vir}| = \frac{3GM^2}{5r_{vir}} = 2K_{vir} = M\sigma_v^2, \tag{1.36}$$

where σ_v is the velocity dispersion generated during the relaxation process, leading to

$$\sigma_v \propto M^{1/3}. \tag{1.37}$$

Another scaling relation appears taking into account that part of the sphere is constituted by baryonic mass in the form of a gas. From the assumption that the mass in a collapsed object has reached the hydrostatic equilibrium, the kinetic energy is a measure of the temperature of the mass, which leads to

$$T \propto M^{2/3}. \tag{1.38}$$

The theory of spherical collapse leads to a model of the structure in LSS. However, this is only an approximation, and, although the constant of proportionality of these scaling relations can be calculated from first principles (e.g. Padmanabhan 1993; Liddle & Lyth 2000), they must be fine-tuned by fitting the parameters in numerical simulations.

1.1.2.2.2 Simulations

The spherical collapse model we see so far, is the simplest model of the formation of a bound structure. However, it cannot explain the LSS as we observe it today. Its evolution, the ellipsoidal collapse model, along with the formation of *pancakes* structures describes something a bit more realistic. These models, however, miss a lot of important details that occur in real structure collapse. The only way to approximate this complexity is to turn to numerical simulations (see Kravtsov & Borgani 2012, for a review). A numerical simulation consists of following the dynamical evolution of DM and baryonic matter, within a fixed volume, given initial conditions prescribed by the cosmological model. The DM is a collisionless fluid, therefore its dynamics are regulated by the collisionless Boltzmann equation (or Vlasov equation). The high dimensionality of the phase-space (three coordinates and three velocities) makes its solution computationally expensive. This issue can be solved using Monte Carlo

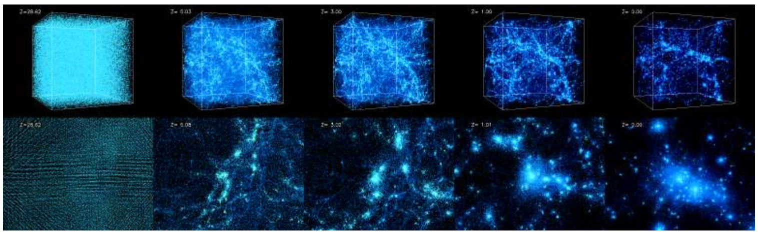

Figure 1.2: Different snapshots, from redshift $z \sim 30$ to the present, of a numerical simulation showing the evolution of LSS (upper panels) and of a galaxy group (lower panels). Credit: simulations performed by Andrey Kravtsov (The University of Chicago) and Anatoly Klypin (New Mexico State University) at the National Center for Supercomputer Applications. Visualisationsby Andrey Kravtsov.

techniques, discretising the phase space and solving the motion equation for a finite N number of particles (or *bodies*) interacting led by the gravitational field. Hydrodynamic methods are used, instead, to evolve the collisional particles, the baryonic mass.

A crucial concept for simulations is the *resolution*. A simulation is characterised by two parameters: the mass resolution and the spatial resolution. The first one determines the mass of the smallest particle, whereas the second one describes the size of each volume element, with a shape (box or sphere) and a density distribution (the number of particles in the volume), in which particles interacts. Ideally, in the limit of infinite spatial and mass resolution one could guess that the simulation can reach the convergence to a true solution. However, an increase in resolutions implies an increased computational time. Moreover, the simulation could also not converge to a true solution because the discretised equation might lead to a solution which is far from the real one (Borgani & Kravtsov 2011). Thanks to the development of the precision of parameter determination, the initial conditions of the simulations can be set in a less and less ambiguous way. With regards to technological progress, there has been an incredible evolution from the first pioneering simulations dating back to the 1970s (Peebles 1970; White 1976), to the ones from today (Borgani & Kravtsov 2011). The increasing mass resolution allows us to investigate the internal behaviour of the structures, e.g. the clusters density profile from Navarro-Frenk-White (NFW Navarro et al. 1997) or the scaling relation between the dynamical state of DM particles and cluster mass (e.g. Evrard et al. 2008). The improvement in computational power also allows us to add baryonic particles to the simulations. Hydrodynamical simulations, which reproduce X-ray observations quite well, have been incredibly useful in understanding the behaviour of the hot intra-cluster gas, e.g. the correlation between hot gas in hydrostatic equilibrium and mass (Evrard et al. 1996). Moreover, the implementation of even better feedbacks and cooling mechanisms are fundamental to the understanding of structure formation and galactic dynamics within the potential well of the collapsed structures. Figure 1.2 shows an example of different snapshots of DM-only simulation.

1.1.2.2.3 Mass Function

We have so far described the formation and evolution of a single bound object, starting from a small perturbation surrounded by a flat and homogenous back- ground. We also know that inflation has ended leaving a primaeval perturbed density field, whose perturbations were Gaussian distributed. Press & Schechter (1974) derived a model capable of estimating the abundance of collapsed objects starting from the properties of the primaeval density field fluctuations. The Press-Schechter formalism considers each peak of a smoothed linear density field exceeding a threshold Δ_c as a collapsed region. The threshold was selected to be the value of the collapsed object provided by the linear perturbation theory

$$\Delta_c = \Delta_L \sim 1.69. \tag{1.39}$$

The smoothing filter has a very important role because it allows us to select the volume of the object one wants to count, and erases all the structures on smaller scales. The selection of a top-hat filter, in real space, is very useful because it represents a sphere of radius R to which a mass can be associated.

Assuming an initial Gaussian field, the probability to find a region of radius R with a density contrast δ is

$$p(\Delta, R, z) = \frac{1}{\sqrt{2\pi}\sigma(R,z)} \exp\left(-\frac{\Delta^2}{2\sigma^2(R,z)}\right) \tag{1.40}$$

where $\sigma^2(R,z)$ is the variance of the smoothed density field, defined as

$$\sigma^2(R,z) \equiv \left\langle \left(\frac{\delta\rho}{\rho}\right)^2 \right\rangle = \int_0^\infty W^2(k,R)\mathcal{P}(k)\frac{\mathrm{d}k}{k}, \tag{1.41}$$

where $W(k,R)$ and $\mathcal{P}(k)$ are the Fourier transformation of the filter function and the power spectrum of the primaeval fluctuations, respectively. Integrating over the tail of the Gaussian probability function (equation 1.40) one obtain the fraction of volume that has collapsed

$$f(>M(R),z)=\frac{2}{\sqrt{2\pi}\sigma(R,z)}\int_{\Delta_c}^{\infty}\exp\left(-\frac{\Delta^2}{2\sigma^2(R,z)}\right)\mathrm{d}\Delta \tag{1.42}$$

where the factor 2 takes into account that in the primaeval Gaussian field, half of the Universe is underdense and, hence, will never overstep the threshold not forming structures. Although this factor is not very well justified in the original Press-Schechter theory (e.g. Liddle & Lyth 2000; Dodelson 2003), other formulations of the same formalism (e.g. Peacock & Heavens 1990; Bond et al. 1991; Bower 1991; Jedamzik 1995; Yano et al. 1996; Betancort-Rijo & Montero-Dorta 2006) give analytic explications to it. As mentioned before, the filtering radius is associated to a mass. An infinitesimal increase in the filtering radius corresponds to an increase of the mass of the collapsed objects from M to $M+\mathrm{d}M$. The fractional change in the collapsed volume per $\mathrm{d}M$ variation is obtained by differentiating equation 1.42 with respect to the filtering mass. By multiplying the present matter density by ρ_0, and dividing them by the mass M, the yield will be the coming matter density of the collapsed object, also called *mass function*

$$\frac{\mathrm{d}n(M,z)}{\mathrm{d}M}=-\sqrt{\frac{2}{\pi}}\frac{\rho_0}{M}\frac{\Delta_c}{\sigma^2(M,z)}\frac{\mathrm{d}\sigma(M,z)}{\mathrm{d}M}\exp\left(-\frac{\Delta^2}{2\sigma^2(M,z)}\right)\mathrm{d}M. \tag{1.43}$$

The integral of equation 1.43 gives the number of collapsed objects with mass above the filtering mass M

$$n(>M,z)=\int_{M}^{\infty}\frac{\mathrm{d}n(M,z)}{\mathrm{d}M}\,\mathrm{d}M. \tag{1.44}$$

It is extremely important to remark the dependence of the mass function on the present matter density and on the variance of the perturbations. For this reason, we can use the cluster number count to restrict the cosmological parameters Ω_m and σ_8. The latter is the variance of the primaeval density field observed in the CMB, smoothed on a scale radius of $8h^{-1}$Mpc that is the typical GC scale. However, Press-Schechter formalism is based on the spherical collapse model, which is only an approximation of structure formation, and underestimates the abundance of massive clusters (Jenkins et al. 2001). Therefore, a more accurate mass function formulation is needed for the cosmological application. This can be determined through cosmological simulations such as, for example, those determined by Tinker et al. (2008).

1.2 Galaxy Clusters and mass proxies

In the previous section, we give a brief description of the theoretical background of structure' formation. In particular, in section 1.1.2.2.3 we described the approximated formalism that provides the GC number density as a function of the mass and redshift and we also see that the latter quantity is sensitive to the cosmological parameters, Ω_m and σ_8. The number of clusters in a given volume of the Universe, as well as their mass, are fundamental elements for this kind of analysis. Consequently, cluster-detection methods, and how they are used to recover mass, are of crucial importance.

Galaxy Clusters are the biggest gravitationally bound systems in the Universe, with masses between $10^{13} - -10^{15}$ $M_\odot$. According to the hierarchical bottom-up scenario, they are the last structure to form (starting around $z \sim 2$), and are, therefore, the perfect tracers of the evolution of structures along the history of the Universe. Galaxy Clusters reside in the deepest potential wells, which are generated by matter overdensities, called Dark Matter (DM) halos (e.g. Springel 2005). Apart from DM, halos include baryonic matter in several forms and phases. In fact, in addition to the galactic component, there are also cold, molecular gas, warm and hot gases and non-thermal plasma which constitute the Intra-Cluster Medium (ICM). This multi-component nature allows us to see a GC from different points of view due to the fact that each component is characterised by peculiar physical processes that we investigate by observing different regions of the electromagnetic spectrum. Results of these observations are quantities that provide crucial information on the physics of the cluster. However, the cluster mass is not directly measurable, so we relate different observables to it through scaling relations. We refer to them as *mass proxies*.

1.2.1 X-ray

In this subsection, we focus our attention on the most energetic part of the electromagnetic spectrum capable of providing information about GCs. The extragalactic X-ray astrophysics was born between the 1960s and 1970s. Rocket-borne detectors allowed us to observe, in X-rays, several extra-galactic sources: M87 (Byram et al. 1966; Bradt et al. 1967), 3C273 and NGC-5128 (Bowyer et al. 1970), NGC1275 (Fritz et al. 1971). Later, the launch of the first X-ray satellite *Uhuru* made the first all-sky survey in this wavelength domain possible, considerably enhancing the number of cosmic X-ray sources (Giacconi et al. 1972, 1973, 1974; Forman et al. 1978). Consequently, the observation of X-ray emission in the Coma cluster (Gursky et al. 1971b,a) was a hint to the

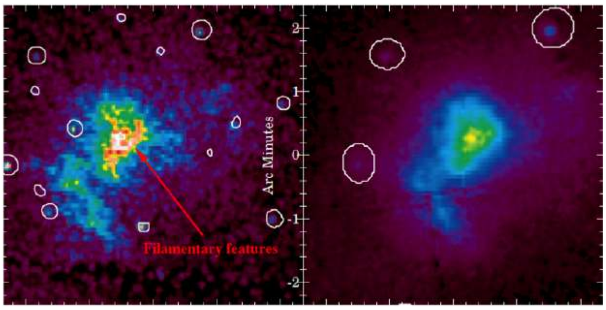

Figure 1.3: X-ray image of PSZ1 G180.25+21.03 (MACS J0717.5+3745) at $z = 0.55$, observed with Chandra (left panel) and *XMM-Newton* (right panel). In the Chandra image (left panel) are well visible AGN point sources (white circles) and the internal filamentary structures of the cluster are clearly visible. Due to the poor resolution of *XMM-Newton*, the same features are not visible in the right image. Credit: image courtesy of Iacopo Bartolucci, CEA, Université Paris-Saclay, Paris, FR.

correlation between diffuse X-ray emissions and groups of galaxies (Cavaliere et al. 1971). After Uhuru, other satellites were launched during the ?70s and the ?80s, both from NASA (e.g. HEAO-1, Einstein) and ESA (e.g. EXOSAT). The launch of ROSAT in 1990 was a turning point in GCs X-ray astronomy. The ROSAT All-Sky Survey (RASS, Voges et al. 1999a) was followed by several X-ray GCs catalogues: the nor- thern clusters (at high galactic latitude $> 20°$) were collected in the ROSAT Brightest Cluster Sample and its extension (BCS, eBCS Ebeling et al. 1998, 2000); the Clusters in the Zone of Avoidance (CIZA Ebeling et al. 2002; Kocevski et al. 2007), results of a systematic search of GCs at low galactic latitude ($< 20°$); the MAssive Cluster Survey (Ebeling et al. 2001, 2010, MACS) with bright and $z > 0.3$ objects; the ROSAT North Ecliptic Pole Survey (Henry et al. 2006, NEP) that surveyed the sky around the north ecliptic pole; the Northern ROSAT All-Sky (Böhringer et al. 2000, NORAS) and the ROSAT-ESO Flux Limited X-ray (Böhringer et al. 2004, REFLEX) covering the northern and the southern sky, respectively. All these catalogues were then unified and homogenised in the Meta-catalogue of X-ray detected clusters of galaxies (Piffaretti et al. 2011, MCXC). The ROSAT mission ended in 1999 and was replaced by the Chandra (NASA) and the *XMM-Newton* (ESA) satellites. These two satellites are complementary to the study of GCs. In fact, Chandra has a very high spatial resolution ($\sim 0.5''$), whereas *XMM-Newton* has higher sensitivity (see Figure 1.3). A detailed description of the two telescopes can be found in Jansen et al. (2001); den Herder et al. (2001); Strüder et al. (2001); Turner et al. (2001); Weisskopf et al. (2002) and references therein.

1.2.1.1 Observables

The potential well of GCs is filled by diffuse gas that corresponds to $\sim 15\%$ of the total cluster mass. During the phase of *violent relaxation*, at the end of the collapse (see section 1.1.2.2.1), adiabatic compression and shocks generated by supersonic motions heat the diffuse gas up to temperatures of several 10^7 K. At these temperatures, the gas is fully ionised and starts to emit *free–free* (or *bremsstrahlung*) radiation, due to the interaction between electrons and ions (Sarazin 1988). The intensity of bremsstrahlung emission (the number of photons emitted per unit of time in a defined energy interval) is proportional to the gas density squared through the emissivity

$$\epsilon(E,T) \propto g(E,T)\,T^{1/2}\,\exp\left(-\frac{E}{k_B\,T}\right) n_e^2, \tag{1.45}$$

where $g(E,T) \propto \ln\left(k_B\,T/E\right)$ is the Gaunt factor. Therefore, X-ray observations are useful in constraining the temperature and density of the ICM (Arnaud 2005).

A spectroscopic analysis is needed to estimate the ICM temperature (Arnaud 2005). The observed spectrum is fitted with an isothermal emission model. The emissivity determines the shape of the continuum of the spectrum. The exponential factor in equation 1.45 implies a cut-off for $E > k_B\,T$. For this reason, the continuum is not very sensitive to the temperature for energies below $k_B\,T$ (Böhringer & Werner 2010; Arnaud 2005). Therefore, the temperature is determined by the position of the exponential cut-off.

If the temperature is estimated from spectroscopic analyses, the gas density is calculated using X-ray images. Since the emissivity is not sensitive to the temperature at low energies, the images sent for this task are taken in the soft energy band ($E \lesssim 2$ keV). The emission measure along the line of sight at projected radius r, is given by

$$EM(r) = \int n_e^2\,\mathrm{d}l = \frac{4\pi(1+z)^4 S(\theta)}{\Lambda(T,z)}, \tag{1.46}$$

with $r = d_a(z)\,\theta$ where d_a is the angular distance and θ is the projected angle. The functions $S(\theta)$ and $\Lambda(T,z)$ are the surface brightness and the emissivity in the considered energy band, respectively. Due to the fact that the emission measure is the integration along the line-of-sight of the electron density squared, to obtain the density profile a deprojection is needed to obtain the density profile in order to estimate the tridimensional density profile. The simplest model, assuming spherical symmetry, is the isothermal β-model (Cavaliere & Fusco-Femiano 1976, 1978; Sarazin & Bahcall 1977), which gives

$$n(r) = n_0 \left[1 + \left(\frac{r}{r_c}\right)^2\right]^{-3\beta/2}, \tag{1.47}$$

$$S(\theta) = S_0 \left[1 + \left(\frac{\theta}{\theta_c}\right)^2\right]^{-3\beta+1/2}, \tag{1.48}$$

where $r_c = d_a\theta_c$ is the *core radius*, defined as the radius at which the density is the half the central value. This model is an extension of the simplest isothermal model that does not take into account that the self-gravitational potential of the clusters is not due only to the gas. In fact, the β parameter is defined as the ratio between the galaxies and gas velocity dispersion squared (Sarazin 1988).

1.2.1.2 Scaling Relations

Under the assumption of a relaxed cluster, one can assume that the diffuse gas has reached the hydrostatic equilibrium that means that the gradient of the self-gravitational potential is balanced in each point by the pressure gradient. Under the assumption of spherical symmetry and of an ideal gas, $p = \rho_g k_B T/\mu m_p$, where m_p and μ are the proton mass and the mean molecular weight, respectively. The hydrostatic condition leads to an equation for the cluster mass in terms of the temperature and the density profiles

$$M_{HE}(< r) = -\frac{k_B\ T(r)\ r}{\mu\ m_p\ G}\left(\frac{\mathrm{d}\ln n}{\mathrm{d}\ln r} + \frac{\mathrm{d}\ln T}{\mathrm{d}\ln r}\right). \tag{1.49}$$

Under the assumption of self-similar evolution of GC, the slopes of scaling relations are independent of cluster mass M (Kaiser 1986). It is trivial to derive that the hydrostatic equilibrium relation leads to

$$T(r) \propto \frac{M(< r)}{r} \propto M(< r)^{2/3}. \tag{1.50}$$

Once the $M - T$ relation is obtained and under the self-similarity assumption, it is possible to derive the relations between the cluster mass and all other X-ray properties. The first property is the bolometric X-ray luminosity defined as $_X = \int \rho_g \Lambda(T(r))\mathrm{d}^3\mathrm{r}$. From this definition, we have (Sarazin 1988; Kravtsov & Borgani 2012)

$$L_\mathrm{X} \propto \frac{M_g^2}{V} T^{1/2} \propto M^{4/3}. \tag{1.51}$$

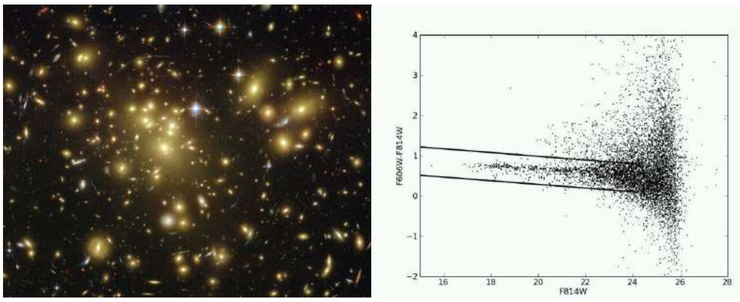

Figure 1.4: Left panel: RGB image of PSZ1 G045.85+57.71 (Abell 1689) from Hubble Space Telescope. Credit: NASA, N. Benitez (JHU), T. Broadhurst (Racah Institute of Physics/The Hebrew University), H. Ford (JHU), M. Clampin (STScI), G. Hartig (STScI), G. Illingworth (UCO/Lick Observatory), the ACS Science Team and ESA. Right Panel: colour-magnitude diagram from Bañados et al. (2010).

where M_g is the gas mass and V is the volume. The second relevant quantity is the entropy of the ICM,

$$K_{\rm X} \equiv \frac{k_B\, T}{n^{2/3}} \propto T \propto M^{2/3}. \qquad (1.52)$$

Finally there is the gas thermal energy $Y_{\rm X}$

$$Y_{\rm X} \equiv M_g\, T \propto M^{5/3}. \qquad (1.53)$$

The last quantity is very important in the SZ analysis, as we will see in section 5.1. All the scaling relations we sketched above are valid under the prescription that their slopes do not depend on the halo mass. However, observations and numerical simulations show that there are deviations from predicted slopes, even if the assumption of self-similarity is not broken (Arnaud & Evrard 1999; Nagai 2006; Stanek et al. 2010). Therefore, the slopes of the scaling have to be refitted using numerical simulations.

1.2.2 Optical and near-Infrared mass proxies

Observations in visible light was the first methodology used to detect GCs. Since the GCs visible and near-infrared radiation is mainly due to the light emitted by stars in galaxies, clusters are identified as regions with overdensities of galaxies characterised by the same colour. In fact, according to the hierarchical structure formation, major mergers lead to a galaxy population of GCs

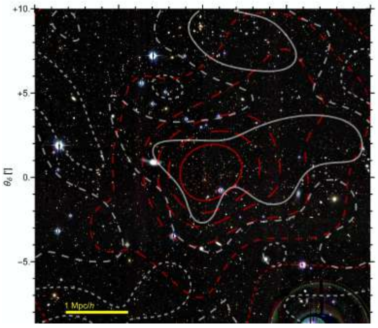

Figure 1.5: Composition of the CFHTLS g', $r'$and i'band images of the cluster PSZ1 G099.84+58.45. White contours follow the DM matter distribution reconstructed from weak lensing analysis, whereas the red ones follow the distribution of the galaxies with photometric redshift within $z_{phot} = \pm 0.06(1 + z_{cl})$, with z_{cl} is the redshift of the cluster. Credit: Sereno et al. (2018)

dominated by early-type galaxies (elliptical and lenticular) occupying a tight locus in colour-magnitude diagrams called red sequence (see right panel of Figure 1.4). Moreover, spectroscopical follow-ups, although extremely expensive in terms of telescope and analysis time, allow us to measure the radial velocity for tens and up to a thousand cluster members. Statistical estimators, applied to these velocities, are used to derive the velocity dispersion of the clusters. The virial relation in equation 1.38 allows the computation of the cluster mass. Since one of the goals of this work is the optical characterization of SZ selected GCs, we will give a more complete description of cluster detection techniques in chapter 2. In this section, we focus our attention on another methodology that allows the inference of cluster DM distribution from optical and near-infrared observation: gravitation lensing.

1.2.2.1 Gravitational Lensing

One of the most important tests of GR was obtained in 1919, after the Eddington expedition that confirms the deflection of the light of a background star caused by the gravitational potential of the Sun (Dyson et al. 1920). In the '30s Zwicky suggests that galaxies , could be used as "natural telescopes" (Zwicky 1937a,b) through the use of the gravitational lensing (GL) effect. However, only thirty years later, gravitational lensing equations were formalized and used for cosmological purposes (Wambsganss 1998). Sjur Refsdal used gravitational lensing to calculate the Hubble constant and to estimate the mass of a lens galaxy (Refsdal 1964). The first study that relates clusters of galaxies and lensing dates back to the early seventies (Noonan 1971). However, the first evidences of clusters acting as gravitational lenses are from the late eighties, when giant arcs (strong lensing) were observed in A370 (Soucail et al. 1987; Lynds & Petrosian 1989) and CL2244-02 clusters (Lynds & Petrosian 1989) and when background galaxies distortions (weak lensing) induced by the A1689 and CL1409+52 clusters was detected (Tyson et al. 1990).

Lensing formalism

The formalism of gravitational lensing is based on the tracking of light rays coming from a source and bent by a gravitational potential that acts as a lens. In other words, the lens equation arises from the solution of the null geodesic equation in a curved space-time under some assumptions (Umetsu 2010):

- Minkowski space time perturbed by isolated mass distribution (single lens approximation);
- small deflection angles;
- the size of the lens is negligible with respect to the distances between the lens, the source and the observer (thin lens approximation).

Its expression is

$$\boldsymbol{\beta}(\boldsymbol{\theta}) = \boldsymbol{\theta} + \boldsymbol{\alpha}(\boldsymbol{\theta}), \tag{1.54}$$

where $\boldsymbol{\beta}$ and $\boldsymbol{\theta}$ are the position of the source in the source plane, and the position of the source image on the lens plane, and where $\boldsymbol{\alpha}$ is the deflection angle. It is very important to remark that generally the lens equation describes a non-linear transformation between the angles $\boldsymbol{\beta}$ and $\boldsymbol{\theta}$. This means that at a given source position, $\boldsymbol{\beta}$ may correspond to different solutions of $\boldsymbol{\theta}$, which are the positions of the multiple images of the source in the sky.

The source plane can be mapped on the lens plane through the Jacobian matrix $\mathcal{A}$

$$\mathcal{A} = (1 - \kappa(\boldsymbol{\theta})) \begin{pmatrix} 1 & 0 \\ 0 & 1 \end{pmatrix} - \begin{pmatrix} \gamma_1(\boldsymbol{\theta}) & \gamma_2(\boldsymbol{\theta}) \\ \gamma_2(\boldsymbol{\theta}) & -\gamma_1(\boldsymbol{\theta}) \end{pmatrix}, \tag{1.55}$$

where $\kappa(\boldsymbol{\theta})$, $\gamma_1(\boldsymbol{\theta})$ and $\gamma_2(\boldsymbol{\theta})$ are the convergence and the two component of the complex shear $\gamma(\boldsymbol{\theta}) \equiv \gamma_1(\boldsymbol{\theta}) + i\gamma_2(\boldsymbol{\theta})$.

Convergence, shear and magnification describe the properties of source images induced by the gravitational lensing effect:

Convergence: it represents how the lens focuses the light. It is proportional to the projected mass density of the lens

$$\kappa(\boldsymbol{\theta}) = \frac{\Sigma_m(\boldsymbol{\theta})}{\Sigma_{cr}}, \tag{1.56}$$

where

$$\Sigma_{cr} \equiv \frac{c^2}{4\pi G}\frac{D_S}{D_L D_{LS}} \tag{1.57}$$

is the *critical surface mass density.* Although the convergence is directly related to the lens mass, it is not an observable but rather a derived quantity;

Gravitational shear: the main cause of the deformation of a background source image. Shear itself is not directly observable, but what is indeed observable, is the *reduced shear*

$$g(\boldsymbol{\theta}) = \frac{\gamma(\boldsymbol{\theta})}{1-\kappa(\boldsymbol{\theta})}. \tag{1.58}$$

Unfortunately, the invariance of $g(\boldsymbol{\theta})$ under the transformations

$$\kappa(\boldsymbol{\theta}) \rightarrow \lambda\kappa(\boldsymbol{\theta}) + (1-\lambda)\,, \qquad \gamma(\boldsymbol{\theta}) \rightarrow \lambda\gamma(\boldsymbol{\theta}), \tag{1.59}$$

with λ an arbitrary constant, do not allow a univocal determination of the κ-profile (Umetsu 2010). This effect known as *mass-sheet degeneracy*, has been studied by several authors that found that degeneracy can be broken measuring magnification (e.g. Broadhurst et al. 1995; Liesenborgs et al. 2008; Umetsu 2010);

Magnification: the measurement of how much the image flux is enhanced with respect to the source one. The lens focusing the light rays causes an area distortion. However, Louville's theorem assures that the surface brightness must be conserved. It follows a flux variation equal to the ratio between the image and the source solid angles

$$\mu = \frac{(\boldsymbol{\theta})}{(\boldsymbol{\beta})}\frac{\mathrm{d}\boldsymbol{\theta}}{\mathrm{d}\boldsymbol{\beta}} = \frac{1}{\det\mathcal{A}} = \frac{1}{(1-\kappa)^2 - |\gamma^2|}. \tag{1.60}$$

Once the convergence profile has been reconstructed, it can be used to fit the parameters of the underling density distribution. By assuming a spherical symmetry for the cluster, the projected 3D NFW density profile is (Bartelmann

1996; Keeton 2001)

$$\Sigma(x) = \begin{cases} \frac{2\rho_s r_s}{x^2-1}\left(1 - \frac{2}{\sqrt{x^2-1}}\arctan\sqrt{\frac{x-1}{x+1}}\right) & (x > 1) \\ \frac{2\rho_s r_s}{x^2-1}\left(1 - \frac{2}{\sqrt{1-x^2}}\operatorname{arctanh}\sqrt{\frac{1-x}{1+x}}\right) & (x < 1) \\ \frac{1}{3} & (x = 1) \end{cases} \tag{1.61}$$

where $x = r/rs$.

In this subsection, we gave a very brief introduction of gravitational lensing formalism. A more extensive treatment is not in the scope of this work and can be found in e.g. Broadhurst et al. (1995); Wambsganss (1998); Umetsu (2010) and references therein.

1.2.3 Radio

Galaxy Clusters can also be detected in the radio domain. In particular, in the region characterized by millimetric wavelengths. In GCs there are galaxies that can be associated with radio emission, e.g. the narrow-tail radio sources (NAT, e.g. Wellington et al. 1973; O'Dea & Owen 1986; O'Dea et al. 1986). Moreover, galaxies can be associated with extended radio emission, e.g. radio halos (e.g. Large et al. 1959; Willson 1970; Govoni et al. 2005; Feretti & Giovannini 2008), radio mini-halos (e.g. Baum & O'Dea 1991; Burns et al. 1992; Giovannini & Feretti 2000; Bacchi et al. 2003; Rizza et al. 2000; Gitti et al. 2004, 2007) and radio relics (e.g. Subrahmanyan et al. 2003; Kempner & Sarazin 2001). This is not a common property of GCs, however, since an extended radio emission has been detected only in 10% of GCs (Ferrari et al. 2008).

The principal manner of detecting GCs in the radio wavelength is to observe the trace of the interaction of the ICM with CMB photons, known as Sunyaev-Zeldovich effect (Sunyaev & Zeldovich 1970, 1972).

1.2.3.1 The Sunyaev-Zeldovich effect

The small spectral distortion induced on the CMB spectrum by the scattering of CMB photons off high energy electrons takes the name of Sunyaev-Zeldovich effect. The result of this interaction, an inverse Compton scattering, is a boost in the CMB photon energy of $k_B\ T = m_e\ c^2$, with k_B being the Boltzmann constant, T the electron temperature and m_e the electron mass. This increased energy is reflected in a small ($T_{CMB} \lesssim 1$ mK) distortion in the CMB spectrum. The detailed calculation can be found in several reviews (Sunyaev & Zeldovich 1980; Rephaeli 1995; Birkinshaw 1999) as well as in the original papers (Sunyaev & Zeldovich 1970, 1972). The distortion of the almost pure blackbody

CMB spectrum can be expressed in terms of temperature changes ΔT_{SZE}, as a function of the frequency

$$\frac{\Delta T_{SZE}}{T_{CMB}} = f(x)\ y, \tag{1.62}$$

where y is the *Compton y-parameter* :

$$y = \int n_e\ \frac{k_B\ T}{m_e c^2}\ \sigma_T\ \mathrm{d}l, \tag{1.63}$$

and the integral is performed along the line-of-sight, σ_T is the Thomson cross section and $m_e c^2$ is the electron rest mass energy. The frequency dependence is given by the function $f(x)$

$$f(x) = \left(x\frac{e^x+1}{e^x-1} - 4 \right)(1 + \delta_{SZE}(x,T)) \tag{1.64}$$

where $x = h\nu/k_B T_{CMB}$ is the dimensionless frequency and $\delta_{SZE}(x,T)$ is a relativistic correction to the frequency dependence.

It is very important to underline that equation 1.62 does not depend on redshift. This unique feature gives the SZ effect the enormous advantage of not suffering redshift dimming, making it an extremely powerful tool in the detection of high redshift GCs (Carlstrom et al. 2002).

As mentioned before, the SZE is typically observed in the millimetre wavelength. It is common to express the spectral distortion in terms of changes in the *specific intensity* rather than temperature change. The temperature ΔT and the specific intensity ΔI are related by the derivative with respect to the temperature of the blackbody

$$I(\nu, T) = \frac{2\ h\ \nu^3}{c^2 \left(e^{\frac{h\ \nu}{k_B\ T}} - 1 \right)} \tag{1.65}$$

In this case equation 1.62 is

$$\frac{\Delta I_{SZE}}{I_0} = g(x)\ y, \tag{1.66}$$

where $I_0 = 12\,(k_B T_{CMB})^3\,/\,(hc)^2$ and the frequency dependence is

$$g(x) = \frac{x^4\ e^x}{(e^x-1)^2}\ \left(x\frac{e^x+1}{e^x-1} - 4 \right)(1 + \delta_{SZE}(x,T)) = \frac{x^4\ e^x}{(e^x-1)^2}\ f(x). \tag{1.67}$$

In the left panel of Figure 1.6 one can see the SZ effect on the spectrum of a GC 1000 times more massive than a typical one. The right panel of the same

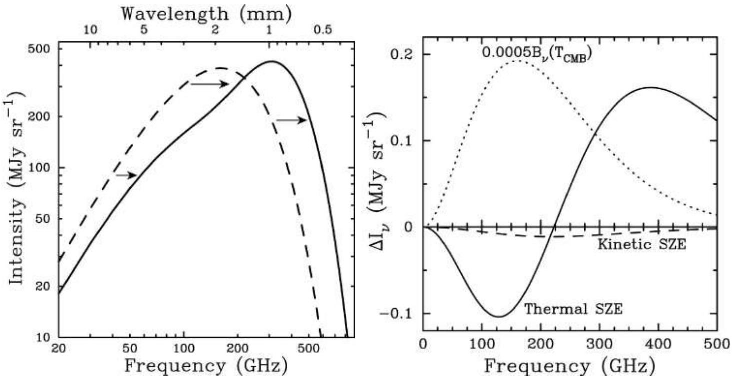

Figure 1.6: Left: sketch of the distorted CMB spectrum (solid line) shift induced by the SZ. Right: spectral distortions in the CMB radiation (dotted line) produced by both thermal (solid line) and kinetic (dashed line) SZ effects. Figures from (Carlstrom et al. 2002)

figure shows that the SZE induces a spectral shift towards higher frequencies, and a spectral distortion enhancing high frequencies and damping lower ones ($\lesssim$ 218GHz). The effect described here is called *thermal Sunyaev-Zeldovich Effect*(tSZE), and only takes into account the interaction of CMB photons with a cluster that is following the Hubble flow and can, therefore, be considered at rest. We know that GCs have peculiar velocities. These velocities induce a further spectral distortion due to the Doppler effect of the moving GC (Sunyaev & Zeldovich 1970, 1972), given by

$$\frac{\Delta T_{SZE}}{T_{CMB}} = \int \sigma_T \; n_e \; \left(\frac{\mathbf{v}}{c} \cdot \hat{\mathbf{n}}\right) \; \mathrm{d}l \sim \tau_e \; \frac{v_{pec}}{c}, \tag{1.68}$$

where τ_e and v_{pec} are the cluster optical depth and the line-of-sigh (LoS) component of the peculiar velocity of the cluster. This effect, known as *kinetic Sunyaev-Zeldovich Effect* (kSZE), produces an absolute temperature shift that is spatially indistinguishable from the CMB anisotropies. This means that the CMB spectrum still remains a perfect black-body, but with the temperature slightly changed according to the sight of v_{pec} with the maximum that correspond to the null of the tSZE at $\sim$ 218GHz (Sunyaev & Zeldovich 1972; Phillips 1995; Birkinshaw 1999; Carlstrom et al. 2002; Adam et al. 2017). For typical clusters, the kSZ is only a second order effect with respect to the tSZE, as shown in the left panel of figure 1.6. Therefore, it is particularly challenging to detect it in individual clusters (Holzapfel et al. 1997; Benson et al. 2003; Adam

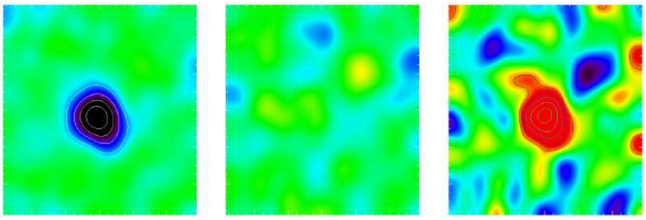

Figure 1.7: The PSZ1 G075.71+13.51 (Abell 2319) observed in 3 *Planck* bands 143 GHz (left), 217 GHz (center), and 353 GHz (right). In the 143 GHz and 353 GHz maps there is an evident SZ signature of the cluster in the form a low and high surface brightness region, respectively, whereas 217 GHz there is the null of the SZ effect. Credit: ESA/ LFI & HFI Consortia

et al. 2014; Sayers et al. 2016) and requires both high angular resolution and high sensitivity (Haehnelt & Tegmark 1996). There are, however, statistical detections of pairwise kSZ effect (Hand et al. 2012).

Since SZE depends on the temperature of the ICM, and its signal is the integrated pressure along the LoS, it can be use as mass proxy. The integral of the SZE over the solid angle of the cluster (Y_{SZ}) gives an estimation of the total thermal energy of the cluster

$$Y \equiv \int \Delta T_{SZE} \mathrm{d}\Omega \propto \frac{n_e \langle T \rangle}{d_A^2} \propto \frac{M \langle T \rangle}{d_A^2} \propto \frac{M^{5/3}}{d_A^2}, \tag{1.69}$$

that is equivalent to equation 1.53 and, as we will describe in section 5.1, it is extremely useful in building the $Y_{SZ} - M$ scaling relation.

1.2.3.2 How to observe the Sunyaev-Zeldovich effect

Unlike X-ray observations, which can be performed only from space, millimetre wavelengths can also be investigated by ground-based telescopes. In the years following the formulation of the SZ effect, pioneering studies were performed by Birkinshaw and collaborators with a single-dish antenna, the Owens Valley Radio Observatory (OVRO) 40-m telescope (Birkinshaw et al. 1978a,b, 1991), addressing observational issues and systematic errors which plagued earlier SZ observations. Since Birkinshaw?s first observations, radio astronomy in the millimetric wavelengths has undergone several improvements. High-electron-mobility transistor (HEMT) receivers and high frequencies transistors used to detect microwave and millimetric radiation were flanked by bolometric cameras

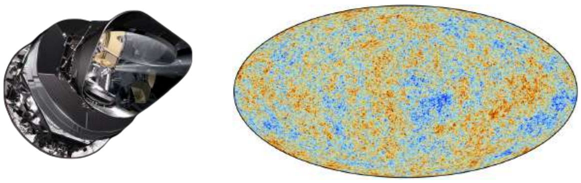

Figure 1.8: *Planck* spacecraft (left) and CMB anisotropies map (right)

in the late 1990s, e.g. MAMBO-1/2, BOLOCAM (Glenn et al. 1998), increasing the sensitivity. The pixels of these cameras are hundreds of bolometers (Bock et al. 1995; Lamarre et al. 2002; Jones et al. 2003b) detecting the incoming radiation and measuring the temperature variation of a solid-state thermometer. The next generation of millimetric radiation detectors are the KID (kinetic inductance detectors) arrays (Day et al. 2003) that ensure high sensitivity and resolution, like NIKA2 (Catalano et al. 2018), mounted on the IRAM 30m telescope in Pico Veleta (Spain).

1.3 The *Planck* catalogues of Sunyaev-Zeldovich sources

In this section we introduce the *Planck* mission. We also introduce one of the most important *Planck* products for this work, the PSZ1 catalogue.

1.3.1 The *Planck* mission

At the end of the 1990s, the European Space Agency (ESA) started the combined CMB mission COBRA/SAMBA that later became the *Planck* mission (Planck Collaboration 2005). The mission lasted more than four years, starting in May 2009 (when the satellite was launched) until October 2013, and operated from Lagrange L2 point. Although the main goal of *Planck* was to study the primary CMB anisotropies with unprecedented precision and resolution $\sim 5'$, it was also designed to extract as much information as possible from the microwave sky. The design of *Planck* also allowed the study of the anisotropies generated after the end of the recombination, namely secondary anisotropies, such the Sunyaev-Zeldovich effect and the Sachs-Wolfe effect. The *Planck* mission has provided observations of infrared and radio emitters such AGN and dusty galaxies, the Milky Way's first all sky map at 3 mm, and a study of the interstellar medium and dust. Finally, the mission has also observed the

Table 1.1: Summary of the *Planck* instruments characteristics (Planck Collaboration 2005)

INTRUMENT CHARACTERISTIC	LFI			HFI					
Detector Technology	HEMT arrays			Bolometer arrays					
Center Frequency [GHz]	30	44	70	100	143	217	353	545	857
Bandwidth [$\Delta\nu/\nu$]	0.2	0.2	0.2	0.33	0.33	0.33	0.33	0.33	0.33
Angular Resolution [arcmin]	33	24	14	10	7.1	5.0	5.0	5.0	5.0

solar system to determine the temperature and the microwave light curve of the planets, the emission from asteroids belts, comets and the zodiac light (Planck Collaboration 2005). The study of this incredible amount of different physical processes has been possible as a result of the extremely wide range of frequencies in which *Planck* has scanned the sky (from 30 to 857 GHz). The *Planck* spacecraft was equipped with two different instruments (see table 1.1):

- LFI (*Low Frequency Instrument*, Bersanelli & Mandolesi 2000; Mandolesi et al. 2000), is the evolution of COBE/DRM and WMAP. Designed to map the sky at 30, 44, and 70 GHz, LFI is constituted by a 22-channel multifrequency array of differential receivers with ultra-low-noise HEMTs amplifiers based on indium phosphide (InP) substrate cooled at 20 K.

- HFI (*High Frequency Instrument*, Lamarre et al. 2003), consists of fifty-two bolometers split into six channels at frequencies between 100 and 857 GHz. The choice of these channels was made not only to optimise the removal of foregrounds (mainly dust emission at these frequencies), but also for the detection of the Sunyaev-Zeldovich effect, which has its null at ~ 217 GHz.

Figure 1.9 shows the intensity maps of the nine *Planck* frequencies. These maps allow us to see that the radiation observed by *Planck* is the result of several physical processes, each of which is predominant in certain channels over others. This is more evident in Figure 1.10 where the contribution of foregrounds is shown compared to the CMB signal at high galactic latitudes. We can see that there is only one window in which the CMB is the dominant component, covered by the 70 and 100 GHz bands. Four mechanisms are responsible for the foreground radiation:

- thermal dust emission is the main component at high frequencies. It is due to the modified blackbody radiation emitted by the interstellar dust grains;

- free-free (bremsstrahlung) radio emission that is produced by free thermal electrons scattered in ionised galactic regions, such HII regions;

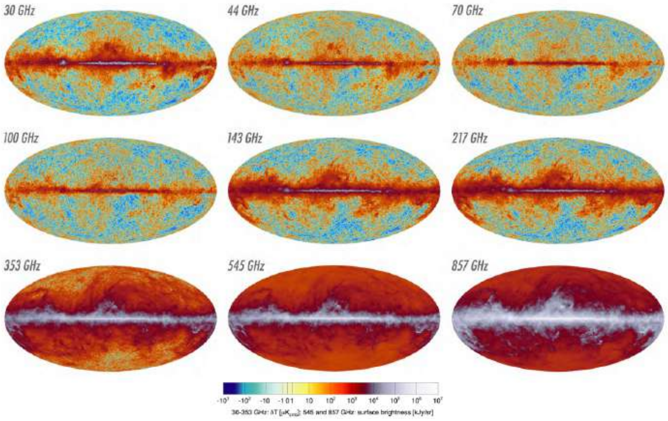

Figure 1.9: The nine *Planck* frequency maps from 30 to 857 GHz in intensity. Credit: Planck Collaboration I (2016).

- synchrotron emission is due to charged particles (typically electrons) spiraling at relativistic velocities through the galactic magnetic field. The synchrotron emission is also the same mechanism responsible for the radio emission in other galaxies;
- spinning dust grains, responsible for an anomalous microwave emission that becomes dominant at frequencies ~ 20 GHz.

The wide range of frequencies covered by LFI and HFI bands allows the accurate separation of the foregrounds components from the CMB (Planck Collaboration XII 2014; Planck Collaboration IX 2016; Planck Collaboration X 2016).

1.3.2 The PSZ1 catalogue

As described in previous sections, optical and near-infrared observations were the first GC detection techniques leading to the first catalogue of galaxy clusters characterised by their richness (Abell 1958; Abell et al. 1989). Nowadays, surveys such as the Sloan Digital Sky Survey (SDSS), Two Micron All Sky Survey (2MASS), Wide-field Infrared Survey Explorer (WISE), and SuperCOSMOS have made it possible to build deeper and more numerous GCs catalogues (e.g., Koester et al. 2007; Wen et al. 2012, 2018; Wen & Han 2018). Moreover, at the beginning of this century, X-rays space mission such as ROSAT, Chandra, and

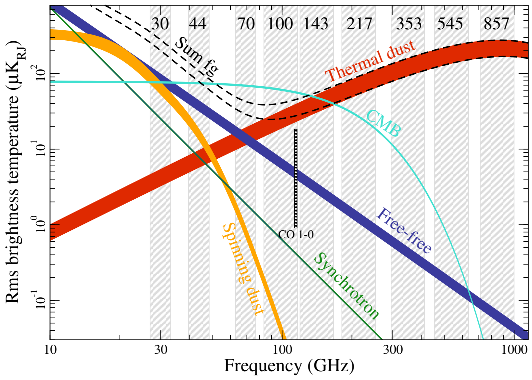

Figure 1.10: Brightness temperature rms of astrophysical components of the high-latitude sky as a function of frequency. Since each component depends also on angular scales, they are smoothed to an angular resolution of 1° FWHM. The grey bands indicates the frequency coverage of the *Planck* channels. Credit: Planck Collaboration I (2016).

XMM-Newton have produced a plethora of GCs catalogues (see section 1.2.1) consisting of cluster counterparts already present in optical catalogues, as well as new discoveries.

Historically, microwaves are the last wavelengths that generate cluster catalogues because of the challenge in observing the SZ effect. The has changed since the use of microwave detectors on survey telescopes dedicated to the observations of CMB. This allowed researchers to build the first large SZE catalogues from both ground-based telescopes such as the South Pole Telescope (SPT, Reichardt et al. 2013) and from the Atacama Cosmology Telescope (ACT, Hasselfield et al. 2013). The high resolution and the unprecedented wide frequency coverage of the *Planck* HFI instrument allowed the creation of catalogues containing hundreds of SZ-selected clusters (Planck Collaboration VIII 2011; Planck Collaboration XXIX 2014; Planck Collaboration XXVII 2016). Since one of the goals of this thesis is the optical characterisation of the *Planck* SZ sources catalogue PSZ1 (Planck Collaboration XXIX 2014), in this section we describe the creation of this catalogue and its properties.

1.3.2.1 Cluster Detection algorithms

The task of any detection method is to recognise a discrete signal immersed in a diffuse background. When chasing this goal, one of the most commonly used

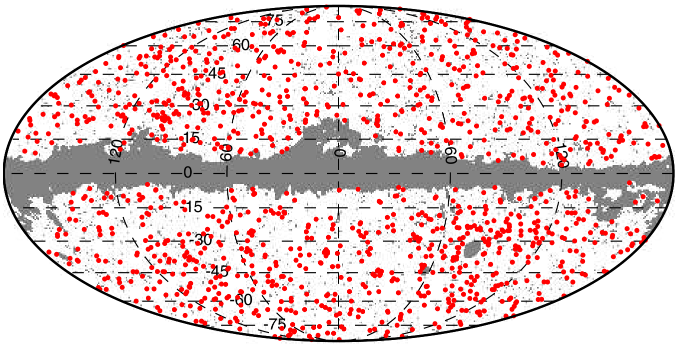

Figure 1.11: Distribution on the sky of the *Planck* PSZ1 clusters candidates (red dots), in a Mollweide projection with the Galactic plane horizontal and centred at galactic longitude zero. In grey is the mask, covering 16.3% of the sky, used to exclude the galactic plane, Magellanic clouds and other point sources.

softwares is `SExtractor` (Bertin & Arnouts 1996a), which subtracts the background from an image approximating it by a low-order polynomial, and detects different sources as sets of connected pixels above some intensity threshold. However, this method is extremely efficient only when the source of interest has a specific length which is much smaller than the smoothly varying background. Some problems arise when the amplitude of the signal and the length-scale on which the background varies are similar to those of the discrete emission one is seeking. This is the case with CMB, where we have a highly variable background embedding the SZ signal due to GCs (Melin et al. 2006; Carvalho et al. 2009). For these reasons, several authors have presented their algorithms to the *Planck* "SZ challenge" (Melin et al. 2012), where they were tested on the *Planck* Sky Model Simulation (PSM) described in Delabrouille et al. (2013). Detection algorithms can be divided in two categories: direct methods that are applied directly on frequencies maps, and indirect methods that first build a thermal SZ map via component separation, and then apply a finding algorithm (typically `SExtractor`) performing astrometry and photometry. The algorithms that have been selected to build the final PSZ1 catalogue are three direct detection algorithms: two different implementations of the matched multi-filter (`MMF`) and a Bayesian multi-frequency method.

Matched multi-filter

The `MMF` method was used first by Haehnelt & Tegmark (1996) in order to estimate peculiar velocities of galaxy clusters via kinetic SZ effect. Then, it was proposed by Herranz et al. (2002a,b) to detect GCs thermal SZ signal. The `MMF` is a detection algorithm that uses a linear combination of maps at different frequencies and applies spatial filters, one for each frequency, in order to enhance the contrast between the cluster and the background and to eliminate noise and contaminants.

The estimate of the central SZ signal is given by a linear combination of frequency maps ($\mathbf{M}(\mathbf{x})$) convolved with a specific filter for each frequency $\Psi_{\theta_c}(\mathbf{x})$

$$\hat{y_0} = \int \mathrm{d}\mathbf{x}\ \Psi^t_{\theta_c}(\mathbf{x} - \mathbf{x_0}) \cdot \mathbf{M}(\mathbf{x}), \qquad (1.70)$$

where the superscript t indicates the transpose (with the complex conjugation if needed). The filter is *matched* with prior information given by instrumental beam, spectral emission and spatial cluster profiles optimising the signal-to-noise, as described in more detail in e.g. Herranz et al. (2002b) and Melin et al. (2006).

At the end of the SZ Challenge, the *Planck* collaboration selected two different implementation of the `MMF` algorithm:

`MMF3`: the algorithm did not use all the *Planck* frequency maps, but only the six from the HFI because the extremely large beam in the LFI bands would have meant an excessive dilution of the SZ signal. The `MMF3` algorithm has been run on a set of 504 patches with an area of 10° × 10°. Each patch overlap with adjacent ones in order to cover 1.22 times the full sky. The detection was performed in three steps:

- convolution of frequency maps;
- identification of candidates performed by varying the cluster position and size $5\theta_{500}$ in order to maximise the S/N of the detection;
- removal of selected objects from filtered maps.

The last two steps were repeated until no candidates remained.

Due to the small redundancy of the `MMF3` (Melin et al. 2006), the algorithm was executed a second time centering on the position of candidates detected in the first run in order to increase the reliability of the detections. After the second execution, a sub-catalogue was created for each patch, containing all the candidates with an S/N above the threshold (4.5 for the PSZ1) in both runs. Consequently, all sub-catalogues were joined into the full sky `MMF3` catalogue.

`MMF1`**:** similarly to the `MMF3`, each full-sky frequency map was divided into an atlas of 640 overlapping patches. Each one covers and area of 14.66° × 14.66°, overlapping regions are of about 6°. Due to the high redundancy given by the high number of patches (covering 3.3 times the whole sky), the `MMF1` (Melin et al. 2011) was run in only one iteration.

PowellSnakes

The third detection algorithm selected was the PowellSnakes (`PwS`, Carvalho et al. 2009, 2012), a completely different approach than `MMF1` and `MMF3`. It is a fast bayesian multi-frequency algorithm that detects compact sources surrounded by a diffuse background by analysing flat sky patches and then adding up the results in a single all-sky catalogue. In analogy with the `MMF1`, each patch has an area of 14.66° × 14.66°. However, the number of patches is more than four times higher than `MMF1` ($\sim$ 2800), granting a coverage of 4.7 times the whole sky.

The detection method is based on the use of Bayesian inference to select between two models. It is extremely interesting that the `PwS` can mimic the behaviour and the results of an `MMF` method. The likelihood manifold is filtered (in the matched filter sense) and then scanned by a peak-finding algorithm in order to make a first ordered list of candidates. After this preliminary step, Powell minimisation chains (snakes) (Press et al. 1992) are launched, starting at each location, to optimise the estimation of source position, dimension and flux. At this step, the application of the detection/rejection criteria, based on S/N, produces lists of sources that are fully compatible with those obtained with an `MMF` algorithm. However, the native nature of the `PwS` is a full bayesian approach. As mentioned before, this approach is based on the comparison of the posterior probability of difference models (the binary case detection, H_1), and non-detection (or null hypothesis, H_0) is only the simplest approach. The decision is then taken by comparing the posterior probabilities of the two models giving a dataset (in this case the maps $\mathbf{M}$) and a set of priors via the *posterior odds ratio*

$$\rho \equiv \frac{\mathrm{Pr}(\mathrm{H}_1|\mathbf{M})}{\mathrm{Pr}(\mathrm{H}_0|\mathbf{M})} = \frac{\mathrm{Pr}(\mathbf{M}|\mathrm{H}_1)}{\mathrm{Pr}(\mathbf{M}|\mathrm{H}_0)}\frac{\mathrm{Pr}(\mathrm{H}_1)}{\mathrm{Pr}(\mathrm{H}_0)}. \tag{1.71}$$

In the detection of SZ sources, the priors are those of the spectral and spatial SZ emission: cluster position, amplitude of the signal, and cluster specific radius. This approach is broadly used in Bayesian inference, and Jaynes & Bretthorst (2003) state that the best way to discriminate between two hypotheses is to compare the odd ratio against a threshold. This simple binary model is not

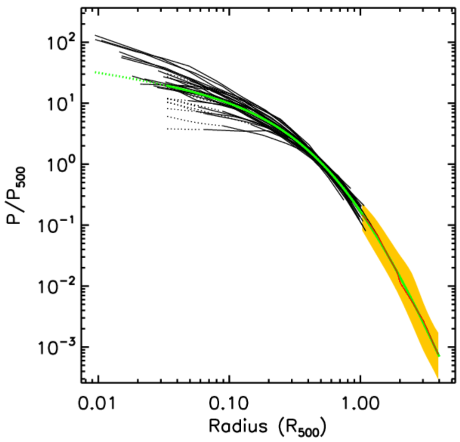

Figure 1.12: The Generalised NFW model (green line), obtained by fitting the observational data, from REXCESS sample (black lines), up to R_{500} and simulated mean cluster pressure profile for $R_{500} < r < 5\ R_{500}$ (red line and orange shadow). Figure taken from Arnaud et al. (2010).

adequately accurate when applied to astrophysical sources, and even less so in case of cluster detection via SZ effect. Statistical background inhomogeneity, point sources and dust emission can populate the final SZ catalogues with a large number of spurious detections. The solution was found by using a multi-model approach that takes into account more than two hypotheses in the loss function. A detailed description of this method is not in the scope of this section. For a detailed description of the `PwS` see Carvalho et al. (2009) and Carvalho et al. (2012).

1.3.2.2 Cluster model

All the algorithms performed a blind search (i.e. there is no assumed prior on known clusters position), assuming priors on cluster ICM pressure profile and SZ signal frequency spectrum in order to enhance the contrast of clusters over a set of observations containing contaminating signals.

As we see in section 1.2.3.1, SZ frequency profile is given by equation 1.62, whereas its intensity is given by the inverse Compton y-parameter given by the integral, along the LoS, of the pressure produced by plasma of electrons (see, equation 1.63).

Although the simplest ICM pressure profile is the isothermal β-model (see equation 1.47), it is not an accurate description of the mass distribution. For this reason, the pressure profile model adopted by the *Planck* Collaboration is a generalization of the NFW (GNFW, Navarro et al. 1997) density profile (see figure 1.12). This model, known as the generalized NFW or *Universal Pressure Profile* (UPP, Arnaud et al. 2010), was constructed by fitting a mean profile by using a mixture of X-ray observations, 20 clusters of the REXCESS sample (Böhringer et al. 2007) for the cluster core $R < R_{500}$, and a set of three hydrodynamical simulations (Borgani et al. 2004; Nagai et al. 2007; Piffaretti & Valdarnini 2008) for the outer part down to 5 R_{500}. The Universal pressure profile differs from the NFW model in the number of free parameters. Unlike the NFW profile that has only two free parameters, the central pressure P_0 and the concentration $c_{500} = R_{500}/R_s$ (R_s is the NFW specific radius), the GNFW

$$p(x) = \frac{P_0}{(c_{500}x)^{\gamma}[1 + (c_{500}x)\alpha]^{(\beta-\gamma)/\alpha}}, \tag{1.72}$$

with $p(x) = P(r)/R_{500}$ and $x = r/R_{500}$, adds 3 new parameters taking into account the different slopes along the profile, γ, α, and β. However, detection algorithms only allowed the central pressure and characteristic scale $\theta_s = \theta_{500}/c_{500}$ to vary, whereas γ, α, and β are fixed to those fitted by Arnaud et al. (2010)

$$\gamma = 0.308, \quad \alpha = 1.05, \quad \beta = 5.49. \tag{1.73}$$

1.3.2.3 $Y - \theta$ degeneracy

As demonstrated before, the three selected algorithms assume the GCs pressure profile and the frequency spectrum of the SZ signal in order to optimise the detection of SZ sources within *Planck* maps. This choice reduces the possibility of spurious detections, and was one of the motivations that led the *Planck* collaboration to the selection of the direct algorithm (Melin et al. 2012). However, the GNFW profile has two free parameters: the central value and the cluster angular size θ_s, that show a large correlation due to the large beam size in comparison with the typical cluster size. Consequently, the uncertainties on the size affect the flux estimates. Moreover, with the large *Planck* beam, the signal is broadened, and its uncertainty propagates to size, flux and measurements, amplifying this problem, especially for non well resolved clusters that correspond to low S/N detections (Planck Collaboration VIII 2011; Planck Collaboration XXIX 2014). For these reasons the *Planck* PSZ1 catalogue provides the full joint posterior probability distribution between θ_s and $Y_{5\theta_{500}}$ (the flux within

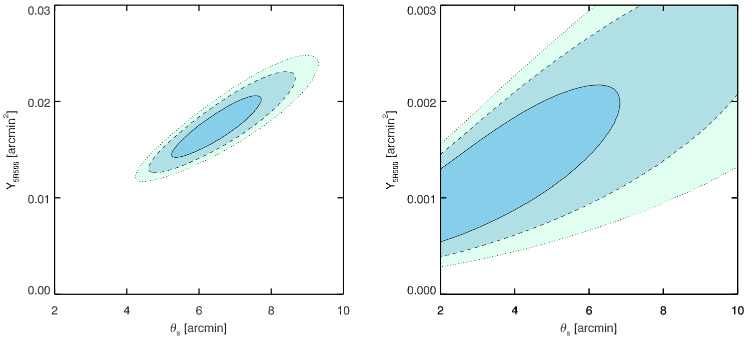

Figure 1.13: full joint posterior probability (68, 95, and 99 percent confidence levels) showing the size–flux degeneracy for a high and a low S/N clusters. On the left Abell 2163 (S/N = 27) and on the right PSZ1 G266.6-27.3 ($S/N = 6$ at $z \sim 1$). Credit: Planck Collaboration XXIX (2014).

$5\theta_{500}$) for each cluster. Breaking this degeneracy will give all the information on cluster size and flux, as we will discuss in chapter 5.

1.3.2.4 Signal to Noise of SZ detection

The S/N of the SZ detection is another important output. The noise level is measured starting from the cross-power spectrum of the background evaluated locally in each sky patch. However, the differences in the cross-power spectrum estimate makes the different algorithms more or less sensitive to the background. This is reflected in different values of the S/N ratio for different algorithms. In particular, the `PwS` shows a higher sensitivity to the SZ signal contamination in the background cross-power spectrum. Then, the lower value of the signal-to-noise ratio is due to an extra component of the background introduced by the SZ signal. For this reason, this effect is prominent in very bright sources ($S/N \geq 15$). Although the `PwS` detects all clusters with S/N above 8.5 (right panel of figure 1.14), the number count of clusters above $S/N \geq 15$ is lower for the `PwS` than the `MMF`, as shown in the left panel of figure 1.14.

1.3.2.5 The Union catalogue

In this subsection we describe how the final PSZ1 catalogue was built. The final PSZ1 catalogue is also called the *union* catalogue because it is the result of joining the three sub-catalogues from `MMF1`, `MMF3` and `PwS`. Each algorithm

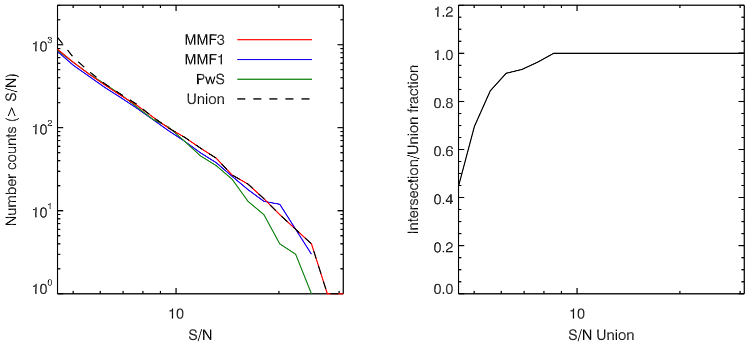

Figure 1.14: Left panel: fraction of cluster detected by each algorithm with respect the union catalogue as a function of the S/N. Right panel: number of cluster detected for each algorithm as a function of the S/N. Credit: Planck Collaboration XXIX (2014).

produces a sub-catalogue obtained by adding the catalogues of each sky patch containing all sources detected above the threshold $S/N = 4.5$. As mentioned before, the background level is different for each detection method leading to different detections with different significance between detection methods.

The PSZ1 union catalogue contains 1227 SZ sources, with $S/N \geq 4.5$ and detected by at least two algorithms. As shown in the right panel of figure 1.14, all clusters above $S/N = 8.5$ are detected by all three algorithms. However, at lower significance, this is not the case. Therefore, the choice to include only the sources detected by at least two methods has the objective to increase their reliability and to avoid spurious entries (Planck Collaboration XXIX 2014). Although the *Planck* Collaboration decided not to include the blind photometry (as explained in previous paragraphs), they must provide position and significance for each detection. For this reason, the *Planck* Collaboration decided to use the `MMF3` results as reference. In case the objects were not detected by the `MMF3`, the reference algorithm were, in order, `PwS` and `MMF1`. Due to the differences in the algorithms, the same SZ source can be detected in a slightly different position. The sources that presented an angular separation $5'$, between different detection methods, were merged in the same sources. The complete description of the PSZ1 catalogue and its outputs can be found in Planck Collaboration XXIX (2014). The catalogue can be downloaded from the *Planck* Legacy Archive (PLA) [1].

---

[1] `http://pla.esac.esa.int/pla/#catalogues`

1.4 Optical Follow-up motivations

Up to now, we have performed a review of the state?of-the-art GC detection, paying particular attention to the SZ observables, the *Planck* mission and its PSZ1 catalogue. In this section, we will explain the framework of this thesis

1.4.1 PSZ1 validation and follow-up

The PSZ1 is a catalogue of the union of all SZ sources detected by the three detection algorithms `MMF3`, `MMF1`, `PwS`. On one hand, the assumption of priors on GCs pressure profile and the SZ spectrum together with the masking of galactic plane and point sources, should ideally ensure that all PSZ1 entries are real clusters. However, point sources, dust, and background noise fluctuations could actually contaminate the sample. On the other hand, a fraction of the *Planck* SZ sources can be associated to previously-known clusters. For these reasons, the PSZ1 catalogue has undergone a validation process, which the first part of this study is based on. The first step of the validation consisted of identifying the SZ candidates associated with known clusters. This goal was achieved by investigating optical, IR, X-ray, and SZ catalogues looking for clusters within $5'$ of the SZ position. However, the positional match alone was not considered sufficient to associate a known cluster to the SZ signal. Therefore, each association passed through a consolidation process depending on the catalogue examined. In the X-ray case, the consolidation criterion is linked to the fact that X-rays and SZ trace the same cluster component. Therefore, an X-ray mass proxy can be constructed and compared with the SZ flux and S/N. In the optical case, however, the consolidation was not made via the mass-richness relation (due to high scatter) but via information extracted from the Rosat All Sky Survey (RASS, Voges et al. 1999b) and the position of the cluster. The second step was to investigate existing X-ray, IR and optical surveys looking for counterparts for the new clusters. Finally, a third step was to make a follow-up of the sources that remained unassociated.

In the following section, we will briefly outline the validation process for each catalogue. For the complete description of the validation process see section 4 of Planck Collaboration XXIX (2014).

During the validation process a reliability flag was assigned to each candidate depending on how certain the association could be considered: $Q = 1$ for a clear association, $Q = 2$ for a reliable association, and $Q = 3$ for a non-association.

X-ray - The research of X-ray known counterparts was performed by cross-checking the PSZ1 with an updated version of the MCXC meta-catalogue (Piffaretti et al. 2011) containing 1789 GCs, almost all with measured redshift and X-ray luminosities $L_{\rm X}$. For each *Planck* candidate we selected the nearest MCXC cluster and assigned aa first reliability flag. Flags were first assigned based on the distance between an X-ray cluster and SZ coordinates D, and compared with the size observed in X-rays $\theta_{500}^{L_{\rm X}}$,

- $Q_{\rm X} = 1$ if $D < 10'$ and $D < \theta_{500}^{L_{\rm X}}$;
- $Q_{\rm X} = 3$ if $D > 10'$ and $D > 2\ \theta_{500}^{L_{\rm X}}$;
- $Q_{\rm X} = 2$ otherwise.

Flag consolidation, in this case, is straightforward. It was done by comparing the SZ flux Y_{500} with its counterpart in X-rays $Y_{500}^{L_{\rm X}}$, obtained by combining the $L_{\rm X,500} - M_{500}$ relations by Pratt et al. (2009) with the $M_{500} - Y_{500}$ by Arnaud et al. (2010), and the measured significance with the expected one from the X-rays analysis $({\rm S/N})^{\rm L_X}$. For these clusters, the SZ flux was re-extracted by assigning a positional prior to the detection algorithm and running it both by leaving the cluster size free or by fixing it to the X-ray one. The re-extracted flux measurements were then compared with both the blind and the X-ray counterparts, as well as the respective S/N. At the end of this process, 472 X-rays known GCs were associated with PSZ1 detections, corresponding to 38.5% of the PSZ1 catalogue.

Optical - Optical counterparts were principally researched within four SDSS based clusters catalogues: MaxBCG (13,823 cluster, Koester et al. 2007), GMBCG (55,424 cluster, Hao et al. 2010), AMF (69,173 cluster, Szabo et al. 2011), and WHL12 (132,684 cluster, Wen et al. 2012), in addition to the Abell (Abell 1958) and Zwicky (Zwicky et al. 1961) ones. In this case, the quality flags Q_{SDSS} are based not only on the distance D, but also on the cluster richness $R_{L^\star}$, which is a proxy for the cluster mass that can be compared with that calculated from the Y_{500}:

- $Q_{SDSS} = 1$ if $D < 5'$ and $R_{L^\star} > 110$;
- $Q_{SDSS} = 2$ if $D < 5'$ and $70 \leq R_{L^\star} \leq 110$;
- $Q_{SDSS} = 3$ if $D > 5'$ and $R_{L^\star} < 70$.

However, the mass-richness relation is characterised by a very huge scatter and, consequently, an enormous uncertainty is associated with the mass estimate. For this reason, the associations were consolidated only if an analysis of RASS data in a region of $5'$ around the *Planck* position gave a signal with $(S/N)_{RASS} \geq 1$.

For Abell and Zwicky counterparts, only positional information and RASS inspection were used, as consolidation. However, objects with $(S/N)_{RASS} < 1$ were also associated after an inspection of WISE data, SZ maps and DSS images.

There are 182 exclusive optical known counterparts, 72 from catalogues based on SDSS data and 110 clusters from Abell and Zwicky catalogues, representing 14.8% of PSZ1 detections.

SZ - ACT and SPT SZ catalogues were also scrutinised in addition to SZ clusters from the literature. As in previous cases, the first association criteria are related with the distance from the *Planck* position. After this, an inspection of ancillary data and a RASS analysis confirmed the association. Due to the fact that ACT and SPT clusters are low-mass systems, only 16 associations are exclusively from SZ catalogues.

NED and SIMBAD - Finally, NED and SIMBAD databases were systematic queried looking for clusters within $5'$ of the *Planck* positions. Therefore, the clusters identified in this way were confirmed via RASS analysis. As expected, the number of clusters from database queries was low, with only 13 counterparts found using this method. After the first step of the validation process, 544 PSZ1 cluster candidates remained unassociated to any previously-known GCs. As mentioned before, data from RASS, WISE, SDSS and DSS surveys were used to confirm clusters associations, especially in the case of optical catalogues. The systematic investigation of these surveys allowed us to assign a reliability flag to the clusters without previously-known counterparts, Q_{RASS}, Q_{WISE}, and $Q_{SDSS,dat}$. Although a detailed description of the analysis of surveys data is beyond the scope of this section, it is important to outline the assignment criteria for reliability flags.

RASS - The investigation of RASS data described in Planck Collaboration Int. IV (2013) and Planck Collaboration XXIX (2014), resulted in the detection of 887 clusters candidates out of the 1227 in the *Planck* catalogue. These objects matched a RASS source with $(S/N)_{RASS} \geq 2$ within $5'$ around the *Planck* position and then were flagged with $Q_{RASS} = 1$. Conversely, RASS sources with $(S/N)_{RASS} < 0.5$ were considered poor detections and were assigned a flag $Q_{RASS} = 3$

SDSS - In addition to researching counterparts within the SDSS based catalogues, SDSS DR9 (Ahn et al. 2012) data were explored in order to search for overdennsities of galaxies characterised by a red sequence. The quality flag assigned to each counterpart found within $5'$ from the *Planck* coordinates were based on the number of galaxies within this radius, with: $Q_{SDSS,dat} = 1$ for $N_{gal} \geq 40$, $Q_{SDSS,dat} = 2$ for $20 < N_{gal} < 40$, and $Q_{SDSS,dat} = 3$ otherwise.

WISE - The last survey to be inspected was WISE. The search of counterparts was performed in two different ways. The first one consisted of a matched filter algorithm based on Kepner et al. (1999). The second one, developed by Aghanim and Fromenteau, conducted a search of overdensities of red galaxies with a high luminosity threshold within $5'$ from the *Planck* candidate position. In this case, the reliability flags were related to the purity of the detection. Purity is defined as the probability of a *Planck* candidate having a counterpart against a serendipitous association. Detection with purity above 80% were considered reliable, $Q_{WISE} = 1$ for purity $> 90\%$, $Q_{WISE} = 2$ for purity between 80% and 90%. For purity below 80% the detection were considered bad, so $Q_{WISE} = 3$.

1.4.1.1 Follow-up programmes

After survey investigations and consequent assignment of quality flags, PSZ1 cluster candidates with no previously-known counterpart underwent a a follow-up process. It is important to underline that follow-up programmes started well before the realization of the PSZ1 catalogue and consisted of the individual observations of 276 candidates, selected within the early version of *Planck* catalogue (Planck Collaboration VIII 2011), mainly using X-ray and optical facilities.

The X-ray part of the follow-up was performed between May 2010 and October 2011 using the Director's discretionary time (DDT) of the *XMM-Newton* satellite. During this period, 51 *Planck* candidates were observed with 10 ks snapshots each, in order to detect X-rays emission and estimate the cluster redshift. The results of these observations are detailed in Planck Collaboration IX (2011); Planck Collaboration Int. I (2012) and Planck Collaboration Int. IV (2013). This part of the validation follow-up was extremely important because it allowed us to understand the physical characteristics of *Planck* candidates and, therefore, better manage the target selection criteria for the optical programmes.

The optical part of the validation follow-up was performed using facilities located in different parts of the globe: Chile, Turkey and Spain (Canary Islands). The Southern hemisphere was covered by the observations performed at the MPG/ESO 2.2 meter Telescope and at the 3.6 m New Technology Telescope (NTT), both located in La Silla Observatory in the Atacama desert of Chile. The first telescope was used to observe 94 candidates using the Wide-Field Imager (WFI) obtaining the photometric redshift of the associated GC. At the the second facility, 33 SZ sources were observed using the EFOSC2 spectrograph following the observational strategy described in Chon & Böhringer (2012).

The majority of the *Planck* optical follow-up was performed in the northern hemisphere. During a three-year programme that started in July 2011, the Russian Turkish 1.5 m Telescope (RTT150) was used to observe 88 cluster candidates using the Russian quote of observational time. The observational strategy and cluster identification process were the same developed for the 400 deg^2 ROSAT PSPC Galaxy Cluster Survey (Burenin et al. 2007). The TÜBİTAK Faint Object Spectrograph and Camera (TFOSC) were used to take *gri* images. If a GC was identified as an enhanced surface number density of galaxies, its members, selected within a red sequence, were then observed spectroscopically through a long slit. This strategy allowed for the spectroscopical confirmation of clusters up to $z \sim 0.4$. Finally, the most extensive optical follow-up of *Planck* sources was conducted by our research group at the Instituto de Astrofisíca de Canarias (IAC), using six telescopes (IAC80, INT, WHT, NOT, TNG, and GTC) located in two different observatories (Observatorio del Roque de Los Muchachos and Observatorio del Teide, in La Palma and Tenerife islands, respectively). The programme connected with the *Planck* Collaboration lasted more than two years (June 2010 to January 2013) leading to the confirmation of 73 new GCs as described in Planck Collaboration Int. XXXVI (2016).

At the time of publication of the PSZ1 catalogue in 2013, the new clusters confirmed by *Planck* Collaborations follow-up programmes were 178, leaving 366 cluster candidates unconfirmed. These remaining sources underwent (i) a visual inspection of the nine HFI maps, cleaned from CMB and galactic emission and of the reconstructed y-maps, (i) an inspection of the SZ spectra from detection algorithms, and (iii) a comparison between y-map, 857 GHz and 217 GHz maps to search for possible correlations with dust emission and carbon monoxide (CO) signal. All this information was summarized and combined in the internal quality flag Q_{SZ} assigned by following the criteria below:

- $Q_{SZ} = 1$ if (i) there is a clear and compact source at the candidate position in the SZ maps, (ii)an evident SZ signature is present (lack of signal below 217 GHz and reasonable emission at 353 GHz), and (iii) no correlation was found with CO emission or dust at 217 GHz and 857 GHz, respectively;
- $Q_{SZ} = 2$ if (i) the presence of SZ signal is evident in the corresponding

Table 1.2: Summary of the *Planck*candidate associated with previously-known clusters, confirmed after the follow-up and unconfirmed candidates. Data taken from Planck Collaboration XXIX (2014).

Category	N	Catalogue, telescope, or reliability		
Previously known	683	472	X-ray:	MCXC meta-catalogue
		182	Optical:	Abell, Zwicky, SDSS cat.
		16	SZ:	SPT, ACT
		13	Misc:	NED, SIMBAD
New confirmed	178		Follow-up, archival data, SDSS survey	
New candidate	366	54	CLASS 1	
		170	CLASS 2	
		142	CLASS 3	
Total *Planck*SZ catalogue	**1227**			

maps or significant spectral signature, and (ii) there is a contaminated signal but without correlation between dust and CO;

- $Q_{SZ} = 3$ if (i) there is a noisy or weak SZ signal, (ii) a strong correlation ($> 80\%$) is present with CO.

This information, in addition tho the one supplied by RASS and WISE reliability flags, was used to divide the remaining candidates in three classes:

- CLASS1: The candidates that fulfilled all the requirement of $Q_{SZ} < 3$, $Q_{WISE} < 3$ and $Q_{RASS} = 1$ were considered *high-reliable* or *pre-confirmed*. These clusters have a clear SZ signature, evident counterparts in RASS and high probability to be associated with a galaxy overdensity in WISE;
- CLASS2: The candidates that have $Q_{SZ} < 3$, but are not necessarily reliable in RASS and WISE together. These objects are considered *reliable cluster candidates*;
- CLASS3: The candidates that have $Q_{SZ} = 3$ or $Q_{RASS} = 3$ are considered *low reliability candidates.*

Table 3.2 summarises the number of PSZ1 sources associated with previously-known clusters, confirmed by follow-up and un-confirmed in CLASS1, CLASS2, or CLASS3.

The 366 cluster candidates were distributed over the whole sky and required a dedicated follow-up to be conformed. This is the framework for the first part of this thesis. In fact, one of the objectives of this work is to obtain data for all SZ cluster candidates above $Dec > -15°$ confirming (at least photometrically) as many clusters as possible. This goal was achieved during a two-year International Time Project (ITP13-08) observational programme, described in chapter 2.

1.4.2 Cosmology with number counts

The *Planck* cluster catalogue is an all-sky sample of GCs selected by their SZ signature. As explained in section 1.2.3.1, the SZ effect does not suffer from redshift dimming, so an SZ selected cluster sample is, substantially, a mass selected sample. This property makes SZ samples extremely suitable for number counts analysis. The cluster number counts, namely the abundance of GCs as a function of redshift, can be used as cosmological tools, exploiting their sensitivity to cosmological parameters (Planck Collaboration XX 2014). Three ingredients are required in order to compute the number of clusters in a redshift interval. These are:

- a cluster?s density distribution as a function of mass and redshift(mass function);
- a survey selection function to determine if a cluster should be detected or not.
- a scaling relation that converts observable quantities into mass.

Therefore, the number counts are defined as

$$\frac{\mathrm{d}N}{\mathrm{d}z} = \int \mathrm{d}\Omega \int \mathrm{d}M_{500}\ \hat{\chi}(z, M_{500}, l, b)\ \frac{\mathrm{d}N}{\mathrm{d}z\mathrm{d}M_{500}\mathrm{d}\Omega}, \tag{1.74}$$

where $\hat{\chi}(z, M_{500}, l, b)$ is the survey selection function, (*Planck* Collaboration call it *survey completeness*) at a given position in the sky, given by the galactic coordinates (l, b), and where $\mathrm{d}N/(\mathrm{d}z\mathrm{d}M_{500}\mathrm{d}\Omega)$ is the mass function.

Mass function As shown in section 1.1.2.2.3, a formulation of the mass function derives the Press-Shechter formalism, assuming a spherical collapse model. a formulation of the mass function derives the Press-Shechter formalism, assuming a spherical collapse model. The *Planck* Collaboration used the Tinker et al. (2008) function as its number counts analysis, which is given by

$$\frac{\mathrm{d}N}{\mathrm{d}M_{500}} = f(\sigma)\frac{\rho_m(z=0)}{M_{500}}\frac{\mathrm{d}\ln\sigma^{-1}}{\mathrm{d}M_{500}}, \tag{1.75}$$

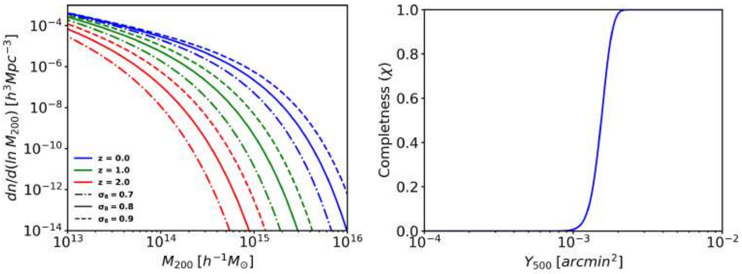

Figure 1.15: Left: Tinker et al. (2008) mass function computed at four different redshifts, $z = 0.0, 1.0, 2.0$ (blue, red and green lines, respectively) and for three different value of σ_8, 0.7, 0.8, 0.9 (dot-dashed, solid, dashed lines, respectively). Right: *Planck* completeness as a function of Y_{500} computed for $\theta_{500} = 6'$.

where $f(\sigma)$ is a universal function of the linear perturbation theory standard deviation. Values for the parameters a, b, c, can be found in Tinker et al. (2008). The left panel of figure 1.15 shows the Tinker et al. (2008) mass function for 3 different values of redshift (red, green, blue lines) and σ_8 (dot-dashed, solid and dashed lines). It is evident that the sensibility of the mass function with σ_8 makes the number counts a very useful cosmological tool.

Survey selection function The *Planck* survey completeness as a function of observables, representing the probability of a cluster of given size and flux to be detected in a given sky position, is given by

$$\chi\left(Y_{500}, \theta_{500}, l, b\right) = \frac{1}{2}\left[1 + \mathrm{erf}\left(\frac{\mathrm{Y}_{500} - \mathrm{q}\ \sigma_{\mathrm{Y}_{500}}\left(\theta_{500}, \mathrm{l}, \mathrm{b}\right)}{\sqrt{2}\ \sigma_{\mathrm{Y}_{500}}\left(\theta_{500}, \mathrm{l}, \mathrm{b}\right)}\right)\right], \tag{1.76}$$

where q is the S/N threshold (in Planck Collaboration XX (2014) number counts analysis $q = 7$) and $\sigma_{Y_{500}}$ is the standard deviation of the Gaussian probability to measure Y_{500}, assumed equal to the noise measured by each detection algorithm. Since each filter depends on the cluster size and the local cross-power spectrum, $\sigma_{Y_{500}}$ is a function of the size and sky position. Figure 1.15 (right panel) shows the completeness as a function of the SZ flux for $\theta_{500} = 6'$. However, for the number counts, a selection function is needed in terms of mass and redshift $\hat{\chi}\left(z, M_{500}, l, b\right)$, given by

$$\hat{\chi}\left(z, M_{500}, l, b\right) = \int \mathrm{d}Y_{500} \int \mathrm{d}\theta_{500}\ P\left(z, M_{500} | Y_{500}, \theta_{500}\right)\ \chi\left(Y_{500}, \theta_{500}, l, b\right), \tag{1.77}$$

where $P\left(z, M_{500}|Y_{500}, \theta_{500}\right)$ is the probability of a cluster with observed flux and size $\left(Y_{500}, \theta_{500}\right)$ to have mass M_{500} at redshift z. It is interesting to remark that since $P\left(z, M_{500}|Y_{500}, \theta_{500}\right)$ is a reflection of the scaling relation between $\left(Y_{500}, \theta_{500}\right)$ and $\left(M_{500}, z\right)$, it introduces a dependence in $\hat{\chi}\left(z, M_{500}, l, b\right)$ on cosmological parameters, whereas the $\chi\left(Y_{500}, \theta_{500}, l, b\right)$, depending only on quantities that can be measured, is not sensible to the cosmology.

Scaling relation Due to the fact that the cluster mass is not directly measurable, observables-mass scaling relations play a fundamental role in the number counts formulation. Therefore, it is crucial for these relations to be unbiased and to have as low of an intrinsic scatter as possible.

As we will discuss more in detail in chapter 5, scaling relations depend on the particular simulation used to constrain them. For this reason, the *Planck* Collaboration chose to determine its $Y_{500} - M_{500}$ relation using real data from X-ray observations. However, real data could suffer from biases that are not always known and understood. The *Planck* $Y_{500} - M_{500}$ relation is

$$E^{-2/3}(z)\left[\frac{D_A^2\ Y_{500}^{\mathrm{SZ}}}{10^{-4}\ \mathrm{Mpc}^2}\right] = 10^{-0.19\pm0.012}\left[\frac{(1-b)\ M_{500}}{6\times10^{14}\ \mathrm{M}_\odot}\right]^{1.79\pm0.08} . \tag{1.78}$$

where the factor $(1-b)$ is *mass bias*, which accounts for all possible biases between the estimated and the true mass. By comparing the scaling relation derived from X-ray data and those from a set of different cosmological simulations, *Planck* Collaboration found that the value of the mass bias is $(1-b) = 0.8^{+0.1}_{-0.2}$.

1.4.2.1 *Planck* clusters cosmological constraints

In this subsection we summarise the result (in terms of cosmological parameters) of the analysis performed by the *Planck* Collaboration for its first data release and reported in Planck Collaboration XX (2014). The study was carried out using a PSZ1 subsample, known as the *cosmological sample* (or *cosmo sample*), constituted by 189 GCs detected through the `MMF3` algorithm, in a region outside a mask covering 35% of the sky, with $S/N > 7$. On the one hand, this high signal-to-noise threshold reduced the number of clusters of the subsample, but, on the other hand, it safeguarded from effects due to the presence of a survey selection threshold, such as the Eddington bias (Eddington 1913), as we will see in section 5.4.1.

The number of clusters per redshift bins, as well as cosmological parameters were constrained using the *Monte Carlo Markov Chain* (MCMC) method implemented in the `CosmoMC` engine. The number counts likelihood is based on

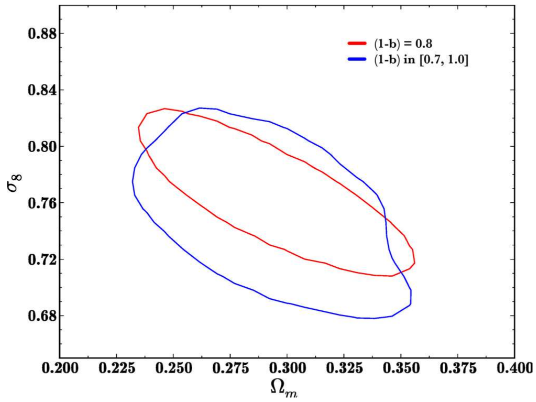

Figure 1.16: Comparison of the 95% confidence levels contours in $(\Omega_m - \sigma_8)$ plane with the mass bias fixed to $(1 - b) = 0.8$ (red) and allowing it to vary in the range $[0.7, 1.0]$ (blue). This plot is taken from Planck Collaboration XX (2014). For reasons of clarity the plot has been modified retaining only the contours of interest for this work.

Poisson statistics following the Cash (1979) formalism

$$\ln \mathcal{L} = \ln \mathcal{P}\left(N_i|n_i\right) = \sum_{i=1}^{N_b} \left[N_i \ln\left(N_i\right) - n_i - \ln\left(N_i!\right)\right], \qquad (1.79)$$

where $\mathcal{P}\left(N_i|n_i\right)$ is the probability of finding N_i objects given the expected number of clusters n_i, dependent on the bin range, scaling relation and cosmological parameters in each redshift bin N_b.

In addition to Ω_m and σ_8, five other ΛCDM model parameters were set free to vary: baryonic density Ω_b, the Hubble constant H_0, the spectral index of scalar perturbations n_s, and the sum of three neutrino masses $\sum m_\nu$. However, the cluster counts are not sensitive to all these parameters and, for this reason, the *Planck* GCs data were combined with other datasets such as the the Big Bang nucleosynthesis constraints from Steigman (2008), and the baryonic acoustic oscillations (BAO) combining the likelihood of Planck Collaboration XVI (2014) and Hinshaw et al. (2013). As mentioned before, the mass bias is a crucial ingredient in this study. The *Planck* Collaboration chose two different strategies: in one,they let the mass bias free to vary assuming a flat prior in the interval $[0.7, 1]]$, in the other, they fixed it to the value $(1-b) = 0.8$. The results of this analysis are shown in figure 1.16, where the blue contours represent the

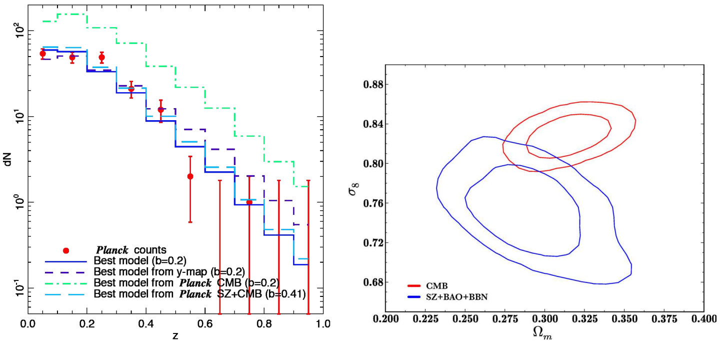

Figure 1.17: Left panel: The observed number counts (red dots) compared to *Planck* Collaboration best-fit models. The solid blue and the dashed purple lines are the *Planck* Collaboration best-fit models, assuming $(1-b) = 0.8$ for the theoretical number counts prediction and for the cluster abundance from *Planck* SZ power spectrum, respectively. The green dot-dashed line represents the cluster abundances derived from CMB analysis with the mass bias fixed to $(1-b) = 0.8$, whereas the cyan long dashed line represents the joint best fit of CMB and SZ with the mass bias let free in order to reduce the tension in σ_8 constraint. Right panel: Likelihood contours in the $(\Omega_m - \sigma_8)$ plane from the CMB only analysis (red) and the *Planck* SZ and BAO and BBN (blue) with $(1-b)$ free to vary in the interval $[0.7, 1]$. Credit: Planck Collaboration XX (2014).

result with $(1-b)$ free to vary, and the red contours shows the fixed (0.8) mass bias. The introduction of a new free parameter $(1-b)$ has the consequence of enlarging the contours along the direction perpendicular to the line of the $\Omega_m - \sigma_8$ degeneracy. This is also reflected in the parameter constraints. While, for $(1-b) = 0.8$, $\Omega_m = 0.29 \pm 0.02$ and $\sigma_8 = 0.77 \pm 0.02$, for $(1-b)$ free in the interval $[0.7, 1]$ $\sigma_8 = 0.75 \pm 0.03$, the constrain on Ω_m remains unchanged (Planck Collaboration XX 2014), reflecting the enlargement only perpendicularly to the degeneracy line.

This analysis provided the pair of parameters (Ω_m, σ_8) in a completely independent way than those obtained studying the CMB primary anisotropies (presented in Planck Collaboration XVI 2014). In principle the constraint obtained with these two different data sets should be compatible. However, the comparison between SZ and CMB ($\Omega_m = 0.3111 \pm 0.0056, \sigma_8 = 0.8102 \pm 0.0060$) constraints in the (Ω_m, σ_8) plane shows a tension mainly on the value of σ_8, as shown in the right panel of Figure 1.17. Consequently, the tension is also reflected in the number counts themselves. Indeed, the σ_8 constraint from CMB analysis (with $(1-b) = 0.8$) leads to an expected number of clusters that is two

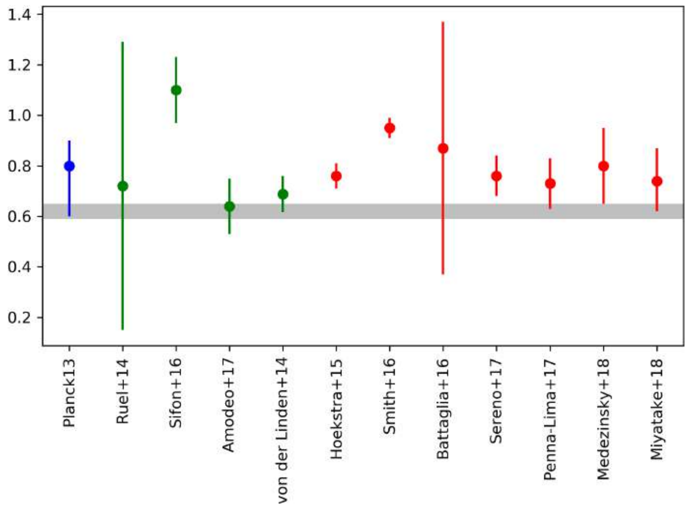

Figure 1.18: Value of $(1-b)$ from previous studies. In blue, the result from Planck Collaboration XX (2014), using a scaling relation from X-ray observations; in green, the mass bias from $M_{dyn} - M_{SZ}$ scaling relations and, in red, those from weak lensing studies, respectively. All these values are listed in table 5.5. The grey shaded region represents the mass bias values that reconcile the tension between CMB and SZ number counts from Planck Collaboration XX (2014).

times higher than the observed one (left panel of figure 1.17, Planck Collaboration XX 2014). The mass bias value is the result of the comparison between the scaling relation obtained correlating X-ray and SZ data and those estimated from different numerical simulations. Although $(1-b)$ accounts for hydrostatic and others observational biases, the gas physics of simulated clusters or the parameters of the $Y - M$ scaling relations might be sources of uncertainties and hidden biases. Therefore, a different value for mass bias could alleviate the tensions in the σ_8 parameter constraint. To achieve this goal, the *Planck* Collaboration performed a joint analysis of the two data sets (SZ and CMB) letting $(1-b)$ free to vary in a wide range, from 0.1 to 1.5. The result of this test is a lower mass bias, $(1-b) = 0.59 \pm 0.05$, lying at almost 2σ from the observed one. Therefore, due to the crucial role of the mass bias, a more precise characterization and reduction of mass bias uncertainties is needed. This issue is one of the scientific goals of this thesis (see section 1.5).

Over the last few years, in concomitance with this work, several groups have worked on the characterisation of the mass bias by combining SZ data with those in other wavelengths, especially from the optical point of view using mas- ses derived from weak lensing and, marginally, from velocity dispersion techniques. Figure 1.18 shows all the mass bias values with their respective uncertainties, published in recent years. The studies that use dynamical masses are plotted in green, those that calculated the mass via weak lensing techniques are plotted in red, and the *Planck* Collaboration value is shown in blue. The grey band represents the interval where $(1-b)$ should lie to alleviate the tension, according to the Planck Collaboration XX (2014) analysis.

The analysis of the PSZ2 number counts results (Planck Collaboration XXIV 2016) is not in the scope of this work. However, it is important to note that these results are completely compatible with those summarised above. Moreover, in this analysis, the *Planck* Collaboration used the fiducial value from Planck Collaboration XX (2014), instead they used as a prior on $(1-b)$ the results of two weak lensing surveys: Weighing the Giants (WtG, $(1-b) = 0.688 \pm 0.072$, von der Linden et al. 2014), Canadian Cluster Comparison Project (CCCP, $(1-b) = 0.780 \pm 0.092$, Hoekstra et al. 2015). In addition, *Planck* Collaboration has chosen another prior derived by comparing SZ masses with those measured through CMB lensing (CMBLens, $(1-b) = 0.99 \pm 0.19$, Lewis & Challinor 2006). Figure 1.19 shows the constrains in the (Ω_m, σ_8) plane (left panel) and the $(1-b)$ posterior probability for each prior and for the SZ-CMB joint analysis. As expected from the 2013 analysis, lower the mass bias prior, lower the discrepancy between SZ and CMB constraints on σ_8.

This work is structured in this context, and one of its principal goals is to characterise the mass bias using data collected during the *Planck* PSZ1 follow-up, as described in chapter 2. Our analysis of the $M_{SZ} - M_{dyn}$ relation to find a $(1-b)$ value derived from optical data is described in chapter 5.

1.5 Objectives of this thesis

This work focuses on the observational study of galaxy clusters in order to build a reference cluster sample useful for future cosmological exploitation. The main scientific goals of this thesis are the following:

- To carry out the optical follow-up of the unconfirmed *Planck* PSZ1 sources in the northern sky with declination of $\delta > -15°$. The reference sample contains 212 clusters to be studied. To develop this goal, we will carry out a two-year observational programme(the ITP13-15) in order to retrieve photometric and spectroscopic information which allow a dynam-

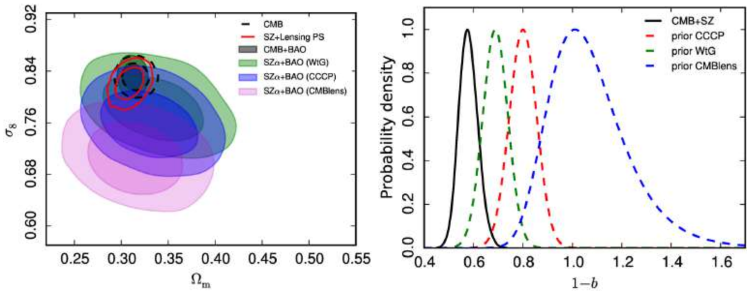

Figure 1.19: Left panel: Comparison of likelihood contours in the (Ω_m, σ_8) plane for the PSZ2 sample. Black dashed contours are the 68% and 95% confidence regions from CMB-only analysis. In green, blue and violet, contours the two-dimensional likelihood, at 68 and 95%, for the SZ+BAO analysis where the mass bias let free with prior given by WtG, CCCP, and CMB lensing mass calibrations, respectively. Right panel: Distribution of mass bias values to reconcile the tension on σ_8, obtained from the SZ and CMB joint analysis with $(1-b)$ let free to vary (black solid). Dashed green, red, and blue distribution show the mass bias priors from WtG, CCCP, and CMB lensing, respectively. Plots from Planck Collaboration XXIV (2016).

ical characterisation of the unknown PSZ1 sources. The first phase of this task will focus on the preparation of observations, data acquisition and reduction, paying special attention to the spectroscopic aspects with the design of MOS masks and determination of the spectroscopic redshift of the galaxies observed using this technique. The second part will consist in the analysis of galaxy samples obtained via MOS spectroscopy, in order to recognise clusters members, to estimate the spectroscopic redshift and, where possible, to estimate the velocity dispersion of the cluster.

- To characterise the scaling relation between masses derived from SZ effect (M_{SZ}) and those from the dynamical analysis of the cluster, M_{dyn}, in order to estimate the mass bias $(1-b)$. The ultimate goal is to provide a measurement of $(1-b)$ within a high level of accuracy. This objective requires us to understand the possible biases introduced in the calculation of dynamical masses. In particular, as a result of the limitations of our observational strategy, we will carry out a theoretical study in order to understand the behaviour of the velocity dispersion and mass estimators in the limit of low number of galaxies members $(N_{gal} < 30)$.
- To understand the implications of the mass bias estimation on the determination of cosmological parameters σ_8 and Ω_m. Particularly, how

the reduction of the uncertainty on the mass bias affects the cosmological parameter constraints and their errors. Since the *Planck* mass bias shows a dependence on the cluster mass, it is also important to study the mass bias obtained by comparing SZ and optical data as a function of the cluster mass in order to understand if this implies a different $Y_{500} - M_{500}$ scaling relation.

2

The *Planck* PSZ1 optical follow-up: observational strategy

This chapter describes the optical follow-up observations of the PSZ1 sources that we have carried out in the IAC. In Section 2.1 we introduce the objectives of the observational programme and the instruments used to achieve it. In section 2.2 we describe the strategy followed during the observational campaign and data reduction procedure. Part of the results presented in this chapter were published in Planck Collaboration Int. XXXVI (2016) and Barrena et al. (2018). A third paper is in preparation (Barrena et al. in prep.).

2.1 The ITP programme

The PSZ1 catalogue, as described in Chapter 1, consists of 1227 SZ sources detected in the *Planck* all-sky maps of the first 15.5 months of observations, by means of their SZ signal with a signal-to-noise ratio (S/N) of 4.5 or higher. The majority of them, 861, were confirmed as GCs after a detailed validation process (Planck Collaboration XXIX 2014) that is geared towards the search for possible counterparts in the ROSAT All-Sky Survey (RASS, Voges et al. 1999b, 2000), the Sloan Digital Sky Survey (SDSS, DR8, Aihara et al. 2011), the WISE all-sky survey Wright et al. (2010), and DSS3 images, as well as cross-correlations with optical, X-ray, and other SZ catalogues (see section 1.4.1). The remaining 366 SZ sources were sent to observing facilities to undergo a confirmation follow-up. During this process, different programmes were carried out, e.g. at the RTT150 telescope (Planck Collaboration Int. XXVI 2015), the MegaCam at CFHT (van der Burg et al. 2016) and one at Canary Islands observatories described in this chapter (Planck Collaboration Int. XXXVI 2016; Barrena et al. 2018, in prep.), which is an important part of this PhD thesis.

2.1.1 The sample

The main goal of our observational programme was to perform a systematic follow-up of the whole set of PSZ1 clusters candidates in the northern sky with no confirmed counterparts at the moment of the catalogue publication.

The sample selection has followed two main criteria: the validation status in the *Planck* catalogue, and the observability from Canary Islands observatories. Objects with declination above $-15°$ are not observable from this latitude at a reasonable air-masses. For this reason, they have been left to other campaigns conducted in the Southern Hemisphere by other *Planck* Collaboration teams.

As explained in section 1.4.1.1, the sources with an unknown external counterpart were classified in three classes of reliability: CLASS1 (high reliable candidates), CLASS2 (reliable candidates), CLASS3 (low reliability candidates) (Planck Collaboration XXIX 2014). This information was stored in the `validation` column of the PSZ1 catalogue. Therefore, our sample is composed by those PSZ1 cluster candidates that fulfil the requirements $Dec \geq -15°$ and `validation` $=$ 1, 2 or 3, for CLASS1, CLASS2 and CLASS3, respectively. The total sample is composed by a total of 212 targets, 24 of which are CLASS1, 98 are of CLASS2 and 90 of CLASS3 (hereafter, the ITP-sample).

2.1.2 Instrumental set-up

Our two-year International Time programme ITP13B-15A (ITP) was accepted by the International Scientific Committee and conducted at the Roque de Los Muchachos observatory (ORM, La Palma). As we were interested in validating GCs photometrically and spectroscopically in a wide range of redshift, $0.1 \lesssim z \lesssim 0.9$, we used a variety of different instruments (summarized in Figure 2.1 and Table 2.1).

Our observational programme was carried out in the framework of a two year International Time programme ITP13B-15A (ITP) accepted by the International Scientific Committee of the Roque de Los Muchachos observatory (ORM, La Palma). As we were interested in validating photometrically and spectroscopically GCs in a wide range of redshift, $0.1 \lesssim z \lesssim 0.9$, we used different instruments. Table 2.1 summarises the telescopes and instruments used during the ITP.

Figure 2.1: On the left we show (from the top to the bottom) INT, WHT (credit: Nik Szymanek), TNG (credit: Avet Harutyunyan/TNG) and GTC (credit: Axel Taferner) telescopes. On the right, the WFC/INT, ACAM/WHT, DOLORES/TNG and OSIRIS/GTC instruments are shown.

INT/WFC: The Wide Field Camera (WFC) is an optical camera mounted at the prime focus of the 2.5m *Isaac Newton Telescope* (INT). The WFC consists of a mosaic of 4 thinned AR coated EEV CCDs measuring $2K \times 4K$ pixels each plus a fifth Loral/Lesser detector dedicated to the autoguiding functions. The camera has a focal ratio of $f/3.29$ and a field of view (FoV) covered by the entire mosaic is $34' \times 34'$ (green shape in Fig. 2.2), corresponding to a plate scale of $0.33''$/pixel. The filter wheel allows a maximum of 6 filters, both broadband and Stromgren, as well as a set of narrowband filters.

WHT/ACAM: The Auxiliary-port CAMera (ACAM) is an instrument mounted in a folded Cassegrain focus of the 4.2m *William Herschel Telescope* (WHT). ACAM has one low-fringing, deep-depletion $2K \times 4K$ pixels EEV CCD. The CCD contains the whole illuminated area and is windowed. Its FoV is $8'$ radius (magenta circle in Fig. 2.2) and the plate scale is $0.253''$/pixel. A set of 11 filters can be mounted on the filter wheel. Broad-band filters (usually Sloan u g r i z) are available by default, but all the *Isaac Newton* Group's (ING) set of filters can be mounted. ACAM allows low resolution spectroscopy as well. A VPH prism provides spectral coverage from $\sim 3500\,\text{Å}$ to $9400\,\text{Å}$ with a resolution of $R \sim 450$ and 900 for the two long-slit (LS) available of $1.0''$ and $0.5''$ respectively.

TNG/DOLORES: The Device Optimized for the LOw RESolution (DOLORES),a low-resolution spectrograph and camera, is found in the Nasmyth-B focus of the 3.6m Telescopio Nazionale *Galileo* (TNG). DOLORES is equipped with a 2048×2048 E2V 4240 thinned back-illuminated, deep-depleted, Astro-BB coated CCD that cover $8'.6 \times 8'.6$ of the sky (light blue square in Fig. 2.2) with a plate scale of $0.252''$/pixel. The filter wheel can contain up to 11 filters, both wide and narrow band. In spectroscopy mode, the slider that contains the slits, called *Tram*, allows the observer to choose between 5 long slits, $0.7''$, $1.0''$, $1.5''$, $2.0''$ and $5.0''$, or up to 5 Multi-Object Spectroscopy (MOS) plates composed by a number of slitlets of $1.1''$ or $1.6''$. The grism wheel contains up to 9 dispersing optical elements and the focusing-pyramid device. For our programme, we chose the LR-B grism that disperses the light over $3000-8430\,\text{Å}$ with a resolution of $R = 585$ for a $1.0''$ slit.

GTC/OSIRIS: OSIRIS (Optical System for Imaging and low-Intermediate-Resolution Integrated Spectroscopy) is an optical spectrograph and imager placed in the Nasmyth-B focus of 10.4 m Gran Telescopio Canarias (GTC). The mosaic of 2 buttable $2K \times 4K$ MAT-44-82 CCDs, from Marconi, consti-

Table 2.1: Telescopes and instrumentation used for the ITP Planck PSZ1 follow-up

Telescope	Aperture [m]	Instrument	FoV	Pixel scale [$''$]	Resolution	Allocated time	N_{ima}	N_{spec}
INT	2.5	WFC	$34' \times 34'$	0.33	–	22 Nights	80	-
WHT	4.2	ACAM	$8' \times 8'$	0.253	$R = 450$	22 Nights	54	31
TNG	3.6	DOLORES	$8'.6 \times 8'.6$	0.252	$R = 585$	24 Nights	-	63
GTC	10.4	OSIRIS	$7'.8 \times 6'$	0.254	$R = 500$	96 Hrs	-	64

Columns 4 to 6 show field of view, pixel scale and resolution of each telescope used (either imaging or spectroscopic mode). Column 7 shows the total number of awarded nights per telescope. The last two columns present the total number of observed SZ clusters in imaging and spectroscopy, repsectively.

tute the detector of this instrument. The plate scale of OSIRIS is $0.254''$/pixel while its FoV is $7'.8 \times 8'.5$. However, significant vignetting in the first 250 pixels of CCD1 reduces it to a $7'.8 \times 7'.8$ unvignetted field (yellow square in Fig. 2.2).

2.2 Observations and data reduction

The S/N of the *Planck* SZ detection gave us the main criterion for ordering the list of targets following a given priority. This way, the targets were observed following their SZ S/N. SZ sources with high S/N were considered as high priority targets in our observational scheduling.

Our follow-up strategy is divided into two steps: photometric and spectroscopic GC confirmation. A preliminary SDSS and DSS screening was performed, searching for possibles optical counterparts. After this process, if a cluster was confirmed, new imaging data were not needed. For these targets, we also investigated the SDSS spectra database and, if we could identify several cluster members, we provided the spectroscopic redshift of the cluster. Otherwise, we consider them in the list of spectroscopic targets. As a first step, we performed photometric observations using g', r' and i' broad-band Sloan filters. This set of filters is very useful to detect the 4000 Å break up and the cluster red sequence (hereafter RS) for sources within the redshift distribution of the *Planck* SZ-detected clusters, $z < 1$ (Planck Collaboration XXIX 2014). Combining g', r' and i'- colours, it is possible to determine the photometric redshift for cluster members candidates with a $z < 0.7$ and detect them up to $z < 1$. In a second phase, our photometric redshift estimate was confirmed through spectroscopic observations, either using long-slit or MOS technique.

2.2.1 Imaging

Imaging observations were performed using the WFC at the INT and ACAM at the WHT in multiple runs from August 2013 to July 2015.

All fields were observed with g', r' and i' Sloan broad-band filters. The integration time per filter, was divided into three different exposures of 500 s and

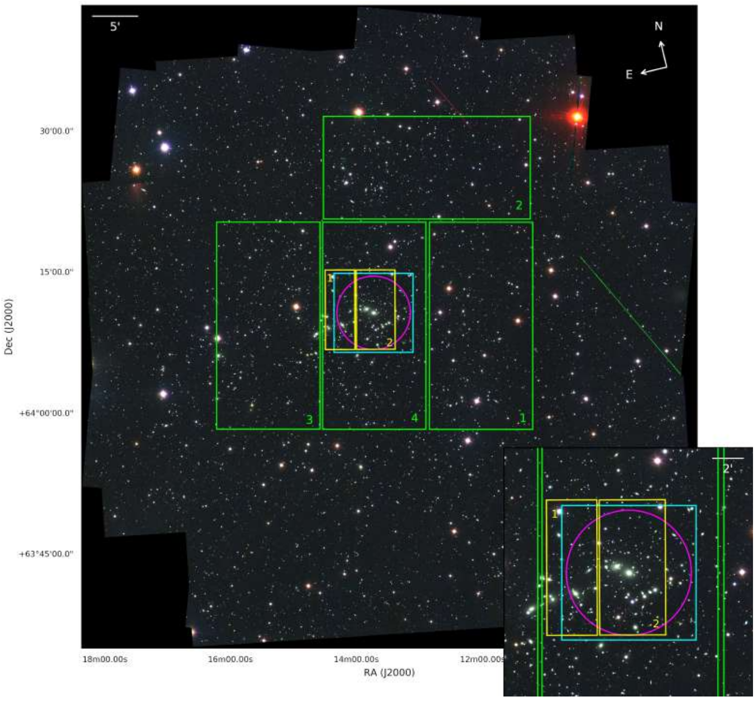

Figure 2.2: RGB image built with a i', r', g' SDSS mosaic fields of PSZ1 G093.93+34.92 with, superposed, the Field of View of INT-WFC (green), WHT-ACAM (magenta), TNG-DOLORES (blue), GTC-OSIRIS (yellow).

300 s, at INT and WHT, respectively, following a three-point dithering pattern with $10'' - 15''$ offset to better remove bad pixels and vignetting, correcting most of the fringing effects present in the CCD and minimising the effect of the cosmic rays. Figure 2.3 shows the RGB composition of PSZ1 G075.29+26.66 (top panel) and of PSZ1 G057.42-10.77 as an example of INT/WFC (CCD4) and ACAM images, respectively.

2.2.1.1 Data reduction and photometry

Optical images were reduced using `IRAF` tasks. The standard reduction procedure starts with bias and flat-field corrections and ends with the astrometric calibrations. The astrometry was performed using *images.imcoords* tasks and USNO B1.0 catalogue as reference. The zero-point calibration refers to SDSS and is based on the observations of standard stars calibrated in the photometric data of the SDSS system (Fukugita et al. 1996). In case of non-photometric nights, targets were calibrated in the following observing runs or using dedicated service time at the Canary Islands Observatories.

The source detection and photometry were performed using *SExtractor* (Bertin & Arnouts 1996b) in single-image mode. Sources were independently detected in each individual band if at least ten connected pixels exceed S/N $\sim$ 3 in the filtered images, which corresponds to the 1.5σ detection thresholds. A variable size elliptical aperture photometry was performed using the MAG_AUTO mode. This procedure gives the total magnitude of an object applying the Kron's "first-moment" algorithm (Kron 1980). The size of the elliptical aperture is determined by the "Kron factor", k. For galaxies convolved with Gaussian seeing, $k = 2.5$ gives an aperture that contains approximately 96% of the object flux. The "minimum radius" parameter is set to 3.5 in order to avoid the presence of small apertures due to low S/N. All photometric catalogues were then merged in order to create a master catalogue containing the three band photometries.

From the diagrams $log(N) - mag$ shown in Figure 2.4, we set the completeness and limit magnitudes as the point where the counts fall to 90% and 30%, respectively of the expected if the $log(N) - mag$ relation was linear. In Table 2.2 we present the magnitudes for g', r' and i' photometry and for the two telescopes, INT and WHT.

Due to WFC large PSF distortions over the large FoV, the star/galaxy classification was very challenging for faint sources with $r' > 18$. So, a star cleaning procedure within small regions containing the cluster candidates was then needed to obtain clear RS in the colour-magnitude diagram (CMD).

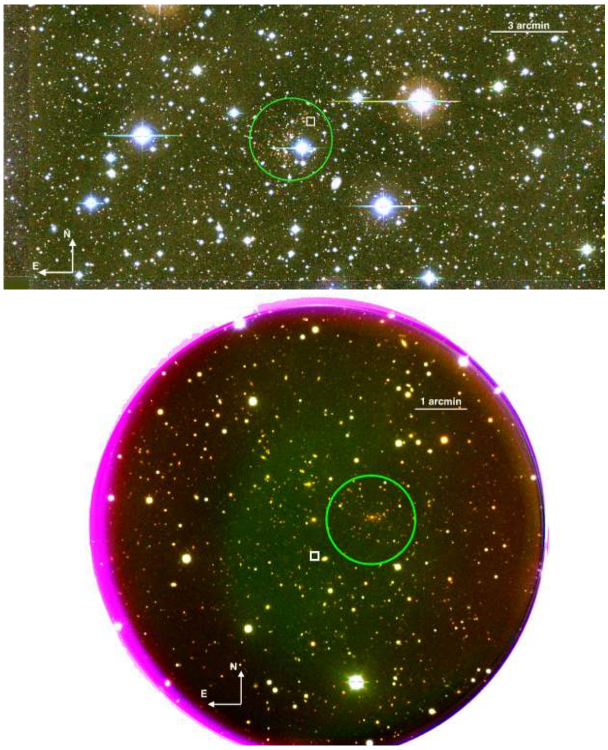

Figure 2.3: RGB image of PSZ1 G075.29+26.66 observed with WFC/INT (top panel) and of PSZ1 G057.42-10.77 observed with ACAM/WHT (bottom panel). The RGB are the composition of g', r' and i' images, obtained by exposing 3×300 s and 3×500 s, at the WHT and INT, respectively, in each filter. Green circles frame the clusters, while the white square represents the nominal *Planck* pointing.

Table 2.2: Completeness and limit magnitudes for each telescopes

	Completeness magnitudes		Limit magnitudes	
Filters	INT(WFC)	WHT(ACAM)	INT(WFC)	WHT(ACAM)
g'	22.4	22.2	24.0	24.2
r'	21.8	22.0	23.2	23.8
i'	21.4	21.4	22.6	23.2

Exposure times of 3×300 s in the ACAM/WHT and 3×500 s in the WFC/INT.

2.2.1.2 Photometric redshift estimation

Our method to detect galaxy clusters in the images consists of finding overdensities of galaxies showing coherent colours. The photometric redshifts calculation is based on the red sequence (RS) method by Gladders & Yee (2000). We select galaxy members using the fitted cluster RS by calculating the mean colour of the five brightest likely members, and fixing the RS slope to -0.039 and -0.017 in (g'- r') and (r'- i') CMD, respectively (see Barrena et al. 2012), and then combining them with the spatial distribution of the full catalogue to search for possible candidates. In addition, galaxies with colours within $RS \pm 0.15$ were considered potential cluster member candidates and were selected as galaxy targets for further spectroscopic observations.

The photometric redshift estimates for these galaxy overdensities arise from a modification of this method with the empirical relations of Lopes (2007) (Planck Collaboration Int. XXXVI 2016). To first order, the photometric redshifts can be estimated with

$$z_{phot} \approx 0.361(g' - r') - 0.278, \qquad if \quad (r' - i') \lesssim 0.75 \tag{2.1}$$

$$z_{phot} \approx 0.364(r' - i') + 0.182, \qquad if \quad (r' - i') \gtrsim 0.75. \tag{2.2}$$

We compared this methodology with the photometric redshifts obtained with the BPZ code (Benítez 2000), and found that the two methods are fully consistent for the colour-selected galaxies in the cluster candidates.

Moreover, the images taken in the g', r' and i' filters were combined in RGB colour frame in order to consolidate our result with a careful visual inspection of each individual image. Figure 2.5 shows an example of CMD for the cluster PSZ1 G183.26+12.25. This visual inspection is particularly important for the identification of high redshift ($z > 0.7$) clusters, fossil groups, poor or even very low redshift systems. In the first case, even though our optical data are not deep enough to identify the cluster RS, the galaxy overdensities corresponding to the brightest members were clearly visible in the RGB images at the minimum detection level. On the other hand, fossil systems (e.g. Jones et al. 2003a; Voevodkin et al. 2010) are very evolved structures with a mass content capable of producing a detectable SZ effect on Planck maps (Pratt et al. 2016). This kind of galaxy clusters, characterised by the presence of a huge Bright Central Galaxy (BCG) and a poor galaxy population, are also particular cases and are not easily detected by automatic algorithms in the colour space. Their RS is usually not very populated due to the 2 magnitude gap beyond the BCG, so this kind of clusters do not fit the standard RS. Thus, visual inspection of RGB images is essential for pinning down these objects.

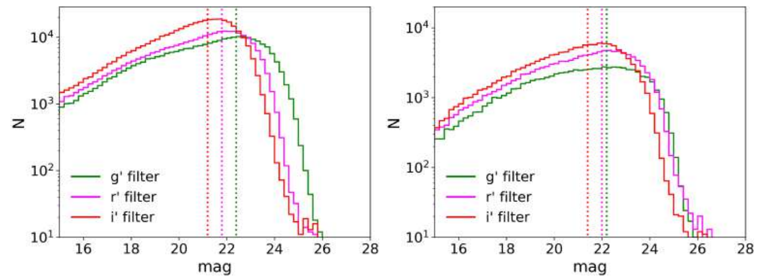

Figure 2.4: Magnitude histograms of the stacked photometry of all fields observed during the ITP programme for the WFC/INT (left panel) and the ACAM/WHT (right panel). The green, magenta and red solid and dotted lines represent g', r' and i' counts and completeness magnitudes, respectively.

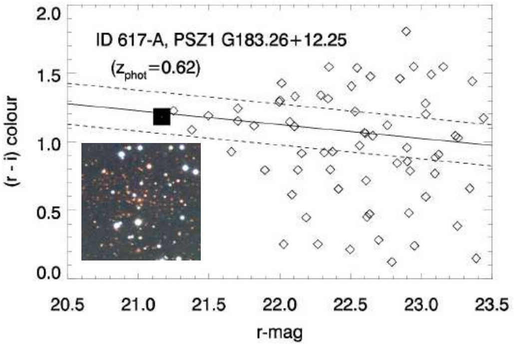

Figure 2.5: CMD (r'-i', r') of the ID 617-A, associated to PSZ1 G183.26+12.25 source. The diagram considers extended sources within a region of $2.'5 \times 2.'5$ (1×1 Mpc) around the BCG of the system (represented by the big filled square in the plot). The solid line represents the fitted RS which yields a $z_{phot} = 0.62$. Dashed lines correspond to $RS \pm 0.15$ locus, where likely cluster members are selected. An RGB image (composed using the g', r' and i' frames) showing the $2.'5 \times 2.'5$ inner region of this cluster is superimposed to the plot. Figure taken from Barrena et al. (2018)

2.2.2 Spectroscopy

Spectroscopic data were acquired with DOLORES at TNG and OSIRIS at GTC from August 2013 to July 2015 in during the ITP. However, in a few cases, ACAM at WHT was also used in its long-slit spectroscopy mode. All DOLORES and some OSIRIS observing blocks were performed in MOS mode, while most of the OSIRIS spectra were obtained with a long slit, due to the absence of the MOS mode for this instrument before 1st March 2014.

2.2.2.1 Mask design

I was especially involved in the mask design process to carry out multi-object observations in DOLORES/TNG and OSIRIS/GTC spectrographs. In particular, I designed more than 100 masks during the two years of the ITP programme. During particularly busy times scheduling requirements , I was able to design about two MOS masks per day. Our priority was to insert as many slitlets into the mask as possible. However, the difficulties in distinguishing stars and galaxies from the INT photometric catalogues, as described in the previous section, made a visual inspection necessary to carry out an appropriate selection of spectroscopic targets. Once the targets were selected, pre-imaging was asked to the telescopes facilities. Pre-imaging is a short exposure, ~ 120 s or ~ 60 s using no filters, centred in the target pointing at TNG and GTC, respectively. This pre-image was used to place the slitlets on the selected objects. After visual inspection of the RGB images produced combining g', r' and i' bands, I picked-up the galaxies with similar colours, using the telescope's designer software.

The TNG Interactive Mask Design Interface (IMDI), developed by Enrico Held (INAF-Padova Observatory), is a graphical interface (GUI) based on IDL widget procedures that allows the observer to easily set-up the observation selecting the grism and slitlet width. Unfortunately, the procedure leads to some limitations, especially in the minimum separation between slits and slit centring. For these reasons, I was able to place between 35 and 45 slitlets with $1.6'' \times 7.5''$ width. To simplify the centring process, around $3-5$ fiducial stars were used as pivot points. In order to observe GCs at $z \leq 0.4$, we selected the LR-B grism, provided in the DOLORES/TNG device, which fits well in the $3600\,\text{Å} \leq \lambda \leq 6000\,\text{Å}$ interval where we expect to detect the main spectral features. The left panel of Figure 2.6 shows an example of TNG mask design obtained using IMDI. Overlaid to the corresponding pre-image, there are horizontal rectangles delimiting the location of the expected spectra.

The OSIRIS/GTC provides its own MOS facility, the MaskDesigner tool

(MD), written in JAVA by Txinto Vaz Cedillo. Its architecture is more complex than the IMDI, but more user-friendly in avoiding the problems explained before. For the design of the OSIRIS masks, we also used a pre-image provided as a 2×2 binned Sloan r'-filter image centred in the scientific target. OSIRIS images contain the two CCDs, both included as different extensions of a single fits file, so the first step is to merge them into one mosaic image, for which the pixel coordinates are continuous and geometrically corrected from field distortions. The observation set-up consists of grism selection and definition of the properties of the slits, orientation and width. The grism selection is a crucial aspect in GTC mask designing; in fact, in low-resolution mode, MD allows to select targets in a portion of the total FoV in order to provide a complete spectral coverage. Due to its high efficiency in the blue part of the spectrum, we selected grism R300B, but his choice reduces the FoV to $7'.5 \times 2'.8$. In OSIRIS, the spectra are dispersed in the vertical direction with the red part at the top and the blue part at the bottom, so the slits were positioned horizontally. The slitlet dimensions are set-up to $5''$ in the spatial direction in order to obtain sky flux on the edge of each slit, and $1.2''$ width, in the spectral direction, to include the majority of the flux of the galaxy cores. This configuration allows to fully fill the OSIRIS mask with up to 60 slitlets and about 4 circular holes for fiducial stars. These 4-5 pivots are essential to perform a correct mask centring on the target field. Figure 2.6 (right panel) shows an example of the OSIRIS mask design performed with the MD Detector Editor on the target.

2.2.2.2 Observations

Spectroscopic observations were performed during 23 nights in visiting mode at TNG, and 96 hours at GTC in queue mode, during the ITP project.

The spectroscopic targets were classified according to their photometric redshifts. The GTC/OSIRIS time was dedicated to high redshift sources with $z_{phot} > 0.4$, while TNG/DOLORES was left for $z_{phot} \leq 0.4$ clusters. In order to obtain S/N$\sim$ 5 for galaxies with r'= 20.5, each mask was exposed with 3×1800 s. However, the visiting mode forced us to observe some nights with seeing $> 1.4''$, so reducing the S/N in some cases. He-Ne and Hg-Ne arcs acquired during the observations allowed us to obtain wavelength calibrations with $rms \sim 0.1$ Å over the whole wavelength range. The more distant clusters were observed in the GTC/OSIRIS acquiring 3×1000 s exposures through the R300B grism and with a seeing $\leq 1.2''$. This set-up yields S/N$\sim$ 5 for galaxies showing magnitudes r'= 21.6. Wavelength calibrations with ~ 0.2 Å accuracy were performed using Hg, Ne, and Ar arcs.

The same observational set-up was used in the long-slit mode ($1.2''$ slits and

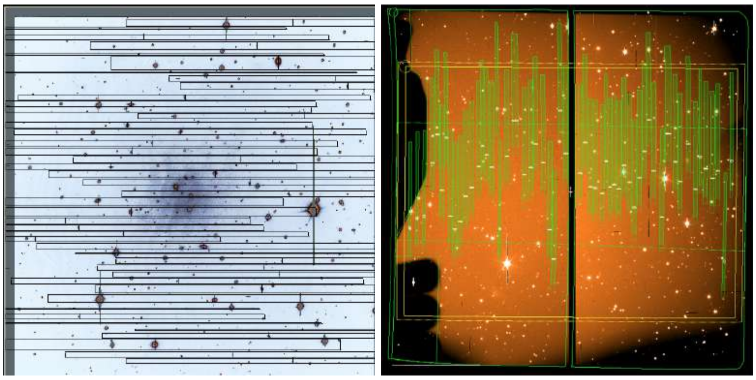

Figure 2.6: Left panel: DOLORES/TNG MOS mask of PSZ1 G150.33–20.04. Right panel: OSIRIS/GTC MOS mask of PSZ1 G141.73+14.22 . The entire MOS FoV is within the yellow lines, while green stripes represent the position of the expected spectra.

R300B grism). These observations were planned in order to get the maximum number of redshift estimates placing between two and four galaxies within a single slit, and performing two slit orientation for each cluster candidate. The BCG was always included in one of the position angles. Therefore, following this scheme in OSIRIS/GTC long slit mode, we were able to obtain even $5-6$ redshifts per cluster candidate.

In very few cases, ACAM/WHT was used to obtain the spectra of the most luminous galaxies of the cluster. Using a $1''$ long-slit and the holographic dispenser with resolution of $R \sim 400$, we exposed 2×1000 s per slit slit and obtaining S/N ~ 5 for galaxies with magnitudes $r' \approx 19.5$.

2.2.2.3 Spectroscopic data reduction

Data reduction was performed using standard `IRAF` procedures. The three exposures were combined with the `IMCOMBINE` task using the median values in order to perform a first cleaning of cosmic rays and bad pixels. After a careful test, we decided not to correct for bias and flat-field. Neither bias nor spectroscopic flat field corrections were performed because the addition of computational noise yields poor final spectra. Each 2D-spectrum was analysed separately. The sky was evaluated in the external region of each slitlets and subtracted from the spectra. The one-dimensional spectra, extracted with the `APALL IRAF` task, were further cleaned from residuals and cosmic rays. The wavelength calibration

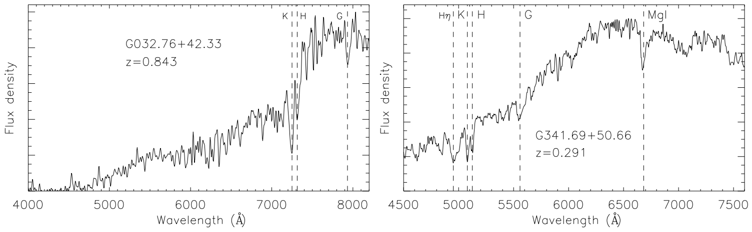

Figure 2.7: Example of the spectra obtained with GTC/OSIRIS (left panel) and TNG/DOLORES (right panel) for two luminous galaxy members, with magnitudes $r'= 21.6$ and 17.8, in the clusters PSZ1 G032.76+42.33 and PSZ1 G341.69+50.66, at $z = 0.843$ and 0.291, respectively. Dashed lines correspond to the wavelength of the absorption features identified in each spectra at the redshift of the clusters. Flux density is plotted in arbitrary units. Figure taken from Barrena et al. (2018).

was carried out using Hg, Ne, Ar and He, Ne, Hg lines from OSIRIS/GTC and DOLORES/TNG arcs, respectively. Finally, we checked for possible deviations in the wavelength-calibrated spectra using the [OI] telluric line at 5577.3 Å.

2.2.2.4 Redshift determination

We estimated radial velocities using the cross-correlation technique (Tonry & Davis 1979) implemented in the `IRAF RVSAO` task. For each spectrum, the task performs a cross-correlation with six spectrum templates of different galaxy morphologies: E, S0, Sa, Sb, Sc, and Irr (Kennicutt 1992). The R parameter provided by the `XCSAO` procedure is linked with the S/N ratio of the cross-correlation peak. We chose the radial velocity corresponding to the template with the highest R-value. Most of the redshifts were estimated using absorption lines only (mainly H and K CaI doublet, G-band and MgI triplet), as it corresponds to a dominant early-type population of galaxies in clusters. However, a few cases presented strong emission lines (mainly [OII], [OIII] doublets and Hα), which were used to determine the redshift. Finally, we visually inspected all spectra to verify the velocity determination, which was particularly difficult for galaxies at $z > 0.7$, due to the low S/N of the spectral continuum and the few spectral features identified within the visible wavelength range. In Figure 2.7 we show two examples of spectra from high redshift (left panel) and low redshift (right panel) galaxies observed with OSIRIS/GTC and DOLORES/TNG, respectively. We also show the main absorption features used to determine the radial velocity. At the end of this process, the cross-correlation yields a mean error in the radial velocity estimates of $\Delta v \sim 75\,\mathrm{km\,s^{-1}}$. However, we were able to determine the true intrinsic velocity errors comparing a set of about 40 spectra (one mask) observed twice, in two different observing runs. By comparing the first and second velocity estimates we obtain a mean error of $\Delta v \sim 110\,\mathrm{km\,s^{-1}}$.This means that actual errors in the redshift estimates are $z \sim 0.0003$, which is in agreement with the predicted value by the resolution set-ups of the spectrographs used for this follow-up.

3

The *Planck* PSZ1 optical follow-up: results

This Chapter shows the results of the ITP observational programme.First, we define the final ITP sample, explaining the procedure of cluster identification and the criteria we adopted in order to associate the SZ signal to a cluster counterpart. Then, in section 3.2, we present the statistical analysis of our sample and of the complete PSZ1 in the northern sky. Part of the results presented here are published in Planck Collaboration Int. XXXVI (2016) and Barrena et al. (2018). There is a third paper in preparation.

3.1 The ITP catalogue

In this section we describe the main results of our follow-up programme, the so-called ITP13B-15A.

3.1.1 Cluster identification

In Section 2.2.1.1 we explained how we identify a galaxy cluster and derive its photometric redshift. Here, we focus on the spectroscopic identification and characterisation of GCs.

Once a mask is fully reduced, a catalogue with the estimated radial velocities is built. We look for overdensities in the radial velocity space first by searching for at least 4 galaxies in a range of $\pm 5000\,\mathrm{km\,s^{-1}}$ around the velocity of the BCG (defined as the brightest galaxy within the overdensity). Since MOS mask targets are selected with a colour compatible with the estimated photometric redshift, in most cases, only one peak is detected. However, sometimes, foreground or background small systems are also present. These cases are more frequent when we perform the analysis by joining our spectroscopic data with those retrieved from the SDSS archive.

GCs are bound structures embedded by the LSS. Therefore, a cluster catalogue could be contaminated by objects not belonging to the cluster itself, but only associated with it. The presence of these galaxies in the LoS of the clusters, called interlopers, may modify the intrinsic distribution of cluster members in the phase-space, biasing the estimation of velocity dispersion and mass (see section 4.2). For this reason, GCs membership is a crucial and ongoing, problem in GCs astrophysics. There are several methods of membership selection. Some of them only take into account information on velocities distribution, e.g. the 3σ clipping by Yahil & Vidal (1977). Other methods consider the whole projected phase-space, taking into account the projected distance from the cluster centre, like the method that uses the escape velocity as a function of the cluster radius (den Hartog & Katgert 1996), the caustic method (Diaferio 1999) or the GalWeight, which assigns a weight to each galaxy according to it position in the phase-space (Abdullah et al. 2018).

In our case, the reduced number of galaxies detected, on average between 10 and 20 per cluster, and the aperture fixed by the MOS FoV do not allow us to properly select members using these techniques. In particular, we tested the caustic method on two GCs, PSZ1 G123.55-10.34 and PSZ1 G060.12+11.42, with 30 and 20 members, respectively. The caustic analysis finds 20 and 10 members distributed in the very center of the galaxy, respectively, implying a very low estimate of the velocity dispersion. In order to obtain good caustic determination, we would require hundreds of galaxy members in a big radius, $r > 2$ Mpc (Diaferio 1999).

We decided to use a selection method mainly based on velocity space information. We performed a 2.5σ clipping around the mean velocity. In other words, only galaxies with $\Delta v \leq 2.5\sigma_v$were considered members. Moreover, we selected a threshold of 2.5 Mpc from the cluster centre (the BCG or the mean position of all the selected members, when a BCG is not clearly identified). This threshold limits the galaxy sample to a distance between 1.5 and 2 R_{200}. This way, we maximise the number of galaxy members, limiting the presence of interlopers to $\sim 10\%$ (Saro et al. 2013). Figure 3.1 shows the 2D projected phase-space and the velocity distribution of the stack of all cluster members (1432 in total) we selected using the procedure explained above. As an example, the velocities? histogram of PSZ1 G206.45+13.89 (top) and PSZ1 G108.26+48.66 (bottom) are shown right panels of figure 3.2.

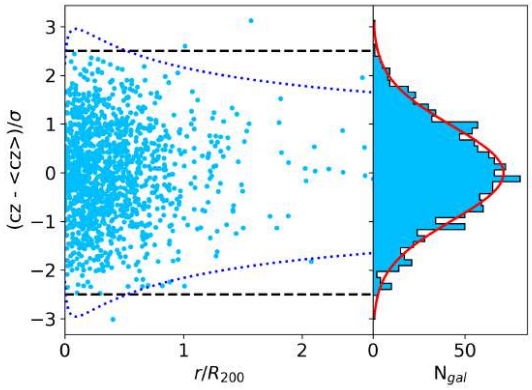

Figure 3.1: Projected phase-space and velocities histogram of the stack of all clusters members of our sample (1432 in total). Members velocities are normalised to the cluster velocity dispersion. The black dashed line represents the 2.5σ clipping, while the blue dotted line is the same clipping, but taking into account the velocity dispersion radial profile as shown in Mamon et al. (2010). Red line represents a Gaussian fit of the stacked velocity histogram.

After the definition of the sample members, we performed the last estimate of cluster redshift and velocity dispersion. We obtained the former by using a robust estimator based on the sample median, the biweight (Tukey 1958)

$$C_{\rm bwt} = M + \frac{\sum_{|u_i|<1} (x_i - M)\,\left(1 - u_i^2\right)^2}{\sum_{|u_i|<1} \left(1 - u_i^2\right)^2} \tag{3.1}$$

where u_i are given by

$$u_i = \frac{(x_i - M)}{c\ \mathrm{MAD}}, \tag{3.2}$$

$c = 6.0$ is a tuning constant, whereas M and $\mathrm{MAD} = \mathrm{median}\,(|x_i - M|)$ are the sample median and the median absolute deviation, respectively. The standard deviation is estimated through the gapper estimator, defined in Eq 4.4, and then corrected for statistical and physical biases following the recipe developed in Chapter 4.

3.1.2 Confirmation Criteria

Since the primary aim of our observational programme is to perform the validation of the SZ sources of the PSZ1 catalogue with no known optical counterparts, we need to establish a set of confirmation criteria for the detected GCs. With this aim in mind, we impose limits in several physical magnitudes related to the expected characteristics of the *Planck* catalogues, i.e. distance from the *Planck* pointing, velocity dispersion and richness.

The first confirmation criterion is the distance of the optical counterpart with respect to the PSZ1 coordinates. As shown in section 1.4.1, during the search of known counterparts within X-rays, optical and IR catalogues, the *Planck* Collaboration only associated clusters within $5'$ from the SZ signal. Therefore, following the Planck Collaboration XXIX (2014) prescriptions, we only consider valid optical counterparts the clusters that present a distance from the nominal position $\leq 5'$.

The mass–redshift distribution of the *Planck* cluster sample provides a good estimate of the limiting magnitude of the SZ signal detectable by *Planck* (Planck Collaboration XXIX 2014). This limiting SZ mass imposes a constraint on the minimum velocity dispersion that a GC must present in order to be associated with the observed SZ signal. However, the combination of noise inhomogeneity in the *Planck* Y_{500} maps (Planck Collaboration XX 2014, see Fig. 4 therein) and statistical effects such as the Eddington bias (see section 5.4.1), may cause low-mass haloes to scatter above the SZ detection threshold for velocity dispersion. This consideration has pushed us not to follow the *Planck* mass–redshift profile rigorously, but to consider two mass thresholds: $M_{500} \sim 1{\times}10^{14}\mathrm{M}_{\odot}$ and $M_{500} \sim 2{\times}10^{14}\mathrm{M}_{\odot}$ for clusters below and above redshift $z = 0.2$, respectively. Assuming a $M - \sigma$ relations, the thresholds on velocity dispersion are well represented by the limits $\sigma_v \geq 500\,\mathrm{km\,s^{-1}}$ ($z \leq 0.2$) and $\sigma_v \geq 650\,\mathrm{km\,s^{-1}}$ ($z > 0.2$).

The high cost, in terms of telescope time, has not allowed us to observe all the sources spectroscopically, forcing us to choose a criterion for the confirmation of the clusters for which only a photometric analysis was possible. This criterion chosen was *richness*, R, a mass proxy that depends only on the number of the likely cluster members (i.e. galaxies within a small colour interval). We decided to calculate the richness as the number of likely members within a projected region of 0.5 Mpc radius from the centre (assumed to be the BCG) at the redshift of the cluster. The members were selected in the $RS \pm 0.15$ mag locus, which represents the $\pm 3\sigma$ colour dispersion of RS at its brightest part, in g'-r' and r'-i' for clusters at $z \leq 0.35$ and $z > 0.35$, respectively, showing magnitudes in the range $[r'_{BCG}, r'_{BCG}{+}3]$. The field contribution was estimated by counting galaxies considering the full set of images excluding the 0.5 Mpc radius regions containing the core of the clusters. The galaxy field counts were scaled to the 0.5 Mpc cluster region, and then subtracted to the likely member counts, thus leading to the final richness value (R). The statistical analysis of the richness obtained for the observed targets allowed us to establish $R > 15$ as

Table 3.1: Confirmation criteria adopted to validate or reject clusters as counterparts of PSZ1 sources.

Flag	Spectroscopy	σ_v limit	R	Distance
1	YES	≥ 500; $0 < z \leq 0.2$	> 15	$\leq 5'$
		≥ 650; $z > 0.2$	> 15	$\leq 5'$
2	NO	–	> 15	$\leq 5'$
3	YES	< 500; $0 < z \leq 0.2$	> 15	$\leq 5'$
		< 650; $z > 0.2$	> 15	$\leq 5'$
	NO	–	≤ 15	$> 5'$
ND	–	–	–	–

Table 3.2: Summary of the *Planck* candidate associated with previously known clusters, confirmed after the follow-up and unconfirmed candidates. Data taken from Planck Collaboration XXIX (2014) and Barrena et al. (2018).

Category	N	Catalogue			
Previously validated	48	48	Confirmed	45	Flag1
				3	Flag2
New observed	212	88	Confirmed	58	Flag1
				30	Flag2
		124	Un-confirmed	48	Flag3
				76	ND
Total ITP sources observed	**260**				

the reference criteria for rich clusters, while poor systems show richness values of $R \leq 15$.

In Table 3.1 we summarise the criteria described above, and we assign the corresponding Flags. Spectroscopically confirmed counterparts, rich and well-centred clusters, are classified with Flag1, whereas rich objects without spectroscopic confirmation are classified as Flag2. The objects classified with Flag3 are confirmed clusters that cannot be associated with the SZ signal because they not fulfil all confirmation criteria. Objects with an R compatible with the field galaxy count level ($R \leq 15$), where no galaxy concentration are detected in the velocity catalogue, or very low-velocity dispersion systems, $\sigma_v < 500\,\mathrm{km\,s^{-1}}$, are considered Non Detections (ND).

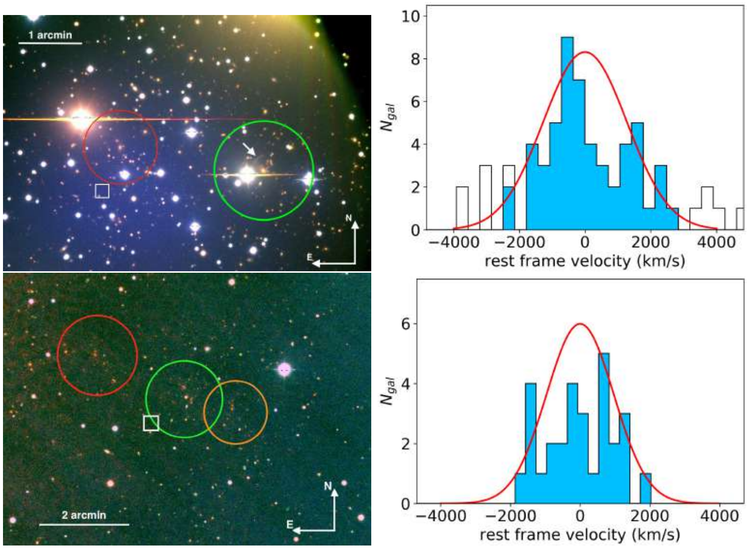

Figure 3.2: Left panels: RGB image of PSZ1 G206.45+13.89 (top) and PSZ1 G108.26+48.66 (bottom), observed with ACAM/WHT and WFC/INT, respectively. These are examples of clusters with substructures. The green, red, and orange circles frame the several clumps composing the clusters, and the white square represents the nominal *Planck* coordinates position. Right panels: radial velocity distributions of PSZ1 G206.45+13.89 (top) and PSZ1 G108.26+48.66 (bottom). The light blue sections represent the distribution of cluster members, while in white are the galaxies not selected as cluster members. The red line represent a Gaussian distribution centred in the mean cluster velocity and with dispersion $\sigma = \sigma_v$, normalised to the observed number of cluster members.

3.1.3 The ITP Galaxy Clusters zoo

In this section, we provide some examples in order to describe the different types of GCs that we found as PSZ1 counterparts.

Substructured clusters: GCs that present substructures are systems that are still in the process of mass accretion, with different clumps interacting with each other to configure more massive structures. The PSZ1 G206.45+13.89 is a medium redshift cluster ($z = 0.406$) showing two different structures. In order to sample both clumps, we performed MOS spectroscopy at OSIRIS/GTC using two masks. In fact, this cluster is the best sampled (57 members) in the whole

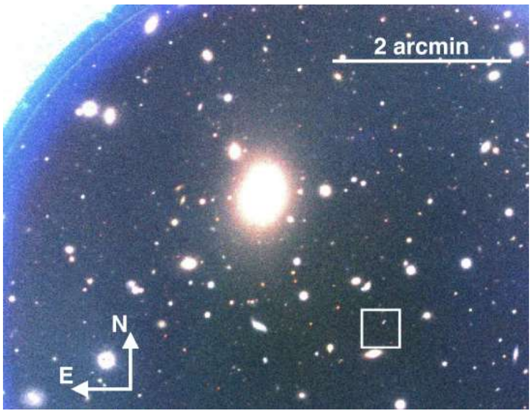

Figure 3.3: The RGB ACAM/WHT image of PSZ1 G103.94+25.81. The square indicates the PSZ1 coordinate for this SZ target. This is an example of a fossil group.

ITP catalogue. This abundance of members allows us to perfectly see the the bimodality of its radial velocity distribution, evidence of the non relaxed stage of the cluster (top right panel of figure 3.2). The WFC/INT image of PSZ1 G108.26+48.66 (figure 3.2, bottom left panel), at redshift $z = 0.671$, shows a more complex structure. The cluster presents a main body (green circle), centred on the BCG, flanked by two substructures (red and orange regions), one on each side. In this case, we acquired spectra with only one mask using OSIRIS/GTC, thus retrieving 29 cluster members. We are able to observe a very complex distribution in the velocity space (see figure 3.2, bottom right panel). In this case, the velocity histogram presents a complex shape with three different peaks, where the galaxies of different clumps spread across the full velocity distribution of the cluster. Substructured systems represent a challenge at the moment of determining their mass. In fact, it is easy to underestimate or overestimate the velocity dispersion, depending on whether individual clumps or the whole system are considered. For such cases, we decided to provide the velocity dispersion for the whole cluster.

Fossil systems: These systems are typically isolated structures, characterised by a giant elliptical galaxy (the BCG) surrounded by dwarf satellites. In these systems $r_{BCG} - r_2 > 2$; where r_{BCG} and r_2 the magnitude, in r' band, of the BCG and of the second brightest galaxy within 0.5 of the virial radius,

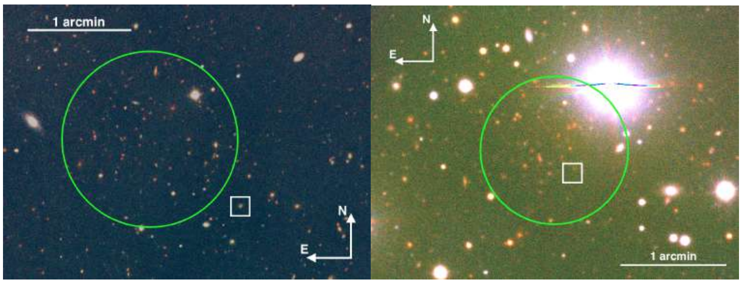

Figure 3.4: RGB images obtained with WFC/INT of the PSZ1 G104.78+40.45 (left panel) and PSZ1 G032.76+42.33 (right panel). These two clusters are the most distant spectroscopically confirmed objects of the whole PSZ1 catalogues in the norther hemisphere at redshift $z = 0.837$ and $z = 0.844$, respectively. The green circles enclose the main body of the cluster. White squares represent *Planck* coordinates

respectively (Jones et al. 2003a; Voevodkin et al. 2010; Aguerri et al. 2011). Figure 3.3 shows an example of fossil clusters, the PSZ1 G103.94+25.81. We spectroscopically confirmed this cluster by observing 17 members at $z = 0.077$.

High redshift clusters: Although the majority of *Planck* clusters are low redshift systems, in our catalogue there are eight high redshift clusters with $z > 0.8$, six of which are confirmed spectroscopically with OSIRIS/GTC. Figure 3.4 shows the two highest redshift clusters (spectroscopically confirmed) of the whole PSZ1 catalogue in the northern sky, the PSZ1 G104.78+40.45 (left panel) at $z = 0.837$ and the PSZ1 G032.76+42.33 (right panel) at $z = 0.844$.

Multiple detections: Due to the large size of the *Planck* beam ($\sim 5'$), it is not rare that the SZ signal detected by *Planck* encloses the contribution of more than one cluster. In other words, we detect more than one possible cluster counterpart associated to a single PSZ1 source. In figure 3.5, we show an example of one such cases. Pointing the WFC/INT at the position of the PSZ1 G183.26+12.25 (white square), we detect two clusters; one at $z = 0.638$ (red circle) and a second one at $z_{phot} = 0.27$ (green circle) spettroscopiacaly and photometrically confirmed, respectively. Although we do not have spectroscopical information on both clusters, the richness of both systems is similar, $R = 25$ and $R = 23$, respectively. Moreover, the two clusters have similar distances from the nominal *Planck* coordinates: $3.44'$ and $4.12'$, respectively. Therefore, both clusters are probably contributing to the total SZ signal.

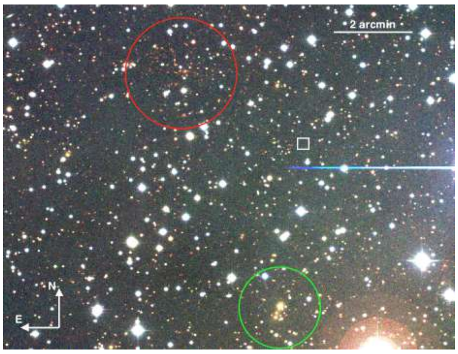

Figure 3.5: WFC/INT RGB image of PSZ1 G183.26+12.25. In this field we were able to identify two different overdensities, both confirmed photometrically. The first one, the most evident, is highlighted in the red circle is a high redshift cluster at $z = 0.638$. The second, in the green circle, is a low redshift object at $z = 0.27$.

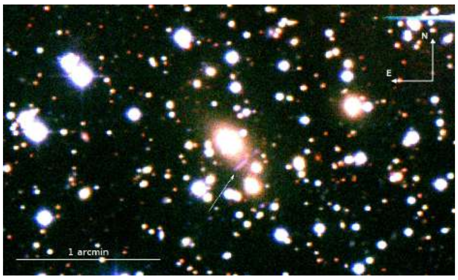

Figure 3.6: WFC/INT RGB image of the cluster PSZ1 G060.12+11.42. The white arrow signals the position of a gravitational arc around the BCG of the cluster.

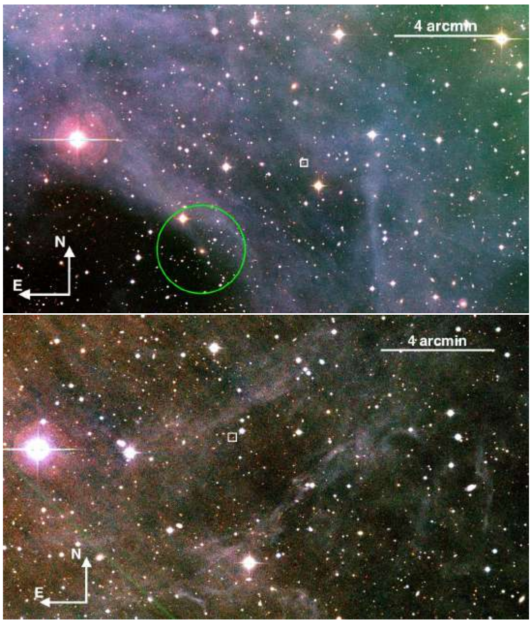

Figure 3.7: RGB images of PSZ1 G206.52-26.37 (top panel) and PSZ1 G092.46-35.25 (bottom panel), obtained with WFC/INT. Both images show severe dust contamination. However, the PSZ1 G206.52-26.37 has been confirmed spectroscopically at $z = 0.391$ (green circle), whereas the PSZ1 G092.46-35.25 is a non detection.

Gravitational arcs: In general, the SZ signal detected by *Planck* is associated to massive clusters ($M_{500}^{SZ} > 1 \times 10^{14}$ M$_{\odot}$).), so it is not surprising to see how some clusters present giant gravitational arcs, typical of strong lensing. Figure 3.6 shows an example of one of those arcs as observed in the cluster PSZ1 G060.12+11.42, at $z = 0.224$. This is not the only example of giant arc. We also observe strong lensing effects in the PSZ1 G206.45+13.89 (see top left panel of figure 3.2) image and PSZ1 G075.29+26.66 images.

High extinction regions: As figure 1.10 shows, the thermal emission of galactic dust might be contributing to the *Planck* frequency detections. For this reason, regions with high galactic extinction may severely contaminate the SZ signal. Thus, we expect that the majority of false detections are associated with regions of high dust emission, such as sky areas at low galactic latitudes (see figure 3.12). In figure 3.7, we show two examples of highly contaminated fields. The top panel shows the WFC/INT image of PSZ1 G206.52-26.37. In this case we find an optical counterpart, spectroscopically confirmed, at $z = 0.391$. The bottom panel shows the WFC/INT image of PSZ1 G092.46-35.25 which has been proven to be a spurious SZ detection. Both sources show high dust contamination. In fact, the signal at their position in the 857 GHz is of 10.57 MJy sr^{-1} and 10.59 MJy sr^{-1}, respectively. As shown in section 3.2.1, the signal at 857 GHz correlates with the fraction of non detections (ND).

3.2 The ITP sample

Table 3.3 lists the 260 SZ sources explored in the ITP follow-up, 48 of which were already confirmed in PSZ1 catalogue by other follow-up programmes. This means that we have successfully observed all the 212 SZ clusters candidates in the northern sky ($Dec \geq -15°$). The first and second columns list the index number and the corresponding name of each object in the PSZ1 catalogue. Column 3 is the S/N ratio of the SZ detection. Columns 4 and 5 are the J2000 equatorial coordinates corresponding to the optical centre of the cluster, assumed to be the position of the BCG in most cases, or the mean position of the cluster members if a BCG was not detected. Column 6 lists the distance between the optical and SZ centres. Columns 7 and 8 show the mean spectroscopic redshift and the redshift of the BCG (if observed), respectively. Columns 9, 10, and 11 compile the number of cluster members with spectroscopic measurements, the photometric redshift, and the optical richness, respectively. In Column 12, we show the cluster confirmation status, by following the Flag scheme described in section 3.1.2. Finally, comments relative to noteworthy features or other possible identifications are given in column 13.

Table 3.3: Clusters candidates from the PSZ1 catalogue studied in this work.

			Position (J2000)										
ID[1]	*Planck* Name	SZ SNR	R. A.	Decl.	Dist.(′)	z_{spec}	$z_{\mathrm{spec,BCG}}$	N_{spec}	z_{phot}	R	`Flag`	Notes
4	PSZ1 G001.00+25.71	6.04	–	–	–	–	–	–	–	–	–	
32	PSZ1 G012.48+27.36	4.54	–	–	–	–	–	–	–	–	–	
34	PSZ1 G012.66+25.79	4.50	–	–	–	–	–	–	–	–	–	
38	PSZ1 G015.42+58.42	4.65	–	–	–	–	–	–	–	–	–	
43	PSZ1 G018.09+26.07	4.76	16:52:12.30	–00:20:15.68	6.89	0.090	0.0894	17	–	–	3	
56	PSZ1 G021.88+17.75	5.64	17:28:16.01	–01:22:58.04	2.58	0.646	0.6488	10	0.60 ± 0.07	44 ± 6.6	1	
67	PSZ1 G027.31+23.79	5.10	–	–	–	–	–	–	–	–	–	
68	PSZ1 G027.75+15.41	4.67	17:47:17.63	+02:29:32.97	1.32	0.340	0.3340	4	0.38 ± 0.03	–	3	
69	PSZ1 G027.95+15.63	4.77	–	–	–	–	–	–	–	–	–	
70	PSZ1 G028.01+25.46	5.98	17:11:54.45	+07:23:13.37	5.45	0.658	0.6641	9	0.61 ± 0.06	17 ± 4.1	1	Liu+15 report a different counterpart
72	PSZ1 G028.15–08.63	5.07	–	–	–	–	–	–	–	–	–	
78	PSZ1 G029.79–17.37	6.59	–	–	–	–	–	–	–	–	–	
79	PSZ1 G030.21–16.91	5.34	–	–	–	–	–	–	–	–	–	
80	PSZ1 G030.70+09.47	4.66	18:13:58.80	+02:22:32.30	4.91	0.051	0.0532	17	0.11 ± 0.02	62 ± 7.9	1	
82	PSZ1 G030.98+22.43	4.98	17:27:59.37	+08:23:50.10	6.10	0.424	0.4236	2	0.50 ± 0.06	17 ± 4.1	3	
84	PSZ1 G031.41+28.75	4.84	17:04:58.60	+11:27:01.00	1.27	0.230	0.2304	4	0.24 ± 0.03	16 ± 4.0	3	vdB+16 report no counterpart
85	PSZ1 G031.44–19.16	4.60	–	–	–	–	–	–	–	–	–	
86	PSZ1 G031.91+67.94	5.23	14:30:23.30	+24:39:06.20	18.61	0.134	–	54	–	–	3	
88	PSZ1 G032.15–14.93	8.21	19:43:11.20	–07:24:56.25	4.89	0.377	0.3775	12	0.43 ± 0.04	51 ± 7.1	3	Substructured
90	PSZ1 G032.76+42.33	4.68	16:15:05.78	+17:46:52.20	0.46	0.844	0.8431	8	0.67 ± 0.05	39 ± 6.2	1	See figure 3.4 (right panel)
91	PSZ1 G033.33–17.54	5.78	19:54:59.67	–07:30:34.70	2.57	–	–	–	0.33 ± 0.04	23 ± 4.8	2	
98	PSZ1 G036.02+12.21	4.70	–	–	–	–	–	–	–	–	–	
99	PSZ1 G036.09–17.40	5.35	–	–	–	–	–	–	–	–	–	
101	PSZ1 G037.22–16.24	5.02	–	–	–	–	–	–	–	–	–	
111	PSZ1 G040.17–41.51	4.57	21:32:51.93	–12:32:33.42	5.92	0.229	0.2264	9	0.22 ± 0.03	30 ± 5.5	3	
112	PSZ1 G040.33–16.55	4.61	–	–	–	–	–	–	–	–	–	
116A	PSZ1 G041.70+21.65	4.51	17:47:09.18	+17:11:01.67	4.70	0.478	0.4773	25	0.45 ± 0.05	69 ± 8.3	1	
116B	PSZ1 G041.70+21.65	4.51	17:47:26.63	+17:06:19.56	1.65	–	–	–	0.34 ± 0.04	44 ± 6.6	2	
117	PSZ1 G042.33+17.46	5.07	18:04:16.10	+16:02:14.90	2.73	0.458	0.4574	3	–	–	1	
121	PSZ1 G042.96+19.11	4.70	17:58:55.06	+17:13:33.40	2.45	0.499	0.4993	8	0.53 ± 0.05	45 ± 6.7	1	Substructured
126	PSZ1 G044.82–31.66	4.67	21:04:46.58	–04:45:44.50	2.14	0.221	0.2213	7	0.21 ± 0.02	23 ± 4.8	3	Liu+15 cluster 126
127	PSZ1 G044.83+10.02	7.27	–	–	–	–	–	–	–	–	–	
132	PSZ1 G045.44–08.73	4.57	–	–	–	–	–	–	–	–	–	
133	PSZ1 G045.54+16.26	4.67	18:14:13.31	+18:17:03.61	2.18	0.206	0.2058	21	0.22 ± 0.02	49 ± 7.0	1	
135	PSZ1 G045.85+57.71	5.32	15:18:20.55	+29:27:40.50	0.39	0.607	0.6094	37	0.66 ± 0.03	50 ± 7.1	1	
136	PSZ1 G046.02–09.13	4.74	–	–	–	–	–	–	–	–	–	
138	PSZ1 G046.13+30.75	4.98	17:17:05.66	+24:04:18.94	1.22	0.568	0.5673	13	–	–	1	
139	PSZ1 G046.35–06.83	4.80	–	–	–	–	–	–	–	–	–	
142	PSZ1 G046.98+66.62	4.52	14:37:40.30	+30:12:00.30	6.74	0.340	0.3398	3	–	–	3	WHL J143740.3+301200
143	PSZ1 G047.44+37.39	4.92	16:50:20.41	+26:58:21.40	3.18	0.230	0.2318	10	0.23 ± 0.02	17 ± 4.1	1	
144	PSZ1 G047.53+08.55	5.82	–	–	–	–	–	–	–	–	–	
149	PSZ1 G048.22–51.60	4.50	22:20:17.44	–12:11:30.03	1.91	0.530	0.5322	30	0.52 ± 0.02	55 ± 7.4	1	
158	PSZ1 G050.01–16.88	5.29	20:23:34.77	+06:41:20.04	8.05	0.120	–	5	0.12 ± 0.02	–	3	
162	PSZ1 G051.42–26.16	4.60	–	–	–	–	–	–	–	–	–	
163	PSZ1 G052.93+10.44	4.91	18:49:11.97	+22:26:39.36	4.09	0.219	0.2194	10	0.24 ± 0.03	12 ± 3.5	3	
165	PSZ1 G053.50+09.56	5.11	–	–	–	–	–	–	–	–	–	vdB+16 report no counterpart
170	PSZ1 G054.59–18.18	5.33	20:36:38.70	+09:47:53.70	4.40	0.446	0.4492	4	0.38 ± 0.04	14 ± 3.7	3	

Table 3.3: continued from previous page

ID[1]	*Planck* Name	SZ SNR	Position (J2000)		Dist.(′)	$z_{\rm spec}$	$z_{\rm spec,BCG}$	$N_{\rm spec}$	$z_{\rm phot}$	R	Flag	Notes
			R. A.	Decl.								
175	PSZ1 G055.72+17.58	4.82	18:25:30.03	+27:44:27.49	4.19	0.195	0.1944	24	–	–	1	
176[a]	PSZ1 G055.83–41.64	5.72	21:56:41.02	–02:32:20.87	8.29	–	–	–	0.63 ± 0.04	16 ± 4.0	3	
179	PSZ1 G056.76–11.60	6.56	20:18:57.20	+15:07:18.3	1.41	0.123	0.1217	21	– – ± – –	66 ± 8.1	1	
184	PSZ1 G057.42–10.77	4.76	20:17:25.72	+16:03:27.30	2.12	0.136	0.1360	25	0.06 ± 0.02	34 ± 5.8	1	
192	PSZ1 G058.45–33.47	4.83	–	–	–	–	–	–	–	–	–	
193	PSZ1 G058.77–26.14	4.55	–	–	–	–	–	–	–	–	–	
194	PSZ1 G058.82–49.66	4.76	22:28:19.10	–05:34:41.70	4.24	0.595	0.5954	5	–	–	1	
199	PSZ1 G059.99+11.06	4.55	19:00:19.37	+28:58:09.73	4.21	0.097	0.0974	12	0.04 ± 0.03	34 ± 5.8	3	
201	PSZ1 G060.12+11.42	6.29	18:58:45.97	+29:15:35.16	0.67	0.226	0.2243	20	–	–	1	Gravitational arc. See figure 3.6
203	PSZ1 G060.51–19.54	4.65	20:54:31.65	+13:38:05.57	2.04	–	–	–	0.59 ± 0.05	41 ± 6.4	2	
208	PSZ1 G063.80+11.42	5.90	19:05:57.46	+32:32:52.99	0.82	0.428	0.4263	13	–	–	1	
209	PSZ1 G063.92–16.75	4.62	20:52:51.70	+17:54:23.02	1.73	0.392	0.3923	16	0.36 ± 0.04	43 ± 6.6	1	
211	PSZ1 G064.30+30.58	4.58	–	–	–	–	–	–	–	–	–	
212	PSZ1 G064.83+35.79	4.54	17:10:08.52	+40:20:53.64	4.35	0.442	0.4429	22	0.46 ± 0.04	39 ± 6.2	1	
213	PSZ1 G065.13+57.53	4.70	15:16:02.04	+39:44:26.40	2.70	0.683	0.6857	22	0.69 ± 0.04	78 ± 8.8	1	Substructured
218	PSZ1 G066.01–23.30	5.06	21:19:26.20	+15:21:06.40	4.09	0.249	0.2487	6	0.26 ± 0.03	–	1	
219	PSZ1 G066.20+12.87	5.06	19:04:15.37	+35:16:01.12	0.76	0.246	0.2461	12	–	–	1	
221	PSZ1 G066.41+27.03	6.46	17:56:52.70	+40:08:06.10	0.87	0.574	0.5748	2	–	–	1	WHL J269.219+40.13
237	PSZ1 G071.57–37.96	4.78	22:17:15.80	+09:03:10.10	2.41	0.288	0.2882	1	–	–	1	ACO 2429
239[a]	PSZ1 G071.64–42.76	8.82	22:30:50.00	+05:39:16.72	1.88	–	–	–	0.69 ± 0.08	7 ± 2.6	3	vdB+16 invalidate this source
246	PSZ1 G073.64+36.49	5.03	17:09:35.56	+47:31:53.90	1.34	0.558	0.5510	9	–	–	1	
250	PSZ1 G074.75–24.59	6.12	21:45:55.10	+20:28:18.80	3.26	–	–	0	0.33 ± – –	–	3	ZwCl 2143.5+2014
251A	PSZ1 G075.29+26.66	5.17	18:08:44.26	+47:41:09.22	5.85	0.281	0.2816	10	0.21 ± 0.03	16 ± 4.0	1	
251B	PSZ1 G075.29+26.66	5.17	18:09:09.02	+47:49:01.11	5.98	–	–	–	0.25 ± 0.03	17 ± 4.1	2	
253	PSZ1 G076.44+23.53	5.72	18:28:21.74	+48:04:29.63	1.81	0.168	0.1682	21	–	–	1	
257[a]	PSZ1 G078.39+46.13	4.90	16:09:01.45	+50:05:11.32	7.46	0.400	0.3999	4	0.41 ± 0.04	38 ± 6.2	3	Liu+15 cluster 257
258	PSZ1 G078.67+20.06	5.11	18:52:02.70	+49:01:17.80	1.85	–	–	0	0.49 ± – –	–	–	
261	PSZ1 G079.88+14.97	4.71	19:23:12.07	+48:16:13.25	0.91	0.101	0.1020	12	0.07 ± 0.02	56 ± 7.5	1	
266	PSZ1 G080.62–46.81	5.96	23:00:59.60	+06:44:58.20	2.37	0.050	–	0	–	–	1	RBS 1929
271[a]	PSZ1 G081.56+31.03	4.71	17:45:54.62	+53:48:45.96	3.33	–	–	–	0.79 ± 0.06	22 ± 4.7	2	vdB+16 invalidate this source
276	PSZ1 G083.35+76.41	4.65	–	–	–	–	–	–	–	–	–	
279	PSZ1 G084.04+58.75	4.84	14:49:00.90	+48:33:24.00	2.98	0.735	0.7302	5	0.70 ± 0.06	58 ± 7.6	1	
282	PSZ1 G084.41–12.43	7.06	21:37:53.37	+35:34:59.86	0.42	0.276	0.2763	20	–	–	1	
284	PSZ1 G084.62–15.86	6.01	21:49:40.60	+33:10:34.60	0.67	0.364	0.3673	2	–	–	1	
288	PSZ1 G084.85+20.63	5.47	19:00:11.62	+54:42:11.77	1.12	0.371	0.3673	9	–	–	1	
289	PSZ1 G085.71+10.67	5.35	20:03:13.30	+51:20:51.00	1.56	0.084	0.0804	12	0.06 ± 0.02	70 ± 8.4	1	
296	PSZ1 G086.93+53.18	4.57	15:14:00.02	+52:48:08.39	0.58	0.766	0.7732	12	–	–	1	
298	PSZ1 G087.25–41.86	5.04	23:05:18.30	+13:34:36.10	2.22	0.048	0.0481	3	0.05 ± 0.01	–	1	
305	PSZ1 G090.14–49.71	4.82	23:28:55.60	+07:52:34.70	5.41	0.355	–	7	0.36 ± 0.02	–	3	Liu+15 report a counterpart at zphot=0.207
306	PSZ1 G090.48+46.89	4.90	15:45:18.76	+57:43:37.59	3.82	–	–	–	0.54 ± 0.04	15 ± 3.9	2	
310	PSZ1 G091.14–38.73	4.79	23:09:10.67	+17:47:38.29	3.19	0.105	0.1048	–	0.10 ± 0.02	42 ± 6.5	2	
311	PSZ1 G091.73–30.23	4.53	–	–	–	–	–	–	–	–	–	
313	PSZ1 G091.82+26.11	7.52	18:31:15.27	+62:14:32.22	0.88	0.822	–	16	–	–	1	
314	PSZ1 G091.93+35.48	5.18	17:09:52.64	+62:22:07.67	2.16	0.276	0.2755	14	0.26 ± 0.02	30 ± 5.5	3	Liu+15 cluster 314
317	PSZ1 G092.41–37.39	5.46	23:10:14.70	+19:21:41.00	2.78	0.114	–	3	0.15 ± 0.04	–	1	

Table 3.3: continued from previous page

			Position (J2000)									
ID[1]	*Planck* Name	SZ SNR	R. A.	Decl.	Dist.($'$)	$z_{\rm spec}$	$z_{\rm spec,BCG}$	$N_{\rm spec}$	$z_{\rm phot}$	R	**Flag**	Notes
318	PSZ1 G092.46–35.25	5.47	–	–	–	–	–	–	–	–	–	See figure 3.7 (bottom panel)
320	PSZ1 G093.04–32.38	5.69	23:02:15.07	+24:03:50.50	7.48	0.512	0.5104	5	0.55 ± 0.05	42 ± 6.5	3	
331	PSZ1 G094.95–36.72	4.79	23:16:25.10	+20:57:23.90	1.79	–	–	–	0.50 ± 0.05	19 ± 4.4	2	
332	PSZ1 G095.00–37.14	4.53	–	–	–	–	–	–	–	–	–	
335	PSZ1 G095.49+16.41	5.09	20:00:06.73	+62:26:39.57	0.30	0.405	0.4022	19	–	–	1	
336	PSZ1 G096.44–10.40	6.55	22:20:12.90	+44:26:16.67	8.17	0.195	0.1948	4	0.22 ± 0.03	14 ± 3.7	3	
338	PSZ1 G096.89+24.17	6.00	18:56:41.37	+66:21:55.69	1.28	0.302	0.3035	23	–	–	1	ZwCl 1856.8+6616
343	PSZ1 G097.93+19.46	5.04	19:44:24.00	+65:52:23.90	2.73	0.248	0.2454	4	–	–	1	4C 65.28
346	PSZ1 G098.42+77.25	4.71	13:18:42.87	+38:43:00.13	9.90	0.234	0.2348	18	0.23 ± 0.02	69 ± 8.3	3	
348	PSZ1 G098.67–07.03	4.99	–	–	–	–	–	–	–	–	–	
356	PSZ1 G099.63+14.85	4.72	–	–	–	–	–	–	–	–	–	
357	PSZ1 G099.84+58.45	5.89	14:14:46.98	+54:47:03.00	0.38	0.616	0.6139	12	–	–	1	
360	PSZ1 G100.18–29.68	6.15	23:21:00.80	+29:12:09.70	2.62	0.485	–	4	–	–	1	WHL J232104.1+291134
361[a]	PSZ1 G100.46–61.45	4.71	00:09:15.84	–00:26:58.94	1.61	0.256	0.2561	1	0.28 ± 0.02	18 ± 4.2	2	
367	PSZ1 G102.00+30.69	4.52	17:47:13.00	+71:23:17.00	1.64	0.214	–	–	–	–	1	Included in RTT150 work
368	PSZ1 G102.86–31.07	6.12	23:33:24.70	+28:43:19.90	3.73	0.591	0.5915	1	–	–	1	
369	PSZ1 G102.97–04.77	5.64	22:34:47.08	+52:42:55.56	0.31	–	–	–	0.52 ± 0.04	27 ± 5.2	2	
370	PSZ1 G103.16–14.95	5.08	23:04:00.34	+43:46:21.40	1.99	–	–	–	0.27 ± 0.03	13 ± 3.6	3	
371	PSZ1 G103.24+16.92	4.55	–	–	–	–	–	–	–	–	–	
372	PSZ1 G103.50+31.36	4.63	17:36:44.28	+72:34:34.07	1.35	0.226	0.2257	18	0.24 ± 0.04	55 ± 7.4	3	
373	PSZ1 G103.56–39.35	4.50	23:47:12.69	+21:06:02.64	5.68	0.488	0.4877	–	0.44 ± 0.03	32 ± 5.7	3	
374	PSZ1 G103.58+24.78	4.75	19:04:54.20	+72:28:33.10	0.77	0.334	–	3	–	–	1	
375	PSZ1 G103.94+25.81	4.78	18:52:09.50	+72:59:33.11	1.96	0.077	0.0777	17	0.06 ± 0.01	–	1	Liu cluster 375. Fossil system. See figure 3.3
377	PSZ1 G104.78+40.45	4.92	15:46:35.33	+69:57:42.01	1.30	0.837	0.8341	10	–	–	1	See figure 3.4 (left panel)
381	PSZ1 G105.91–38.39	7.16	–	–	–	–	–	0	–	–	–	
382	PSZ1 G106.07–17.42	4.73	23:23:20.46	+42:33:15.32	1.89	0.818	0.8144	9	0.60 ± 0.10	–	1	
383	PSZ1 G106.15+25.76	4.64	18:56:51.95	+74:55:52.73	0.58	–	–	–	0.60 ± 0.04	76 ± 8.7	2	
385	PSZ1 G106.49–10.43	5.40	23:10:58.60	+49:12:28.21	3.80	–	–	–	0.49 ± 0.05	9 ± 3.0	3	
387	PSZ1 G106.81–36.44	4.66	–	–	–	–	–	–	–	–	–	
393	PSZ1 G108.13–09.21	5.39	–	–	–	–	–	–	–	–	–	
394	PSZ1 G108.18–11.53	6.36	23:22:30.61	+48:44:45.14	1.75	0.334	0.3311	17	–	–	1	
395	PSZ1 G108.26+48.66	4.88	14:27:04.57	+65:39:46.94	1.06	0.671	0.6752	29	0.69 ± 0.05	–	1	Substructured. See figure 3.2 (bottom left panel)
396	PSZ1 G108.52+32.30	4.55	17:08:10.76	+76:29:12.43	1.87	0.270	0.2693	10	–	–	1	
397	PSZ1 G108.90–52.04	6.89	00:16:26.74	+09:53:53.60	2.88	0.461	0.4620	4	0.54 ± 0.06	–	1	
398	PSZ1 G109.09–52.45	4.55	–	–	–	–	–	–	–	–	–	
349	PSZ1 G098.85–07.27	4.87	–	–	–	–	–	–	–	–	–	
412	PSZ1 G112.60–39.30	4.76	–	–	–	–	–	–	–	–	–	
420	PSZ1 G114.81–11.80	4.85	00:01:14.70	+50:16:32.16	2.48	0.228	0.2281	1	0.21 ± 0.02	38 ± 6.2	2	Included in RTT150 work
421	PSZ1 G114.98+19.10	5.19	21:55:54.81	+79:13:49.25	4.71	0.818	–	5	0.60 ± 0.20	–	1	
424	PSZ1 G115.34–54.89	4.80	–	–	–	–	–	0	–	–	–	
425	PSZ1 G115.59–44.47	5.46	00:29:06.30	+18:08:56.80	6.32	0.167	0.1670	1	–	–	3	
426	PSZ1 G115.70+17.51	5.85	22:26:30.35	+78:18:48.93	1.33	0.363	0.3586	11	–	–	1	
430	PSZ1 G117.29+13.44	4.54	23:22:12.90	+75:19:28.74	2.15	0.466	0.4677	31	0.49 ± 0.04	60 ± 4.1	1	
432	PSZ1 G118.06+31.10	5.99	15:54:38.73	+84:10:28.36	0.19	0.195	0.1944	15	–	–	1	

Table 3.3: continued from previous page

			Position (J2000)									
ID[1]	*Planck* Name	SZ SNR	R. A.	Decl.	Dist.(′)	$z_{\rm spec}$	$z_{\rm spec,BCG}$	$N_{\rm spec}$	$z_{\rm phot}$	R	Flag	Notes
436	PSZ1 G118.61+10.55	4.96	23:53:24.56	+72:59:00.33	3.11	–	–	–	0.77 ± 0.07	50 ± 7.1	2	
437	PSZ1 G118.87+42.71	4.51	13:35:21.87	+74:04:10.10	1.30	0.215	–	8	0.17 ± 0.03	23 ± 4.1	3	
444	PSZ1 G121.27+23.08	4.72	–	–	–	–	–	–	–	–	–	
446	PSZ1 G121.69+24.47	5.35	–	–	–	–	–	–	–	–	–	
449	PSZ1 G123.37+25.34	5.90	01:45:31.18	+88:12:16.91	2.48	–	–	–	0.95 ± 0.11	22 ± 4.7	2	
450	PSZ1 G123.39+30.62	4.53	12:24:40.09	+86:27:46.51	1.25	0.200	0.1979	9	0.29 ± 0.03	98 ± 9.9	1	
451	PSZ1 G123.55–10.34	5.55	00:55:24.54	+52:29:20.83	1.77	0.106	0.1064	30	–	–	1	
453	PSZ1 G123.79+25.86	5.04	03:00:48.59	+88:30:09.18	1.31	–	–	–	0.54 ± 0.04	48 ± 6.9	2	
455	PSZ1 G124.56+25.38	4.76	–	–	–	–	–	–	–	–	–	
456	PSZ1 G124.64+29.38	4.89	10:35:55.45	+87:16:34.35	1.39	–	–	–	0.35 ± 0.03	36 ± 6.0	2	
458*A*[a]	PSZ1 G125.54–56.25	4.86	00:57:09.25	+06:35:05.92	2.04	0.548	0.5475	1	0.59 ± 0.04	26 ± 5.1	2	
458*B*[a]	PSZ1 G125.54–56.25	4.86	00:57:08.84	+06:34:06.15	2.49	0.169	0.1676	12	–	–	1	
458*C*[a]	PSZ1 G125.54–56.25	4.86	00:57:22.23	+06:38:27.27	3.29	0.296	0.2961	1	0.27 ± 0.03	33 ± 5.7	2	
462	PSZ1 G126.44–70.36	5.40	00:55:57.36	–07:33:42.46	4.20	0.325	0.3246	3	0.33 ± 0.04	21 ± 4.6	2	
464	PSZ1 G127.02+26.21	4.95	05:58:02.70	+86:13:49.31	1.33	0.577	0.5760	13	0.63 ± 0.05	36 ± 6.0	1	
465	PSZ1 G127.36–10.69	5.58	–	–	–	–	–	–	–	–	–	
466	PSZ1 G127.55+20.84	5.91	–	–	–	–	–	0	–	–	–	
468	PSZ1 G128.75–17.97	4.95	–	–	–	–	–	–	–	–	–	
471	PSZ1 G130.15–17.01	4.83	01:30:55.20	+45:17:18.74	1.40	0.211	0.2097	20	–	–	1	
476	PSZ1 G133.50–46.77	4.91	01:21:25.03	+15:30:56.84	1.38	–	–	–	0.68 ± 0.09	14 ± 3.7	–	
478	PSZ1 G134.08–44.61	5.42	–	–	–	–	–	–	–	–	–	
479	PSZ1 G134.31–06.57	4.81	02:10:25.09	+54:34:09.80	1.61	0.333	0.3341	20	–	–	1	
481	PSZ1 G134.64–11.77	4.84	02:02:37.80	+49:26:28.00	1.59	0.207	–	–	–	–	1	Included in RTT150 work
483	PSZ1 G134.75–56.53	4.57	01:17:21.05	+05:46:08.09	3.39	0.206	0.2077	11	0.21 ± 0.03	50 ± 7.1	1	
489	PSZ1 G135.68+45.61	4.58	–	–	–	–	–	–	–	–	–	
490	PSZ1 G135.92+76.21	5.22	12:35:46.89	+40:27:55.53	6.29	0.406	–	9	0.39 ± 0.04	14 ± 3.7	3	
492	PSZ1 G136.37–44.50	4.90	–	–	–	–	–	–	–	–	–	
496	PSZ1 G137.51–10.01	5.33	02:22:53.51	+50:14:40.11	1.93	–	–	–	0.14 ± 0.02	67 ± 8.2	2	
497	PSZ1 G137.56+53.88	5.73	11:41:11.96	+61:06:58.26	12.26	0.148	0.1483	9	0.17 ± 0.01	–	3	
501	PSZ1 G138.60–10.85	8.26	02:27:06.70	+49:00:29.30	4.49	0.700	0.7023	4	–	–	1	
503	PSZ1 G139.61+24.20	7.94	06:21:48.71	+74:42:03.23	1.71	0.266	0.2660	22	–	–	1	
504	PSZ1 G140.10+50.09	4.90	11:11:30.47	+63:35:16.76	5.33	–	–	–	0.70 ± 0.05	26 ± 5.1	3	
507	PSZ1 G141.59+23.69	4.83	06:23:55.16	+72:50:15.69	8.97	0.306	0.3071	14	0.26 ± 0.03	35 ± 5.9	3	
508	PSZ1 G141.73+14.22	4.97	04:41:05.88	+68:13:15.13	0.94	0.819	0.8208	20	0.78 ± 0.06	52 ± 7.2	1	
509	PSZ1 G142.17+37.28	5.79	09:19:05.16	+70:55:11.39	3.26	0.240	0.2393	6	0.23 ± 0.02	–	1	Liu+15 report a zphot=0.28
511	PSZ1 G142.38+22.82	5.81	06:13:49.84	+71:52:54.78	0.96	0.394	0.3927	2	0.34 ± 0.05	20 ± 4.5	2	
515	PSZ1 G143.70–08.59	4.56	–	–	–	–	–	–	–	–	–	
517	PSZ1 G144.99+54.39	4.63	11:14:21.86	+58:23:19.76	11.36	0.206	0.2063	24	0.21 ± 0.02	103 ± 10.1	3	
522	PSZ1 G146.00–49.42	6.62	01:51:19.80	+10:47:30.00	5.00	0.097	–	4	0.10 ± 0.01	–	1	WHL J015128.7+104912
529	PSZ1 G148.20+23.49	8.40	06:37:54.60	+66:51:06.20	3.42	0.098	0.0980	2	–	35 ± 5.9	2	Liu+15 cluster 529
534	PSZ1 G150.33–20.04	4.75	02:59:31.65	+35:56:30.47	11.7	0.189	–	7	0.17 ± 0.03	15 ± 3.9	3	
536	PSZ1 G150.94–39.06	5.09	02:22:04.63	+18:46:28.10	3.22	–	–	–	0.21 ± 0.02	51 ± 7.1	2	
538	PSZ1 G151.44–64.86	4.70	01:38:13.13	–04:30:50.78	7.20	0.158	0.1583	2	0.15 ± 0.03	37 ± 6.1	3	
539	PSZ1 G151.80–48.06	5.59	02:08:07.55	+10:27:17.54	0.98	0.201	0.1999	2	–	23 ± 4.8	1	ACO 307
542	PSZ1 G153.41+36.58	6.85	08:42:42.90	+62:30:21.60	4.18	0.650	–	3	–	–	1	
543	PSZ1 G153.56+36.23	5.96	08:39:33.40	+62:26:12.10	5.32	0.132	–	6	0.13 ± 0.01	–	3	MaxBCG J129.79086+62.44628

Table 3.3: continued from previous page

ID[1]	*Planck* Name	SZ SNR	Position (J2000)		Dist.(′)	$z_{\rm spec}$	$z_{\rm spec,BCG}$	$N_{\rm spec}$	$z_{\rm phot}$	R	Flag	Notes
			R. A.	Decl.								
544	PSZ1 G153.87+41.05	4.79	09:18:21.40	+61:10:29.30	7.01	0.279	0.2794	4	0.29 ± 0.02	–	3	WHL J091821.4+611029
546	PSZ1 G155.25–68.42	6.43	01:37:24.90	–08:27:22.70	2.02	0.566	0.5661	5	–	–	1	WHL J24.3324??8.477
549	PSZ1 G157.07–33.66	4.90	02:51:35.96	+21:07:05.30	0.60	–	–	–	0.62 ± 0.05	21 ± 4.6	2	vdB+16 invalidate this source
551	PSZ1 G157.44+30.34	7.54	07:48:54.35	+59:42:05.77	1.46	0.407	0.4046	4	–	18 ± 4.2	1	[ATZ98] B100
553	PSZ1 G157.84+21.23	4.63	06:40:32.70	+57:45:36.00	3.66	0.363	–	–	–	–	1	Included in RTT150 work
554	PSZ1 G158.34–47.49	4.63	02:24:56.13	+08:49:47.59	2.17	0.311	0.3115	8	0.29 ± 0.01	57 ± 7.5	1	
555	PSZ1 G158.58–52.47	4.51	–	–	–	–	–	–	–	–	–	
557	PSZ1 G159.29–24.66	4.76	03:21:00.12	+27:26:50.70	0.29	–	–	–	0.56 ± 0.05	28 ± 5.3	2	
559	PSZ1 G160.59+17.41	4.67	06:21:11.30	+53:56:33.81	2.87	–	–	–	0.33 ± 0.04	88 ± 6.9	2	
564	PSZ1 G162.30–26.92	6.56	03:24:19.02	+23:57:49.82	3.37	0.391	0.3917	3	0.34 ± 0.03	44 ± 6.6	2	
566	PSZ1 G163.03–27.80	4.50	–	–	–	–	–	–	–	–	–	
575	PSZ1 G165.76+31.15	4.99	07:57:58.70	+52:38:16.70	2.92	0.259	0.2593	6	–	–	1	MaxBCG J119.49440+52.63797
576	PSZ1 G165.94+50.48	4.51	10:01:38.80	+50:00:54.00	1.89	0.172	0.1709	2	–	–	1	GMBCG J150.41158+50.01489
580	PSZ1 G167.43–38.04	6.11	–	–	–	–	–	0	–	–	–	
586A	PSZ1 G169.80+26.10	5.32	07:30:32.02	+48:17:39.05	4.21	–	–	–	0.73 ± 0.07	36 ± 6.0	2	
586B	PSZ1 G169.80+26.10	5.32	07:30:29.09	+48:20:39.15	3.53	–	–	–	0.83 ± 0.10	19 ± 4.6	2	
588	PSZ1 G170.22+09.74	14.4	06:03:16.80	+42:14:42.00	1.15	0.228	–	–	–	–	1	Included in RTT150 work
590	PSZ1 G171.01+15.93	4.89	06:35:47.93	+44:10:15.14	1.36	0.281	0.2823	20	0.28 ± 0.03	53 ± 7.2	1	
591	PSZ1 G171.96–40.64	12.7	03:12:57.77	+08:23:00.10	0.63	0.271	–	16	–	–	1	
595	PSZ1 G172.93+21.31	5.82	07:07:37.96	+44:19:22.13	0.14	0.336	0.3386	17	–	–	1	
597	PSZ1 G173.07–36.12	4.95	–	–	–	–	–	–	–	–	–	
605	PSZ1 G178.10+18.58	5.01	07:01:31.33	+38:52:48.60	9.28	–	–	–	0.38 ± 0.03	12 ± 3.5	–	
611	PSZ1 G181.12–29.42	4.82	–	–	–	–	–	–	–	–	–	
612	PSZ1 G181.21–30.73	5.87	04:02:56.76	+09:44:29.10	0.76	0.540	0.5406	3	0.41 ± 0.04	26 ± 5.1	2	Liu+15 cluster 612
616	PSZ1 G182.49–57.09	5.09	02:42:42.19	–08:05:23.01	26.08	0.137	–	7	0.03 ± 0.01	–	3	
618A	PSZ1 G183.26+12.25	5.43	06:43:09.84	+31:50:55.47	3.44	0.638	0.6352	2	0.62 ± 0.05	25 ± 5.0	2	See figure 3.5
618B	PSZ1 G183.26+12.25	5.43	06:42:58.24	+31:45:01.07	4.12	–	–	–	0.27 ± 0.03	23 ± 4.8	2	See figure 3.5
624	PSZ1 G185.42–32.03	6.15	04:07:50.12	+06:07:06.29	1.76	–	–	–	0.08 ± 0.02	43 ± 6.6	2	
625	PSZ1 G185.53–33.97	4.98	–	–	–	–	–	–	–	–	–	
626	PSZ1 G185.93–31.21	5.90	04:11:52.31	+06:17:11.80	3.47	0.094	0.0947	2	0.11 ± 0.02	22 ± 4.7	2	Fossil system
629	PSZ1 G186.54+85.60	4.51	–	–	–	–	–	–	–	–	–	
630	PSZ1 G186.81+07.31	5.79	06:29:28.41	+26:32:11.10	0.61	0.221	–	20	–	–	1	WHL J97.3409+26.50
634	PSZ1 G188.36–35.00	5.28	04:04:18.02	+02:23:55.46	1.30	0.275	0.2723	4	–	29 ± 5.4	1	ZwCl 0401.8+0219
639	PSZ1 G189.29+07.44	5.10	06:34:44.47	+24:20:42.31	2.65	0.504	0.5041	4	0.55 ± 0.05	46 ± 6.8	2	
641	PSZ1 G189.82–37.25	6.99	–	–	–	–	–	–	–	–	–	
645	PSZ1 G191.05+12.85	4.51	06:59:50.96	+25:05:20.20	4.10	0.088	0.0895	15	0.07 ± 0.04	20 ± 4.5	1	
646	PSZ1 G191.78–26.64	4.76	04:38:54.25	+04:49:18.16	8.20	0.206	0.2082	4	0.24 ± 0.04	60 ± 7.7	3	
653	PSZ1 G194.74–10.10	5.19	05:41:05.73	+11:10:05.32	0.76	–	–	–	0.75 ± 0.10	30 ± 5.5	2	
650	PSZ1 G194.24+75.22	4.56	11:46:17.30	+30:56:18.50	3.85	0.388	0.3927	2	–	–	1	
651	PSZ1 G194.68–49.73	5.00	–	–	–	–	–	0	–	–	–	
652	PSZ1 G194.70–58.93	4.62	–	–	–	–	–	–	–	–	–	
659	PSZ1 G198.06–12.52	4.82	–	–	–	–	–	–	–	–	–	
663	PSZ1 G199.70+37.01	4.89	–	–	–	–	–	–	–	–	–	
666	PSZ1 G200.95–28.16	4.75	04:50:24.30	–02:58:36.70	2.16	–	–	0	0.27 ± – –	–	1	
671	PSZ1 G203.42–04.03	4.70	–	–	–	–	–	–	–	–	–	
673	PSZ1 G204.07+16.51	6.25	07:35:47.52	+15:06:50.83	0.61	0.121	0.1222	22	–	–	1	ZwCl 0733.1+1514

Table 3.3: continued from previous page

ID[1]	*Planck* Name	SZ SNR	Position (J2000)		Dist.($'$)	$z_{\rm spec}$	$z_{\rm spec,BCG}$	$N_{\rm spec}$	$z_{\rm phot}$	R	Flag	Notes
			R. A.	Decl.								
674	PSZ1 G204.24+14.51	5.76	07:28:35.40	+14:07:42.10	0.97	0.349	0.3484	5	–	–	1	WHL J112.147+14.12
675	PSZ1 G204.73+15.85	5.71	07:34:27.81	+14:16:39.33	0.53	0.347	0.3470	19	–	–	1	
677	PSZ1 G205.52–44.21	4.60	03:59:32.89	–13:39:56.41	2.33	0.252	0.2523	–	0.31 ± 0.03	81 ± 9.0	1	
682	PSZ1 G206.45+13.89	5.90	07:30:00.30	+11:56:54.14	0.58	0.406	0.4123	57	0.33 ± 0.05	–	1	Substructured, Gravitational arc. See figure 3.2 (top left panel)
683	PSZ1 G206.52–26.37	5.38	05:06:17.20	–06:34:52.50	5.15	0.391	0.3910	1	–	–	3	See figure 3.7 (top panel)
684	PSZ1 G206.64–21.17	6.62	–	–	–	–	–	–	–	–	–	
690	PSZ1 G209.80+10.23	5.80	07:22:23.74	+07:24:30.30	0.92	0.678	0.6780	5	–	–	1	
698	PSZ1 G212.63+07.45	4.72	–	–	–	–	–	–	–	–	–	
699	PSZ1 G212.80+46.65	4.77	–	–	–	–	–	–	–	–	–	
701	PSZ1 G213.27+78.35	4.71	11:58:25.80	+26:29:52.98	12.12	0.138	0.1381	24	–	–	3	GMBCG J179.84162+26.45111
713	PSZ1 G216.27+10.10	5.16	07:33:20.03	+01:36:36.06	3.14	–	–	–	0.15 ± 0.02	31 ± 5.6	2	
723	PSZ1 G218.54+13.26	5.24	07:48:51.66	+01:06:39.61	1.80	0.266	0.2682	17	0.26 ± 0.03	–	1	
743	PSZ1 G223.80+58.50	4.57	10:41:43.18	+17:33:47.50	6.93	0.603	–	4	–	–	3	
746	PSZ1 G224.01–11.14	6.13	06:30:55.30	–14:51:00.00	1.59	0.560	–	–	–	–	1	Included in RTT150 work
748	PSZ1 G224.45+05.25	4.55	07:31:13.82	–07:48:33.48	4.47	0.067	0.0670	17	0.06 ± 0.03	97 ± 9.8	1	
752	PSZ1 G224.82+13.62	5.51	08:01:41.61	–04:03:46.23	0.14	0.274	0.2759	28	0.25 ± 0.03	–	1	
753	PSZ1 G225.39+04.23	4.52	–	–	–	–	–	–	–	–	–	
786	PSZ1 G234.12+10.45	4.61	08:09:06.41	–13:30:34.99	1.67	0.294	0.2979	29	0.40 ± 0.04	69 ± 8.3	1	
791	PSZ1 G235.93+38.21	4.79	09:46:34.48	+00:28:02.13	6.66	0.455	0.4507	2	0.47 ± 0.03	39 ± 6.2	3	
792	PSZ1 G235.93+38.21	4.52	10:20:37.82	+06:01:46.13	6.28	0.111	–	26	–	–	1	
798	PSZ1 G237.94+21.65	5.05	–	–	–	–	–	–	–	–	–	
808	PSZ1 G240.39+07.91	5.28	08:13:55.50	–20:06:56.00	0.70	0.332	0.3315	3	–	–	1	
809	PSZ1 G240.42+77.58	4.59	12:03:40.71	+21:02:59.83	11.97	0.342	0.3417	5	–	–	3	
827	PSZ1 G244.48+34.06	8.14	09:49:46.94	–07:30:12.32	1.40	0.135	0.1342	7	0.15 ± 0.03	–	3	
845	PSZ1 G249.01+73.75	7.14	11:57:05.60	+16:57:35.40	5.00	0.156	–	2	0.16 ± 0.02	–	1	WHL J115659.6+165833
900	PSZ1 G262.45+49.34	4.60	–	–	–	–	–	–	–	–	–	
909	PSZ1 G264.01+59.77	4.68	11:37:53.50	+02:38:55.50	4.95	0.141	0.1409	2	–	–	1	
928	PSZ1 G268.86+55.92	4.66	–	–	–	–	–	–	–	–	–	
992	PSZ1 G286.25+62.68	5.52	12:21:05.35	+00:48:22.29	1.46	0.211	0.2107	11	0.18 ± 0.05	–	3	
1080	PSZ1 G306.96+50.58	4.61	13:01:09.63	–12:04:16.73	13.69	0.420	–	5	0.44 ± 0.05	61 ± 7.8	3	
1122	PSZ1 G318.61+83.80	6.93	–	–	–	–	–	–	–	–	–	Liu+15 cluster 1159
1159[a]	PSZ1 G332.30+72.17	4.76	13:26:33.97	+11:18:06.50	2.96	0.089	0.0898	24	–	–	3	
1189	PSZ1 G341.69+50.66	5.48	14:25:12.30	–04:56:34.19	3.90	0.293	0.2913	26	0.24 ± 0.02	–	3	Substructured. Liu+15 cluster 1189-A
1198	PSZ1 G345.81+42.38	4.80	–	–	–	–	–	–	–	–	–	
1199	PSZ1 G346.57+42.71	4.60	–	–	–	–	–	–	–	–	–	
1212	PSZ1 G352.04+42.25	4.74	–	–	–	–	–	–	–	–	–	
1221	PSZ1 G357.43+30.60	5.47	15:54:53.89	–12:13:16.75	4.45	–	–	–	0.13 ± 0.02	13 ± 3.6	–	
1217	PSZ1 G355.14+55.96	4.52	–	–	–	–	–	–	–	–	–	

[1] SZ targets identified with the ID followed by an A, B or C label indicate the presence of multiple counterparts.

[a] Photometric and/or spectroscopic redshift obtained from SDSS DR12 data.

Our optical follow-up programme produced a final catalogue with 136 SZ sources with actual cluster counterparts (103 with Flag1 and 33 whit Flag2), representing 52.3% of the sample, and 124 (47.7%) of unconfirmed sources (48 Flag3 and 76 ND). We remark that 48 of the 260 clusters observed during the ITP programme were previously validated. Therefore, by removing these known sources, we found 88 new validated PSZ1 targets (58 Flag1 and 30 Flag2), and 124 unconfirmed sources, representing 42.5% and 58.5% of the sample, respectively.

The *Planck* Collaboration provided the CLASS of each cluster candidate, in the `VALIDATION` column of the PSZ1 catalogue. It is therefore interesting to investigate the reliability assigned by the *Planck* Collaboration (see section 1.4.1.1). Twenty-one of the 24 CLASS1 candidates (87.5%) were confirmed as actual counterparts. However, two of the three unconfirmed candidates assigned as FLAG3 by us were classified as CLASS1 by *Planck*. This signifies that we detect clusters in these fields, but according to our confirmation criteria, we could not associate them to the SZ signal. The first one is the PSZ1 G030.98+22.43 ($z = 0.42$). Its distance from the *Planck* pointing is $6.1'$. The second is the PSZ1 G103.50+31.36 ($z = 0.23$), which shows a velocity dispersion of $\sigma = 535\,\mathrm{km\,s^{-1}}$, which is not high enough for clusters at $z > 0.2$. Regarding the third object, PSZ1 G135.68+45.61, it is a field characterised by many small groups, however, none of them can be associated with the SZ signal.

CLASS2 and CLASS3 show very similar percentages of confirmed clusters: 37.7% and 33.3%, respectively. This suggests that the *Planck* classification of cluster candidates in classes of reliability works very well for the CLASS1 candidates, whereas the distinction between CLASS2 and CLASS3 is less clear. Unfortunately, the *Planck* Collaboration does not provide the class of reliability Q_{SZ}, Q_{RASS}, and Q_{WISE}. Therefore, we cannot study the presence of correlation between non confirmations and these quantities.

Figure 3.8 shows the spatial distribution of optical centres of confirmed clusters, even those not associated with the SZ signal, with respect to the PSZ1 detection coordinates. Ninety-six percent of the confirmed optical counterparts (Flag1 and Flag2), 126 GCs, are within the region of $3'.8$ enclosing 68% of the detected clusters. In Figure 3.9, we show the relative distance between the optical and SZ centres as a function of cluster redshift. Although at low redshift ($z < 0.1$) the typical projected virial radius of 1 Mpc subtends a bigger angle in the sky $> 10'$, 93% of the clusters detected lie within $5'$. The unconfirmed counterparts (Flag3 clusters) placed at a distance $\leq 5'$ from the SZ nominal pointing, do not fulfil the criteria relative to the velocity dispersion and/or richness. These low mass systems (Flag3) and ND may contain background high mass clusters not visible in optical, may be affected by Eddington bias

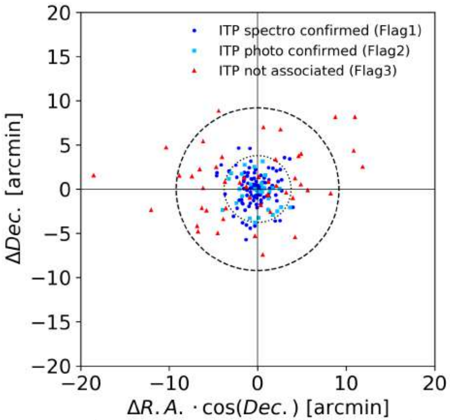

Figure 3.8: Relative positions between optical counterpart centres and nominal PSZ1 coordinates for Flag1 (blue circles), Flag2 (light blue squares), and Flag3 (red triangles) clusters in Table 3.3. Inner dotted and external dashed lines show the region enclosing 68% and 95% of the confirmed clusters.

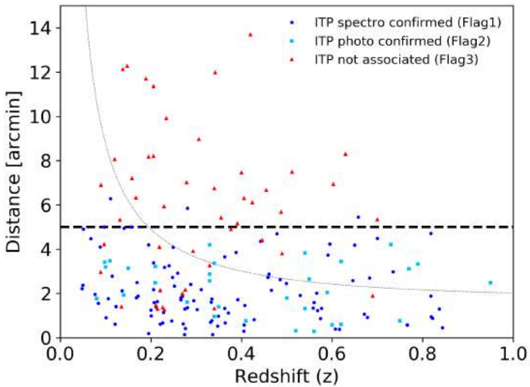

Figure 3.9: Cluster optical centre distance from their Planck SZ position as a function of cluster redshift. The dashed horizontal line at 5′ shows the maximum distance within which clusters are associated with the SZ signal. The dotted line corresponds to the angle subtended by a projected 1 Mpc as a function of the redshift. Symbols used are the same as in Figure 3.8.

(see section 5.4.1), or even show high dust emission.

In Figure 3.10, we investigate how the sample is distributed as a function of the redshift (upper panel) and S/N of SZ detection (bottom panel). The average redshift of the whole ITP sample is ~ 0.3, even when only considering the cluster candidate subsample. Similarly, the median S/N is ~ 4.9 both the whole ITP sample and the subsample without previously validated clusters. It is interesting to remark that the median S/N remains stable for confirmed (Flag1 and Flag2) and unconfirmed sources (Flag3 and ND). However, if we take into account only the low S/N bins ($S/N < 4.9$), the percentage of unconfirmed sources (64.2%) almost doubles that of confirmed ones (35.8%). This fact could be a hint that regions with high contamination are less reliable.

3.2.1 Purity of the PSZ1 in the northern sky

In order to compare the entire PSZ1 sample with the one observed in the ITP validation programme, we selected PSZ1 sources with $Dec \geq -15°$. We named this PSZ1 subsample as PSZ1-North. In this section we analysed the statistical properties mainly associated with the purity, in order to obtain conclusions related to the full PSZ1 catalogue.

The PSZ1-North sample contains 753 SZ sources (61% of the full PSZ1 catalogue) which can be divided in two different subsets. The first one includes 541 sources with declination above -15°, already validated at the time of the first PSZ1 publication in 2013 (Planck Collaboration XXIX 2014). We will refer to this as the PSZ1-Val sample. The second subset is called the ITP-sample (see 2.1.1) and it is composed by the 260 sources that we observed during the ITP programme, from which we removed the 48 already-known clusters.

Figure 3.11 (top panel) shows the number of clusters normalised to the total PSZ1-North clusters. We note that the median redshift of the PSZ1-North samples is 0.23, while ITP-sample median redshift is 0.32, as we saw in the previous section. This is not completely unexpected. In fact, it is probable that low redshift massive clusters might already have been observed in other wavelengths, especially in X-rays.

The bottom panel of figure 3.11 shows the distribution of PSZ1-North sources as a function of S/N. The histogram shows that the median value is $S/N = 5.1$, which is comparable to the value that we found for the ITP-sample ($S/N = 4.9$). In the ITP sample we noted that the fraction of non-confirmed clusters is higher in the low S/N half of the sample. This is more evident when we take into account the entire ITP-North sample. In this case, the percentage of non-validated sources in the low S/N half of the ITP-North sample is 23.4%, whereas for $S/N \geq 5.1$ this same fraction is only 9.5%.

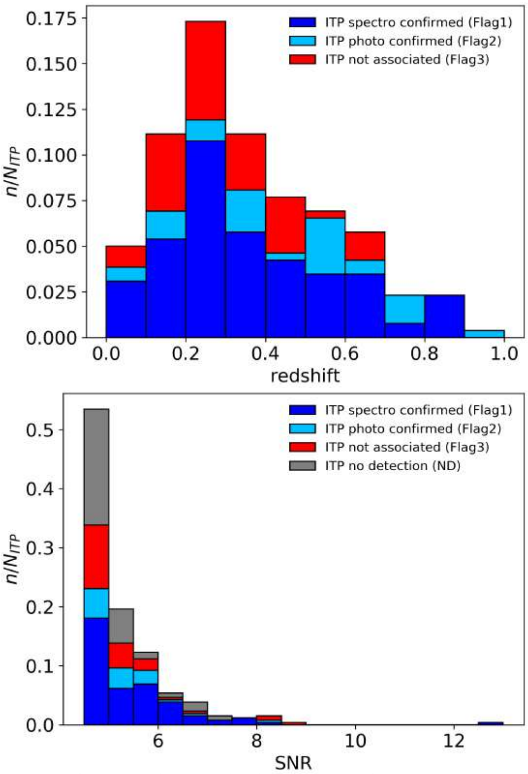

Figure 3.10: Redshift (top panel) and S/N (bottom panel) histograms of ITP SZ selected sample used in this thesis normalised to the total number of sources within the sample. In blue, light blue, red and grey we plot the subsamples of spectroscopically confirmed clusters (Flag1), photometrically confirmed clusters (Flag2), GCs detected but not associated with the SZ signal (Flag3) and the non detections (ND), respectively.

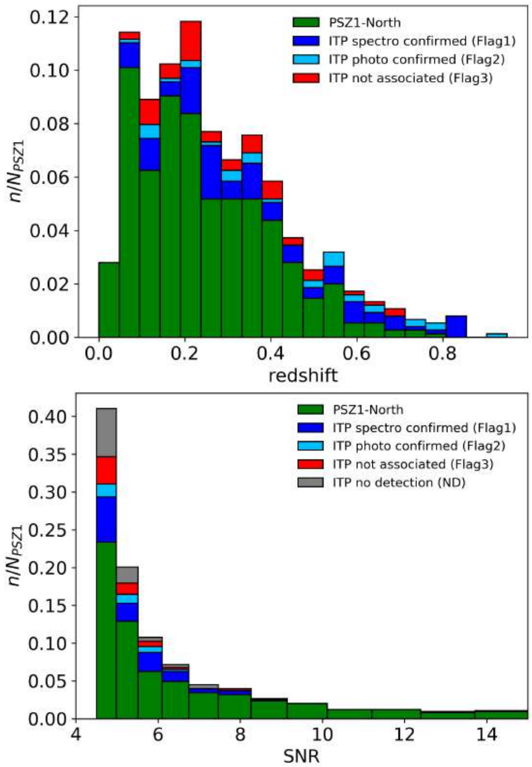

Figure 3.11: Number of PSZ1 sources, in northern sky, as a function of the redshift (top panel) and of the S/N (bottom panel), normalised to the total number of PSZ1-North sources. The PSZ1-North sample is represented in green. The confirmed clusters are shown in dark blue (Flag1) and light blue (Flag2).The non associated clusters are shown in red (Flag3), while the grey represents the fraction of non detections (ND).

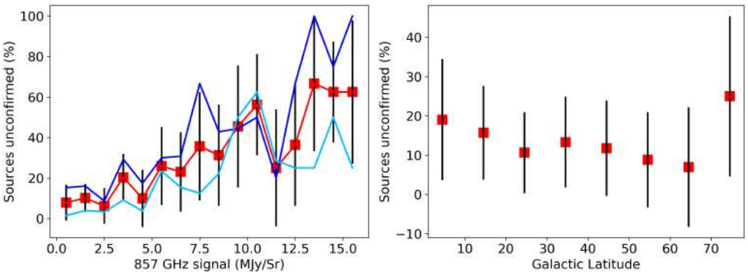

Figure 3.12: Left panel: Fraction of unconfirmed sources with respect the total number of elements of the PSZ1-North sample ($Dec \geq 15°$) as a function of the 857 GHz signal in MJy sr^{-1} taking into account the entire sample (red squares), the $S/N < 5.1$ subsample (dark blue line), and the $S/N \geq 5.1$ subsample (light blue line). Right panel: percentage of unconfirmed sources with respect the total number of elements of the PSZ1-North sample as a function of the galactic latitude. Error bars represents the Poisson error of the total number of sources, in each bin.

These data could be explained in terms of dust contamination of non-validated sources. In fact, as we introduced in section 3.1.3, thermal dust emission may hardly influence the SZ signal. This effect may produce false SZ detections, especially around regions showing high galactic extinction.

With this in mind, we studied these sources in the sky looking at the mm emission in the 857 GHz *Planck* map. The left panel of figure 3.12 shows how the fraction of non-validated sources (Flag3 and ND), with respect to the total number of PSZ1-North sample sources (red squares), correlates with the signal at 857 GHz, calculated as the mean signal within a region of 0.5° around the nominal PSZ1 coordinates. In the regions where the dust contamination is very low (< 5 MJy sr^{-1}), the fraction of non-confirmed sources is well below 20%. However, fields with high dust emission also show high fractions ($> 60\%$) of non detections. Moreover, taking into account the $S/N < 5.1$ (dark blue line) and the $S/N \geq 5.1$ (light blue line) bins separately, we note that $\sim 100\%$ of low S/N sources that show a very high contamination (> 13 MJy sr^{-1}) are non-validated.

In the right panel of figure 3.12 we show that this fraction also slightly correlate with the galactic latitude (b), as expected. In fact, the fraction of non-validated sources is higher at low galactic latitudes. However, at very high galactic latitude ($|b| > 70°$) we detect an unexpected high numbers of non-confirmed sources.

Finally, we can summarise all this information with accumulated purity. Finally, we can summarise all this information with accumulated purity. Here,

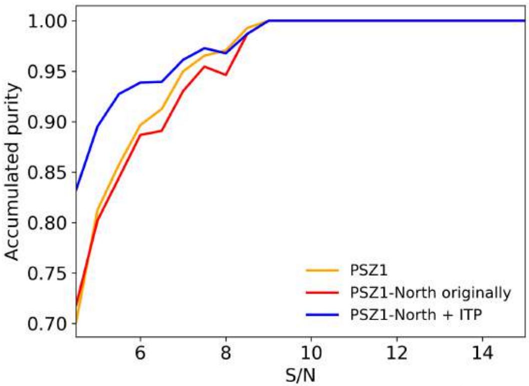

Figure 3.13: Fraction of confirmed clusters as a function for the S/N of the PSZ1-North sample. The red line represents the purity at the moment of the publication of the PSZ1 catalogue and blue line represents purity after the ITP follow-up (this work). The orange line represents the accumulated purity of the full PSZ1 catalogue at the moment of its first publication.

purity is defined as the fraction of confirmed clusters with respect to the total number of SZ sources. In figure 3.13, we show how this purity behaves as a function of S/N. We conclude that the 88 new confirmations recorded by our ITP follow-up have improved the purity of the PSZ1-North sample especially at very low S/N, passing from 72% to 82%, at $S/N = 4.5$. It is important to remark that the purity of the original PSZ1-North sample (red line) and of the full PSZ1 catalogue (orange line) were compatible. This allows us to extrapolate our results (in terms of fraction of ND and statistical completeness and purity) to the full PSZ1 catalogue.

4

Biases in galaxy cluster velocity dispersion and mass estimates in the small number of galaxies regime

In this chapter, we present a study of the statistical properties of three velocity dispersion and mass estimators, namely biweight, gapper and standard deviation, in the small number of galaxies regime ($N_{\rm gal} \leq 75$). This is motivated by our observational strategy.

First, we present a comparison of the bias and variance for three scale estimators–biweight, gapper, and standard deviation–as a function of the number of galaxy members considered for both the ideal Gaussian case and the case of simulated GCs. In section 4.2, we test the robustness of the three estimators in the case galaxy samples containing interlopers. In section 4.3, we quantify the effect induced on the velocity dispersion estimate by sampling galaxy members in only a fraction of visible objects and within apertures different from R_{200}. In sections 4.4.1 and 4.5, we describe how the mass can be biased even in presence of an unbiased velocity dispersion. Finally, we apply the correction to a set of simulated observations based on the Planck PSZ1 optical follow-up (Planck Collaboration Int. XXXVI 2016; Barrena et al. 2018) described in chapter 2, and we give the recipe to correct for the biases in velocity dispersion and mass estimates. The results of the work described in this chapter will be published in Ferragamo et al. (2019, submitted).

4.1 Statistical Bias and Variance for Velocity Dispersion estimators in small GC spectroscopic samples

As shown in table 3.3, the majority of our clusters are spectroscopically sampled with a low number of galaxy members and sampling, in the same sense, a fraction of the virial radius. In this situation, it is important to characterise whether a limited number of spectroscopic members ($N_{gal} \lesssim 30$) might lead to biased estimates of the velocity dispersion and/or the cluster mass. In fact, in order to use GCs for cosmological studies, it is crucial to obtain an accurate, precise, and unbiased estimate for the velocity dispersion and, consequently, for the mass.

4.1.1 Velocity dispersion estimators

Beers et al. (1990) presented a set of mean and scale estimators, and studied their efficiency in the presence of deviations from a Gaussian-distribution. In this paper, we decided to focus our attention on three of those estimators, namely the standard deviation, the biweight and the gapper. The standard deviation,

$$S_{\rm std}(N_{\rm gal}) = \sqrt{\frac{1}{N_{\rm gal}-1}\sum_{i=1}^{N_{\rm gal}}(x_i-\mu)^2}, \tag{4.1}$$

is defined as the lowest variance scale estimator for a Gaussian distribution. However, its dependence on μ (the mean of the distribution) makes it a non-robust estimator.

The biweight scale estimator is a function of the sample median (Tukey 1958), and it is defined as

$$S_{\rm bwt}(N_{\rm gal}) = \left(\frac{{N_{\rm gal}}^2}{N_{\rm gal}-1}\right)^{1/2} \frac{\left[\Sigma_{|u_i|<1}\,(x_i-M)^2\,(1-u_i^2)^4\right]^{1/2}}{\left|\Sigma_{|u_i|<1}\,(1-u_i^2)\,(1-5u_i^2)\right|}, \tag{4.2}$$

where u_i are given by

$$u_i = \frac{(x_i - M)}{c \times {\rm MAD}} \tag{4.3}$$

where $c = 9.0$, and ${\rm MAD} = {\rm median}\,(|x_i - M|)$ are the tuning constant and the median absolute deviation respectively. Finally, the gapper is a robust estimator (Wainer & D. 1976) based on the gaps of an order statistics, $x_i, x_{i+1}, \ldots, x_n$. It is defined as a weighted average of gaps:

$$S_{\rm gap}(N_{\rm gal}) = \frac{\sqrt{\pi}}{N_{\rm gal}\,(N_{\rm gal}-1)}\sum_{i=1}^{N_{\rm gal}-1} w_i\, g_i, \tag{4.4}$$

where the gaps are given by

$$g_i = x_{i+1} - x_i, \qquad i = 1, \ldots, N_{\rm gal} - 1 \tag{4.5}$$

and the (approximately Gaussian) weights are given by

$$w_i = i\,(N_{\rm gal} - 1). \tag{4.6}$$

For a more detailed description of these estimators, see Beers et al. (1990). Throughout this chapter we will use $S_{\rm X}(N_{\rm gal})$ to refer to any of the three scale estimators, with X= “std”, “bwt” or “gap”, for each one of the three cases.

4.1.2 The ideal case: Gaussian distributions

Our aim is to characterise the statistical behaviour of these three methods as a function of the number of galaxies, by quantifying the possible bias of each technique specifically in the small number of galaxies regime. With this purpose in mind, we started our study from the ideal case of a Gaussian radial velocity distribution. This case is of particular interest because it allowed us to analytically derive the functional form of the statistical bias as a function of the number of galaxies.

4.1.2.1 Analytic derivation of the statistical bias

Let us consider a real-valued random variable x, for which we have a set of N independent measurements x_i, each one with probability p_i (for equal probability measurements, we would have $p_i = 1/N$). Then, we can compute any ordinary moment as:

$$E[x^j] \equiv \sum_{i=1}^{N} x_i^j p_i. \tag{4.7}$$

The second order moment is related to the variance v, defined as $E[v] = Var(x) \equiv E[x^2] - E[x]^2$, which turns out to be unbiased for any number of data measurements N.

Let us now compute how a bias is introduced when estimating a derived quantity which is calculated as a nonlinear function of variance, $m = g(v)$. In practice, we have to evaluate $E[g(v)]$, which is the expectation value of the function $g(v)$. We can use as the function g as the estimator of m, applied at the estimated value of $E[v]$,

$$E[g(v)] = g(E[v]). \tag{4.8}$$

The estimator $g(E[v])$ will be unbiased only if the function $g(v)$ is linear. In case it is a non-linear function of the variance (as is the case of the standard deviation or the mass estimation), we can write the mean of $g(E[v])$ as:

$$< g(E[v]) >\simeq g(v) + g'(v) < \Delta E[v] > + \frac{1}{2} g''(v) < (\Delta E(v))^2 > . \tag{4.9}$$

If the variable v is unbiased, we can assume that $\langle \Delta E[v] \rangle = 0$ and

$$\left\langle (\Delta E[v])^2 \right\rangle = var(E[v]) = \frac{2v^2}{N}, \tag{4.10}$$

which implies that the unbiased estimate of $g(v)$ is

$$E[g(v)] = g(v) - \frac{1}{2} g''(v) \frac{2v^2}{N}. \tag{4.11}$$

In the particular case of standard deviation, we have $\sigma = v^{1/2}$, and thus the previous equation gives

$$E[\sigma] = \sigma - \frac{1}{4} \frac{\sigma}{n}. \tag{4.12}$$

4.1.2.2 Numerical derivation of the statistical bias

In the previous section, we derived the analytical expression of the bias for the standard deviation. This analytical calculation is possible because standard deviation is defined as a non-linear function of the variance. However, we cannot do the same thing for the biweight and gapper, since they are defined in different ways.

In order to investigate their biases, we have to perform a numerical study. To do this, we generated 73 Gaussian distributions by fixing the mean, $\mu = 0$ and the dispersion $\sigma = S_{\rm true}$. We then evaluated the bias and the variance of the three scale estimators $S_{\rm X}(N_{\rm gal})$, exploring 20 different values for $N_{\rm gal}$, between $N_{\rm gal} = 8$ and $N_{\rm gal} = 75$, logarithmically spaced to better analyse the low-$N_{\rm gal}$ tail. We estimated $S_{\rm X}(N_{\rm gal})$ for each one of 50 000 different configurations and by repeating this procedure for each $N_{\rm gal}$ and for each Gaussian distribution. The average values for $S_{\rm X}(N_{\rm gal})$ were obtained by averaging the $73 \times 50\,000$ dispersions normalised with respect to $S_{\rm true}$.

In the left panel of Fig. 4.1 we show that each estimator is able to asymptotically recover the dispersion $S_{\rm true}$. In the low-$N_{\rm gal}$ regime, the biweight had a strong dependence on the number of elements used for the estimation. For $N_{\rm gal}$ smaller than 30, it underestimated the true dispersion by up to 4% at $N_{\rm gal} = 10$. A very similar behaviour is shown by the standard deviation. We note that in

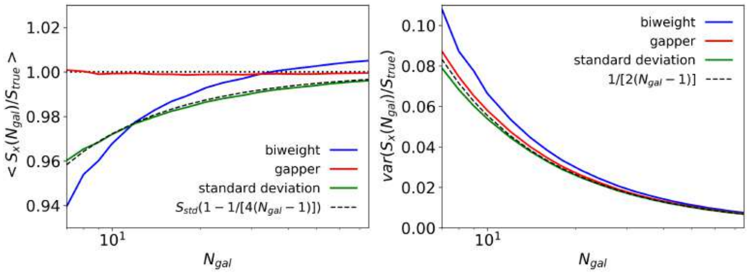

Figure 4.1: The mean velocity dispersion $S_{\rm X}(N_{\rm gal})/S_{\rm true}$ as a function of the number of galaxies $N_{\rm gal}$ (left panel) and its variance (right panel), for a sample of Gaussian-distributed random velocities. The dispersion $S_{\rm X}(N_{\rm gal})$ is calculated for the standard deviation (green line), biweight (blue line), and gapper (red line) estimators.

Table 4.1: Parameters of the functions $S_{\rm X}(N_{\rm gal})$ for Gaussian distributions.

	BWT	GAP	STD
D	0.72 ± 0.03	0	0.25
B	-0.007 ± 0.001	0.0007 ± 0.0002	0
β	1.28 ± 0.03	1	1

this later case, the dependence on $N_{\rm gal}$ can be theoretically predicted, as shown in section 4.1.2.1, giving the analytic form $1 - 1/(4(N_{\rm gal} - 1))$.

Based on this dependence on $N_{\rm gal}$, we have have obtained a numerical fit to those curves in the left panel of Figure 4.1, using the following parametric term:

$$1 - \left(\left(\frac{D}{(N_{\rm gal} - 1)} \right)^{\beta} + B \right). \tag{4.13}$$

Table 4.1 shows the best-fit values for the parameters D, β and B, for each one of the three estimators (biweight, gapper and standard deviation).

In addition to the bias, another crucial aspect for selecting a σ_v estimator is its variance. We would expect the standard deviation to be the lowest variance estimator for a Gaussian distribution. This is confirmed in the right panel of Fig. 4.1, which shows the variance of the three estimators, $Var(S_{\rm X}(N_{\rm gal}))$. Moreover, this measured variance follows the optimal one expected for the theoretical behaviour given by

$$Var(S_{\rm X}(N_{\rm gal})/S_{\rm true}) = \frac{c}{4(N_{\rm gal} - 1)}. \tag{4.14}$$

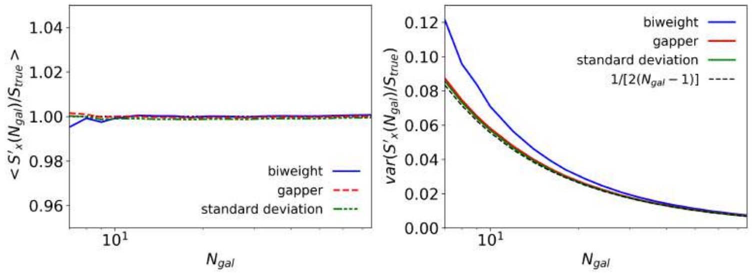

Figure 4.2: Mean (left panel) and variance (right panel) of the corrected estimators $S'_{\rm X}(N_{\rm gal})/S_{\rm true}$, as a function of the number of galaxies $N_{\rm gal}$ in a sample of Gaussian-distributed random velocities, for the standard deviation (green line), biweight (blue line), and gapper (red line).

where c is a parameter related to the kurtosis of the distribution defined as

$$c = \frac{1}{N_{\rm gal}} \sum_{i=1}^{N_{\rm gal}} \frac{\langle x_i^4 \rangle - \langle x_i^2 \rangle^2}{\langle x_i^2 \rangle^2}. \tag{4.15}$$

We would expect $c = 2$ for a perfect Gaussian sample. We found that the variance of the gapper is also very close to the optimal one, whereas for low $N_{\rm gal}$ values ($\lesssim 20$), the variance of the biweight estimator was significantly worse.

Using either the parametric fitting given in equation 4.13, or the numerical values from the left panel of Figure 4.1, we could then construct unbiased velocity dispersion estimators, by explicitly correcting for that statistical bias. We will use the primed notation $S'_{\rm X}(N_{\rm gal})$ when referring to these "corrected" estimators, which will be given by

$$\begin{aligned} S'_{\rm X}(N_{\rm gal}) &\equiv S_{\rm X}(N_{\rm gal}) \left(1 - \left(\left(\frac{D}{(N_{\rm gal}-1)} \right)^{\beta} + B \right) \right)^{-1} \\ &\approx S_{\rm X}(N_{\rm gal}) \left(1 + \left(\left(\frac{D}{(N_{\rm gal}-1)} \right)^{\beta} + B \right) \right). \end{aligned} \tag{4.16}$$

and where the approximation in the second line uses the fact that the correction term is small compared to unity.

Figure 4.2 is equivalent to Fig. 4.1, but computed for the set of corrected estimators defined in equation 4.16. By construction, the new $S'_{\rm X}(N_{\rm gal})$ estimators are then unbiased (left panel), and their variance (right panel) have increased only by a small amount. As for unprimed estimators, the corrected standard deviation was still the minimum variance estimator, although the three of them presented very similar values for $N_{\rm gal} \gtrsim 30$.

Up to this point, we see that the standard deviation in the low-$N_{\rm gal}$ limit is a biased dispersion estimator. In section 4.1.2.1 we analytically derived that this bias is due to the standard deviation nature of a non-linear function of the variance, which is an unbiased quantity. Indeed, from a theoretical point of view, the variance is one of the ordinary moments of a distribution and cannot be biased. It is also interesting to then investigate the behavior of the quantity equivalent to the variance for the biweight and the gapper, $\langle {S_{\rm X}}^2(N_{\rm gal})/{S_{\rm true}}^2 \rangle$. In the left panel of Fig. 4.3 the variance (green line) is, as expected, unbiased. With respect to what we argued in Fig 4.1, relative differences between the three estimators, in the high-$N_{\rm gal}$ limit, are then increased. However, the gapper seemed to recover the real variance asymptotically, due to its downward profile from $N_{\rm gal} = 7$ to $N_{\rm gal} = 75$. Finally, the biweigh shows a falling profile for $N_{\rm gal} < 30$. Regarding the variance of the variance, in the right panel of Fig. 4.3 we show that the standard deviation is the lowest variance estimator following the theoretical value given by

$$var({S_{\rm X}}^2(N_{\rm gal})/{S_{\rm true}}^2) = \frac{2}{(N_{\rm gal}-1)}. \tag{4.17}$$

In contrast with what we show in Fig. 4.1, the gapper has a very similar trend to that of the biweight, which, however, remains the estimator with the worst variance.

4.1.3 The realistic case: GCs from hydrodynamic simulation

Once we know how biweight, gapper, and standard deviation work under ideal conditions, we can test them with the set of simulated GCs.

4.1.4 Simulations

In order to carry out the proposed analyses, we used a sample of 73 simulated massive clusters selected from the simulations described in Munari et al. (2013). The original full sample contained about 300 cluster-sized or group-sized structures with masses $M_{200} > 10^{13} M_{\odot}$. Here, our selected sample corresponds to all clusters located at five redshifts ($z = 0.12, 0.36, 0.46, 0.6, 0.82$), and with masses $M_{200} > 2 \times 10^{14} M_{\odot}$.

The simulations were generated in 29 Lagrangian regions, centred around the massive haloes identified in a parent, large-volume simulation box of $1\,{\rm h}^{-1}$ Gpc

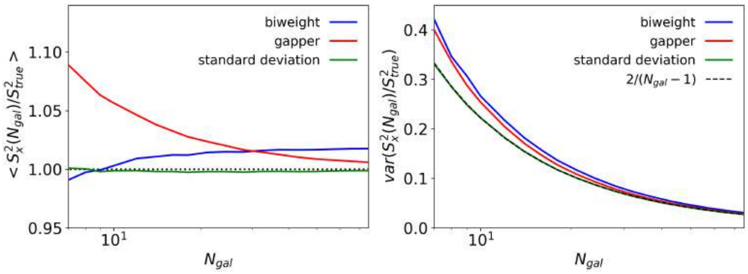

Figure 4.3: Mean ${S_{\rm X}}^2(N_{\rm gal})/{S_{\rm true}}^2$ as a function of the number of galaxies $N_{\rm gal}$ (left panel) and its variance (right panel), for sample Gaussian-distributed random velocities.The dispersion $S_{\rm X}(N_{\rm gal})$ is calculated with the standard deviation (green line), biweight (blue line), and gapper (red line).

a side, and then re-simulated with higher resolution. The simulation started under the initial conditions described in Bonafede et al. (2011), and was carried out in two subsequent steps, at different resolutions. The entire simulation was performed using the hydro-dynamical `GADGET-3` code (Springel et al. 2001a). Gravitational forces were simulated using the `TreeePM` method, in which the Plummer-equivalent softening length $\epsilon = 5\,{\rm h}^{-1}\,{\rm kpc}$ is assumed in physical units for $z < 2$ and fixed in comoving units for $z > 2$. This simulation followed the evolution of 1024^3 dark matter (DM) particles with mass $m_{\rm DM} = 8.47 \times 10^8\,{\rm h}^{-1}\,M_\odot$ and the same number of gas particles with initial mass $m_{\rm gas} = 1.53 \times 10^8\,M_\odot$, assuming the Λ-CDM cosmological model with $\Omega_{\rm DM} = 0.24$, $\Omega_{\rm b} = 0.04$, $\Omega_\Lambda = 0.72$, $H_0 = 72\,{\rm km\,s^{-1}\,Mpc^{-1}}$, $\sigma_8 = 0.8$, and $n_{\rm S} = 0.96$.

The simulation takes into account the effects of supernova (SN) and active galactic nuclei (AGN) feedbacks, implemented following the model of Springel et al. (2005), in which the energy released is caused by gas accretion on supermassive black holes. It also included the effect of cooling, computed as in Wiersma et al. (2009), and the presence of the CMB, ultraviolet/X-ray background radiation from quasars and galaxies (Haardt & Madau 2001). For a more accurate description of the simulation, see Munari et al. (2013) and Rasia et al. (2015).

The bound structures were identified through a Friend-of-Friend (FoF) algorithm. Then, the identifications were refined using the `SUBFIND` algorithm (Springel et al. 2001b; Dolag et al. 2009). The galaxies were selected to be sub-halos containing a bounded stellar mass $10^9\,{\rm M}_\odot$. This choice guarantees a

Table 4.2: Ratio of the relative bias $S_{\rm X}(< R_{200})/S_{\rm Y}(< R_{200})$ between two estimators X and Y, obtained from our numerical simulations.

X / Y	BWT	GAP	STD
BWT	1.000	1.013 ± 0.009	1.021 ± 0.017
GAP	0.987 ± 0.008	1.000	1.008 ± 0.010
STD	0.980 ± 0.017	0.992 ± 0.010	1.000

set of sub-halos with masses $\sim 10^{11}\,{\rm M}_\odot$ corresponding to 72 DM particles.

4.1.5 Bias estimation

We first characterised the distribution of velocities in our set of simulations. Figure 4.4 shows the histogram of the radial velocities along the three main projection axes, of all cluster members within R_{200} for the 73 GCs. Even though these global distributions are apparently close to a Gaussian, each one of the 73 individual GC distribution is not, due to the presence of substructures. A quantitative analysis showed that there is indeed a deviation from gaussianity in the overall distributions. In particular, we estimated the kurtosis of the distribution by means of the c parameter (equation 4.15). By evaluating the factor c for each of the 73 clusters, we found a mean value $c = 1.6 \pm 0.05$ that implies a departure from a Gaussian of the simulated GC velocity distributions.

In analogy with what we had done for the Gaussian velocity distributions, we tested 20 numbers between $N_{\rm gal} = 8$ and $N_{\rm gal} = 75$. Then, we generated 2250 configurations by randomly selecting galaxies projected in a circle of radius R_{200}, 750 times for each main axis as line of sight and avoiding galaxy repetition. For each configuration, we estimated $S_{\rm X}(N_{\rm gal})$ by repeating this procedure for each $N_{\rm gal}$ and for each galaxy cluster. The profiles $S_{\rm X}(N_{\rm gal})$ were obtained by averaging the 73×2250 velocity dispersions normalised with respect to $S_{\rm std}(< R_{200})$, which represents the velocity dispersion of all the galaxies in the simulation within a circle of projected radius R_{200}, and calculated using the standard deviation estimator. For completeness, we also present in Table 4.2 the ratio of this relative bias when calculated with different estimators.

In the left panel of Fig. 4.5 we show how each estimator is able to recover the velocity dispersion, when compared to the standard deviation of the full sample $S_{\rm std}(< R_{200})$. We obtained a very similar result with respect to that in Figure 4.1. By construction, for high $N_{\rm gal}$ (i.e., when using all galaxies in the simulation within R_{200}), the standard deviation estimator $S_{\rm std}(N_{\rm gal})/S_{\rm std}(< R_{200})$ tends to one, while the other two estimators recover the asymptotic value given in Table 4.2.

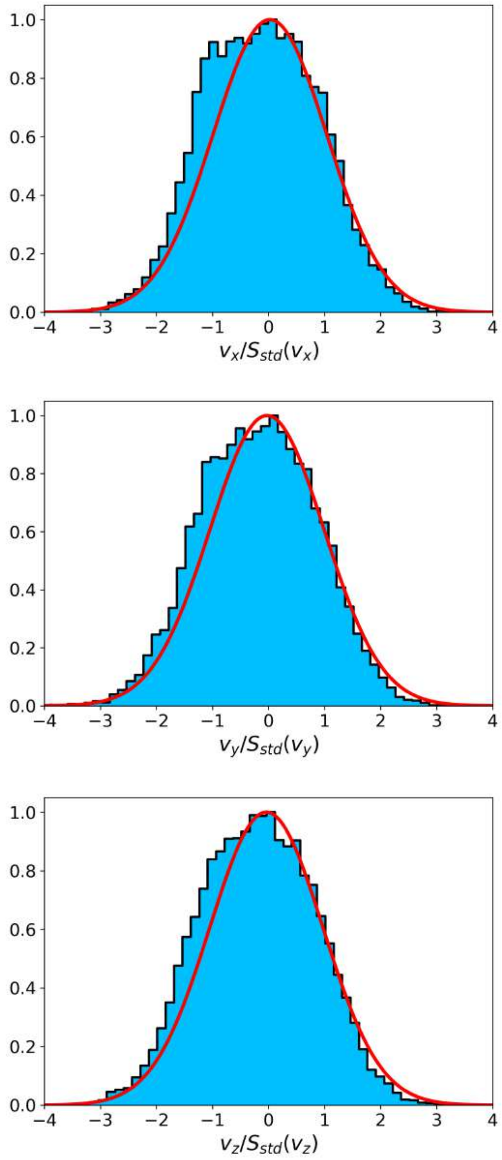

Figure 4.4: Histograms showing the distribution of individual line-of-sight velocities of all cluster members inside R_{200}, for all the 73 simulated GCs simultaneously, and for three possible orientations of the simulation box along the line of sight (x, y and z axes). The red line corresponds to a Gaussian profile with the same mean and variance of the full sample.

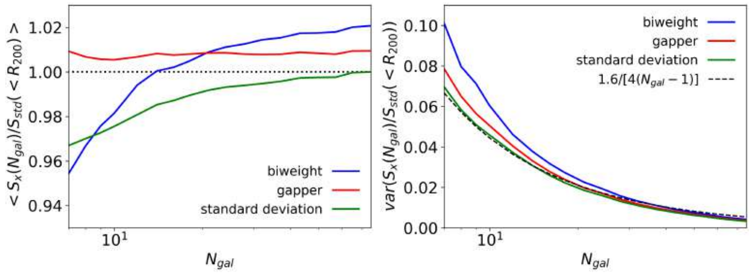

Figure 4.5: The mean velocity dispersion $S_{\rm X}/S_{\rm std}(< R_{200})$ as a function of the number of galaxies $N_{\rm gal}$ (left panel) and its variance (right panel), for our sample of 73 simulated galaxy clusters. The dispersion $S_{\rm X}(N_{\rm gal})$ is calculated for the standard deviation (green line), biweight (blue line), and gapper (red line) estimators.

Table 4.3: Best-fit parameters to be used in the parametric function given in equation 4.16 describing the bias of the three estimators. See text for details.

	BWT	GAP	STD
D	0.72 ± 0.03	0	0.25
B	-0.0225 ± 0.0002	-0.0080 ± 0.0002	-0.0037 ± 0.0003
β	1.28 ± 0.03	1	1

In the right panel of Fig. 4.5 we show that variance profiles, $var(S_{\rm X}(N_{\rm gal})/S_{\rm std}(< R_{200}))$, are very similar to those encountered for the Gaussian distributions. In this case, the biweight also shows the highest variance while the standard deviation follows the theoretical behaviour given by equation 4.14, when using the measured c value.

Following the methodology used in the Gaussian case, we defined the unbiased estimators $S'_{\rm X}(N_{\rm gal})$ by fitting the parameters of equations 4.13. The results are shown in Table 4.3.

Figure 4.6 shows the set of corrected estimators $S'_{\rm X}$ from equation 4.13 with the parameters in table 4.1. We show that the estimators are unbiased (by construction), whereas in the right panel we show their associated variance. The variance of standard deviation diverged from the theoretical behaviour to almost reach the variance of the gapper, which remained untouched, while the biweight still remained the estimator with the worst variance, in analogy with the case of Gaussian velocity distributions.

For completeness, in figure 4.7 we present the $\langle {S_{\rm X}}^2(N_{\rm gal})/{S_{\rm true}}^2 \rangle$ (left panel) and their variance (right panel). Similarly to what we have observed in the case of dispersion, they have similar shapes to those obtained in the Gaussian case

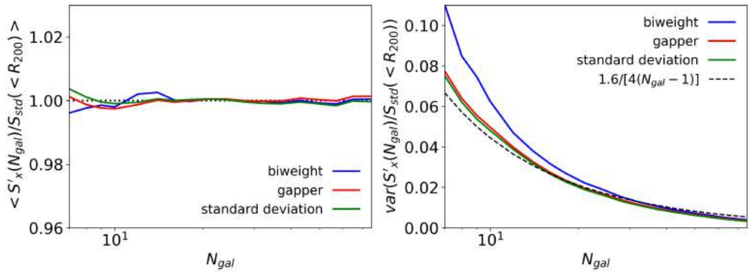

Figure 4.6: Mean (left panel) and variance (right panel) of the corrected estimators $S'_{\mathrm{X}}(N_{\mathrm{gal}})/S_{\mathrm{std}}(< R_{200})$, as a function of the number of galaxies N_{gal} in our sample of 73 simulated galaxy clusters, for the standard deviation (green line), biweight (blue line), and gapper (red line).

but with enhanced relative biases.

4.2 Bias from interlopers contamination

Galaxy clusters are not isolated structures in the Universe. This implies that any spectroscopic sample of cluster members could be, in principle, contaminated by galaxies with similar redshifts to those belonging to the large scale structure that surrounds the cluster itself. This population of 'pseudo cluster members', called interlopers, modifies the velocity distribution and therefore affects the estimation of velocity dispersion. There are several member-selection methods that one can use in order to obtain a galaxy sample that is as least contaminated as possible (see references in table 1 of Wojtak et al. 2018). However, none of these are capable of completely removing all contaminants (Wojtak et al. 2018). Moreover, although these techniques obtain good results when applied to large galaxy samples (hundreds of members), they are not effective with small samples (tens of members), as in the case of the caustic method (Diaferio 1999).

According to the definition of interlopers given in Pratt et al. (2019), one must distinguish between two very different types of contaminants:

i. galaxies gravitationally bound to the clusters that are far from the cluster centre ($> 3R_{200}$, according to the definition given in Saro et al. (2013)), but that, due to projection effects appear within a smaller radius;

ii. background/foreground galaxies with similar redshifts to the cluster, but

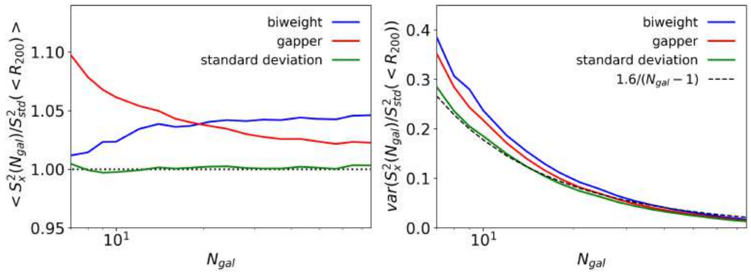

Figure 4.7: The mean velocity dispersion squared $S_{\rm X}{}^2(N_{\rm gal})/S_{\rm true}{}^2$ as a function of the number of galaxies $N_{\rm gal}$ (left panel) and its variance (right panel), for our sample of 73 simulated galaxy clusters. The dispersion $S_{\rm X}(N_{\rm gal})$ is calculated for the standard deviation (green line), biweight (blue line), and gapper (red line) estimators.

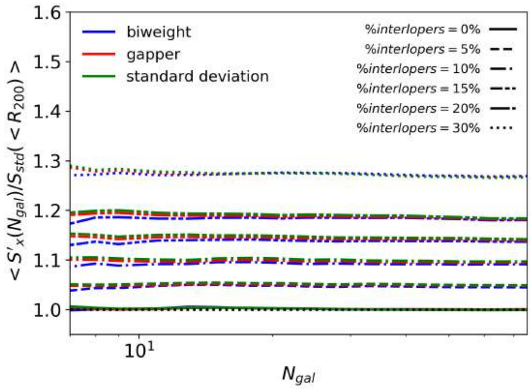

Figure 4.8: Effect of interlopers on $S'_{\rm X}/S_{\rm std}(< R_{200})$, as a function of the number of galaxies. The velocity dispersion, $S'_{\rm X}(N_{\rm gal})$, is first computed using a pure galaxies sample (solid lines). We also evaluated the response of biweight (blue lines), standard deviation (green lines), and gapper (red lines) using samples contaminated by 0% (solid line), 5% (dashed lines), 10% (dot dashed lines), 15% (three-dot-dashed lines), 20% (two-dot-long-dashed lines) and 30% (dotted lines) of interlopers at any $N_{\rm gal}$.

belonging to the large scale structure that surrounds the cluster itself.

The first type of interlopers are considered easier to handle. In fact, by clipping the galaxy velocity distribution tails, one could be sure that the most distant objects are removed from the sample.

The second type of interlopers, belonging to a uniform distribution overlapping the cluster member one, are challenging to handle. They lie well inside the cluster member distribution, and their fraction is not significantly reduced by the sigma clipping, which remains above 20% (Mamon et al. 2010).

In order to illustrate the robustness of our three estimators, we proceeded by fixing the fraction of contaminants at any $N_{\rm gal}$. We simulated a member selection by clipping cluster velocity distributions at 3σ. We then repeated the procedure described in the previous section, this time replacing galaxies from the cluster distribution with random values from a uniform distribution that mimicked a field of background and foreground galaxies in the velocity interval $[-3, 3]\, S_{\rm std}(< R_{200})$. In Figure 4.8 we show the results obtained for five different fractions of interlopers: 5% (dashed lines), 10% (dot-dashed lines), 15%(three-dot-dashed lines), 20% (two-dot-long-dashed lines) and 30% (dotted lines). The effect of the interloper contamination consists of a velocity dispersion overestimation which is as high as their relative fraction (up to $\sim 30\%$). In practice, the interloper contamination is the most damaging source of biases in the velocity estimation estimation. It is also noteworthy that the three estimators are similarly affected by interloper contamination.

It is important to remark that the simulations we used in this thesis are not a simulation of the entire cone along the LoS. This makes the formulation of a method to remove the second type of interlopers beyond the scope of this tesis.

In real observations, the fraction of interlopers depends strictly on the observation strategy and the particular algorithms and procedures used for member selection. However, we emphasise that, for reliable velocity estimation, the bias due to these interlopers has to be taken into account and corrected specifically for each particular survey, using the curves in Figure 4.8.

4.3 Physical Biases on velocity dispersion estimators

In an ideal scenario, in which we can choose a uniformly selected sample of true cluster members inside R_{200}, the corrected set of scale estimators presented above will provide an unbiased estimation of the velocity dispersion of the cluster. However, observational strategies and technical limitations prevented us from reaching this scenario. In this section we study two possible ways in

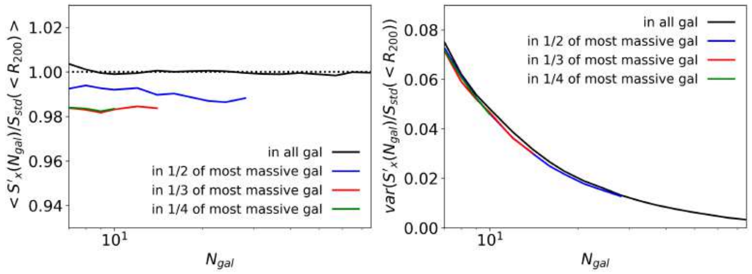

Figure 4.9: Left panel: Mean of $S'_{\rm std}/S_{\rm std}(< R_{200})$ as a function of the number of galaxies $N_{\rm gal}$ calculated by choosing galaxies within 100% (black solid line), 50% (blue solid line), 33% (red solid line), and 25% (green solid line) of the complete cluster member samples. Right panel: Variance of $S'_{\rm std}/S_{\rm std}(< R_{200})$ as a function of the number of galaxies $N_{\rm gal}$. The dashed line represents the theoretical expectation for the variance of the dispersion according to equation 4.14.

which a particular selection of cluster members might produce biased velocity dispersion estimates.

4.3.1 Effects due to the selected fraction of massive galaxies

For a fixed integration time, the telescope aperture limits the detection magnitude and prevents us from detecting faint objects. In other cases, the technical requirements of spectrographs make it impossible to sample the cluster members adequately. Therefore, in practice, line-of-sight velocity samples contain only a fraction of GC members, generally the brightest objects in the GC, which are also the most massive. This fraction of objects is particularly small for high redshift GCs. In this subsection, we investigate if there is an induced bias due to this mass segregation.

In order to simulate this effect, we mimicked observational conditions by selecting three percentages of all visible galaxies (50%, 33%, and 25%) by sorting the cluster members by mass and dividing them in 2, 3, and 4 mass bins. For each case, as explained in Sec. 4.1.5, we averaged 2250 configurations (750 for each axis, x, y, z), considering numbers of galaxies between 8 and 75 by avoiding galaxy repetition and evaluating the dispersion with the biweight, gapper, and standard deviation methods.

Figure 4.9 (left panel) shows $S'_{\rm std}(N_{\rm gal})/S_{\rm std}(< R_{200})$ as function of $N_{\rm gal}$ calculated with the corrected standard deviation estimator, and using galaxies picked from 100% (black line), 1/2 (blue line), 1/3 (red line) and 1/4 (green

Table 4.4: Impact of mass segregation in our estimates. We show the relative biases between $\langle S'_{\rm X}/S_{\rm std}(< R_{200})\rangle$ calculated for several fractions of massive galaxies

	BWT	GAP	STD
1	1.013	1.008	1
1/2	1.004	0.999	0.990
1/3	0.996	0.992	0.981
1/4	0.992	0.993	0.982

line) of the complete cluster member samples. A bias appears, with a non-linear dependence with the fraction of massive galaxies considered in each case, but almost insensitive to the $N_{\rm gal}$ parameter. This means that the velocity dispersion is sensitive to the fraction of massive galaxies used to estimate it. In particular, taking into account only the most massive galaxies of the clusters (1/4 of the sample), one would find a velocity dispersion that could be underestimated by up to two per cent. We can interpret this velocity bias in terms of a physical mechanism, dynamical friction (Chandrasekhar 1943), that mostly affects the most massive galaxies, so that the velocity dispersion is lower with respect to that obtained using objects randomly selected from the complete galaxy sample. Table 4.4 shows the average bias of the primed estimators $S'_{\rm X}$, calculated with respect to the full set of cluster members within R_{200} (i.e., $S_{\rm std}(< R_{200})$), for each fraction under exam, and for the three estimators (biweight, gapper, and standard deviation). As this physical bias is almost independent of $N_{\rm gal}$, we could in principle, directly use those values to produce a new corrected (unbiased) estimator.

In the right panel of Figure 4.9 we show the variance of $S'_{\rm std}(N_{\rm gal})/S_{\rm std}(< R_{200})$. The fraction of massive galaxies does not significantly affect the dispersion estimator variance.

4.3.2 Effect of aperture sub-sampling

All the analyses presented above include galaxies piked within the complete sample of cluster members, or within a fraction of the most massive of them, but the sample is always being selected within R_{200}. There is already evidence in the literature that the velocity dispersion estimate needs to be corrected if galaxies are not sampled out to the cluster's virial radius (e.g., Mamon et al. 2010; Sifón et al. 2016).

In this subsection, we investigate how the selection region affects the σ_v estimate in our simulations, by characterising the physical bias introduced when evaluating the velocity dispersion enclosed in a radius r from the galaxy

Table 4.5: Average velocity dispersion profile within a given enclosed radius r, $< S'_{\rm std}(< r)/S_{\rm std}(< R_{200}) >$, normalised to R_{200}. Values computed from the simulations. Uncertainties are the standard deviation.

r/R_{200}	$S'_{\rm std}(< r)/S_{\rm std}(< R_{200})$
0.2	1.044 ± 0.128
0.3	1.051 ± 0.106
0.4	1.047 ± 0.089
0.5	1.036 ± 0.071
0.6	1.030 ± 0.053
0.7	1.020 ± 0.039
0.8	1.012 ± 0.026
0.9	1.005 ± 0.015
1.0	0.998 ± 0.001
1.1	0.992 ± 0.016
1.2	0.986 ± 0.024
1.3	0.982 ± 0.034
1.4	0.978 ± 0.042
1.5	0.973 ± 0.045

cluster center, which differs from R_{200}. In particular, we computed the velocity dispersion using all the galaxies inside a cylinder of variable radius $0.2 \leq r/R_{200} \leq 1.2$. In addition, we averaged all 73 simulated GCs and construct the $\langle S'_{\rm X}(< r)/S_{\rm std}(< R_{200})\rangle$ as a function of the r/R_{200} profile (red line in the left panel of Fig. 4.10). The corresponding numerical values are given in Table 4.5. The velocity dispersion is, on average, overestimated where the region explored by the spectroscopic sample is smaller than R_{200}. The results are consistent with those obtained by Sifón et al. (2016) when using the biweight estimator for both $S'_{\rm X}(< r)$ and $S_{\rm X}(< R_{200})$ (see Figure 4 and Table 3 in that paper).

Finally, we evaluated the combined effect of this aperture sub-sampling and the selection effect of a fraction of massive galaxies discussed in the previous subsection. We performed the same analysis described above for eight fractions of R_{200}, i.e. $r/R_{200} = 0.2, 0.3, 0.4, 0.5, 0.8, 1.0, 1.2$ and 1.5, also considering different fractions of massive members. Unfortunately, we were unable to calculate the dispersion for the smaller fractions for radii less than half R_{200} for our simulation set, because not all the simulated clusters contained at least seven galaxies in these inner regions. For larger radii ($r \gtrsim R_{200}$), however, we found that the bias caused by the used fraction of massive galaxies remained almost constant at all radii. Therefore, we could apply the correction factors presented in Table 4.4, in combination with the radial correction profile shown in the left

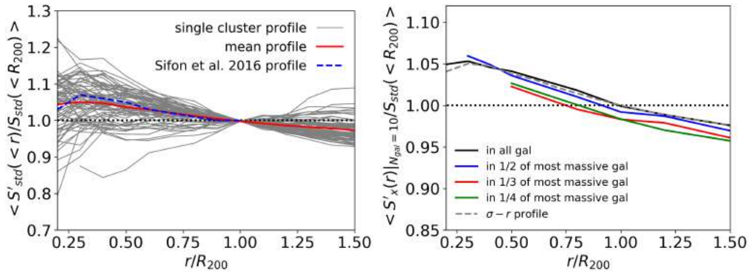

Figure 4.10: Left panel: Average velocity dispersion profile as a function of the radius r, $S'_{\rm std}(< r)/S_{\rm std}(< R_{200}) >$, normalised to R_{200}. The red line represents the mean at each radius of the 73 simulated GC profiles (grey lines). The numerical values are given in Table 4.5. The dashed blue line represents the Sifón et al. (2016) profile, which is almost coincident with our derived profile. Right panel: mean of $S'_{\rm std}/S_{\rm std}(< R_{200})$ as a function of r/R_{200}, calculated for $N_{\rm gal} = 10$. The profiles are calculated choosing $N_{\rm gal}$ within the 100% (black solid line), 50% (blue solid line), 33% (red solid line), and 25% (green solid line) of the complete cluster member samples.

panel of Figure 4.10 and in Table 4.5, to correct for both effects simultaneously. The combination of these two effects is shown in the right panel of Fig. 4.10.

4.4 Bias in the mass estimation

4.4.1 Statistical bias in the estimation of M_{200}

In the previous sections we studied how velocity dispersion estimators can be affected by different statistical and physical factors, and we quantified the expected bias in those cases. In this section, we show how mass estimators are also affected by the same effects, in both cases of Gaussian velocity distributions and simulated GCs.

4.4.1.1 The ideal case

The mass of a GC is not a direct observable. When we estimate the cluster mass using velocity dispersion estimates, we basically apply a scaling relation M–σ_v that has been previously calibrated either in simulations or using observations. Using DM only or hydrodynamic cosmological simulations, Evrard et al. (2008), Munari et al. (2013), and Saro et al. (2013) characterised the relations between GCs velocity dispersion of tracers (namely DM particles, galaxies and sub-halos)

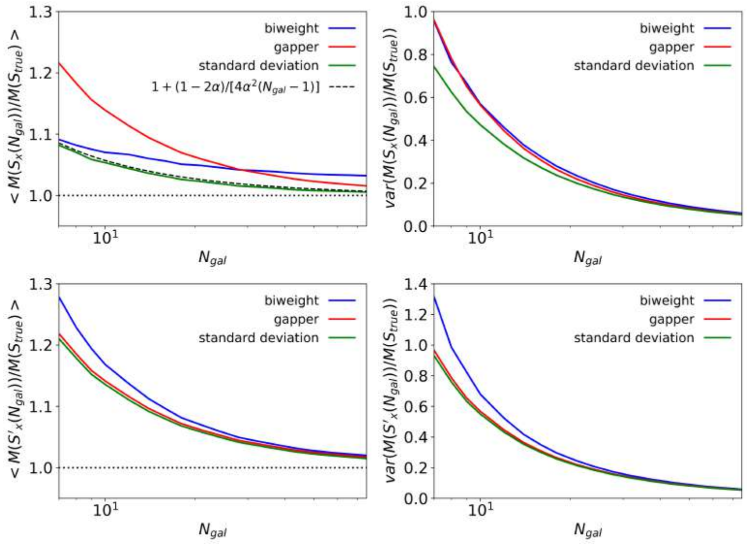

Figure 4.11: Top panels: mean (right) and variance (left) of $M\left(S_{\rm X}(N_{\rm gal})\right)/M(S_{\rm true})$, calculated with eq. 4.18 with $\alpha = 0.364$ and $A = 1177$ from Munari et al. (2013), for 50 000 samples of Gaussian-distributed random velocities. The dashed line in the left panel represents the analytic formula for the dependence of $M(S_{\rm std})$ on $N_{\rm gal}$. Bottom panels: mean (right) and variance (left) of $M\left(S'_{\rm X}(N_{\rm gal})\right)/M(S_{\rm true})$, where $S'_{\rm X}$ is the unbiased velocity dispersion estimator defined in eq. 4.16. Green, red, and blue lines represent respectively the behavior of the standard deviation, gapper, and biweight estimators.

and the cluster mass. Generally, these equations have the following parametric form:

$$\frac{M(S_{\rm X})}{10^{15}\,{\rm M}_\odot} = \left(\frac{S_{\rm X}}{A}\right)^{\frac{1}{\alpha}}. \tag{4.18}$$

However, DM particles, sub-halos and galaxies lead to different values of parameters A and α (Munari et al. 2013). Moreover, owing to the triaxiality of GCs and to the non-virialised state of some clusters, all the constraints for α are slightly different from the value $\alpha = 1/3$ derived from the virial theorem. The 73 clusters that we used in this chapter are a subset of those used by Munari et al. (2013); Therefore, we adopted the scaling relation derived in this article with parameters $A = 1177.0\,{\rm km\,s}^{-1}$ and $\alpha = 0.364$.

In analogy to what we have seen in sect. 4.1, even if we used an unbiased estimator for the velocity dispersion, and due to the fact that equation 4.18 contains a non-linear function of the variance, we expected a statistical bias with some dependence at low $N_{\rm gal}$. Using the results from subsection 4.1.2.1, as the transformation to obtain the mass is of the type $f(v) \propto v^{1/(2\alpha)}$ with $1/\alpha \sim 3$, we can predict the amount of bias.

As for the study of the dispersion estimators, in the case of mass estimators, we also generated Gaussian-distributed random velocities fixing the dispersion $S_{\rm true}$. In the top row of Fig. 4.11 we show the results of the bias (left panel) and associated variance (right panel) of the mass estimator based on eq. 4.18, using $S_{\rm X}(N_{\rm gal})$ as the velocity estimator. This case is noted as $\langle M(S_{\rm X})/M(S_{\rm true})\rangle$, and $M(S_{\rm true})$ represents the mass obtained using eq. 4.18 for the input value of $S_{\rm true}$.

We see that this mass estimator $M(S_{\rm std})$ is positively biased by a factor

$$\frac{1-2\alpha}{4\alpha^2(N_{\rm gal}-1)}, \tag{4.19}$$

as predicted by equation 4.11. In a similar way, the $M(S_{\rm bwt})$ (blue line) and $M(S_{\rm gap})$ (red line) mass estimators are also positively biased.

For comparison, the bottom row of Fig. 4.11 shows the equivalent results of the bias (left panel) and associated variance (right panel) of the mass estimator but now using $S'_{\rm X}(N_{\rm gal})$ as the input velocity estimation. These quantities are represented as $\langle M(S'_{\rm X})/M(S_{\rm true})\rangle$. It is interesting to note that the velocity dispersion bias is propagated into the mass bias, as seen by comparing the top and bottom panels on that figure. On one hand, as the bias on $S_{\rm gap}$ is almost independent from $N_{\rm gal}$, in the transformation from the normal estimator to the bias-corrected one, the only thing that changed is the normalisation (i.e. a constant factor, and therefore, the variance does not increase). On the other hand, the mass bias of $S_{\rm std}$ (top panel) was mitigated by the fact that normal standard deviation tends to underestimate the velocity dispersion at low $N_{\rm gal}$. This effect is not present in the $M(S'_{\rm std})$ profile (bottom panel) because $S'_{\rm std}$ is, by construction, unbiased. Focusing our attention on the variance of these mass estimators (shown in the right panels of Fig. 4.11) we see that for $M(S_{\rm X})$ (top panel), the standard deviation has the lowest variance, whereas the gapper and biweight show almost the same behavior as functions of $N_{\rm gal}$. Instead, in the bottom panel, the three $Var(M(S'_{\rm X}))$ functions show a behavior similar to what we see for the dispersion estimators. The gapper variance remained almost untouched, and the standard deviation behaved like the gapper, whereas the biweight has the higher variance.

As in sect. 4.1, we proposed a parametric description of the bias as a function of $N_{\rm gal}$, based on the analytic form of the bias for the standard deviation case. We also used three parameters (E,F and γ) to apply it to the gapper- and biweight-based mass estimators:

$$\frac{1-E\alpha}{(E\alpha)^2(N_{\rm gal}-1)^{\gamma}}+F \tag{4.20}$$

The best-fit parameters describing the bias for the unprimed $M(S_{\rm X})$ and primed $M(S'_{\rm X})$ mass estimators are listed in Tables 4.6 and 4.7, respectively.

Once we fitted for this bias, we can propose bias-corrected mass estimators for those two cases, by defining

$$M'\left(S_{\rm X}(N_{\rm gal})\right) = M\left(S_{\rm X}(N_{\rm gal})\right)\left[\frac{1-E\alpha}{(E\alpha)^2(N_{\rm gal}-1)^{\gamma}}+F\right]^{-1} \tag{4.21}$$

$$M'\left(S'_{\rm X}(N_{\rm gal})\right) = M\left(S'_{\rm X}(N_{\rm gal})\right)\left[\frac{1-E'\alpha}{(E'\alpha)^2(N_{\rm gal}-1)^{\gamma'}}+F'\right]^{-1}. \tag{4.22}$$

Following the same convention for the notation adopted in previous sections, these bias-corrected estimators are hereafter represented with a “prime”, i.e. $M'(S_{\rm X}(N_{\rm gal}))$ and $M'(S'_{\rm X}(N_{\rm gal}))$.

Fig. 4.12 shows the bias and variance of $M'(S_{\rm X})$ (top panel) and $M'(S'_{\rm X})$ (bottom panel). Both estimators are actually unbiased by construction. As expected, the biweight had the largest variance, whereas standard deviation behaved similarly to the gapper but still remained the lowest variance estimator.

4.4.1.2 The realistic case

We then applied the same methodology described in the previous subsection to our set of simulated clusters. In analogy with what we have done in sub-

Table 4.6: Best-fit parameters for the function describing the bias in $\langle M(S_\mathrm{X})/M(S_\mathrm{true})\rangle$ for Gaussian-distributed random velocieties, as described in equation 4.20.

	BWT	GAP	STD
E	2.22 ± 0.02	1.505 ± 0.007	2
F	1.023 ± 0.001	1.0013 ± 0.0005	1
γ	0.82 ± 0.04	1.088 ± 0.009	1

Table 4.7: Best-fit parameters for the function describing the bias in $\langle M(S'_\mathrm{X})/M(S_\mathrm{true})\rangle$ for simulated clusters, as described in equation 4.20.

	BWT	GAP	STD
E'	1.28 ± 0.01	1.504 ± 0.007	1.521 ± 0.007
F'	1.0078 ± 0.0008	1.0032 ± 0.0005	1.0009 ± 0.0005
γ'	1.23 ± 0.01	1.088 ± 0.009	1.083 ± 0.008

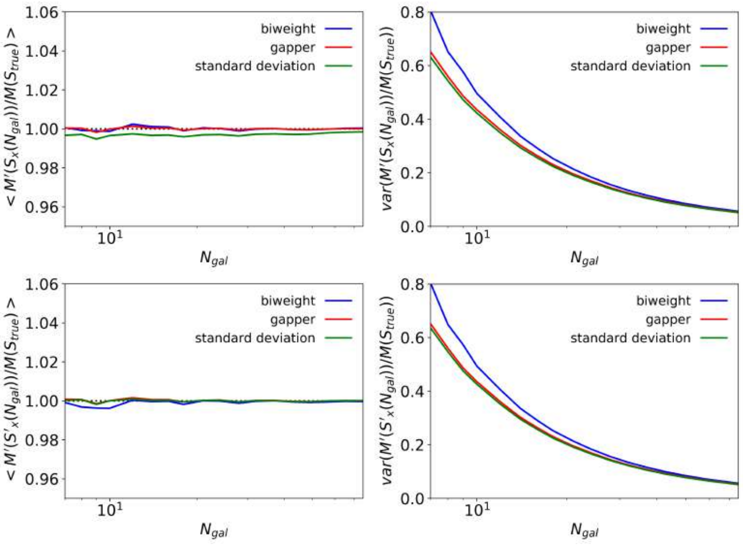

Figure 4.12: Mean (right panels) and variance (left panels) of the unbiased mass estimators $M'\left(S_\mathrm{X}(N_\mathrm{gal})\right)/M(S_\mathrm{true})$, and $M'\left(S'_\mathrm{X}(N_\mathrm{gal})\right)/M(S_\mathrm{true})$ defined in eq. 4.21. S_X and S'_X are normal and unbiased velocity dispersion estimators, in green the standard deviation, in red the gapper, and in blue the biweight.

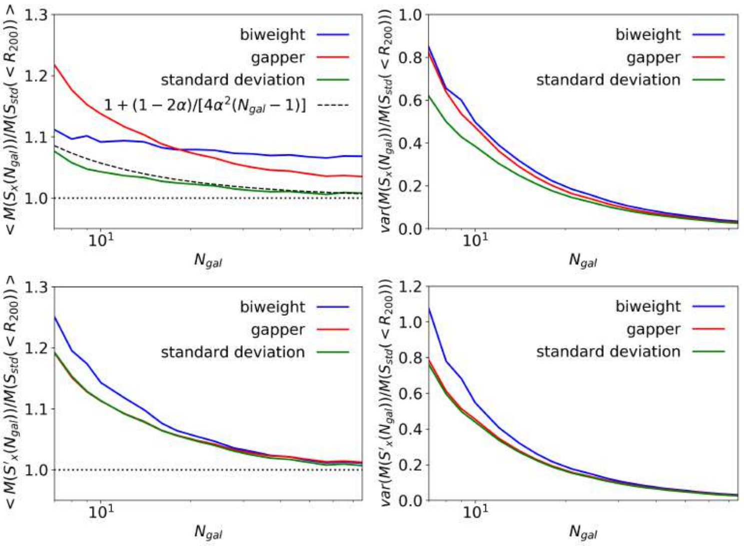

Figure 4.13: Mean (left panels) and variance (right panels) of $M\left(S_{\mathrm{X}}(N_{\mathrm{gal}})\right)/M\left(S_{\mathrm{std}}(< R_{200})\right)$ and $M\left(S'_x(N_{\mathrm{gal}})\right)/M\left(S_{\mathrm{std}}(< R_{200})\right)$, which represent the standard mass estimator, eq. 4.18, applied to normal and unbiased velocity dispersion estimators, standard deviation (green), gapper (red), and biweight (blue). The theoretical expectation for $M\left(S_{\mathrm{std}}(N_{\mathrm{gal}})\right)/M\left(S_{\mathrm{std}}(< R_{200})\right)$ is represented with the black dashed line.

Table 4.8: Best-fit parameters for the function describing the bias in $\langle M(S_{\mathrm{X}})/M(S_{\mathrm{std}}(<R_{200}))\rangle$ for simulated clusters, as described in equation 4.20.

	BWT	GAP	STD
E	2.36 ± 0.06	1.49 ± 0.03	1.97 ± 0.07
F	1.058 ± 0.004	1.023 ± 0.002	1.003 ± 0.002
γ	0.7 ± 0.1	1.17 ± 0.04	1.15 ± 0.09

Table 4.9: Best-fit parameters for the function describing the bias in $\langle M(S'_{\mathrm{X}})/M(S_{\mathrm{std}}(<R_{200}))\rangle$ for simulated clusters, as described in equation 4.20.

	BWT	GAP	STD
E'	1.31 ± 0.03	1.50 ± 0.03	1.53 ± 0.03
F'	1	1	1
γ'	1.24 ± 0.03	1.17 ± 0.04	1.11 ± 0.04

section 4.1.5, we also selected the velocity dispersion estimated with standard deviation using all the galaxies within R_{200} as the reference. Fig. 4.13 showns $\langle M\left(S_{\mathrm{X}}(N_{\mathrm{gal}})\right)/M(S_{\mathrm{std}}(<R_{200}))\rangle$ and $\langle M\left(S'_{\mathrm{X}}(N_{\mathrm{gal}})\right)/M(S_{\mathrm{std}}(<R_{200}))\rangle$ with their variances in the top and bottom panel respectively. These results are in complete agreement with respect to those obtained from the analysis of Gaussian velocity distributions. On one hand, the relative biases between the three estimators S_{X} are enhanced when the function $M(S_{\mathrm{X}})$ is applied to the velocity dispersion, as we show in subsection 4.1.3. On the other hand, when we applied the function M to the unbiased dispersion estimators (S'_{X}) we obtained very similar results to those in the Gaussian case. The standard deviation and gapper behave in the same way and they are completely indistiguishable, whereas the biweight is the estimator that overestimates the reference mass $M(S_{\mathrm{std}}(<R_{200}))$ the most.

Also, for the simulated clusters, we fit the parameters of equation 4.18. These parameters are listed in Tables 4.8 and 4.9 for $\langle M\left(S_{\mathrm{X}}(N_{\mathrm{gal}})\right)/M(S_{\mathrm{std}}(<R_{200}))\rangle$ and $\langle M\left(S'_{\mathrm{X}}(N_{\mathrm{gal}})\right)/M(S_{\mathrm{std}}(<R_{200})\rangle$, respectively.

The bias and variance of $M'(S_{\mathrm{X}})$ and $M'(S'_{\mathrm{X}})$ are shown in the top and bottom rows of Fig. 4.14, respectively. We see that both estimators are unbiased (by construction) and, in this case as well, the general behaviour of the variance of these estimators is very similar to what we showed with Gaussian distributions

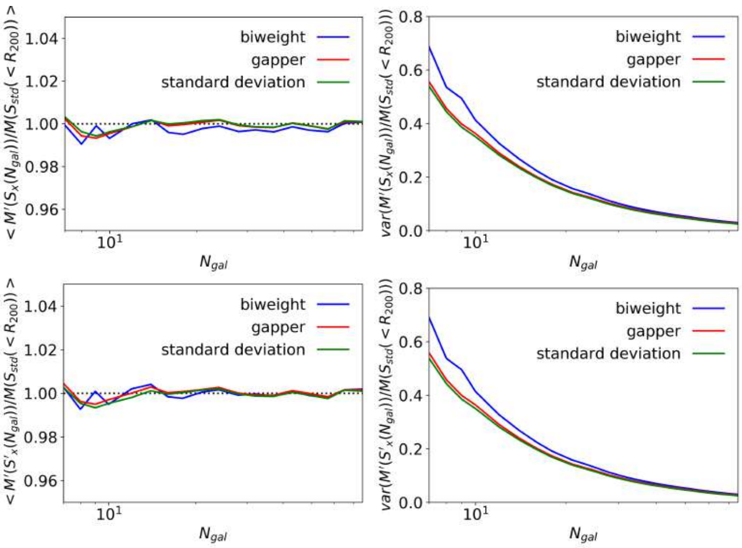

Figure 4.14: Mean (left panels) and variance (right panels) of $M'\left(S_{\rm X}(N_{\rm gal})\right)/M\left(S_{\rm std}(< R_{200})\right)$ and $M'\left(S'_x(N_{\rm gal})\right)/M\left(S_{\rm std}(< R_{200})\right)$, which represent the unbiased mass estimator, eq. 4.21, applied to normal and unbiased velocity dispersion estimators, standard deviation (green), gapper (red), and biweight (blue).

4.5 Physical biases in M_{200} estimation

In section 4.3 we explained how biases in velocity dispersion estimation could appear by only taking into account the more massive cluster members, or by sampling a fraction of the virial radius R_{200}. These biases, due to the physics of galaxy clusters, are also propagated to the mass estimation.

In the top panels of Fig. 4.15 we show how choosing galaxies from the subset of the most massive ones also introduces a bias to the mass estimation. For illustration purposes, we show the effect on the $M'(S_{\mathrm{X}})$ estimator only, but a similar figure can be generated for $M'(S'_{\mathrm{X}})$. We find that the mass could be underestimated up to 5% when using 1/4 of the sample containing the most massive galaxies. It is clear that the small biases in the velocity estimation are now amplified, especially at low N_{gal}.

The aperture effect on the mass estimators is also shown in the bottom panel of Fig. 4.15. In addition, as expected, all the biases are bigger than in the case of the velocity dispersion with a profile that prevents steeper sampling going to bigger apertures. Furthermore, variance increases in the core of the cluster and remains almost untouched for $r \geq R_{200}$.

It is evident that, owing to the high variance of mass estimation, the combination of these effects may be considered negligible for a single cluster mass determination, but in order to determine the mean bias of a scale relation, it is very important to obtain the most accurate mass estimation possible.

4.6 Applying corrections to a realistic case

In this section, we show how well we can retrieve a bias-corrected velocity dispersion and mass estimation for a simulated sample of galaxy clusters under realistic observing conditions. By following the methodology described in the previous sections, we give a recipe to obtain velocity dispersion and mass estimates in the small galaxy number regime, corrected for both statistical and physical biases. The basic steps are:

i. Use the unbiased estimator S'_{X}, defined in equation 4.16, to estimate the cluster velocity dispersion.

ii. Correct this velocity dispersion for the two physical effects (mass fraction and sampling aperture) described in the text, using Table 4.4 (or Fig. 4.9) and Table 4.5 (or Fig. 4.10), respectively. The second correction requires a first-order estimation of R_{200}, which can be obtained from the S'_{X} value from the previous step and the σ_{200}–M_{200} relation in equation 5.12.

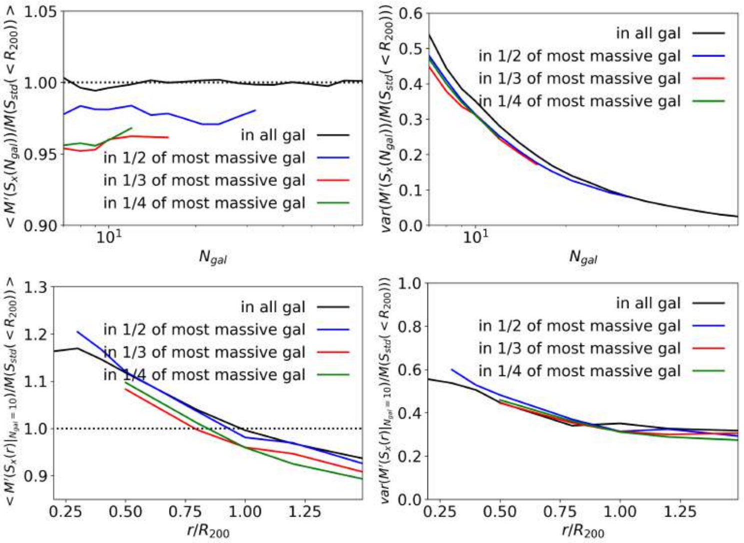

Figure 4.15: Mean and variance of the $M'(S_{\rm X})/M'(S_{\rm std}(< R_{200}))$ mass estimator, as a function of the number of galaxies $N_{\rm gal}$ (top panels), and as a function of the aperture radius r (bottom panels). In black, blue, green, and red red are the fractions that include 100%, 1/2, 1/3 and 1/4 of the most massive galaxies, respectively.

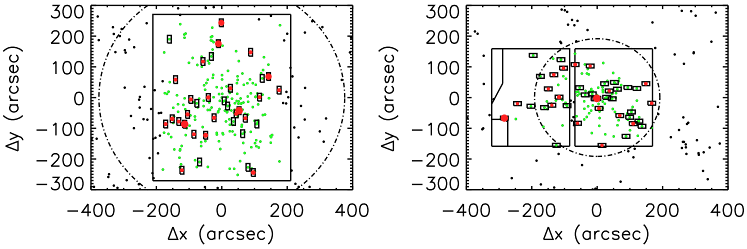

Figure 4.16: Left panel: Example of DOLORES/TNG simulated mask. Right panel: Example of OSIRIS/GTC simulated mask. See text for details. Black and green dots represent cluster members outside or inside the telescope field of view, respectively. Black rectangles are the slitlets, and the red points are the galaxies with line-of-sight velocity measurement (the symbol size is proportional to the mass of each galaxy with respect to the most massive one in the mask). The circle in dot-dashed line represents the projected R_{200} radius.

iii. Estimate the percentage of contaminants (interlopers) in the cluster members sample and correct, the velocity dispersion using the curves in Fig. 4.8 if needed. This provides the final velocity dispersion estimate, corrected for all effects described in this chapter. We do not provide a recipe for this, as it will generally depend on the particular selection procedure for each sample. However, we emphasise that a correction is needed, because this error is the dominant contribution to the total bias.

iv. Compute the galaxy cluster mass by using the unbiased mass estimator $M'(S'_{\mathrm{X}})$ defined in equation 4.22, and using as input the corrected S'_{X} value from the previous step as the input.

To perform this test, we decided to mimic the observational strategy that we adopted in our Planck PSZ1 follow-up ITP programme (Planck Collaboration Int. XXXVI 2016; Barrena et al. 2018, in prep.). This observational programme aimed to validate and characterise the unknown Planck SZ sources of the PSZ1 catalog in the northern hemisphere. To do this we used the DOLORES and OSIRIS spectrographs at the 3.5 m Telescopio Nazionale Galileo (TNG) and the 10.4 m Gran Telescopio Canarias (GTC) respectively, both located at Roque de los Muchachos Observatory (La Palma, Spain).

These facilities allowed multi-object spectroscopy (MOS) observations that fit our aim very well. However, the high number of clusters to be observed (about 200), and the need to obtain spectroscopy of very faint objects ($r'\sim 24$) did not allow us to use more than one MOS mask or a couple of long slits per cluster. For this reason, we could only obtain a reduced number of cluster members ($N_{\mathrm{gal}} < 40$). Our observational strategy started with the photometric redshift estimation. Once the z_{phot} (see eq. 2.1 and 2.2) was determined, we divided the GC sample into two redshift bins, $z \leq 0.4$ and $z > 0.4$, in order to observe them at the TNG and the GTC respectively. Here, we mimicked the galaxy selection procedure and the resultant galaxy catalogs. Given the different fields of view () of the two instruments and the differences in the two-mask designer software, we decided to implement both configurations following the same procedure described above. In Fig. 4.16 we show two examples of a TNG and GTC mask scheme. There are some differences in the two configurations: i) TNG masks are always centered on the GC center while GTC masks, because of the gap between the two CCD, are shifted $\sim$ 100” to the left; ii) the GTC mask designer tool is more precise than the TNG one. For this reason, the minimum distance between galaxies is 5.4” and 8” for GTC and TNG masks respectively.

In order to simulate a cluster observation, we selected each cluster at a random orientation and fraction of visible galaxies. Also, to mimic observational issues such as spectral contamination or wrong mask centering, we set a random number of slits as the effective catalog of measured radial velocities. We repeated this procedure to obtain 100 mock samples out of the 73 GCs object simulated in this study. For each of these samples we calculated the mean ratio between the estimated and the reference cluster velocity dispersion. Because the parameters of the scaling relation between σ_{200}–M_{200} (eq. 5.12), were constrained using the biweight estimation of the velocity dispersion, $S_{\rm bwt}(< R_{200})$, we decided to use it as a reference velocity dispersion for this analysis. For each of these samples we calculated the mean ratio between the estimated and the reference velocity dispersion of each cluster. Averaging over all the mock samples we obtained

$$\begin{aligned}
\langle S_{\rm bwt}(N_{\rm gal}, r)/S_{\rm bwt}(< R_{200})\rangle &= 0.96 \pm 0.03,\\
\langle S_{\rm gap}(N_{\rm gal}, r)/S_{\rm bwt}(< R_{200})\rangle &= 0.99 \pm 0.03,\\
\langle S_{\rm std}(N_{\rm gal}, r)/S_{\rm bwt}(< R_{200})\rangle &= 0.96 \pm 0.02.
\end{aligned} \tag{4.23}$$

Using the estimators $S'_{\rm X}$ defined in eq. 4.16 with the parameters in Table 4.3, we corrected the bias due to the number of galaxies. To correct the biases due to GC physics, the first step was to identify the fraction of massive galaxies in which the detected cluster members reside. The second step was to calculate the aperture radius, which is the sampling radius. To do this, we first needed to estimate R_{200}. Based on a first estimate of the cluster mass using $S_{\rm X}(N_{\rm gal})$, we could derive a first-order approximation of that radius, noted as $R^{\rm X}_{200}$. This value was used to apply the aperture correction shown on the right panel of Fig. 4.10 to $S'_{\rm X}$. In our case, each velocity dispersion was corrected individually after averaging over all the clusters, and then averaging over all the 100 configurations to obtain

$$\begin{aligned}
\left\langle S'_{\rm bwt}(N_{\rm gal}, r)/S_{\rm bwt}(< R_{200})\right\rangle &= 1.00 \pm 0.03,\\
\left\langle S'_{\rm gap}(N_{\rm gal}, r)/S_{\rm bwt}(< R_{200})\right\rangle &= 1.00 \pm 0.02,\\
\left\langle S'_{\rm std}(N_{\rm gal}, r)/S_{\rm bwt}(< R_{200})\right\rangle &= 1.00 \pm 0.02,
\end{aligned} \tag{4.24}$$

which represent bias-corrected estimates of the velocity dispersion.

Using these velocity dispersions, we could then calculate the cluster masses, $M(S'_{\rm X})$, obtaining

$$\begin{aligned}
\left\langle M\left(S'_{\rm bwt}(N_{\rm gal}, r)\right)/M\left(S_{\rm bwt}(< R_{200})\right)\right\rangle &= 1.17 \pm 0.09,\\
\left\langle M\left(S'_{\rm gap}(N_{\rm gal}, r)\right)/M\left(S_{\rm bwt}(< R_{200})\right)\right\rangle &= 1.14 \pm 0.08,\\
\left\langle M\left(S'_{\rm std}(N_{\rm gal}, r)\right)/M\left(S_{\rm bwt}(< R_{200})\right)\right\rangle &= 1.13 \pm 0.07.
\end{aligned} \tag{4.25}$$

As shown above, these masses are overestimated, and in order to correct for this bias, we had to use the primed mass estimator, M', as explained in Sec. 4.4.1. In this case, we obtained

$$\begin{aligned}\left\langle M'\left(S'_{\rm bwt}(N_{\rm gal},r)\right)/M'\left(S_{\rm bwt}(<R_{200})\right)\right\rangle &= 1.00\pm0.07,\\ \left\langle M'\left(S'_{\rm gap}(N_{\rm gal},r)\right)/M'\left(S_{\rm bwt}(<R_{200})\right)\right\rangle &= 1.00\pm0.07,\\ \left\langle M'\left(S'_{\rm std}(N_{\rm gal},r)\right)/M'\left(S_{\rm bwt}(<R_{200})\right)\right\rangle &= 1.00\pm0.06.\end{aligned}\tag{4.26}$$

It is also interesting to compare these mass estimates with the true mass, M_{200} directly estimated from the simulation as the mass of all particles within R_{200}. Those values were used to constrain the parameters in equation 5.12 (Munari et al. 2013). The direct estimation of the velocity dispersion using $S_{\rm X}$ led to a biased estimation of M_{200}:

$$\begin{aligned}\langle M\left(S_{\rm bwt}\left(N_{\rm gal},r\right)\right)/M_{200}\rangle &= 1.07\pm0.09,\\ \langle M\left(S_{\rm gap}\left(N_{\rm gal},r\right)\right)/M_{200}\rangle &= 1.13\pm0.08,\\ \langle M\left(S_{\rm std}\left(N_{\rm gal},r\right)\right)/M_{200}\rangle &= 1.03\pm0.08,\end{aligned}\tag{4.27}$$

Even if the dispersion estimator is the corrected one, $S'_{\rm X}$, we did not obtain an unbiased mass:

$$\begin{aligned}\left\langle M\left(S'_{\rm bwt}\left(N_{\rm gal},r\right)\right)/M_{200}\right\rangle &= 1.18\pm0.10,\\ \left\langle M\left(S'_{\rm gap}\left(N_{\rm gal},r\right)\right)/M_{200}\right\rangle &= 1.13\pm0.09,\\ \left\langle M\left(S'_{\rm std}\left(N_{\rm gal},r\right)\right)/M_{200}\right\rangle &= 1.13\pm0.08,\end{aligned}\tag{4.28}$$

Finally, M' provided the final, unbiased estimate of M_{200}:

$$\begin{aligned}\left\langle M'\left(S'_{\rm bwt}\left(N_{\rm gal},r\right)\right)/M_{200}\right\rangle &= 1.00\pm0.08,\\ \left\langle M'\left(S'_{\rm gap}\left(N_{\rm gal},r\right)\right)/M_{200}\right\rangle &= 1.00\pm0.07,\\ \left\langle M'\left(S'_{\rm std}\left(N_{\rm gal},r\right)\right)/M_{200}\right\rangle &= 0.99\pm0.07,\end{aligned}\tag{4.29}$$

These numbers show that, in this realistic situation as well, the proposed set of corrected estimators were able to recover an unbiased estimate for both the velocity dispersion and mass of the galaxy clusters.

The ultimate aim of this procedure was not only to correct the velocity dispersion and mass estimates of a single cluster, but also to develop a method to obtain bias-corrected mean mass estimates in order to constrain the parameter of mass scaling relations. For this reason, in this section, we applied these techniques to a set of mock observations. In the next chapter, we will apply the recipe and corrections described above to a set of 207 real GCs selected though their SZ emission from the *Planck* Collaboration, in order to retrieve bias-corrected mean velocity dispersion and mass.

5

Dynamical mass vs. SZ mass scaling relation

This chapter describes how we characterised the scaling relation by comparing masses derived from SZ measurements (Y_{500}) and our Dynamical proxies (σ_{200}). In section 5.1, we explain how to compute the SZ masses for the Planck PSZ1 catalogue, by breaking the size-flux degeneracy through the $Y_{\mathrm{X}} - M_{500}$ relation. This procedure follows the one proposed in the *Planck* Collaboration papers. In section 5.2 we depict how to estimate dynamical masses. In section 5.3, we describe the ITP and the SDSS GC samples used for the cosmological analyses of this thesis. In particular, we constrain the mass bias parameter, $(1 - B)$, explaining how much the Eddington bias affects our sample and the importance of correcting it. Finally, in section 5.5, we compare our results with those from *Planck* Collaboration and those from the literature, using both the velocity dispersion and the Weak Lensing analysis as mass proxies. We also discuss the implications on the σ_8 tension with CMB measurements. The results described in this chapter will be published in Ferragamo et al. (in prep.).

5.1 SZ mass estimates

The first step to characterise a scaling relation between dynamical and SZ masses is to understand how the latter are related to observable quantities. In the previous chapter, we discussed the biases in the estimation of velocity dispersion and dynamical mass of a cluster of galaxies. The latter quantity, not being directly measurable, is obtained from the velocity dispersion through Eq. 5.12. This equation was first calibrated by Evrard et al. (2008) using an N-body simulation with DM only, finding a good agreement with the virial relation. After this study, different authors constrained the parameter of this relation for simulated galaxies instead of DM particles. Saro et al. (2013) used galaxies defined from semi-analytical models applied on DM-only simulations, whereas Munari et al. (2013) used the galaxies generated in hydrodynamic simulations with AGN feedback, star formation, SN feedback, cooling, CMB and ultraviolet/X-ray background. Both analyses showed non-negligible deviations from the virial relation.

As described in chapter 1, the observable related to the SZ effect that we use as mass proxy is the Compton parameter, Y_{500}. The *Planck* Collaboration characterised the $Y_{500} - M_{500}$ relation using real data instead of simulated ones. This choice is due to the fact that, although the simulations allow us to obtain a relation between *true* physical quantities and *true* mass, these *true* quantities strongly depend on the models that describe the non-gravitational phenomena that occur in the ICM (Planck Collaboration XX 2014).

Since the GCs X-ray emission and SZ effect are both signatures of the ICM, it was natural for the *Planck* Collaboration to choose the mass from an X-ray proxy as a reference in order to constrain its scaling relation. Observables such as the gas mass, $M_{\rm g}$, the luminosity or temperature, $T_{\rm X}$, are the most used X-ray mass proxies. However, each one of these observables suffer a different intrinsic scatter. In this context, several studies showed that the gas thermal energy $Y_{\rm X}$ provides a lower intrinsic scatter scaling relation than any other observable (Kravtsov et al. 2006; Arnaud et al. 2007; Vikhlinin et al. 2009). Introduced by Kravtsov et al. (2006), $Y_{\rm X}$ is the X-ray analog of Y_{SZ} , defined as

$$Y_{\rm X} \equiv M_{g,500}\ T_{\rm X}, \tag{5.1}$$

where $T_{\rm X}$ is the mean spectroscopic X-ray temperature evaluated in the $[0.15 - 1]R_{500}$ (Mazzotta et al. 2004; Vikhlinin 2006), and $M_{g,500}$ is the gas mass enclosed within R_{500}, excluding the cluster core, derived from X-ray imaging data.

5.1.1 From $Y_{\rm X} - M_{500}^{\rm HE}$ to $Y_{500}^{\rm SZ} - M_{500}^{Y_{\rm X}}$

As a consequence of the above, the first step to constrain the relation $Y_{500} - M_{500}$ is to characterise the relation between $Y_{\rm X}$ and the cluster mass, assuming hydrostatic equilibrium, $M_{500}^{\rm HE}$ (see eq. 1.38). As shown in Eq.1.53, this is usually a power law relation such as

$$E^{-2/3}(z)\ Y_{\rm X} = 10^{A \pm \sigma_A} \left[M_{500}^{\rm HE}\right]^{\alpha \pm \sigma_\alpha}, \tag{5.2}$$

where $E(z) = H(z)/H_0$. The *Planck* Collaboration used the best fit established by Arnaud et al. (2010) using 20 local ($z < 0.2$) relaxed clusters observed with *XMM-Newton* and REXCESS data:

$$E^{-2/3}(z)\left[\frac{Y_{\rm X}}{10^{-4}\ {\rm M}_\odot\ {\rm keV}}\right] = 10^{0.376\pm0.018}\left[\frac{M_{500}^{\rm HE}}{6\times10^{14}\ {\rm M}_\odot}\right]^{1.78\pm0.06}, \quad (5.3)$$

that became

$$E^{-2/3}(z)\left[\frac{Y_{\rm X}}{10^{-4}\ {\rm Mpc}^2}\right] = 10^{-0.171\pm0.018}\left[\frac{M_{500}^{\rm HE}}{6\times10^{14}\ {\rm M}_\odot}\right]^{1.78\pm0.06}, \quad (5.4)$$

by expressing $Y_{\rm X}$ in unit of 10^{-4} Mpc^2 (Planck Collaboration XX 2014).

Once the $Y_{\rm X} - M_{500}^{\rm HE}$ relation is constructed, the second step is to characterise the $Y_{500}^{\rm SZ} - M_{500}$ one. To do this, the Planck Collaboration used a subsample of 71 clusters from the *Planck* cosmological sample with $S/N > 7$ (Planck Collaboration XX 2014). This sample contains clusters from a previous study: 58 *Planck* Early SZ (ESZ) (Planck Collaboration XI 2011), 4 from *Planck* detected Local Cluster Substructure Survey (LoCuSS) (Planck Collaboration Int. III 2013) and 9 from the *XMM-Newton* validation programme (Planck Collaboration IX 2011; Planck Collaboration Int. I 2012; Planck Collaboration Int. IV 2013). For each cluster, $Y_{\rm X}$, $R_{500}^{Y_{\rm X}}$ and $M_{500}^{Y_{\rm X}}$ can be estimated from the gas mass profile, the observed temperature and Eq. 5.4, following the iterative procedure described in Kravtsov et al. (2006). The SZ signal Y_{500}^{SZ} was extracted using the `MMF` from the *Planck* frequency maps by using the X-ray peak and the $R_{500}^{Y_{\rm X}}$ as prior for position and radius, respectively. Assuming that the ICM follows the universal pressure profile by Arnaud et al. (2010), this profile was integrated along the line-of-sight to obtain a measurement of the flux within a cylinder of aperture $5 \times R_{500}^{Y_{\rm X}}$, and then converted to the Y_{500}^{SZ} within a sphere of radius $R_{500}^{Y_{\rm X}}$ (Planck Collaboration IX 2011).

Due to redshift and S/N, the cut-off of the sample could be affect by selection effects such as the Malmquist bias. To correct for this bias, each cluster SZ flux was rescaled for the mean bias by following the procedure described in Vikhlinin et al. (2009) and Pratt et al. (2009). The fit using the 71 clusters corrected for Malmiquist bias led to

$$E^{-2/3}(z)\left[\frac{D_A^2\ Y_{500}^{\rm SZ}}{10^{-4}\ {\rm Mpc}^2}\right] = 10^{-0.186\pm0.011}\left[\frac{M_{500}^{Y_{\rm X}}}{6\times10^{14}\ {\rm M}_\odot}\right]^{1.79\pm0.06}. \quad (5.5)$$

This result, although determined with better accuracy, is compatible within 1σ error to the one found in Planck Collaboration IX (2011) using 62 clusters of

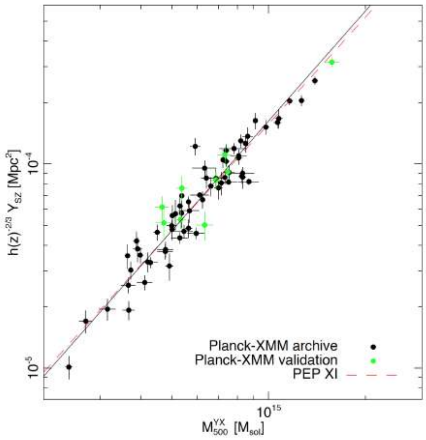

Figure 5.1: Best scaling relation between $M_{500}^{Y_{\rm X}}$ and $Y_{500}^{\rm SZ}$ after the correction of the Malmquist bias. Credit: Planck Collaboration XX (2014).

the ESZ sample observed with *XMM-Newton*. Figure 5.1 shows the best fit, Eq. 5.5 (black line) compared to the relation from Planck Collaboration IX (2011).

5.1.2 The $Y_{500}^{\rm SZ} - M_{500}$ relation

In previous sections, we see that the relation between $Y_{500}^{\rm SZ}$ and $M_{500}^{Y_{\rm X}}$ is based on X-ray observations and how $M_{500}^{Y_{\rm X}}$ is related to $M_{500}^{\rm HE}$ through $Y_{\rm X}$. However, the mass estimated through the hydrostatic equilibrium assumption is expected to be biased due to deviations from the hydrostatic equilibrium, temperature inhomogeneities, absolute instrument calibration, residual selection biases, etc. (Planck Collaboration XX 2014). All these biases can be included in one single parameter, the *mass bias* parameter. Therefore, the relation between the hydrostatic mass and the *true* mass is given by

$$M_{500}^{\rm HE} \equiv (1-b)\ M_{500}. \tag{5.6}$$

Consequently, the power law relation between $Y_{\rm X}$ and $M_{500}^{\rm HE}$ becomes a relation between the gas thermal energy and the true mass

$$E^{-2/3}(z)\ Y_{\rm X} = 10^{A\pm\sigma_A}\left[(1-b)\ M_{500}\right]^{\alpha\pm\sigma_\alpha}. \tag{5.7}$$

The calibration between Y_{X} and M_{500} is equivalent to the relation $M_{500}^{Y_{\mathrm{X}}} - M_{500}$

$$M_{500}^{Y_{\mathrm{X}}} = 10^{\pm\sigma_A/\alpha}\,[(1-b)\ M_{500}]^{1\pm\sigma_\alpha/\alpha}\,. \tag{5.8}$$

according to the fact that $M_{500}^{Y_{\mathrm{X}}}$ is defined from the best fit $Y_{\mathrm{X}} - M_{500}^{\mathrm{HE}}$

$$E^{-2/3}(z)\ Y_{\mathrm{X}} = 10^{A}\left[M_{500}^{Y_{\mathrm{X}}}\right]^{\alpha}. \tag{5.9}$$

By Combining Eq. 5.8 with Eq. 5.5, the *Planck* Collaboration obtained the scaling relation $Y_{500}^{\mathrm{SZ}} - M_{500}$

$$E^{-2/3}(z)\left[\frac{D_A^2\ Y_{500}^{\mathrm{SZ}}}{10^{-4}\ \mathrm{Mpc}^2}\right] = 10^{-0.19\pm0.012}\left[\frac{(1-b)\ M_{500}}{6\times10^{14}\ \mathrm{M}_\odot}\right]^{1.79\pm0.08}. \tag{5.10}$$

It is interesting to underline that Eq. 5.8 does not affect the best fit parameters, but increases their uncertainties, which are added quadratically as the determinations of the two relations are independent.

5.1.3 Breaking the $\theta_{500} - Y_{500}$ degeneracy

As we described in section 1.3.2, the *Planck* detection algorithms `MMF1`, `MMF3` and `PwS`, give the two parameters of the GNFW profile used to detect the SZ signal. However, the posterior likelihood shows a correlation between the angular size θ_{500} and $Y_{5R_{500}}$, which denotes the Compton parameter within $5R_{500}$, or, equivalently, $5\theta_{500}$.

There are different ways to break this degeneracy in order to estimate Y_{500}. The more direct one leads to the so called blind measure of Y. This method consists in the marginalisation of the posterior probability in the (Y_{500}, θ_{500}) plane over the θ_{500} axis. Although this method does not require any other analysis, it leads to an estimate of the Compton parameter that is, on average, biased to high values. This effect is due to the fact that the non-linear nature of the degeneracy tends to over-estimate the cluster size (Planck Collaboration XXIX 2014). Moreover, this issue will affect the unresolved or marginally resolved clusters more than others. It is also more difficult to constrain the size of these clusters due to resolution problems. Another crucial aspect is that the degeneracy more than doubles the uncertainty on Y_{500}, even knowing the *true* value of θ_{500} (Planck Collaboration VIII 2011).

These issues can be mitigated by putting a prior on the cluster size. Due to the precision, $\sim 1\%$, the radius estimated from X-ray mass proxies such as Y_{X} or T_{X}, is usually used as prior. There is nothing to prevent choosing a prior from other kinds of analyses, e.g. dynamical studies. However, a higher

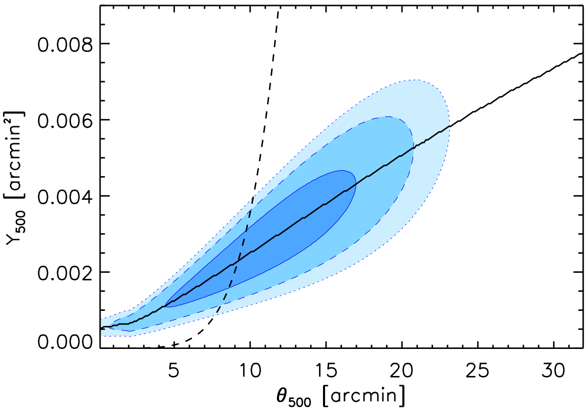

Figure 5.2: Example of the SZ size-flux degeneracy for the cluster PSZ1 G123.55-10.34 ($S/N = 5.55$ at $z = 0.106$). The contours show the 68%, 95% and 99% confidence levels. The black solid line shows the best size-flux curve, obtained by taking the maximum of the Y_{500} probability distribution for each θ. The black dotted line represents the curve obtained from the $Y_{\rm X} - M_{500}$ relation.

uncertainty on θ_{500} is reflected in a higher uncertainty in the estimation of Y_{500}. The *Planck* Collaboration retrieved R_{500} and z from the MCXC meta-catalogue. This catalogue provides a compilation of redshift, X-Ray luminosity $L^{\rm X}_{500}$, mass M_{500} and radius R_{500} homogenised from the ROSAT All Sky Survey (RASS)-based (NORAS, REFLEX, BCS, SGP, NEP, MACS, and CIZA) and ROSAT serendipitous (160SD, 400SD, SHARC, WARPS, and EMSS) cluster catalogues (Piffaretti et al. 2011). By assuming the Arnaud et al. (2010) profile the *Planck* Collaboration re-extracted the SZ signal from the *Planck* frequency maps at the peak position of the X-ray emission. This methodology reduces the scatter and should also reduce the mean bias (Planck Collaboration XXIX 2014). However, the X-ray size is deduced from the $M_{500} - L^{\rm X}_{500}$, which tends to underestimate the mass of morphological disturbed systems (Planck Collaboration XI 2011; Pratt et al. 2009).

Another way to break the size-flux degeneracy, knowing the cluster redshift z, is by using an estimation of θ_{500} based on the $M_{500} - Y_{500}$ relations assuming cluster spherical symmetry

$$\theta_{500} = \theta_* \left[\frac{h}{0.7}\right]^{1/3} \left[\frac{(1-b)\ M_{500}}{3\times 10^{14}\ \mathrm{M}_\odot}\right]^{1/3} E^{-2/3}(z) \left[\frac{D_A(z)}{500\ \mathrm{Mpc}}\right]^{-1} \tag{5.11}$$

where $\theta_* = 6.997'$. This equation combined with the mass-flux relation (Eq. 5.10) gives a function that intersects with the curve obtained by connecting the best Y values at each θ (see figure 5.2), and gives a value of Y_{500} that is equivalent to the X-ray mass proxy Y_X (Planck Collaboration XXIX 2014). As explained in 5.1, this estimator is the lower intrinsic scatter estimator. Moreover, this SZ flux estimate does not depend on X-ray observations of the cluster allowing to calculate the SZ mass also for *Planck* clusters validated with observations in others wavelengths.

In the following analysis, we will use Y_{500} evaluated in the latter method, in order to estimate SZ masses, denoted by M_{500}^{SZ}, through Eq. 5.10.

5.2 Dynamical mass estimates

The second step to constrain the scaling relation is to determine the GCs dynamical mass. In sections 3.1.1, we described the method that we used to determine the cluster membership. It consists of a selection based on galaxy position in the projected phase space (r, cz), where r is the projected distance from the cluster centre, and cz is the galaxy LoS velocity. We defined a region of membership by performing a cut at $r = 2.5$ Mpc and an iterative 2.5σ clipping.

Once the cluster membership was determined, we estimated the velocity dispersion. We used the bias-corrected gapper estimator defined in Eq. 4.16. As explained in section 4.1.3, this first estimate of the velocity dispersion is affected by physical biases due to the aperture radius and the fraction of massive galaxies composing the sample. Although we quantified both biases in section 4.3, we were able to only correct for the aperture radius. In fact, the poorness of our cluster members samples does not allow us to construct a luminosity function. Therefore, we could not determine the fraction of massive galaxies we observed spectroscopically.

Thereafter, we computed the dynamical mass M_{200}^{dyn} by using the bias-corrected mass estimator, Eq. 4.21, based on the Munari et al. (2013) scaling relation

$$\frac{\sigma}{\mathrm{km\ s^{-1}}} = A \left[\frac{h(z)\ M_{200}}{10^{15}\ \mathrm{M}_\odot}\right]^{\alpha}, \tag{5.12}$$

where $A = 1177.0$ and $\alpha = 0.364$. Although there are several different $\sigma - M_{200}$ relations (Evrard et al. 2008; Saro et al. 2013; Munari et al. 2013), we chose the one from Munari et al. (2013) for two main reasons:

- the parameters of this relation were constrained by using the velocity dispersion of galaxies in a hydrodynamic simulation. Contrary to those from Evrard et al. (2008) and Saro et al. (2013), both are based on DM-only simulations. The first, by calculating the velocity dispersion with DM particles; the second, by using galaxies from a semianalytical model;
- we determined the corrections for velocity dispersion and mass analysing a subsample of the simulated clusters used to constrain the Munari et al. (2013) relation.

Since the relation between Y_{500}^{SZ} and M_{500}^{SZ} was constructed starting from X-ray observations, the result was the mass within a sphere 500 times denser than the critical density of the Universe, ρ_c. For this reason, in order to compare SZ and dynamical masses, we needed to rescale M_{200} to M_{500}. To do this, we assumed a NFW density profile (Navarro et al. 1997)

$$\rho(r) = \frac{\rho_c}{(r/r_s)\,(1+r/r_s)^2} \tag{5.13}$$

where ρ_c and r_s are the characteristic density and the scale radius, respectively. These parameters are related with R_{200} and $\rho_{200} \equiv 200 \times \rho_c$ through the concentration parameter c, defined as

$$c_{200} \equiv R_{200}/r_s \tag{5.14}$$

$$\rho_c = \frac{\rho_{200} c^3 g(c)}{3} \tag{5.15}$$

where $g(x) = 1/\left[\ln(1+\mathrm{x}) - \mathrm{c}/(1+\mathrm{x})\right]$. We can write the equation for a mass by assuming spherical symmetry

$$M(r_\Delta) = \frac{g(c_{200})}{g(c_{200}\; r_\Delta/R_{200})} M_{200}, \tag{5.16}$$

where Δ is the density contrast at which we want to obtain the mass; in our case, $\Delta = 500$. We then need to select a mass-concentration relation to scale our masses (Łokas & Mamon 2001). Following the procedure in Komatsu et al. (2011), we chose the Duffy et al. (2008) relation, constrained using N-body simulations and WMAP 5-year cosmological parameters

$$c_{200} = \frac{5.71}{(1+z)^{0.47}} \left(\frac{M_{200}}{2 \times 10^{12} h^{-1} \mathrm{M}_\odot} \right)^{-0.084}. \tag{5.17}$$

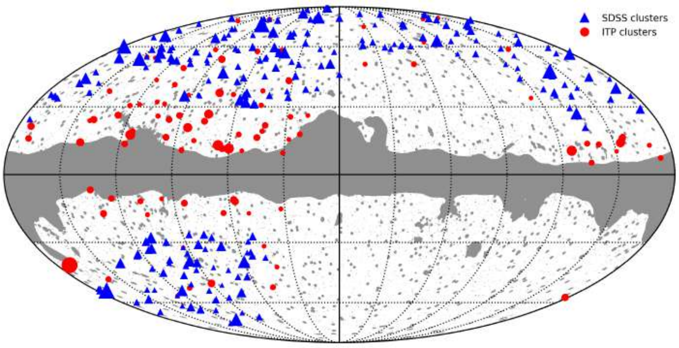

Figure 5.3: Sky distribution of the 207 PSZ1 clusters used to characterise the scaling relation $M_{500}^{SZ} - M_{500}^{dyn}$. Red circles and blue triangles represent ITP (see table 5.1) and SDSS clusters (see table 5.2), respectively, with the size proportional to the cluster mass. In grey, we show the position of the mask used to produce the CMB map, in Mollweide projection with the Galactic plane horizontal and centred at longitude zero, excluding 27% of the sky in the region of Galactic plane, Magellanic clouds and point sources.

5.3 Cluster samples used in this thesis

In chapters 2 and 3, we described the optical follow-up of the unknown PSZ1 sources that we observed between the second semester of 2013 and first semester of 2015. In this section, we briefly describe the sample of selected clusters that we used to characterise the scaling relation $M_{500}^{SZ} - M_{500}^{dyn}$. Figure 5.3 shows the sky distribution of the cluster of the ITP sample (red dots) and the SDSS sample (blue triangles).

5.3.1 ITP sample

The ITP sample is composed by 61 objects selected between the sources confirmed as GC and associated with the SZ signal listed in Table 3.3 with Flag 1. In order to characterise the scaling relation, we decided to discard all PSZ1 sources with multiple counterparts. Since the SZ signal is integrated along the line-of-sight, the output of *Planck* detection algorithms is a single posterior probability in the (Y_{500}, θ_{500}) space. Therefore, in presence of two or more clusters, each one gave overestimated Y_{500} results, biasing the estimation of the SZ mass.

In Table 5.1 we list dynamical and SZ masses of the GCs selected from the ITP optical follow-up sample. The first and second columns list the index number and the name of each cluster in the PSZ1 catalogue. Columns 3 and 4 are spectroscopic redshift and number of cluster members with spectroscopic measurements per each GC. Columns 5, 6 compile the velocity dispersion and the corresponding dynamical mass. The last two columns show the SZ masses before and after correcting for Eddington bias, respectively.

Table 5.1: Properties of for the GCs selected in the ITP optical follow-up sample.

Planck ID	*Planck* NAME	z	N_{gal}	σ_{200} (km/s)	M_{500}^{dyn} ($10^{15}\mathrm{M}_{\odot}$)	M_{500}^{SZ} ($10^{15}\mathrm{M}_{\odot}$)	$M_{500}^{SZ_{cor}}$ ($10^{15}\mathrm{M}_{\odot}$)
80	PSZ1 G030.70+09.47	0.052	17	595 ± 95	0.14 ± 0.06	0.25 ± 0.02	0.18 ± 0.02
90	PSZ1 G032.76+42.33	0.844	8	1220 ± 309	0.53 ± 0.34	0.81 ± 0.10	0.27 ± 0.03
116	PSZ1 G041.70+21.65	0.478	25	1017 ± 128	0.46 ± 0.15	0.66 ± 0.08	0.29 ± 0.03
121	PSZ1 G042.96+19.11	0.499	8	720 ± 182	0.16 ± 0.10	0.67 ± 0.08	0.29 ± 0.03
133	PSZ1 G045.54+16.26	0.206	21	953 ± 133	0.46 ± 0.17	0.41 ± 0.05	0.26 ± 0.03
135	PSZ1 G045.85+57.71	0.607	37	1069 ± 105	0.50 ± 0.13	0.82 ± 0.08	0.41 ± 0.04
138	PSZ1 G046.13+30.75	0.568	13	780 ± 146	0.20 ± 0.10	0.73 ± 0.09	0.32 ± 0.04
143	PSZ1 G047.44+37.39	0.230	10	653 ± 144	0.15 ± 0.09	0.39 ± 0.06	0.27 ± 0.04
149	PSZ1 G048.22–51.60	0.530	30	911 ± 102	0.34 ± 0.10	0.64 ± 0.08	0.28 ± 0.03
175	PSZ1 G055.72+17.58	0.195	24	777 ± 100	0.27 ± 0.09	0.43 ± 0.05	0.29 ± 0.03
179	PSZ1 G056.76–11.60	0.123	21	1022 ± 143	0.59 ± 0.22	0.40 ± 0.03	0.34 ± 0.03
184	PSZ1 G057.42–10.77	0.136	25	969 ± 122	0.51 ± 0.17	0.30 ± 0.04	0.23 ± 0.03
201	PSZ1 G060.12+11.42	0.226	20	1329 ± 192	1.11 ± 0.42	0.56 ± 0.05	0.44 ± 0.04
208	PSZ1 G063.80+11.42	0.428	13	1080 ± 203	0.54 ± 0.26	0.66 ± 0.06	0.44 ± 0.04
209	PSZ1 G063.92–16.75	0.392	16	892 ± 147	0.34 ± 0.15	0.54 ± 0.07	0.26 ± 0.03
212	PSZ1 G064.83+35.79	0.442	22	666 ± 91	0.15 ± 0.05	0.55 ± 0.07	0.26 ± 0.03
213	PSZ1 G065.13+57.53	0.683	22	899 ± 122	0.29 ± 0.10	0.68 ± 0.08	0.24 ± 0.03
219	PSZ1 G066.20+12.87	0.246	12	1386 ± 273	1.17 ± 0.60	0.48 ± 0.05	0.32 ± 0.03
246	PSZ1 G073.64+36.49	0.558	9	1304 ± 307	0.78 ± 0.47	0.65 ± 0.07	0.28 ± 0.03
253	PSZ1 G076.44+23.53	0.168	21	949 ± 133	0.47 ± 0.17	0.36 ± 0.03	0.26 ± 0.02
261	PSZ1 G079.88+14.97	0.101	12	597 ± 117	0.13 ± 0.07	0.24 ± 0.03	0.18 ± 0.02
282	PSZ1 G084.41–12.43	0.276	20	999 ± 144	0.50 ± 0.19	0.59 ± 0.05	0.49 ± 0.04
288	PSZ1 G084.85+20.63	0.371	9	1319 ± 310	0.91 ± 0.55	0.48 ± 0.05	0.28 ± 0.03
289	PSZ1 G085.71+10.67	0.084	12	780 ± 154	0.28 ± 0.14	0.23 ± 0.02	0.18 ± 0.02
296	PSZ1 G086.93+53.18	0.766	12	1245 ± 245	0.62 ± 0.32	0.59 ± 0.07	0.19 ± 0.02
313	PSZ1 G091.82+26.11	0.822	16	1209 ± 200	0.57 ± 0.25	0.75 ± 0.05	0.57 ± 0.04
335	PSZ1 G095.49+16.41	0.405	19	1037 ± 154	0.50 ± 0.20	0.53 ± 0.06	0.28 ± 0.03
338	PSZ1 G096.89+24.17	0.302	23	958 ± 127	0.44 ± 0.15	0.45 ± 0.04	0.32 ± 0.03
357	PSZ1 G099.84+58.45	0.616	12	724 ± 143	0.16 ± 0.08	0.68 ± 0.06	0.39 ± 0.04
375	PSZ1 G103.94+25.81	0.077	17	630 ± 100	0.16 ± 0.07	0.16 ± 0.02	0.12 ± 0.01
377	PSZ1 G104.78+40.45	0.837	10	875 ± 193	0.23 ± 0.13	0.57 ± 0.06	0.20 ± 0.02
382	PSZ1 G106.07–17.42	0.818	9	672 ± 158	0.11 ± 0.07	0.78 ± 0.09	0.26 ± 0.03
394	PSZ1 G108.18–11.53	0.334	17	895 ± 143	0.35 ± 0.15	0.77 ± 0.07	0.59 ± 0.05
395	PSZ1 G108.26+48.66	0.671	29	994 ± 114	0.39 ± 0.12	0.53 ± 0.05	0.21 ± 0.02
426	PSZ1 G115.70+17.51	0.363	11	1389 ± 289	1.08 ± 0.58	0.73 ± 0.07	0.48 ± 0.04
430	PSZ1 G117.29+13.44	0.466	31	1032 ± 114	0.49 ± 0.14	0.64 ± 0.08	0.28 ± 0.03
432	PSZ1 G118.06+31.10	0.195	15	509 ± 87	0.08 ± 0.04	0.46 ± 0.04	0.34 ± 0.03
450	PSZ1 G123.39+30.62	0.199	9	710 ± 167	0.19 ± 0.12	0.43 ± 0.06	0.27 ± 0.04
451	PSZ1 G123.55–10.34	0.106	30	866 ± 97	0.39 ± 0.11	0.39 ± 0.04	0.31 ± 0.03
458	PSZ1 G125.54–56.25	0.169	12	506 ± 100	0.08 ± 0.04	0.42 ± 0.05	0.28 ± 0.03
464	PSZ1 G127.02+26.21	0.577	13	1161 ± 218	0.59 ± 0.29	0.74 ± 0.08	0.32 ± 0.04
471	PSZ1 G130.15–17.01	0.211	20	987 ± 142	0.50 ± 0.19	0.46 ± 0.05	0.31 ± 0.04
479	PSZ1 G134.31–06.57	0.333	20	1022 ± 147	0.51 ± 0.19	0.67 ± 0.07	0.40 ± 0.04
503	PSZ1 G139.61+24.20	0.266	22	1007 ± 137	0.52 ± 0.18	0.72 ± 0.05	0.62 ± 0.04
508	PSZ1 G141.73+14.22	0.819	20	1347 ± 194	0.78 ± 0.29	0.76 ± 0.09	0.27 ± 0.03
554	PSZ1 G158.34–47.49	0.311	8	898 ± 228	0.33 ± 0.21	0.60 ± 0.08	0.33 ± 0.04
590	PSZ1 G171.01+15.93	0.281	20	951 ± 137	0.44 ± 0.17	0.58 ± 0.06	0.34 ± 0.04
591	PSZ1 G171.96–40.64	0.271	16	1764 ± 291	2.27 ± 0.98	1.12 ± 0.06	0.96 ± 0.05
595	PSZ1 G172.93+21.31	0.336	17	1087 ± 173	0.60 ± 0.25	0.63 ± 0.07	0.45 ± 0.05
630	PSZ1 G186.81+07.31	0.221	20	753 ± 109	0.24 ± 0.09	0.61 ± 0.05	0.46 ± 0.04
645	PSZ1 G191.05+12.85	0.088	15	566 ± 97	0.12 ± 0.05	0.29 ± 0.04	0.21 ± 0.03
673	PSZ1 G204.07+16.51	0.121	22	866 ± 118	0.38 ± 0.13	0.41 ± 0.04	0.33 ± 0.03
675	PSZ1 G204.73+15.85	0.347	19	1114 ± 166	0.64 ± 0.25	0.66 ± 0.07	0.43 ± 0.04
682	PSZ1 G206.45+13.89	0.406	57	1319 ± 97	1.01 ± 0.19	0.76 ± 0.07	0.50 ± 0.05
723	PSZ1 G218.54+13.26	0.266	17	870 ± 138	0.34 ± 0.14	0.58 ± 0.06	0.34 ± 0.04
748	PSZ1 G224.45+05.25	0.067	17	769 ± 122	0.28 ± 0.12	0.23 ± 0.02	0.17 ± 0.02

Table 5.1: continued from previous page

Planck ID	*Planck* NAME	z	N_{gal}	σ_{200} (km/s)	M_{500}^{dyn} ($10^{15}\mathrm{M}_{\odot}$)	M_{500}^{SZ} ($10^{15}\mathrm{M}_{\odot}$)	M_{500}^{SZcor} ($10^{15}\mathrm{M}_{\odot}$)
752	PSZ1 G224.82+13.62	0.274	28	861 ± 101	0.34 ± 0.11	0.59 ± 0.06	0.38 ± 0.04
786	PSZ1 G234.12+10.45	0.294	29	1353 ± 155	1.14 ± 0.34	0.52 ± 0.06	0.29 ± 0.03

5.3.2 Archival data from SDSS

In order to improve the precision of the cosmological parameters estimation it is crucial to constrain the value of the mass bias as small an error as possible. In fact, as described in section 1.4.2.1, the value of the mass bias not only affects the posterior probability distribution in the (σ_8, Ω_m) space, but its uncertainty is also reflected in the width of the probability distribution itself.

On one hand, mass measurements need to be very precise. Unfortunately, though, the only way to reduce the error in the dynamical mass estimate is to observe a large number of clusters members. Observing about 100 galaxy members per cluster, however, is very expensive from the point of view of the telescope time (and data reduction). On the other hand, a large number of GCs is very helpful, because the error on the parameter scales with the square root of the number of objects.

Archival data are very useful for this purpose, especially very large surveys. We decided to enlarge our GCs catalogue by searching in the SDSS Data Release 14 (Aihara et al. 2011). For each of the 391 PSZ1 objets within the SDSS footprint, we retrieved all spectroscopic redshifts within $15'$ radius around the nominal *Planck* coordinates. Eighty-one point one percent of these sources has already been validated, mainly with X-ray observations. In these cases, we analysed each catalogue in the same way we treated the clusters of the optical follow-up, as described in section 3.1.1. We used the position of the brightest galaxy in the radial velocities catalogue as the cluster centre, within a range of $\pm 2500\,\mathrm{km\,s^{-1}}$ around the *Planck* validation redshift. In most cases, this position corresponded to the BCG galaxy, but sometimes it did not. In these events, after a visual inspection of SDSS RGB images, we selected the centre as the position of a clear BCG (not observed spectroscopically), or we used the cluster members mean coordinates as the centre. We restricted our SDSS sample only to the 146 SZ sources showing one clear optical counterpart at the same redshift as the validation counterpart, and within $5'$ from the *Planck* pointing. Although these prescriptions allowed us to use only 37.3% of the PSZ1 clusters within the SDSS archive, these restrictions guaranteed a clean GC SDSS sample. A detailed and systematic study of the optical counterparts

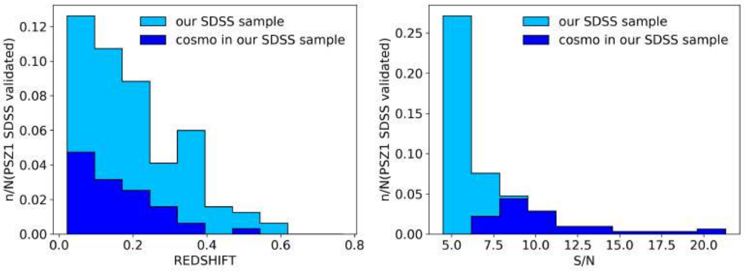

Figure 5.4: Number of SDSS clusters as function of the redshift (left panel) and SZ S/N (right panel) used in this work and normalised to the total number of PSZ1 sources within the SDSS footprint (light blue). Dark blue shows the histograms for the subsample of SDSS clusters within the *Planck* cosmological sample.

of previously validated clusters of PSZ1 catalogue is not the aim of this thesis. The SDSS-selected sample doubled the size of our original sample.

In figure 5.4, we show the number of GCs in our SDSS sample (light blue), normalised to the total PSZ1 clusters within the SDSS footprint, as a function of the redshift (left panel) and of the S/N (right panel). The number of *Planck cosmological sample* (hereafter, PlCS) clusters contained in our SDSS sample is plotted in dark blue. We can observe that the majority of the selected clusters are low redshift and low S/N systems. In fact, the median redshift and S/N are 0.17 and 5.74, respectively. It is also interesting to note that although the validated PSZ1 clusters comprised in SDSS are 25.8%, only 18.6% are in the PlCS. However, 42 (28.8 %) of the 146 SDSS clusters that we selected are part of the PlCS, with a median redshift equal to 0.11 and median S/N of 9.39. Using this sample of SDSS-selected clusters, we can also test how good our SZ mass estimate is with respect to the one obtained by the *Planck* Collaboration. In figure 5.5, we show the very good agreement between our mass estimation and the one retrieved from the PSZ1 union catalogue, for the cosmological subsample (red points) as well.

In Table 5.2 we list the dynamical and SZ masses for the 147 clusters selected from the SDSS sample. The first three columns list the index number, the name of each cluster in the PSZ1 catalogue and the alternative names of each clusters, respectively. The last seven columns are the same as in table 5.1.

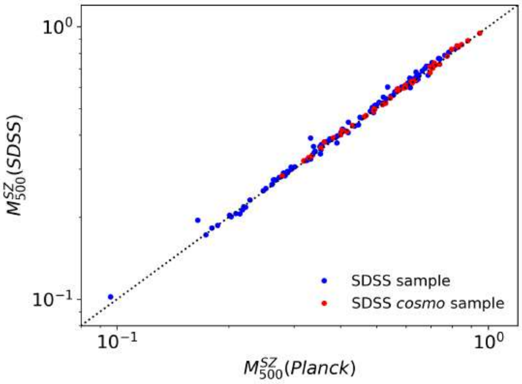

Figure 5.5: Comparison between the SZ masses taken from the PSZ1 union catalogue, $M_{500}^{SZ}(Planck)$ and mass estimated by using prescriptions presented in section 5.1.3, $M_{500}^{SZ}(this\ work)$, for the whole SDSS sample (blue dots) and for the SDSS cosmo sample (red dots).

Table 5.2: Properties of the SDSS sample GCs.

Planck ID	*Planck*NAME	Alt NAME	z	N_{gal}	σ_{200} (km/s)	M_{500}^{dyn} (10^{15}M$_\odot$)	M_{500}^{SZ} (10^{15}M$_\odot$)	M_{500}^{SZcor} (10^{15}M$_\odot$)
35	PSZ1 G012.79+49.68	RXC J1523.0+0836; A2063	0.035	77	786 ± 46	0.32 ± 0.05	0.20 ± 0.02	0.16 ± 0.01
53	PSZ1 G021.09+38.01	WHL J244.011+7.864	0.385	18	865 ± 133	0.31 ± 0.13	0.64 ± 0.07	0.38 ± 0.04
73	PSZ1 G028.66+50.16	RXC J1540.1+1752	0.091	53	780 ± 60	0.30 ± 0.06	0.31 ± 0.03	0.23 ± 0.02
81	PSZ1 G030.91+34.36	ACO 2224	0.186	13	970 ± 182	0.47 ± 0.23	0.42 ± 0.05	0.30 ± 0.03
86	PSZ1 G031.91+67.94	–	0.134	23	770 ± 102	0.27 ± 0.09	0.38 ± 0.04	0.28 ± 0.03
87	PSZ1 G031.94+78.71	RXC J1341.8+2622; A1775	0.073	98	1257 ± 61	1.10 ± 0.13	0.29 ± 0.02	0.26 ± 0.02
89	PSZ1 G032.31+37.06	WHL J248.764+15.48	0.476	7	753 ± 208	0.18 ± 0.13	0.64 ± 0.08	0.28 ± 0.03
113	PSZ1 G040.63+77.13	RXC J1349.3+2806; A1800	0.076	66	729 ± 48	0.25 ± 0.04	0.33 ± 0.02	0.29 ± 0.02
118	PSZ1 G042.53+35.14	WHL J253.734+22.63	0.180	8	893 ± 226	0.35 ± 0.23	0.41 ± 0.05	0.28 ± 0.03
120	PSZ1 G042.85+56.63	RXC J1522.4+2742; A2065	0.073	135	1233 ± 43	1.05 ± 0.08	0.43 ± 0.02	0.39 ± 0.02
122	PSZ1 G044.24+48.66	RXC J1558.3+2713; A2142	0.090	167	959 ± 24	0.53 ± 0.02	0.89 ± 0.03	0.80 ± 0.02
129	PSZ1 G045.07+67.80	ACO 1929	0.221	7	863 ± 238	0.31 ± 0.22	0.48 ± 0.06	0.33 ± 0.04
142	PSZ1 G046.98+66.62	–	0.340	8	1232 ± 312	0.76 ± 0.49	0.54 ± 0.07	0.30 ± 0.04
147	PSZ1 G048.08+57.17	RXC J1521.2+3038; A2061	0.078	112	706 ± 30	0.23 ± 0.02	0.39 ± 0.02	0.35 ± 0.02
153	PSZ1 G049.22+30.84	RXC J1720.1+2637; RXJ1720.1+2638	0.160	29	522 ± 60	0.10 ± 0.03	0.64 ± 0.03	0.57 ± 0.03
154	PSZ1 G049.35+44.36	RXC J1620.5+2953; A2175	0.096	74	792 ± 48	0.31 ± 0.05	0.40 ± 0.03	0.33 ± 0.03
160	PSZ1 G050.41+31.18	RXC J1720.1+2740; A2259	0.160	18	1048 ± 161	0.61 ± 0.24	0.41 ± 0.04	0.30 ± 0.03
166	PSZ1 G053.52+59.52	RXC J1510.1+3330; A2034	0.114	75	1116 ± 67	0.78 ± 0.12	0.50 ± 0.03	0.45 ± 0.03
167	PSZ1 G053.53–29.80	RXC J2113.8+0233; IC 1365	0.048	7	720 ± 199	0.21 ± 0.15	0.17 ± 0.02	0.13 ± 0.02
173	PSZ1 G054.99+53.42	RXC J1539.7+3424; A2111	0.227	11	792 ± 165	0.26 ± 0.14	0.56 ± 0.05	0.42 ± 0.04
174	PSZ1 G055.58+31.87	RXC J1722.4+3208; A2261	0.227	13	1244 ± 233	0.90 ± 0.44	0.73 ± 0.05	0.65 ± 0.04
180	PSZ1 G056.79+36.30	RXC J1702.7+3403; A2244	0.099	89	1055 ± 55	0.68 ± 0.09	0.42 ± 0.02	0.38 ± 0.02
185	PSZ1 G057.63+34.92	RXC J1709.8+3426; A2249	0.085	98	1012 ± 49	0.61 ± 0.07	0.38 ± 0.02	0.34 ± 0.02
187	PSZ1 G057.84+87.98	RXC J1259.7+2756; Coma	0.023	205	1021 ± 15	0.65 ± 0.00	0.52 ± 0.01	0.47 ± 0.01
195	PSZ1 G059.20+32.92	WHL J260.275+35.32	0.389	9	1010 ± 238	0.44 ± 0.27	0.60 ± 0.06	0.32 ± 0.03
206	PSZ1 G062.48–46.45	RXC J2223.8-0138; A2440	0.090	9	971 ± 229	0.48 ± 0.29	0.32 ± 0.03	0.28 ± 0.02
207	PSZ1 G062.94+43.69	RXC J1628.6+3932; A2199	0.031	106	852 ± 38	0.40 ± 0.04	0.28 ± 0.01	0.26 ± 0.01
222	PSZ1 G066.79+68.47	RXC J1421.6+3717; A1902	0.162	16	1250 ± 207	0.96 ± 0.42	0.37 ± 0.04	0.25 ± 0.03
224	PSZ1 G067.19+67.44	RXC J1426.0+3749; A1914	0.166	26	753 ± 92	0.25 ± 0.08	0.68 ± 0.03	0.61 ± 0.03
228	PSZ1 G068.32+81.81	RXC J1322.8+3138	0.314	20	1193 ± 172	0.78 ± 0.30	0.69 ± 0.05	0.56 ± 0.04
229	PSZ1 G068.59–46.56	RXC J2235.6+0128; A2457	0.058	25	751 ± 94	0.27 ± 0.09	0.20 ± 0.02	0.15 ± 0.01
232	PSZ1 G070.09–31.79	RXC J2155.6+1232; A2396	0.191	12	1176 ± 232	0.78 ± 0.40	0.49 ± 0.04	0.37 ± 0.03
236	PSZ1 G071.44+59.57	RXC J1501.3+4220; ZwCl7215	0.292	12	1055 ± 208	0.55 ± 0.28	0.53 ± 0.05	0.34 ± 0.03
247	PSZ1 G073.85–54.94	RXC J2308.3-0211; A2537	0.299	13	1055 ± 198	0.55 ± 0.27	0.64 ± 0.06	0.46 ± 0.04
248	PSZ1 G073.98–27.83	RXC J2153.5+1741; A2390	0.231	8	913 ± 231	0.36 ± 0.24	0.95 ± 0.04	0.84 ± 0.04
256	PSZ1 G077.89–26.62	RXC J2200.8+2058; A2409	0.145	20	989 ± 143	0.53 ± 0.20	0.55 ± 0.03	0.49 ± 0.03
263	PSZ1 G080.16+57.63	ACO 2018	0.088	56	601 ± 45	0.15 ± 0.03	0.25 ± 0.02	0.20 ± 0.02
265	PSZ1 G080.41–33.24	RXC J2226.0+1722; A2443	0.110	14	708 ± 127	0.21 ± 0.10	0.37 ± 0.03	0.29 ± 0.03
269	PSZ1 G081.16–41.92	RXC J2250.3+1054; A2495	0.080	15	595 ± 102	0.14 ± 0.06	0.29 ± 0.03	0.22 ± 0.02
270	PSZ1 G081.29–68.54	RXC J2354.2-1024; A2670	0.076	110	843 ± 36	0.37 ± 0.04	0.29 ± 0.02	0.24 ± 0.02
274	PSZ1 G083.12+66.58	RXC J1413.7+4339; A1885	0.090	27	691 ± 83	0.21 ± 0.07	0.21 ± 0.03	0.16 ± 0.02
275	PSZ1 G083.30–31.01	RXC J2228.6+2036; RXJ2228.6+2037	0.412	24	1171 ± 151	0.71 ± 0.24	0.81 ± 0.06	0.63 ± 0.05
277	PSZ1 G083.62+85.08	RXC J1305.9+3054; A1677	0.184	28	741 ± 87	0.24 ± 0.07	0.54 ± 0.04	0.43 ± 0.04
287	PSZ1 G084.84+35.04	RXC J1718.1+5639; Zw 1717.9+5636	0.113	29	630 ± 72	0.16 ± 0.05	0.29 ± 0.03	0.23 ± 0.02
290	PSZ1 G085.85+35.45	RXC J1715.3+5724; NGC 6338 i)	0.029	47	566 ± 48	0.13 ± 0.03	0.10 ± 0.01	0.08 ± 0.01
294	PSZ1 G086.53–26.66	RXC J2226.8+2550; A2445	0.166	26	830 ± 102	0.33 ± 0.11	0.36 ± 0.04	0.23 ± 0.03

Table 5.2: continued from previous page

Planck ID	*Planck*NAME	Alt NAME	z	N_{gal}	σ_{200} (km/s)	M_{500}^{dyn} (10^{15}M$_{\odot}$)	M_{500}^{SZ} (10^{15}M$_{\odot}$)	M_{500}^{SZcor} (10^{15}M$_{\odot}$)
297	PSZ1 G087.03–57.37	RXC J2337.6+0016; A2631; ACTJ2337.6+0016	0.276	13	852 ± 160	0.31 ± 0.15	0.71 ± 0.05	0.58 ± 0.04
304	PSZ1 G089.79–39.53	RXC J2307.0+1631	0.250	7	1147 ± 317	0.65 ± 0.46	0.60 ± 0.06	0.41 ± 0.04
319	PSZ1 G092.67+73.44	RXC J1335.3+4059; A1763	0.232	22	1529 ± 208	1.62 ± 0.58	0.84 ± 0.04	0.75 ± 0.04
322	PSZ1 G093.44–43.21	RXC J2324.3+1439; A2593	0.041	95	659 ± 33	0.20 ± 0.02	0.21 ± 0.02	0.16 ± 0.02
323	PSZ1 G093.84–38.80	RXC J2317.1+1841; A2572a	0.039	18	562 ± 86	0.12 ± 0.05	0.21 ± 0.02	0.16 ± 0.02
325	PSZ1 G093.93+34.92	RXC J1712.7+6403; A2255	0.080	164	1193 ± 31	0.96 ± 0.05	0.52 ± 0.02	0.47 ± 0.02
339	PSZ1 G097.04–53.67	RXC J2350.8+0609; A2665	0.056	31	706 ± 78	0.23 ± 0.07	0.20 ± 0.02	0.15 ± 0.02
345	PSZ1 G098.24–41.15	WHL J353.600+17.98	0.434	22	813 ± 111	0.26 ± 0.09	0.77 ± 0.08	0.45 ± 0.05
353	PSZ1 G099.48+55.62	RXC J1428.4+5652; A1925	0.106	54	695 ± 53	0.22 ± 0.04	0.30 ± 0.02	0.26 ± 0.02
355	PSZ1 G099.63–58.64	RXC J0003.8+0203; A2700	0.095	27	815 ± 98	0.33 ± 0.10	0.27 ± 0.03	0.21 ± 0.02
364	PSZ1 G101.52–29.96	WHL J351.609+29.36	0.227	18	950 ± 146	0.45 ± 0.18	0.58 ± 0.05	0.44 ± 0.04
379	PSZ1 G105.36–50.41	RXC J0006.3+1052; ZwCl15	0.166	30	728 ± 82	0.23 ± 0.07	0.39 ± 0.05	0.25 ± 0.03
380	PSZ1 G105.51+77.20	RXC J1311.1+3913; A1691	0.072	74	780 ± 47	0.30 ± 0.05	0.23 ± 0.02	0.18 ± 0.02
384	PSZ1 G106.41+50.81	RXC J1425.3+6311; A1918	0.140	24	858 ± 111	0.36 ± 0.12	0.27 ± 0.03	0.21 ± 0.02
399	PSZ1 G109.14–28.02	WHL J358.303+33.26	0.457	13	1380 ± 259	1.02 ± 0.50	0.83 ± 0.07	0.60 ± 0.05
403	PSZ1 G109.99+52.87	RXC J1359.8+6231; Zw 1358.1+6245	0.328	7	701 ± 193	0.16 ± 0.11	0.50 ± 0.05	0.36 ± 0.03
404	PSZ1 G110.08–70.23	RXC J0033.8-0750; A56; WHL J8.47143-7.869	0.305	10	1464 ± 323	1.28 ± 0.73	0.64 ± 0.06	0.42 ± 0.04
409	PSZ1 G111.74+70.35	RXC J1313.1+4616; A1697	0.181	30	651 ± 73	0.17 ± 0.05	0.41 ± 0.04	0.29 ± 0.03
410	PSZ1 G112.38–32.88	RXC J0010.8+2909; WHL J2.71414+29.16	0.329	28	1217 ± 143	0.83 ± 0.26	0.58 ± 0.07	0.32 ± 0.04
411	PSZ1 G112.48+57.02	RXC J1336.1+5912; A1767	0.070	105	868 ± 39	0.41 ± 0.05	0.32 ± 0.02	0.29 ± 0.01
414	PSZ1 G113.26–29.69	RXC J0011.7+3225; A0007	0.103	40	1024 ± 96	0.61 ± 0.15	0.33 ± 0.03	0.26 ± 0.03
417	PSZ1 G114.29+64.91	RXC J1315.1+5149; A1703	0.274	17	1193 ± 190	0.80 ± 0.33	0.60 ± 0.05	0.49 ± 0.04
419	PSZ1 G114.78–33.72	RXC J0020.6+2840; A0021	0.095	36	889 ± 89	0.42 ± 0.11	0.39 ± 0.03	0.34 ± 0.03
422	PSZ1 G114.99+70.36	RXC J1306.9+4633; A1682	0.225	29	789 ± 90	0.28 ± 0.08	0.63 ± 0.04	0.56 ± 0.04
423	PSZ1 G115.20–72.07	RXC J0041.8-0918; A0085	0.056	103	820 ± 38	0.35 ± 0.04	0.49 ± 0.02	0.44 ± 0.02
427	PSZ1 G116.48–44.47	RXC J0032.1+1808; WHL J8.03426+18.10	0.374	30	1040 ± 117	0.53 ± 0.16	0.76 ± 0.07	0.45 ± 0.04
429	PSZ1 G116.90–53.55	RXC J0037.0+0909; A68	0.253	8	1368 ± 347	1.06 ± 0.69	0.63 ± 0.06	0.45 ± 0.04
438	PSZ1 G118.88+52.40	RXC J1314.4+6434; A1704	0.217	13	996 ± 187	0.50 ± 0.24	0.40 ± 0.04	0.28 ± 0.03
447	PSZ1 G121.75+51.81	ZwCl 1256.1+6537	0.233	20	765 ± 110	0.25 ± 0.09	0.39 ± 0.04	0.24 ± 0.03
448	PSZ1 G122.98–35.52	RXC J0051.6+2720; WHL J12.9109+27.33	0.358	22	1102 ± 150	0.62 ± 0.22	0.68 ± 0.07	0.36 ± 0.04
454	PSZ1 G124.20–36.47	RXC J0055.9+2622; A115	0.192	26	905 ± 111	0.41 ± 0.13	0.72 ± 0.04	0.65 ± 0.04
459	PSZ1 G125.68–64.12	RXC J0056.3-0112; A0119	0.044	77	935 ± 55	0.50 ± 0.08	0.33 ± 0.02	0.30 ± 0.02
460	PSZ1 G125.72+53.87	RXC J1236.9+6311; A1576	0.298	25	1108 ± 139	0.66 ± 0.22	0.61 ± 0.04	0.52 ± 0.04
463	PSZ1 G126.65–72.86	ACO 117	0.055	65	581 ± 39	0.14 ± 0.02	0.22 ± 0.02	0.16 ± 0.02
480	PSZ1 G134.59+53.41	WHL J177.705+62.33	0.347	17	1032 ± 164	0.51 ± 0.21	0.53 ± 0.06	0.31 ± 0.03
482	PSZ1 G134.73+48.89	RXC J1133.2+6622; A1302	0.115	68	711 ± 46	0.23 ± 0.04	0.36 ± 0.03	0.31 ± 0.02
486	PSZ1 G135.12+57.90	RXC J1201.9+5802; A1446	0.103	61	762 ± 53	0.28 ± 0.05	0.26 ± 0.03	0.21 ± 0.02
494	PSZ1 G136.90–53.31	RXC J0125.0+0841; A193	0.048	7	633 ± 175	0.15 ± 0.10	0.18 ± 0.02	0.14 ± 0.02
495	PSZ1 G136.94+59.46	RXC J1200.3+5613; A1436	0.065	85	701 ± 38	0.23 ± 0.03	0.19 ± 0.02	0.15 ± 0.02
500	PSZ1 G138.35–39.80	RXC J0142.0+2131; RXJ0142.0+2131	0.279	38	1212 ± 117	0.86 ± 0.22	0.62 ± 0.07	0.37 ± 0.04
502	PSZ1 G139.17+56.37	RXC J1142.5+5832; A1351	0.326	15	1296 ± 223	0.95 ± 0.43	0.73 ± 0.05	0.63 ± 0.04
510	PSZ1 G142.18–53.27	ACO 220	0.372	8	737 ± 187	0.19 ± 0.12	0.70 ± 0.09	0.37 ± 0.05
520	PSZ1 G145.68+59.31	ACO 1294	0.346	28	1092 ± 128	0.62 ± 0.19	0.53 ± 0.06	0.31 ± 0.04
528	PSZ1 G147.86+53.24	SL J1057.5+5759	0.601	12	1603 ± 316	1.37 ± 0.70	0.65 ± 0.08	0.26 ± 0.03
530	PSZ1 G149.21+54.17	RXC J1058.4+5647; A1132	0.136	42	757 ± 69	0.27 ± 0.06	0.62 ± 0.03	0.56 ± 0.03
535	PSZ1 G150.56+58.32	RXC J1115.2+5320	0.466	21	963 ± 135	0.40 ± 0.15	0.83 ± 0.06	0.69 ± 0.05
541	PSZ1 G153.07–58.27	RXC J0152.7+0100; A0267	0.230	28	1091 ± 128	0.66 ± 0.20	0.52 ± 0.06	0.33 ± 0.04

Table 5.2: continued from previous page

Planck ID	*Planck*NAME	Alt NAME	z	N_{gal}	σ_{200} (km/s)	M_{500}^{dyn} (10^{15}M$_\odot$)	M_{500}^{SZ} (10^{15}M$_\odot$)	M_{500}^{SZcor} (10^{15}M$_\odot$)
552	PSZ1 G157.67+77.99	WHL J184.380+36.68	0.367	26	975 ± 120	0.45 ± 0.14	0.67 ± 0.06	0.44 ± 0.04
567	PSZ1 G163.69+53.52	RXC J1022.5+5006; A980	0.156	58	1177 ± 86	0.87 ± 0.17	0.50 ± 0.03	0.44 ± 0.03
571	PSZ1 G164.63+46.37	ZwCl 0934.8+5216	0.342	20	801 ± 116	0.26 ± 0.10	0.56 ± 0.06	0.33 ± 0.04
572	PSZ1 G165.06+54.13	RXC J1023.6+4907; A0990	0.142	41	1092 ± 100	0.71 ± 0.17	0.47 ± 0.03	0.42 ± 0.03
574	PSZ1 G165.41+66.17	WHL J170.907+43.05	0.194	16	680 ± 112	0.18 ± 0.08	0.38 ± 0.04	0.26 ± 0.03
577	PSZ1 G165.99+40.99	ACO 736	0.217	25	774 ± 97	0.26 ± 0.09	0.44 ± 0.05	0.28 ± 0.03
578	PSZ1 G166.11+43.40	RXC J0917.8+5143; A0773	0.219	26	1258 ± 154	0.98 ± 0.32	0.71 ± 0.04	0.63 ± 0.04
581	PSZ1 G167.63–65.57	RXC J0159.8-0850; MCS J0159.8-0849	0.405	9	896 ± 211	0.31 ± 0.19	0.66 ± 0.09	0.32 ± 0.04
583	PSZ1 G168.02–59.95	RXC J0214.6-0433; A329	0.140	33	789 ± 83	0.29 ± 0.08	0.41 ± 0.04	0.32 ± 0.03
584	PSZ1 G168.34+69.73	ACO 1319	0.292	19	934 ± 139	0.41 ± 0.16	0.55 ± 0.05	0.36 ± 0.04
585	PSZ1 G169.64+33.84	WHL J124.192+49.54	0.346	15	889 ± 153	0.34 ± 0.15	0.60 ± 0.08	0.33 ± 0.04
592	PSZ1 G172.57+34.62	RXC J0822.1+4705; A0646	0.127	32	762 ± 82	0.27 ± 0.08	0.32 ± 0.04	0.24 ± 0.03
593	PSZ1 G172.64+65.29	RXC J1111.6+4050; A1190	0.075	79	702 ± 41	0.23 ± 0.03	0.22 ± 0.02	0.16 ± 0.02
594	PSZ1 G172.65+35.16	RXC J0825.5+4707; A0655	0.127	52	712 ± 56	0.23 ± 0.05	0.35 ± 0.04	0.26 ± 0.03
596	PSZ1 G172.97–53.54	ACO 370	0.374	7	1645 ± 454	1.57 ± 1.11	0.79 ± 0.07	0.52 ± 0.05
600	PSZ1 G175.60+35.47	RXC J0828.0+4445; A667	0.145	35	782 ± 80	0.29 ± 0.08	0.35 ± 0.04	0.26 ± 0.03
601	PSZ1 G175.89+24.24	ZwCl 0723.4+4239	0.182	20	766 ± 110	0.26 ± 0.10	0.43 ± 0.05	0.29 ± 0.03
602	PSZ1 G176.25–52.57	RXC J0248.2-0216; A384	0.237	21	773 ± 108	0.26 ± 0.09	0.65 ± 0.05	0.55 ± 0.04
604	PSZ1 G177.64–53.52	RXC J0248.0-0332; A0383	0.190	24	973 ± 125	0.50 ± 0.17	0.44 ± 0.06	0.28 ± 0.04
606	PSZ1 G179.13+60.14	RXC J1040.7+3956; A1068	0.140	23	1462 ± 193	1.53 ± 0.53	0.37 ± 0.03	0.30 ± 0.03
617	PSZ1 G182.55+55.83	RXC J1017.0+3902; A963	0.205	28	1299 ± 152	1.08 ± 0.33	0.59 ± 0.04	0.50 ± 0.03
619	PSZ1 G183.27+34.97	WHL J127.437+38.46	0.390	7	724 ± 200	0.17 ± 0.12	0.61 ± 0.08	0.32 ± 0.04
631	PSZ1 G186.98+38.66	RXC J0850.2+3603; ZwCl1953	0.378	19	1307 ± 194	0.96 ± 0.37	0.76 ± 0.06	0.57 ± 0.05
638	PSZ1 G189.27+59.24	RXC J1031.7+3502; A1033	0.123	41	765 ± 70	0.28 ± 0.07	0.34 ± 0.03	0.27 ± 0.02
647	PSZ1 G192.19+56.12	RXC J1016.3+3338; A961	0.127	34	662 ± 69	0.19 ± 0.05	0.38 ± 0.03	0.33 ± 0.03
657	PSZ1 G197.13+33.46	WHL J128.694+26.97	0.459	7	946 ± 261	0.34 ± 0.24	0.72 ± 0.08	0.34 ± 0.04
680	PSZ1 G205.85+73.77	WHL J174.518+27.97	0.447	13	1184 ± 222	0.68 ± 0.33	0.72 ± 0.07	0.42 ± 0.04
685	PSZ1 G207.87+81.31	RXC J1212.3+2733; A1489	0.354	9	693 ± 163	0.16 ± 0.10	0.73 ± 0.06	0.57 ± 0.05
694	PSZ1 G211.23+38.63	RXC J0911.1+1746	0.503	13	681 ± 128	0.15 ± 0.07	0.63 ± 0.08	0.30 ± 0.04
703	PSZ1 G213.37+80.60	WHL J182.349+26.67	0.559	17	1018 ± 162	0.43 ± 0.18	0.74 ± 0.08	0.32 ± 0.03
715	PSZ1 G216.60+47.00	RXC J0949.8+1707; RX J0949.8+1708	0.391	10	1567 ± 345	1.45 ± 0.83	0.85 ± 0.06	0.72 ± 0.05
724	PSZ1 G218.64+71.31	RXC J1129.8+2347; A1272	0.138	41	627 ± 58	0.16 ± 0.04	0.36 ± 0.04	0.27 ± 0.03
728	PSZ1 G219.13+34.65	RXC J0906.4+1020; A743	0.136	28	662 ± 78	0.18 ± 0.06	0.35 ± 0.04	0.28 ± 0.03
742	PSZ1 G223.51+26.81	RXC J0845.5+0327	0.333	7	1421 ± 392	1.09 ± 0.77	0.59 ± 0.07	0.35 ± 0.04
745	PSZ1 G223.97+69.31	RXC J1123.9+2129; A1246	0.193	22	1029 ± 140	0.57 ± 0.20	0.47 ± 0.05	0.31 ± 0.03
758	PSZ1 G226.19+76.78	RXC J1155.3+2324; A1413	0.139	29	870 ± 100	0.38 ± 0.12	0.60 ± 0.03	0.54 ± 0.03
770	PSZ1 G228.98+58.89	RXC J1047.5+1513; A1095	0.211	13	798 ± 150	0.27 ± 0.13	0.42 ± 0.05	0.27 ± 0.03
773	PSZ1 G229.70+77.97	RXC J1201.3+2306; A1443	0.263	8	982 ± 249	0.43 ± 0.28	0.78 ± 0.05	0.67 ± 0.04
783	PSZ1 G232.84+38.13	ACO 847	0.151	18	778 ± 120	0.27 ± 0.11	0.31 ± 0.04	0.19 ± 0.03
792	PSZ1 G236.51+48.39	–	0.111	26	616 ± 76	0.15 ± 0.05	0.28 ± 0.04	0.21 ± 0.03
800	PSZ1 G238.76+63.22	RXC J1112.9+1326; A1201	0.166	16	584 ± 96	0.12 ± 0.05	0.46 ± 0.04	0.35 ± 0.03
817	PSZ1 G241.80+50.30	ACO 1047	0.155	11	588 ± 122	0.12 ± 0.07	0.39 ± 0.05	0.25 ± 0.03
820	PSZ1 G242.10+43.30	RXC J1013.7-0006; A0954	0.094	37	793 ± 78	0.31 ± 0.08	0.26 ± 0.04	0.19 ± 0.03
824	PSZ1 G243.60+67.74	RXC J1132.8+1428; A1307	0.081	83	806 ± 45	0.33 ± 0.05	0.41 ± 0.02	0.37 ± 0.02
896	PSZ1 G261.89+62.90	WHL J175.299+5.734	0.098	72	708 ± 44	0.23 ± 0.04	0.29 ± 0.03	0.22 ± 0.02
951	PSZ1 G273.54+63.23	RXC J1200.4+0320; A1437	0.134	48	1347 ± 112	1.26 ± 0.28	0.59 ± 0.03	0.53 ± 0.03
980	PSZ1 G282.45+65.18	RXC J1217.6+0339; Zw 1215.1+0400	0.077	113	938 ± 40	0.50 ± 0.05	0.47 ± 0.03	0.43 ± 0.02

Table 5.2: continued from previous page

Planck ID	*Planck*NAME	Alt NAME	z	N_{gal}	σ_{200} (km/s)	M_{500}^{dyn} ($10^{15}\mathrm{M}_\odot$)	M_{500}^{SZ} ($10^{15}\mathrm{M}_\odot$)	$M_{500}^{SZ_{cor}}$ ($10^{15}\mathrm{M}_\odot$)
988	PSZ1 G285.63+72.72	RXC J1230.7+1033; A1553	0.166	18	1020 ± 157	0.56 ± 0.23	0.58 ± 0.04	0.52 ± 0.03
1003	PSZ1 G287.41+81.13	RXC J1241.3+1834; A1589	0.072	104	821 ± 38	0.35 ± 0.04	0.28 ± 0.02	0.24 ± 0.02
1051	PSZ1 G301.08+60.03	RXC J1247.7-0247; A1612	0.183	12	817 ± 161	0.29 ± 0.15	0.45 ± 0.05	0.32 ± 0.03
1078	PSZ1 G306.71+61.04	RXC J1258.6-0145; A1650	0.084	61	728 ± 51	0.25 ± 0.05	0.40 ± 0.03	0.35 ± 0.02
1123	PSZ1 G318.61+58.52	ACO 1729	0.114	11	691 ± 143	0.19 ± 0.10	0.34 ± 0.04	0.26 ± 0.03
1154	PSZ1 G331.13+62.31	RXC J1342.0+0213 ; A1773	0.077	75	772 ± 46	0.29 ± 0.05	0.27 ± 0.03	0.20 ± 0.02
1179	PSZ1 G339.47+63.59	RXC J1353.0+0509; A1809	0.079	90	710 ± 37	0.24 ± 0.03	0.28 ± 0.03	0.22 ± 0.02
1182	PSZ1 G340.37+60.57	RXC J1401.0+0252; A1835	0.251	13	995 ± 187	0.48 ± 0.24	0.86 ± 0.05	0.74 ± 0.04
1227	PSZ1 G359.99+78.04	RXC J1334.1+2013; A1759	0.171	17	923 ± 147	0.43 ± 0.18	0.52 ± 0.04	0.41 ± 0.03

5.4 The $M_{dyn} - M_{SZ}$ scaling relation

In this section, we describe the results of the $M_{500}^{dyn} - M_{500}^{SZ}$ scaling relation using the PSZ1 GC samples described above.

Following the definition given in Planck Collaboration XX (2014), we define the bias of SZ derived masses as

$$M_{500}^{SZ} \equiv (1 - b_{SZ})\, M_{500}^{true}. \tag{5.18}$$

Although in chapter 4 we quantified different physical effects affecting the velocity dispersion and dynamical mass estimations in the low N_{gal} regime, we are not able to correct for all those biases. Indeed, we are unable to estimate the galaxy mass fraction within which cluster members lie because the small amount of data does not allow us to characterise a deep luminosity function for each cluster. For this reason, we define the bias of the dynamical masses as

$$M_{500}^{dyn} \equiv (1 - b_{dyn})\, M_{500}^{true}. \tag{5.19}$$

Combining these two equations we obtain

$$M_{500}^{SZ} = (1 - B)\, M_{500}^{dyn}, \tag{5.20}$$

where the mass bias is defined as the ratio between SZ and dynamical mass biases with $(1 - B) \equiv (1 - b_{SZ}) \,/\, (1 - b_{dyn})$. We fit this relation with a power-law in log-space by using the orthogonal regression method implemented in the python *scipy.odr* package. This method takes into account the uncertainties in both variables and allows us to fix the power to 1.

Figure 5.6 shows the fit for the ITP sample (left panel) and the SDSS sample (blue line in right panel). We find a different mass bias for the two samples:

$$(1 - B)_{ITP} \;\; = 1.28 \pm 0.10; \tag{5.21}$$

$$(1 - B)_{SDSS} = 0.91 \pm 0.03. \tag{5.22}$$

Since the clusters in the two samples were analysed in the same way, this discrepancy cannot be explained by a heterogeneous mass calculation. We ascribe this discrepancy to the different S/N distribution of cluster samples. In fact, the median S/N for the ITP sample is 4.9, whereas the SDSS sample one is 5.7. Moreover, if we divide the SDSS sample in the *cosmo* and *not cosmo* we obtain two samples with median S/N 9.4 and 5.2, respectively. The fit performed with these two new samples, shown in right panel of figure 5.6, yields $(1 - B) = 0.86 \pm 0.05$ (red line) and $(1 - B) = 1.07 \pm 0.05$ (green line) for the *cosmo* and *not cosmo*, respectively.

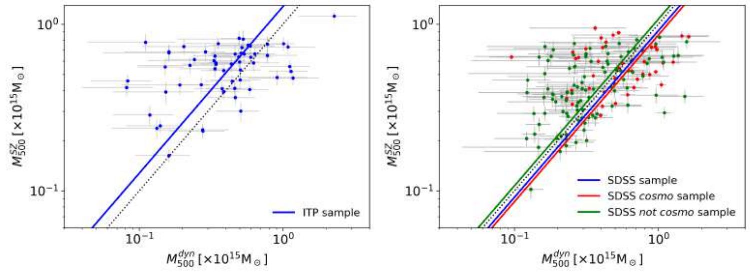

Figure 5.6: $M_{500}^{dyn} - M_{500}^{SZ}$ scaling relation for the ITP (left panel) and SDSS (right panel) samples. Red and green dots represent the SDSS clusters included and excluded in the PlCS, respectively. Red, green and blue lines are the best fit for the SDSS *cosmo*, the SDSS *not cosmo* and the whole SDSS sample, respectively. The differences between these fits point out a hint of Eddington bias contamination.

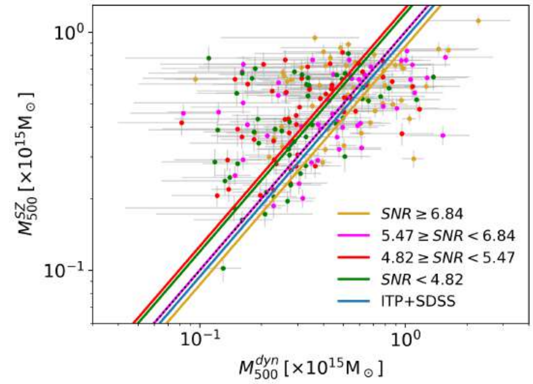

Figure 5.7: Scaling relation $M_{500}^{dyn} - M_{500}^{SZ}$ for the whole sample, ITP+SDSS, used in this thesis (blue line). Green, red, magenta and yellow dots and lines represents the clusters within the four S/N bins: $S/N < 4.82$, 4.82 ≤S/N< 5.47, 5.47 ≤S/N< 6.84 and $S/N \geq 6.84$ and their best fits, respectively.

Table 5.3: Value of the mass bias before and after the Eddigton bias correction for the S/N bins

S/N bin	$(1-B)$	
	Eddington bias not corrected	Eddington bias corrected
$S/N < 4.82$	1.20 ± 0.09	0.73 ± 0.05
$4.82 \leq S/N < 5.47$	1.26 ± 0.07	0.85 ± 0.05
$5.47 \leq S/N < 6.84$	1.00 ± 0.07	0.77 ± 0.05
$S/N \geq 6.84$	0.87 ± 0.05	0.78 ± 0.05

In order to understand the influence of S/N of clusters in the $(1-B)$ fits, we divided the catalogue in 4 S/N bins with the same number of clusters, performing the $M_{dyn} - M_{SZ}$ fit in each bin and for the whole sample. Figure 5.7 shows that the mass bias decreases from lower to higher value of S/N (see Table 5.3). This difference suggests that we might be affected (totally or partially) by Eddington bias.

5.4.1 Eddington bias correction

The whole PSZ1 catalogue contains 1227 SZ sources detected with $S/N \geq 4.5$, but only 189 confirmed GCs were included in the first PlCS (Planck Collaboration XX 2014). These clusters were selected according to their S/N above the threshold of $S/N = 7$. This choice was made in order to achieve a sample affected as little as possible by Eddington bias (Eddington 1913). This effect artificially raises the number of sources just above the survey detection threshold with low S/N objects scattered by the statistical noise. However, as discussed in section 5.3, our sample has median S/N equal to 5.47. Therefore, our cluster sample is dominated by objects whose SZ mass is overestimated because of Eddington bias, as it is shown in figures 5.6 and 5.7 for the ITP and SDSS samples separately and for the whole GCs sample, respectively. van der Burg et al. (2016), in order to correct their sample of 28 low S/N GCs candidates from PSZ2 catalogue, constructed a 30.000 deg^2 mock SZ catalogue by taking into account the Tinker et al. (2008) halo mass function, the redshift-dependent comoving volume element and the *Planck* noise maps properties. They reproduced the effect of the noise on the *true* S/N as a random gaussian variable added to the *true* S/N. They showed that the effect of the bias is more severe the lower the threshold is, becoming extremely important for $S/N \leq 4.5$ (see figure 5.8). Moreover, they found that the effect of the Eddington bias also depends on the redshift, affecting the high redshift clusters more due to the steepness of the halo mass function at a given signal to noise. We corrected the SZ masses by using the curves in van der Burg et al. (2016) (reproduced

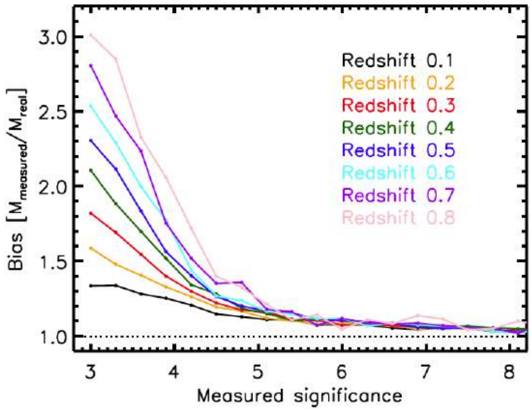

Figure 5.8: Mean fractional difference between the measured mass and the *true* mass of the Planck SZ mass proxy as a function of the measured significance and redshift showing the magnitude of Eddington bias. Figure taken from van der Burg et al. (2016)

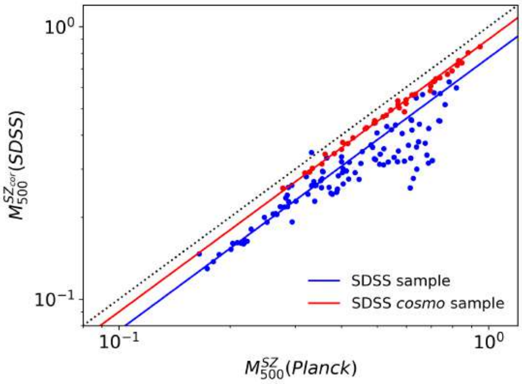

Figure 5.9: Comparison between SZ masses for the whole SDSS clusters (blue and red dots) and for those within the cosmo sample (red dots) after the Eddington bias correction. By comparing with figure 5.5, it is evident that the SDSS cosmo clusters ($S/N \geq 7$) are less biased and, hence, suffer a smaller correction with respect to the SDSS not cosmo clusters. Blue and red lines represent the fit taking into account the whole SDSS sample and the clusters in the cosmo sample, respectively. Dotted line shows the 1:1 relations.

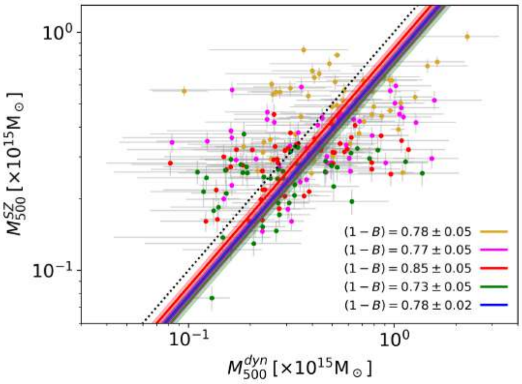

Figure 5.10: Scaling relation $M_{500}^{dyn} - M_{500}^{SZ}$ after Eddington bias correction. Magenta, red, yellow and green dots represent the clusters within the four S/N bins: $S/N < 4.82$, 4.82 ≤S/N< 5.47, 5.47 ≤S/N< 6.84 and $S/N \geq 6.84$, respectively. After correcting for the Eddington bias, performed following the prescriptions by van der Burg et al. (2016), the best fit within S/N bins (magenta, red, yellow and green lines) are now compatible, within the errors, with each other and with respect to the best fit of our whole sample (blue line).

in figure 5.8). Although these curves have been created using the PSZ2 noise maps, we consider them a good approximation of those built for the PSZ1 noise levels, which we will produce in future work. In figure 5.9 we show how the correction affects the mass of the whole SDSS sample (blue and red dots) and the SDSS *cosmo* sample only (red dots) with respect the nominal PSZ1 masses. By comparing figure 5.9 and 5.5, we see that, as expected, the *cosmo* sample is less affected by the correction than the whole SDSS sample. In fact, the $(1-B)$ value considering the corrected mass of the SDSS *cosmo* sample is 0.89, whereas for the whole SDSS sample (see table 5.3), we obtain $(1-B) = 0.78$. In figure 5.10, we show the $M_{500}^{dyn} - M_{500}^{SZ}$ fit for the whole sample (blue line) and for the S/N bins (green, yellow, red and magenta circles and lines) and we see that, after the correction, all the $(1-B)$ values are compatible with each other. As explained above, van der Burg et al. (2016) found that the magnitude of the Eddington bias is redshift-dependent. Therefore, we can test this by analysing the behaviour of the mass bias parameter as function of the redshift. The left panel of Figure 5.11 shows that the uncorrected SZ masses lead to very different values of $(1-B)$. In particular, we see that the highest redshift bin (green dots and line) is the only one that largely differs from the *true* bias value, as expected

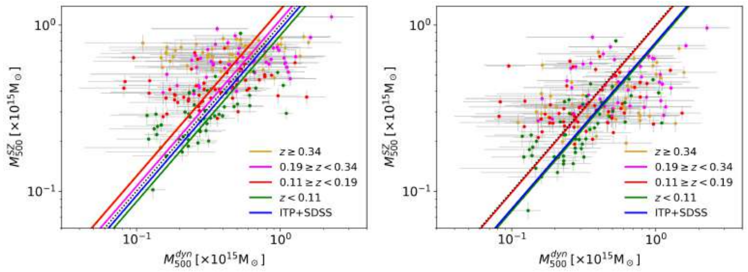

Figure 5.11: Scaling relation $M_{500}^{dyn} - M_{500}^{SZ}$ for 4 different redshift bins, $z < 0.11$ (magenta dot and line), $0.11 \leq z < 0.19$ (red dot and line), $0.19 \leq z < 0.34$ (yellow dot and line) and $z \geq 0.34$ (green dot and line), before (left panel) and after (right panel) the Eddington bias correction. As expected from van der Burg et al. (2016), the high redshift bins are more biased with respect to the low redshift ones.

Table 5.4: Value of the mass bias before and after the Eddigton bias correction for the redshift bins

redshift bin	$(1 - B)$	
	Eddington bias not corrected	Eddington bias corrected
$z < 0.11$	0.86 ± 0.05	0.76 ± 0.04
$0.11 \leq z < 0.19$	1.23 ± 0.11	0.98 ± 0.09
$0.19 \leq z < 0.34$	1.07 ± 0.08	0.77 ± 0.06
$z \geq 0.34$	1.24 ± 0.07	0.77 ± 0.04

from figure 5.8. Instead, $M_{500}^{dyn} - M_{500}^{SZ}$ relations after the M_{500}^{SZ} correction (right panel) show the same value of the $(1 - B)$ for the whole redshift bin. However, the bin containing the clusters at redshift interval [0.11, 0.19] (red dots) yields a relation (red line) that is very different from the other three fits, although it follows the same trend after the Eddington bias correction (see table 5.4).

5.4.2 The mass bias

After the Eddington bias correction by fitting the $M_{500}^{dyn} - M_{500}^{SZ}$ relation for the whole GCs sample, we obtain

$$(1 - B) = 0.78 \pm 0.02. \tag{5.23}$$

However, the *Planck* analysis suggests that the mass bias could be a function of the cluster mass (Planck Collaboration XX 2014). For this reason, we decided to fit a linear scaling relation, in the log-space, using the BCES orthogonal

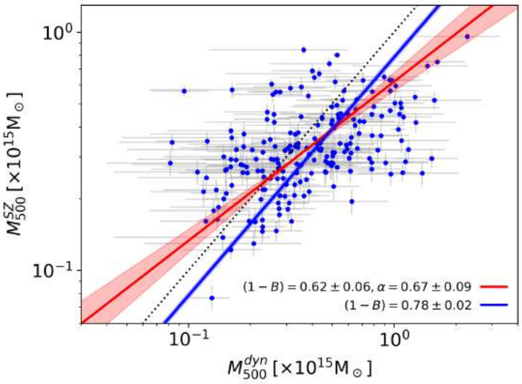

Figure 5.12: Scaling relation between M_{500}^{SZ} and M_{500}^{dyn}. The blue line represents the relation obtained fixing the slope to $\alpha = 1$ (blue line), whereas the red line represents the relation obtained letting the slope free to vary.

method (Akritas & Bershady 1996), obtaining

$$\frac{M_{500}^{SZ}}{10^{15}\ \mathrm{M}_\odot} = (0.62 \pm 0.06) \times \left(\frac{M_{500}^{dyn}}{10^{15}\ \mathrm{M}_\odot}\right)^{0.67\pm0.09}, \tag{5.24}$$

valid in the mass range $[0.08, 3] \times 10^{15}\mathrm{M}_\odot$. This result leads to a mass bias:

$$\frac{M_{500}^{SZ}}{\times 10^{14}\ \mathrm{M}_\odot} = (0.74 \pm 0.04) \times \left(\frac{M_{500}^{dyn}}{6 \times 10^{14}\ \mathrm{M}_\odot}\right)^{0.67\pm0.09}, \tag{5.25}$$

at the pivot mass $6 \times 10^{14}\mathrm{M}_\odot$, which is compatible within 1σ with the one in Eq. 5.23. Figure 5.12 shows the two fits of the $M_{500}^{dyn} - M_{500}^{SZ}$ scaling relation, both with the slope fixed to 1 (blue line) and with the slope free to vary (red line).

5.5 Comparison with other works

In previous sections we discussed the importance of the multi-component nature of GCs and how multi-wavelength studies allow us to assess the biases of observables and mass proxies. In this section, we compare our results with those obtained by other authors using different mass proxies and methodologies.

In table 5.5 and figure 5.13 we summarise all the mass bias values obtained by all the surveys described below.

5.5.1 Mass bias from *Planck* Collaboration analysis

As we described in section 5.1, the *Planck* Collaboration calibrates the SZ masses using X-ray observations of nearby relaxed clusters. For this reason, the mass bias they found is homologous to the Hydrostatic Equilibrium mass bias. They compared the parameter of the $Y_{500} - M_{500}$ relations derived using data from 7 different simulations (Nagai 2006; Yang et al. 2010; Sehgal et al. 2010; Krause et al. 2012; Battaglia et al. 2012; Kay et al. 2012; Sembolini et al. 2013) with respect to the relation found following the process described in section 5.1 to find the value of the mass bias. They found a bias with a strong dependence from the mass, being $(1-b) = \left[1 - b\left(M_{500}^{true}\right)\right]$. This dependence is due to the fact that the slope of each simulation is different from the *Planck* one (Planck Collaboration XX 2014). Assuming that the scaling relation between he observed SZ flux and the observed mass, as well as between the *true* values of Y and M, is a law of power

$$Y_{obs} = A_{obs}\left[M_{500}^{obs}\right]^{\alpha} \tag{5.26}$$

$$Y_{true} = A_{true}\left[M_{500}^{true}\right]^{\beta} \tag{5.27}$$

and, that the observed and the *true* mass are related through the mass bias,

$$M_{500}^{obs} = (1-b)\,M_{500}^{true}. \tag{5.28}$$

thus, they obtained

$$(1-b) = \left[\frac{A_{true}}{A_{obs}}\left(M_{500}^{true}\right)^{\beta-\alpha}\right]^{4/(4\alpha-1)}. \tag{5.29}$$

With these formulas, it is possible to compare the observed relation with any simulated one.

From the comparison with the seven simulations listed above, due to the mass dependence, the *Planck* collaboration decided to assume $(1-b)$ as the median value obtained for a mass pivot point $M_{500} = 6 \times 10^{14} \mathrm{M}_{\odot}$ (Planck Collaboration XX 2014)

$$(1-b) = 0.8^{+0.2}_{-0.1}. \tag{5.30}$$

5.5.2 Bias on dynamical mass estimate

Several groups studied the relation $M^{dyn} - M^{SZ}$ using SZ data from *Planck* PSZ2 catalogue (Amodeo et al. 2017), Atacama Cosmology Telescope (ACT) (Sifón et al. 2016), South Pole Telescope (SPT) (Ruel et al. 2014) and spectroscopic data from the Gemini Multi-Object Spectrograph (GMOS), installed at the Gemini telescopes. Although these three studies compare the SZ and dynamical masses, each one shows important differences with respect to our analysis.

South Pole Telescope cluster sample

The first of these analyses was published by Ruel et al. (2014). Their analysis used 43 SZ selected GCs within SPT catalogues (Vanderlinde et al. 2010; Williamson et al. 2011; Reichardt et al. 2013). The sample consists of massive, $2.7 \leq M_{500}^{SPT} \leq 18.0$ ($\times 10^{14}$ M$_\odot$), clusters at $z \geq 0.3$ and with more than 15 members. The most important differences with respect to our study are the scaling relation between observables and masses. From the SZ point of view, M_{500}^{SPT} were calculated using the $Y - M$ scaling in Reichardt et al. (2013). This relation presents a slightly less steep slope when compared to the one from Planck Collaboration XX (2014). This could results in some difference in the mass estimate, especially for the more massive clusters. From the dynamical point of view, the SPT group used the Saro et al. (2013) relation, which, as shown in Sifón et al. (2016), tends to overestimate the dynamical masses (especially for massive clusters) when compared to the Munari et al. (2013) relation used in this work. Another difference is that, following the prescription in Beers et al. (1990), they used the biweight as the velocity dispersion estimator applied on cluster members selected by an iterative 3σ clipping around the mean velocity. Contrary to what we have done in this work, Ruel and collaborators decided to scale the SZ masses from M_{500}^{SPT} to M_{200}^{SPT}. However, in order to perform this convention, they assumed a NFW profile and the Duffy et al. (2008) mass-concentration relation, in analogy with our methodology. Finally, Ruel et al. (2014) found that

$$exp\left[\left\langle \ln\left(\frac{\mathrm{M}_{200}^{\mathrm{SPT}}}{\mathrm{M}_{200}^{\mathrm{dyn}}}\right)\right\rangle\right] = (1 - B) = 0.72 \pm 0.57, \tag{5.31}$$

which, besides its large error, is compatible with our result.

Atacama Cosmology Telescope cluster sample

The second scaling relation, performed by using dynamical masses, was the one obtained by Sifón et al. (2016). For their cosmological analysis, they used a subsample of ACT clusters composed by 21 objects detected with a $S/N > 5.1$, at redshifts $0.2 \leq z \leq 1.06$, in a mass interval $1.0 < M_{200}^{dyn} < 13.0$, which configure the *cosmological sample*. The 21 GCs were observed spectroscopically using two different spectrographs: GMOS (Hook et al. 2004) at the Gemini-South telescope (Chile) and RSS (Burgh et al. 2003) at the SALT telescope (South Africa) obtaining a median number of observed member $N_{gal} = 55$. In this case, there are fewer differences between our methodology and the one of the ACT group. In fact, they used the same scaling relations $Y_{500} - M_{500}$ and $\sigma_{200} - M_{200}$, the pressure profile by Arnaud et al. (2010) and the AGN fit by Munari et al. (2013). The main difference is regarding the mass-concentration relation used to scale M_{200}^{dyn} to M_{500}^{dyn}. While we used the Duffy et al. (2008) relation, they considered the Dutton & Macciò (2014) one. Aside from the member selection algorithm, they also used the biweight as a velocity dispersion estimator. It is also important to remark that the Sifón's research group applied an aperture correction to the velocity dispersion estimate and also took into account the Eddington bias correcting the Y_{500} estimation as explained in Hasselfield et al. (2013). In this case, the ACT group did not fit the relation M_{dyn} to M_{SZ}, but they defined the mass bias as the ratio between the mean SZ and the mean dynamical mass, obtaining

$$\frac{\langle M_{SZ} \rangle}{\langle M_{dyn} \rangle} = \frac{(1 - b_{SZ})}{\beta_{dyn}} = 1.10 \pm 0.13, \tag{5.32}$$

where β_{dyn} is the bias of dynamical masses defined as $\langle M_{dyn} \rangle = \beta_{dyn} \langle M_{true} \rangle$. The tension between our result (Eq. 5.23) and that obtained by Sifón et al. (2016) is 2.5σ.

Planck PSZ2 sample

The most recent scaling relation published is the one obtained by Amodeo et al. (2017) using 17 low redshift ($z < 0.5$) cluster from the PSZ2 catalogue, in the mass interval $3.0 < M_{200}^{dyn} < 14.0$ and with a median $N_{gal} = 20$. In this case, the SZ masses were estimated following the same prescription considered in this work. However, they selected a different velocity dispersion-mass relation. This choice was dictated by the method used to determine the bias. Similarly to the *Planck* Collaboration, they decided not to compare the masses themselves, but to do the comparison with the $\sigma_{200} - M_{200}$ scaling relation normalisation parameter by assuming the self-similar slope ($\alpha = 1/3$). To do this, they scaled the *Planck* M_{500}^{SZ} to M_{200}^{SZ} assuming the mass-concentration relation by Dutton & Macciò (2014) and fitted the $\sigma_{200}^{obs} - M_{200}^{SZ}$ relation with fixed slope $\alpha = 1/3$; thus obtaining the normalisation parameter $A = 1158 \pm 61$. They compared this result with the Evrard et al. (2008) relation, which was constrained with N-body DM only simulation with normalisation parameter $A_{DM} = 1082.9 \pm 4.0$, obtaining

$$(1-b) = \left(\frac{A_{DM}}{A}\right)^3 b_v^3 \, f_{EB} \, f_{corr} = 0.64 \pm 0.11, \tag{5.33}$$

where b_v, f_{EB} and f_{corr} are the velocity bias, the Eddington bias correction and the correction for the correlated scatter between velocity dispersion and *Planck* masses, respectively. The velocity bias is defined as $b_v = A_{gal}/A_{DM}$, which arises by assuming that the DM and the galaxies of a cluster can have different velocities. Munari et al. (2013), using a hydrodynamical simulation fitted the $\sigma - M$ relation considering both the DM particles and galaxies obtaining two different values for the normalisation parameters, that lead to a velocity bias $b_v = 1.08$. In this thesis, we accounted for the velocity bias using the AGN fit by Munari et al. (2013). Instead, the Evrard et al. (2008) fit was made with DM only simulations. The Eddington bias correction is, in this case, a global correction quantified in $f_{EB} = 0.84 \pm 0.027$ and the correlated scatter correction arises from the Stanek et al. (2010) study on the covariance between observables and estimated using the Millennium Gas Simulation (Hartley et al. 2008). Stanek et al. (2010) found a significant correlation between velocity dispersion and SZ signal due to non-gravitational processes in GCs. Amodeo et al. (2017) quantified this bias as $f_{corr} = 1.01$.

Therefore, comparing the result obtained by Amodeo et al. (2017) (Eq. 5.33) relative to the mass estimation, we detected a mild tension at $\sim 1.25\sigma$

5.5.3 Weak Lensing mass bias

As described in chapter 1, the Weak Lensing (WL) technique studies the distortion of the background galaxies, allowing the modelling of the GCs DM distribution. In this way, by assuming a GC density profile and geometry, it is possible to estimate the cluster mass without any assumption on the dynamical state of the cluster (Bartelmann 2010). There are several research groups that studied the SZ mass bias assuming the WL mass as the *true* mass.

Weighing the Giants project

In 2014, the group of the Weighing the Giants (WtG) project studied the relation between the M_{500}^{SZ} and the M_{500}^{WL} using a sample of 38 GCs in common with the PSZ1 catalogue (von der Linden et al. 2014). For a complete description of the WL mass estimate and for the GCs catalogue used to constrain the scaling relation see Applegate et al. (2014). von der Linden et al. (2014) found, through a bootstrap realisation of the unweighted mean of the ratio between WL and SZ masses, the following value:

$$\left\langle \frac{M_{500}^{SZ}}{M_{500}^{WtG}} \right\rangle = (1-b) = 0.698 \pm 0.062. \tag{5.34}$$

This result is compatible at 1.25σ with our estimation of the mass bias.

A subsample of 22 GCs of the WtG catalogue is part of the PSZ1 PlCS. Repeating the analysis with this subsample only, they obtained

$$(1-b) = 0.688 \pm 0.072. \tag{5.35}$$

This result is smaller than the previous one. However, they are perfectly compatible with each other. This result was used by the *Planck* Collaboration, in its 2015 cosmological analysis, as a prior on the value of the mass bias. The WtG group performed the fit by letting the slope of the power law free to vary. By using the Bayesian linear regression method developed by Kelly (2007), the found

$$\frac{M_{500}^{SZ}}{10^{15}\ \mathrm{M}_{\odot}} = \left(0.699^{+0.059}_{-0.060}\right) \left(\frac{M_{500}^{WtG}}{10^{15}\ \mathrm{M}_{\odot}}\right)^{0.68^{+0.15}_{-0.11}} \tag{5.36}$$

and

$$\frac{M_{500}^{SZ}}{10^{15}\ \mathrm{M}_{\odot}} = \left(0.697^{+0.077}_{-0.095}\right) \left(\frac{M_{500}^{WtG}}{10^{15}\ \mathrm{M}_{\odot}}\right)^{0.76^{+0.39}_{-0.20}}, \tag{5.37}$$

for the whole and the cosmological sample, respectively. Both these results are compatible, within errors, to our fit Eq. 5.24.

Canadian Cluster Comparison Project

Hoekstra et al. (2015) show the comparison between the WL masses, estimated by the Canadian Cluster Comparison Project (CCCP), and the masses from the PSZ1 catalogue of 37 GCs, 20 of them with $S/N \geq 7$. Through a linear fit, they found

$$(1-b) = 0.76 \pm 0.05, \tag{5.38}$$

$$(1-b) = 0.78 \pm 0.07, \tag{5.39}$$

for the whole sample of 37 clusters and for the 20 with $S/N \geq 7$, respectively. These two results are perfectly compatible with our estimation of $(1-b)$.

During the comparison of their results with the ones of WtG, Hoekstra et al. (2015) fitted a power law function to investigate if there was a dependence of the bias with the mass in their data as well. Using the entire sample, they found

$$\frac{M_{500}^{SZ}}{10^{15}\ h_{70}^{-1}\mathrm{M}_{\odot}} = (0.76 \pm 0.04) \times \left(\frac{M_{500}^{CCCP}}{10^{15}\ h_{70}^{-1}\mathrm{M}_{\odot}}\right)^{0.64\pm0.17} . \tag{5.40}$$

The compatibility between the slope obtained by von der Linden et al. (2014), Hoekstra et al. (2015) and this thesis, supports the conclusion by von der Linden et al. (2014) that the bias of *Planck* masses depend on the cluster mass.

Local Cluster Substructure Survey

Smith et al. (2016) analysed the mass bias with a sample of 44 clusters in common with the Local Cluster Substructure Survey (LoCuSS) and the PSZ2 catalogue, obtaining

$$(1-b) = 0.95 \pm 0.04. \tag{5.41}$$

The LoCuSS sample consists of clusters at redshift $0.15 \leq z \leq 0.3$ with WL masses, estimated in Okabe & Smith (2016), between $2.12 \leq M_{200}^{WL} \leq 12.75$ ($10^{14}\mathrm{M}_{\odot}$). In this case, the mass bias is defined as the weighted mean of the logarithmic ratio of SZ and WL masses

$$(1-b) = \exp\left[\frac{\sum_{\mathrm{i=1}}^{\mathrm{n}}\ \omega_{\mathrm{i}}\ \ln\left(\frac{\mathrm{M_{SZ,i}}}{\mathrm{M_{WL,i}}}\right)}{\sum_{\mathrm{i=1}}^{\mathrm{n}}\ \omega_{\mathrm{i}}}\right], \tag{5.42}$$

with weight defined by

$$\omega_i = \left[\left(\frac{\delta M_{SZ,i}}{\langle\delta M_{SZ}\rangle}\right)^2 + \left(\frac{\delta M_{WL}}{\langle\delta M_{WL,i}\rangle}\right)^2\right]^{-1} . \tag{5.43}$$

This LoCuSS measurement is higher than our value of $(1-B) = 0.78 \pm 0.02$. Since no Eddington bias correction is cited neither in Smith et al. (2016), nor in Okabe & Smith (2016), we decided to repeat the fit limiting our sample only to the clusters within the range $0.15 \leq z \leq 0.3$. As a result, we obtained $(1-B) = 0.91 \pm 0.08$. However, this last result could be biased by the clusters within the $0.11 \leq z < 0.19$ (see figure 5.11 and table 5.4).

Canada-France-Hawaii Telescope Stripe 82 Survey

The sample used by Battaglia et al. (2016) to determine the mass bias consists of 19 GCs from the ACT equatorial sample (Hasselfield et al. 2013) observed during the Canada-France-Hawaii Telescope Stripe 82 Survey (CS82). They divided their sample into two S/N bins. The first contains nine clusters with $S/N > 5$, $\langle M_{500}^{SZ} \rangle = 4.7 \pm 1.0 (\times 10^{14}\ \mathrm{M}_{\odot})$, and the second is constituted by 10 clusters within the range $4 < S/N < 5$, with $\langle M_{500}^{SZ} \rangle = 2.7 \pm 1.0 (\times 10^{14}\ \mathrm{M}_{\odot})$. The mass bias they found, defined as the ratio of the mean SZ and WL masses, is

$$(1-b)_{S/N>5} = 0.87 \pm 0.50, \tag{5.44}$$

$$(1-b)_{S/N<5} = 0.82 \pm 0.75, \tag{5.45}$$

For a detailed description of WL mass estimation see Battaglia et al. (2016) and the references therein, and for SZ mass estimates see Hasselfield et al. (2013). It is important to remark that the ACT SZ masses are corrected for Eddington bias as explained in Hasselfield et al. (2013). Furthermore, Battaglia et al. (2016) estimated that, by comparing 31 clusters in common between ACT and *Planck*, the corrected ACT masses are, on average, 0.89 times lower than those of *Planck*. This result is consistent with the one showed in figure 5.9 for the SDSS *cosmo* sample. As we can see, these results are compatible with our estimation of the bias but are not in agreement with the result by Sifón et al. (2016), who used SZ masses from the same catalogue.

PSZ2LenS

Sereno et al. (2017) used 32 clusters from the PSZ2LenS sample with SZ signal published in *Planck* catalogues to estimate the $(1-b)$ parameter. The PSZ2LenS sample consists of 35 galaxy GCs detected by *Planck* and within the sky coverage of the Canada France Hawaii Telescope Lensing Survey (CFHTLenS, Heymans et al. 2012) and the Red Cluster Sequence Lensing Survey (RCSLenS, Hildebrandt et al. 2016). The PSZ2Lens clusters lie in a wide mass range, $M_{500}^{WL} = 0.9 - 14.8 \times 10^{14}\ \mathrm{M}_{\odot}$. SZ masses are taken from *Planck* catalogues (Planck Collaboration XXIX 2014; Planck Collaboration XXVII 2016) and, therefore, calculated as explained in section 5.1. For a detailed description of the WL analysis see Sereno et al. (2017) and references therein. The PSZ2LenS research group, after assuming the Eddington bias correction from Battaglia et al. (2016) and Sereno & Ettori (2015), found

$$\exp\left(\frac{\ln\langle \mathrm{M_{SZ}} \rangle}{\ln\langle \mathrm{M_{WL}} \rangle}\right) = (1-\mathrm{b}) = 0.76 \pm 0.08. \tag{5.46}$$

This value is consistent with our result. They also used a subsample of 15 PSZ2LenS clusters within the *Planck* cosmological sample, finding $(1-b) = 0.67 \pm 0.09$. This result is lower, but it is compatible with our result at 1.2σ.

Cluster Lensing And Supernova survey with Hubble

The WL masses of 21 GCs from the Cluster Lensing And Supernova survey with Hubble (CLASH, Postman et al. 2012)) were used by Penna-Lima et al. (2017) to compare with the respective SZ masses from *Planck* catalogues. They performed a Bayesian analysis to contrain the mass bias $(1-b)$. After the correction of M_{SZ} for Eddington bias from Battaglia et al. (2016), they found

$$(1-b) = 0.73 \pm 0.10, \tag{5.47}$$

which is fully compatible with our result.

HYPER SUPRIME-CAM SUBARU STRATEGIC PROGRAM

Hyper Suprime-Cam Subaru Strategic Program (HSC-SSP, Aihara et al. 2018a,b) group published two studies comparing their WL masses with SZ masses from *Planck* PSZ2 and ACTPol (Atacama Cosmology Telescope Polarimeter experiment). In the first one, Medezinski et al. (2018) used 5 clusters from the HSC-SSP fist year catalogue (Planck Collaboration XXVII 2016) in common with the PSZ2 catalogue. They chose the mean M_{500}^{WL}, defined as the weighted stack of the WL signal of those 5 clusters. The mean SZ mass is the weighted mean of the masses retrieved from the PSZ2 corrected for Eddington bias using the prescription given by Battaglia et al. (2016). The weight for the WL stack and for the SZ mean is the same and depends on the errors on the galaxy shape measurement for each cluster. The ratio of the mean WL and SZ mass is the bias

$$\frac{\langle M_{SZ} \rangle}{\langle M_{WL} \rangle} = (1-b) = 0.80 \pm 0.14, \tag{5.48}$$

which is compatible with our result.

In the second study, Miyatake et al. (2018) used 8 GCs in common with the ACTPol (Hilton et al. 2018) sample. As in the previous analysis, the mean WL mass is the result of the weighted stack of the all clusters taken into account, whereas $\langle M_{500}^{SZ} \rangle$ is the weighted mean of the corrected SZ masses from the ACTPol catalogue. The mass bias for this sample is

$$\frac{\langle M_{SZ} \rangle}{\langle M_{WL} \rangle} = (1-b) = 0.74^{+0.13}_{-0.12}. \tag{5.49}$$

Table 5.5: Summary of mass bias value from the literature

SURVEY	REFERENCE SAMPLE	N. CLUSTERS	(1-b)	reference
X-RAY				
	Planck	189	$0.8^{+0.1}_{-0.2}$	Planck Collaboration XXIX (2014)
VELOCITY DISPERSION				
	SPT	44	0.72 ± 0.57	Ruel et al. (2014)
	ACT	21	1.10 ± 0.13	Sifón et al. (2016)
	*Planck*PSZ2	17	0.64 ± 0.11	Amodeo et al. (2017)
	*Planck*PSZ1	207	0.78 ± 0.02	This work
WEAK LENSING				
WtG	*Planck*	38	0.688 ± 0.072	von der Linden et al. (2014)
CCCP	*Planck*	37	0.76 ± 0.05	Hoekstra et al. (2015)
LoCuSS	*Planck*	44	0.95 ± 0.04	Smith et al. (2016)
CS82	ACT	19	0.87 ± 0.50	Battaglia et al. (2016)
PSZ2LenS	*Planck*	32	0.76 ± 0.08	Sereno et al. (2017)
CLASH	*Planck*	21	0.73 ± 0.10	Penna-Lima et al. (2017)
HSC-SSP	*Planck*	5	0.80 ± 0.15	Medezinski et al. (2018)
HSC-SSP	ACTPol	8	$0.74^{+0.13}_{-012}$	Miyatake et al. (2018)

Also in this case, the value of the mass bias is compatible with respect to that obtained in our analysis.

5.6 Discussion

In this section we briefly discuss the cosmological implications of our mass bias result.

In section 1.4.2.1 we described the importance of the mass bias in order to constrain the cosmological parameters using the galaxy cluster number counts. In fact, this quantity is extremely sensitive to Ω_m and σ_8 through the mass function. However, the cosmological analysis performed by the *Planck* Collaboration results in a tension between the constraints from the primordial CMB power spectrum analysis and those derived from the cluster number counts (Planck Collaboration XX 2014; Planck Collaboration XXIV 2016). The main cause of this tension was originally ascribed to the value of the mass bias. The *Planck* Collaboration, through the joint analysis of SZ, X-rays data and simulations, constrained this parameter to the value of $(1 - b) = 0.8^{+0.2}_{-0.1}$.

The main result of this study is an independent estimation of the mass bias through the comparison of the cluster mass derived using SZ and dynamical mass proxies. In order to do this, we used the largest subsample of PSZ1 clusters (207) observed both in microwave and optical wavelengths. Our result $(1 - B) = 0.78 \pm 0.02$ provides the measurement with the lowest statistical error obtained so far and it is compatible with the *Planck* one. Although we did not perform a cosmological analysis using this result, we are able to draw

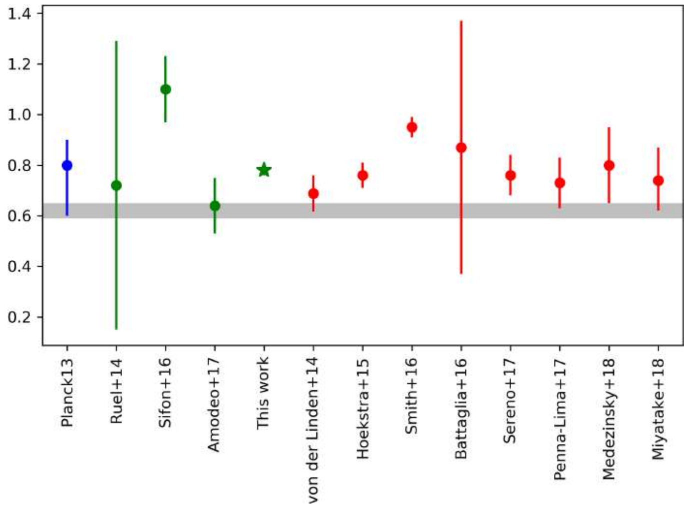

Figure 5.13: Value of $(1-b)$ from previous studies. In blue, the result from Planck Collaboration XX (2014), using a scaling relation from X-ray observations; in green, the mass bias from $M_{dyn}-M_{SZ}$ scaling relations and, in red, those from weak lensing studies, respectively. All these values are listed in table 5.5. The grey shaded region represents the mass bias values that reconcile the tension between CMB and SZ number counts from Planck Collaboration XX (2014). The green star represents the mass bias value found in this work. The error bars are not visible because are smaller than the star.

some qualitative conclusions. In fact, due to the compatibility with respect to the *Planck* Collaboration result, we expect that a full cosmological analysis will lead to a posterior probability in the (Ω_m, σ_8) space that lies in a similar region to the *Planck* Collaboration one (see figure 1.16). The combination of Ω_m and σ_8 estimated by the*Planck* Collaboration is $\sigma_8(\Omega_m/0.27)^{0.3} = 0.764 \pm 0.025$ and $\sigma_8(\Omega_m/0.27)^{0.3} = 0.782 \pm 0.010$ when the mass bias is let free in the interval $[0.7, 1]$ and fixed to $(1-b) = 0.8$, respectively. Due to the very small uncertainty ($\sim 2\%$) on our mass bias estimate, we conclude that by using it as prior we may reduce the error on the combination of Ω_m and σ_8 by a factor of ~ 2. This means that we may have a similar result to the *Planck* Collaboration one with the fixed (1-b). This implies that our result is not able to alleviate the tension between the constraint on Ω_m and σ_8 from CMB and GCs analysis. Moreover, the low statistical uncertainty of our result suggests that the origin of the tension is not ascribed to the determination of the mass bias.

We now discuss possible explanations of this tension:

i. Salvati et al. (2018) demonstrated that the value of the optical depth affects the measure of the $(1-b)$ parameter. Their joint analysis between CMB and cluster number counts show that the decreased value of τ yielded a higher value of the mass bias, $(1-b) = 0.62 \pm 0.07$. Although this result lie at 2.2σ from our value, it is in better agreement than the result of Planck Collaboration XIII (2016). However, this improvement in the compatibility is to be attributed to the error in the their $(1-b)$ estimate. In fact, the Planck Collaboration VI (2018b) analysis constraining the mass bias at $(1-b) = 0.62 \pm 0.03$, confirmed the Salvati et al. (2018) result, but increased the tension with our value. This implies that although the change of optical depth acts in the right direction, it is not enough to explain the tension. Salvati et al. (2018) also performed the joint analysis with CMB, cluster number counts and tSZ power spectrum data. In this case, the mass bias value needed to reconcile the cosmological parameter from CMB and clusters studies, increases up to $(1-b) = 0.63 \pm 0.04$.

ii. Salvati et al. (2018) also proposed that an alternative way to alleviate the tension is to include parameters beyond the ΛCDM model, by using the sum of the neutrino masses as a free parameter. The complete joint analysis gives enlarged contours, with smaller values of σ_8 and higher values of Ω_m. This alleviates the tension in the cosmological parameter estimation, and it is also reflected in a higher value of the mass bias $(1-b) = 0.67 \pm 0.04$, that is at 2.4σ from our result. This discussion is still valid also when we left the slope of the $M_{500}^{SZ} - M_{500}^{dyn}$ relation free to

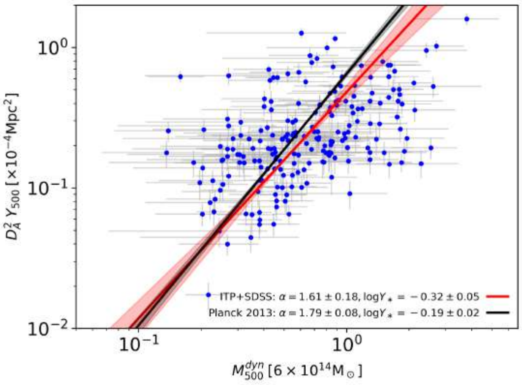

Figure 5.14: Scaling relation $Y_{500} - M_{500}$. The red line represents our fit $\log Y_* = -0.32 \pm 0.05$ and $\alpha = 1.61 \pm 0.18$, obtained by using the dynamical mass M_{500}^{dyn}. The $Y - M$ relation from Planck Collaboration XX (2014) with $\log Y_* = -0.19 \pm 0.02$ and $\alpha = 1.79 \pm 0.08$, is represented in black.

vary. In this case our result is $(1 - B) = 0.74 \pm 0.04$, at the pivot mass of $6 \times 10^{14}\mathrm{M}_\odot$.

iii. Another possible explanation for the tension in the mass bias estimate is given by the relativistic correction of the SZ power spectrum.This correction acts directly on the Y_{SZ}, reducing the signal detected. This also affects the detection algorithms that use this profile to detect the SZ sources within the *Planck* frequency maps. As shown in Remazeilles et al. (2019), this effect could drive the mass bias from the CMB+tSZ analysis to higher values, reconciling it with the results from the cluster number counts study.

iv. The constraints on the mass bias not only affect the estimation of cosmological parameters, but are also useful in order to characterise the physics of GCs. As we described in section 5.5.1, in Planck Collaboration XX (2014) the mass bias rises from the comparison between theoretical (simulated) and observed $Y_{500} - M_{500}$ scaling relations. Following Eq. 5.29, different slopes in the $Y - M$ relations lead to a mass bias that depends on the cluster mass (Planck Collaboration XX 2014).

In section 5.4.2, we show that there is a dependence with the mass in our estimation of $(1 - B)$, with a slope of $\alpha = 0.67$. This fact suggests that the slope of the of the $Y_{500} - M_{500}^{dyn}$ relation should be different from the one used by the *Planck* Collaboration (equation 5.10). In figure 5.14, we show in red the result of our fit, $\log Y_* = -0.32 \pm 0.05$ and $\alpha = 1.61 \pm 0.18$, compared with the *Planck* Collaboration one, $\log Y_* = -0.19 \pm 0.02$ and $\alpha = 1.79 \pm 0.08$, in black. Consequently, we can explain the mass dependence we see in the $M_{500}^{SZ} - M_{500}^{dyn}$ relation with this difference of slope. Moreover, we see that our constraints on the slope of the $Y_{500} - M_{500}$ relation are compatible at 1σ with the ones prescribed by the self similar cluster evolution, $\alpha = 5/3 \sim 1.66$. This result, directly affecting the determination of the SZ cluster mass, could imply a different value of the mass bias and, consequently, of the cosmological parameters. This result suggests a reanalysis of the cluster number counts, which will be performed in future works. However, the method we used to break the $Y_{500} - \theta_{500}$ degeneracy, gives a value of the Compton parameter that is not independent from the $Y_{500} - M_{500}$ relation. For this reason, in order to obtain a completely reliable result an independent estimates of Y_{500} is needed.

These results confirm the power of the dynamical mass to constrain the mass bias and the parameters of scaling relations between observables and cluster mass.

v. The considerations above are only based on the value of the statistical error, without taking into account the error arising from systematics in our determination of $(1 - B)$. However, only when the statistical uncertainty became so small, it is possible to study the effect of systematics in depth. Some of the main sources of systematics are the scaling relations between observables and mass. In the particular case of the dynamical analyses, the scaling relation increases the intrinsic scatter and also reduces the statistical power of huge samples. It would be extremely useful to develop a formalism that allows one to use clusters observable directly to perform cosmological analyses. Moreover, these high levels of precision confirm the importance of multi-wavelength analysis to better understand the physics of galaxy clusters.

6

Conclusions

This thesis had two main objectives: the first one, purely observational, connected with the validation programmes of the PSZ1 catalogue; and a second, related to the cosmological implications of the mass bias.

Optical follow-up

The first part of this thesis presented the results of our systematic optical follow-up of the unconfirmed SZ sources from the *Planck* PSZ1 catalogue in the northern hemisphere ($Dec \geq -15°$). This work was performed during an observational campaign carried out under an International Time Project (ITP programme), lasting from August 2013 to July 2015. The optical follow-up has led to the following results:

- We performed the systematic follow-up of 260 target selected among the PSZ1 sources with $Dec \geq -15°$. For each of them, we acquired images in three different bands: i', $r'$and g'; using the WFC/INT (86 sources in 21 nights) and ACAM/WHT (118 sources in $\sim$ 15 nights), or we retrieved photometrical information from SDSS-DR9 archive data. The purpose of this preliminary step was to obtain a first confirmation of the presence of a GC associated with the SZ source. The study of the colour of likely galaxy members allowed us to estimate the photometric redshift of the cluster. This step was fundamental in discriminating between low and high redshift clusters, which allowed us to perform spectroscopic observations more efficiently.

- We retrieved spectroscopic information for 187 targets. To perform this task, we mainly used the OSIRIS/GTC and DOLORES/TNG spectrographs, for clusters at $z_{phot} \geq 0.4$ and $z_{phot} < 0.4$, respectively. The remaining 37 clusters were observed using ACAM/WHT in long-slit mode. In order to maximise the number of detected cluster members, we decided to perform MOS spectroscopy in both OSIRIS/GTC and DOLORES/TNG spectrographs when this technique was available. In this way, 100 targets were observed, with at least one MOS mask per target. This observational strategy yielded an average of ~ 15 members for each cluster, which allowed us to estimate a reliable velocity dispersion and cluster mass.

- We completed the validation of the PSZ1 catalogue in the northern hemisphere by observing all the 212 non-validated SZ sources, at the time of the publication of the PSZ1 catalogue. We confirmed 88 new GCs; 58 spectroscopically and 30 photometrically.

- We performed the statistical characterisation of the PSZ1 catalogue in the northern hemisphere ($Dec \geq -15°$). We observed a correlation between the number of non-confirmed sources and their signal in the 857 GHz *Planck* map. This thermal emission of galactic dust could explain the high number of non-validated sources at low S/N ($S/N < 5.1$).

- We were able to characterise the purity of the PSZ1 catalogue in the northern hemisphere ($Dec \geq -15°$). The presence of 88 new confirmed clusters is reflected in an increase of the accumulated purity, especially at low S/N, from 72% to 82%.

- Using hydrodynamical simulations, we studied the statistical and physical biases in velocity dispersion and mass estimate in the low number of members regime. To achieve this goal we analysed the response of three velocity dispersion estimators (standard deviation, gapper, and biweight) as a function of the number of clusters. We also studied the effect on the velocity dispersion estimate due to mass selection effects and miss-sampling of R_{200}. This analysis resulted in to the definition of a bias-corrected estimator for velocity dispersion and mass. The leading effect, however, is the presence of interlopers.

Scaling relations

In the second part of this thesis, we used the ITP confirmed clusters to build a reference sample of SZ selected and spectroscopically confirmed GCs in order to constrain the scaling relation between SZ and dynamical masses. In the following list we summarise the results of our study:

- By using the bias-corrected velocity dispersion, we calculated the velocity dispersion and mass of all 65 confirmed clusters with more than 7 cluster members. We, then, removed all the clusters that presented a clear multiple detection or sub-structured clusters, which had not been properly sampled. In this way, the final ITP sample included 61 GCs.

- In order to increase the statistical meaning of our sample, we extended our dynamical analysis to the 402 PSZ1 sources within the SDSS footprint. By retrieving spectroscopic data from the SDSS-DR12 archive we performed cluster identification using the same procedure adopted for the ITP clusters. We restricted the SDSS sample to the 147 clusters clearly associable to those used to validate the PSZ1 sources.

- The union of the ITP and our SDSS samples yielded 208 clusters (61 from ITP sample and 147 from SDSS sample). This sample represents the largest set of SZ selected clusters for which both the SZ and the dynamic masses have been calculated. We used this sample to constrain the parameters of the scaling relation between SZ and dynamical masses. In particular, we found the mass bias to be $(1 - B) = 0.78 \pm 0.02$. This result represents the smallest error bar on $(1 - B)$ so far in the literature. It is compatible with that found by the *Planck* Collaboration in their cosmological analysis (Planck Collaboration XX 2014).

- The dimension of our cluster catalogue allowed us to reduce the uncertainty of the mass bias down to 2.6%. This means that we could reduce the uncertainty of the estimate of the combination of the cosmological parameters σ_8 and Ω_m by a factor of ~ 2. Our results confirmed the tension in the cosmological parameters estimate results of the CMB and GCs analyses. However, the high precision of $(1 - B)$ parameter estimate suggested that the solution of this tension is not a variation of the value of the mass bias.

- We found a dependence of the mass bias with the clusters mass. Indeed, by letting the slope of the $M_{500}^{SZ} - M_{500}^{dyn}$ free, we found $\alpha = 0.67 \pm 0.09$ which is compatible with the results of von der Linden et al. (2014) and Hoekstra et al. (2015). In this case, we found a mass bias at the pivot point of $6 \times 10^{14}\,\mathrm{M}_{\odot}$, of $(1 - B) = 0.74 \pm 0.04$, that is compatible with respect to the previous result.

- The dependence of the $(1-B)$ parameter on the mass suggests that the slope of the $Y_{500}^{SZ}-M_{500}^{dyn}$ relation may differ from that found by the *Planck* Collaboration using X-ray data. We fitted the $Y_{500}^{SZ}-M_{500}^{dyn}$ relation finding $\alpha = 1.61 \pm 0.18$. This result may explain the dependence on the mass of the mass bias. However, it is compatible with both the self similar relation and the *Planck* result, making further studies necessary.

Future perspectives

The work developed in this thesis leads to the opportunity of new projects, both in the study of the physics of galaxy clusters and in the framework of cosmological analysis.

- The *Planck* Collaboration performed its 2013 cosmological analysis using only a subsample of the PSZ1 catalogue composed by 189 clusters with $S/N >= 7$. We intend to complete the work presented in this thesis by performing a cluster counts study using the entire PSZ1-North sample of 628 confirmed GC estimating the σ_8 and Ω_m parameters.

- In this thesis we used the scaling relation $Y_{500}-M_{500}$ constrained by the *Planck* Collaboration. This scaling relation does not present the theoretical slope of 5/3 prescribed by the self-similar evolution of the structures, but found in the staking of the central galaxies in SDSS (Planck Collaboration Int. XI 2013). As we discussed above, this may bias the SZ mass estimate. For this reason, it is crucial to develop new scaling relations between SZ observables and mass both using simulated and real data.

- In this context, programmes such the XMM Heritage Cluster Project and the NIKA2 Large Program are very useful to construct multi-wavelength GC catalogues that are as large as possible. Moreover, since the cluster mass is not an observable, studying GCs in different wavelengths may allow the development of a scaling relation between the GC observable. In this way one can avoid the biases caused by the observable mass scaling relations.

- The internal physics of GCs may be an important source of bias in mass calculation. Therefore, it will be important to test how scaling relations behave for clusters in different evolution stages or dynamical states with cosmological simulations.

- Our analysis of numerical simulations confirmed that interloper contamination is the more detrimental effect in the velocity dispersion estimation. Using simulations taking into account the whole light cone will allow the systematic study of these contaminants. In fact, mimicking real observational strategies it would be possible to predict the percentage of interlopers.

- This thesis has been focused on the optical follow-up and cosmological analysis of the PSZ1 catalogue. In the last years we performed the twin programme of the ITP devoted to the optical follow-up of the PSZ2 sources in the northern hemisphere in the framework of a long-time programme (LP15, Streblyanska et al. 2019; Aguado-Barahona et al. 2019, submitted). Using LP15 data, we will characterise a new $M_{500}^{dyn} - M_{500}^{SZ}$ relation for PSZ2 and we will perform an independent estimation of the mass bias for this sample. It would be interesting to compare both $(1 - B)$ retrieved for PSZ1 and PSZ2 sample by using the same technique based in dynamical mass of clusters.

- WEAVE (WHT Enhanced Area Velocity Explorer) is a new multi-object survey spectrograph for the 4.2-m *William Herschel Telescope* (WHT). This spectrograph will operate with two observing modes. One mode allows to take optical spectra of up to $\sim$ 1000 targets over a two-degree field of view in a single exposure (MOS); and an alternative mode which provides integral-field spectroscopy using one large fixed integral-field unit (LIFU). One of the scientific surveys of this instruments will be dedicated to the study of Galaxy Clusters in a Cosmological frame, this is the Cosmological Cluster Survey (WCC; PI: J. A. Rubiño-Martín and R. Barrena). The WCC survey will be carried out in a five-years observational programme (2020-2024) and will require 300 h of telescope time. A sample of 70 PSZ2 clusters will be spectroscopically sampled using the MOS and LIFU observing modes to obtain radial velocities of galaxy cluster members. The strategy designed for the WCC survey is homologous to that presented in this thesis. Therefore, scaling relations and mass bias will be estimated by comparing dynamical masses with SZ ones. Given the homogeneity of the two techniques used in this thesis and in the WCC survey, it would be interesting to compare the results obtained by the WCC survey considering PSZ2 clusters with the $(1 - B)$ values obtained in this thesis for PSZ1 targets. The results presented in this thesis, in the LP15 and in the WCC survey will represent the most complete work on the mass bias and scaling relations using both PSZ1 and PSZ2 cluster samples.

Bibliography

Abdullah, M. H., Wilson, G., & Klypin, A. 2018, ApJ, 861, 22

Abell, G. O. 1958, The Astrophysical Journal Supplement Series, 3, 211

Abell, G. O., Corwin, Harold G., J., & Olowin, R. P. 1989, The Astrophysical Journal Supplement Series, 70, 1

Adam, R., Comis, B., Macías-Pérez, J. F., et al. 2014, A&A, 569, A66

Adam, R., Bartalucci, I., Pratt, G. W., et al. 2017, A&A, 598, A115

Adelman-McCarthy, J. K., Agüeros, M. A., Allam, S. S., et al. 2006, The Astrophysical Journal Supplement Series, 162, 38

Aguado-Barahona, A., Barrena, R., Streblyanska, A., et al. 2019, submitted, A&A

Aguerri, J. A. L., Girardi, M., Boschin, W., et al. 2011, A&A, 527, A143

Ahn, C. P., Alexandroff, R., Allende Prieto, C., et al. 2012, The Astrophysical Journal Supplement Series, 203, 21

Aihara, H., Allende Prieto, C., An, D., et al. 2011, ApJS, 193, 29

Aihara, H., Armstrong, R., Bickerton, S., et al. 2018a, Publications of the Astronomical Society of Japan, 70, S8

Aihara, H., Arimoto, N., Armstrong, R., et al. 2018b, Publications of the Astronomical Society of Japan, 70, S4

Akritas, M. G., & Bershady, M. A. 1996, ApJ, 470, 706

Allen, S. W., Evrard, A. E., & Mantz, A. B. 2011, ARA&A, 49, 409

Amodeo, S., Mei, S., Stanford, S. A., et al. 2017, ApJ, 844, 101

Applegate, D. E., von der Linden, A., Kelly, P. L., et al. 2014, MNRAS, 439, 48

Arnaud, M. 2005, in Background Microwave Radiation and Intracluster Cosmology, ed. F. Melchiorri & Y. Rephaeli, 77

Arnaud, M., & Evrard, A. E. 1999, MNRAS, 305, 631

Arnaud, M., Pointecouteau, E., & Pratt, G. W. 2007, A&A, 474, L37

Arnaud, M., Pratt, G. W., Piffaretti, R., et al. 2010, A&A, 517, A92

Bañados, E., Hung, L.-W., De Propris, R., & West, M. J. 2010, ApJ, 721, L14

Bacchi, M., Feretti, L., Giovannini, G., & Govoni, F. 2003, A&A, 400, 465

Barrena, R., Ferragamo, A., Rubiño-Martín, J. A., & Streblyanska, A. in prep.

Barrena, R., Girardi, M., Boschin, W., & Mardirossian, F. 2012, A&A, 540, A90

Barrena, R., Streblyanska, A., Ferragamo, A., et al. 2018, A&A, 616, A42

Bartelmann, M. 1996, A&A, 313, 697

—. 2010, Classical and Quantum Gravity, 27, 233001

Battaglia, N., Bond, J. R., Pfrommer, C., & Sievers, J. L. 2012, ApJ, 758, 74

Battaglia, N., Leauthaud, A., Miyatake, H., et al. 2016, Journal of Cosmology and Astro-Particle Physics, 2016, 013

Baum, S. A., & O'Dea, C. P. 1991, MNRAS, 250, 737

Beers, T. C., Flynn, K., & Gebhardt, K. 1990, AJ, 100, 32

Benítez, N. 2000, ApJ, 536, 571

Benson, B. A., Church, S. E., Ade, P. A. R., et al. 2003, ApJ, 592, 674

Bersanelli, M., & Mandolesi, N. 2000, Astrophysical Letters and Communications, 37, 171

Bertin, E., & Arnouts, S. 1996a, Astronomy and Astrophysics Supplement Series, 117, 393

—. 1996b, A&AS, 117, 393

Betancort-Rijo, J. E., & Montero-Dorta, A. D. 2006, ApJ, 650, L95

Birkinshaw, M. 1999, Phys. Rep., 310, 97

Birkinshaw, M., Gull, S. F., & Northover, K. J. E. 1978a, Nature, 275, 40,41

—. 1978b, MNRAS, 185, 245

Birkinshaw, M., Hughes, J. P., & Arnaud, K. A. 1991, ApJ, 379, 466

Bock, J. J., Chen, D., Mauskopf, P. D., & Lange, A. E. 1995, Space Sci. Rev., 74, 229

Böhringer, H., & Werner, N. 2010, Astronomy and Astrophysics Review, 18, 127

Böhringer, H., Voges, W., Huchra, J. P., et al. 2000, The Astrophysical Journal Supplement Series, 129, 435

Böhringer, H., Schuecker, P., Guzzo, L., et al. 2004, A&A, 425, 367

Böhringer, H., Schuecker, P., Pratt, G. W., et al. 2007, A&A, 469, 363

Bonafede, A., Dolag, K., Stasyszyn, F., Murante, G., & Borgani, S. 2011, MNRAS, 418, 2234

Bond, J. R., Cole, S., Efstathiou, G., & Kaiser, N. 1991, ApJ, 379, 440

Borgani, S., & Kravtsov, A. 2011, Advanced Science Letters, 4, 204

Borgani, S., Murante, G., Springel, V., et al. 2004, MNRAS, 348, 1078

Bower, R. G. 1991, MNRAS, 248, 332

Bowyer, C. S., Lampton, M., Mack, J., & de Mendonca, F. 1970, ApJ, 161, L1

Bradt, H., Mayer, W., Naranan, S., Rappaport, S., & Spada, G. 1967, ApJ, 150, L199

Broadhurst, T. J., Taylor, A. N., & Peacock, J. A. 1995, ApJ, 438, 49

Burenin, R. A., Vikhlinin, A., Hornstrup, A., et al. 2007, The Astrophysical Journal Supplement Series, 172, 561

Burgh, E. B., Nordsieck, K. H., Kobulnicky, H. A., et al. 2003, in Society of Photo-Optical Instrumentation Engineers (SPIE) Conference Series, Vol. 4841, Instrument Design and Performance for Optical/Infrared Ground-based Telescopes, ed. M. Iye & A. F. M. Moorwood, 1463–1471

Burns, J. O., Sulkanen, M. E., Gisler, G. R., & Perley, R. A. 1992, ApJ, 388, L49

Byram, E. T., Chubb, T. A., & Friedman, H. 1966, Science, 152, 66

Carlstrom, J. E., Holder, G. P., & Reese, E. D. 2002, Annual Review of Astronomy and Astrophysics, 40, 643

Carvalho, P., Rocha, G., & Hobson, M. P. 2009, MNRAS, 393, 681

Carvalho, P., Rocha, G., Hobson, M. P., & Lasenby, A. 2012, MNRAS, 427, 1384

Cash, W. 1979, ApJ, 228, 939

Catalano, A., Adam, R., Ade, P. A. R., et al. 2018, Journal of Low Temperature Physics, 193, 916

Cavaliere, A., & Fusco-Femiano, R. 1976, A&A, 500, 95

—. 1978, A&A, 70, 677

Cavaliere, A. G., Gursky, H., & Tucker, W. H. 1971, Nature, 231, 437

Chandrasekhar, S. 1943, ApJ, 97, 255

Chon, G., & Böhringer, H. 2012, A&A, 538, A35

Day, P. K., LeDuc, H. G., Mazin, B. A., Vayonakis, A., & Zmuidzinas, J. 2003, Nature, 425, 817

De Felice, A., & Tsujikawa, S. 2010, Living Reviews in Relativity, 13, 3

Delabrouille, J., Betoule, M., Melin, J. B., et al. 2013, A&A, 553, A96

den Hartog, R., & Katgert, P. 1996, MNRAS, 279, 349

den Herder, J. W., Brinkman, A. C., Kahn, S. M., et al. 2001, A&A, 365, L7

Diaferio, A. 1999, MNRAS, 309, 610

Dodelson, S. 2003, Modern cosmology

Dolag, K., Borgani, S., Murante, G., & Springel, V. 2009, MNRAS, 399, 497

Duffy, A. R., Schaye, J., Kay, S. T., & Dalla Vecchia, C. 2008, MNRAS, 390, L64

Dutton, A. A., & Macciò, A. V. 2014, MNRAS, 441, 3359

Dyson, F. W., Eddington, A. S., & Davidson, C. 1920, Philosophical Transactions of the Royal Society of London Series A, 220, 291

Ebeling, H., Edge, A. C., Allen, S. W., et al. 2000, MNRAS, 318, 333

Ebeling, H., Edge, A. C., Bohringer, H., et al. 1998, MNRAS, 301, 881

Ebeling, H., Edge, A. C., & Henry, J. P. 2001, ApJ, 553, 668

Ebeling, H., Edge, A. C., Mantz, A., et al. 2010, MNRAS, 407, 83

Ebeling, H., Mullis, C. R., & Tully, R. B. 2002, ApJ, 580, 774

Eddington, A. S. 1913, MNRAS, 73, 359

Einstein, A. 1916, Annalen der Physik, 354, 769

Evrard, A. E., Metzler, C. A., & Navarro, J. F. 1996, ApJ, 469, 494

Evrard, A. E., Bialek, J., Busha, M., et al. 2008, ApJ, 672, 122

Feretti, L., & Giovannini, G. 2008, Clusters of Galaxies in the Radio: Relativistic Plasma and ICM/Radio Galaxy Interaction Processes, ed. M. Plionis, O. López-Cruz, & D. Hughes, 24

Ferragamo, A., Barrena, R., Rubiño-Martín, J. A., Streblyanska, A., & Aguado-Barahona, A. in prep.

Ferragamo, A., Rubiño-Martín, J. A., Betancort-Rijo, J., et al. 2019, submitted, submitted

Ferrari, C., Govoni, F., Schindler, S., Bykov, A. M., & Rephaeli, Y. 2008, Space Sci. Rev., 134, 93

Forman, W., Jones, C., Cominsky, L., et al. 1978, The Astrophysical Journal Supplement Series, 38, 357

Fritz, G., Davidsen, A., Meekins, J. F., & Friedman, H. 1971, ApJ, 164, L81

Fukugita, M., Ichikawa, T., Gunn, J. E., et al. 1996, AJ, 111, 1748

Giacconi, R., Gursky, H., Kellogg, E., et al. 1973, ApJ, 184, 227

Giacconi, R., Murray, S., Gursky, H., et al. 1974, The Astrophysical Journal Supplement Series, 27, 37

—. 1972, ApJ, 178, 281

Giovannini, G., & Feretti, L. 2000, New Astron., 5, 335

Gitti, M., Brunetti, G., Feretti, L., & Setti, G. 2004, A&A, 417, 1

Gitti, M., Ferrari, C., Domainko, W., Feretti, L., & Schindler, S. 2007, A&A, 470, L25

Gladders, M. D., & Yee, H. K. C. 2000, AJ, 120, 2148

Glenn, J., Bock, J. J., Chattopadhyay, G., et al. 1998, in Society of Photo-Optical Instrumentation Engineers (SPIE) Conference Series, Vol. 3357, Advanced Technology MMW, Radio, and Terahertz Telescopes, ed. T. G. Phillips, 326–334

Gordon, C., Wands, D., Bassett, B. A., & Maartens, R. 2001, Phys. Rev. D, 63, 023506

Govoni, F., Murgia, M., Feretti, L., et al. 2005, A&A, 430, L5

Gursky, H., Kellogg, E., Murray, S., et al. 1971a, ApJ, 167, L81

Gursky, H., Kellogg, E. M., Leong, C., Tananbaum, H., & Giacconi, R. 1971b, ApJ, 165, L43

Guth, A. H. 1981, Phys. Rev. D, 23, 347

Haardt, F., & Madau, P. 2001, in Clusters of Galaxies and the High Redshift Universe Observed in X-rays, ed. D. M. Neumann & J. T. V. Tran

Haehnelt, M. G., & Tegmark, M. 1996, MNRAS, 279, 545

Hand, N., Addison, G. E., Aubourg, E., et al. 2012, Phys. Rev. Lett., 109, 041101

Hao, J., McKay, T. A., Koester, B. P., et al. 2010, The Astrophysical Journal Supplement Series, 191, 254

Hartley, W. G., Gazzola, L., Pearce, F. R., Kay, S. T., & Thomas, P. A. 2008, MNRAS, 386, 2015

Hasselfield, M., Hilton, M., Marriage, T. A., et al. 2013, Journal of Cosmology and Astro-Particle Physics, 2013, 008

Henry, J. P., Mullis, C. R., Voges, W., et al. 2006, The Astrophysical Journal Supplement Series, 162, 304

Herranz, D., Sanz, J. L., Barreiro, R. B., & Martínez-González, E. 2002a, ApJ, 580, 610

Herranz, D., Sanz, J. L., Hobson, M. P., et al. 2002b, MNRAS, 336, 1057

Heymans, C., Van Waerbeke, L., Miller, L., et al. 2012, MNRAS, 427, 146

Hildebrandt, H., Choi, A., Heymans, C., et al. 2016, MNRAS, 463, 635

Hilton, M., Hasselfield, M., Sifón, C., et al. 2018, The Astrophysical Journal Supplement Series, 235, 20

Hinshaw, G., Larson, D., Komatsu, E., et al. 2013, The Astrophysical Journal Supplement Series, 208, 19

Hoekstra, H., Herbonnet, R., Muzzin, A., et al. 2015, MNRAS, 449, 685

Holzapfel, W. L., Ade, P. A. R., Church, S. E., et al. 1997, ApJ, 481, 35

Hook, I. M., Jørgensen, I., Allington-Smith, J. R., et al. 2004, PASP, 116, 425

Hubble, E. 1929, Proceedings of the National Academy of Science, 15, 168

Jansen, F., Lumb, D., Altieri, B., et al. 2001, A&A, 365, L1

Jaynes, E. T., & Bretthorst, G. L. 2003, Probability Theory

Jedamzik, K. 1995, ApJ, 448, 1

Jenkins, A., Frenk, C. S., White, S. D. M., et al. 2001, MNRAS, 321, 372

Jones, L. R., Ponman, T. J., Horton, A., et al. 2003a, MNRAS, 343, 627

Jones, W. C., Bhatia, R., Bock, J. J., & Lange, A. E. 2003b, in Society of Photo-Optical Instrumentation Engineers (SPIE) Conference Series, Vol. 4855, Millimeter and Submillimeter Detectors for Astronomy, ed. T. G. Phillips & J. Zmuidzinas, 227–238

Kaiser, N. 1986, MNRAS, 222, 323

Kay, S. T., Peel, M. W., Short, C. J., et al. 2012, MNRAS, 422, 1999

Keeton, C. R. 2001, arXiv e-prints, astro

Kelly, B. C. 2007, ApJ, 665, 1489

Kempner, J. C., & Sarazin, C. L. 2001, ApJ, 548, 639

Kennicutt, Jr., R. C. 1992, ApJS, 79, 255

Kepner, J., Fan, X., Bahcall, N., et al. 1999, ApJ, 517, 78

Kocevski, D. D., Ebeling, H., Mullis, C. R., & Tully, R. B. 2007, ApJ, 662, 224

Koester, B. P., McKay, T. A., Annis, J., et al. 2007, ApJ, 660, 239

Komatsu, E., Smith, K. M., Dunkley, J., et al. 2011, ApJS, 192, 18

Krause, E., Pierpaoli, E., Dolag, K., & Borgani, S. 2012, MNRAS, 419, 1766

Kravtsov, A. V., & Borgani, S. 2012, ARA&A, 50, 353

Kravtsov, A. V., Vikhlinin, A., & Nagai, D. 2006, ApJ, 650, 128

Kron, R. G. 1980, ApJS, 43, 305

Lamarre, J. M., Piat, M., Ade, P. A. R., et al. 2002, in Low Temperature Detectors, ed. F. S. Porter, D. McCammon, M. Galeazzi, & C. K. Stahle, Vol. 605, 571–576

Lamarre, J. M., Puget, J. L., Bouchet, F., et al. 2003, New Astronomy Reviews, 47, 1017

Large, M. I., Mathewson, D. S., & Haslam, C. G. T. 1959, Nature, 183, 1663

Lemaître, G. 1927, Annales de la Société Scientifique de Bruxelles, 47, 49

Lewis, A., & Challinor, A. 2006, Phys. Rep., 429, 1

Liddle, A. R., & Lyth, D. H. 2000, Cosmological Inflation and Large-Scale Structure

Liesenborgs, J., de Rijcke, S., Dejonghe, H., & Bekaert, P. 2008, MNRAS, 386, 307

Łokas, E. L., & Mamon, G. A. 2001, MNRAS, 321, 155

Lopes, P. A. A. 2007, MNRAS, 380, 1608

Lynds, R., & Petrosian, V. 1989, ApJ, 336, 1

Mamon, G. A., Biviano, A., & Murante, G. 2010, A&A, 520, A30

Mandolesi, N., Bersanelli, M., Burigana, C., & Villa, F. 2000, Astrophysical Letters and Communications, 37, 151

Mantz, A., Allen, S. W., Rapetti, D., & Ebeling, H. 2010, MNRAS, 406, 1759

Mazzotta, P., Rasia, E., Moscardini, L., & Tormen, G. 2004, MNRAS, 354, 10

Medezinski, E., Battaglia, N., Umetsu, K., et al. 2018, Publications of the Astronomical Society of Japan, 70, S28

Melin, J. B., Bartlett, J. G., & Delabrouille, J. 2006, A&A, 459, 341

Melin, J. B., Bartlett, J. G., Delabrouille, J., et al. 2011, A&A, 525, A139

Melin, J. B., Aghanim, N., Bartelmann, M., et al. 2012, A&A, 548, A51

Miyatake, H., Battaglia, N., Hilton, M., et al. 2018, ArXiv e-prints, arXiv:1804.05873

Munari, E., Biviano, A., Borgani, S., Murante, G., & Fabjan, D. 2013, MNRAS, 430, 2638

Nagai, D. 2006, ApJ, 650, 538

Nagai, D., Kravtsov, A. V., & Vikhlinin, A. 2007, ApJ, 668, 1

Navarro, J. F., Frenk, C. S., & White, S. D. M. 1997, ApJ, 490, 493

Noonan, T. W. 1971, AJ, 76, 765

O'Dea, C. P., & Owen, F. N. 1986, ApJ, 301, 841

O'Dea, C. P., Sarazin, C. L., & Owen, F. N. 1986, National Radio Astronomy Observatory Workshop, 16, 275

Okabe, N., & Smith, G. P. 2016, MNRAS, 461, 3794

Padmanabhan, T. 1993, Structure Formation in the Universe (Cambridge University Press)

Peacock, J. A., & Heavens, A. F. 1990, MNRAS, 243, 133

Peebles, P. J. E. 1970, AJ, 75, 13

—. 1980, The large-scale structure of the universe

—. 1982, ApJ, 263, L1

Penna-Lima, M., Bartlett, J. G., Rozo, E., et al. 2017, A&A, 604, A89

Perlmutter, S., Aldering, G., Goldhaber, G., et al. 1999, ApJ, 517, 565

Phillips, P. R. 1995, ApJ, 455, 419

Piffaretti, R., Arnaud, M., Pratt, G. W., Pointecouteau, E., & Melin, J.-B. 2011, A&A, 534, A109

Piffaretti, R., & Valdarnini, R. 2008, A&A, 491, 71

Planck Collaboration. 2005, ESA publication ESA-SCI(2005)/01, arXiv:astro-ph/0604069

Planck Collaboration Int. I. 2012, A&A, 543, A102

Planck Collaboration Int. III. 2013, A&A, 550, A129

Planck Collaboration Int. IV. 2013, A&A, 550, A130

Planck Collaboration Int. XXXVI. 2016, A&A, 586, A139

Planck Collaboration IX. 2011, A&A, 536, A9

Planck Collaboration VI. 2018a, ArXiv e-prints, arXiv:1807.06209

—. 2018b, arXiv e-prints, arXiv:1807.06209

Planck Collaboration VIII. 2011, A&A, 536, A8

Planck Collaboration XI. 2011, A&A, 536, A11

Planck Collaboration XIII. 2016, A&A, 594, A13

Planck Collaboration XX. 2014, A&A, 571, A20

Planck Collaboration XXIV. 2016, A&A, 594, A24

Planck Collaboration VIII. 2011, A&A, 536, A8

Planck Collaboration IX. 2011, A&A, 536, A9

Planck Collaboration XII. 2014, A&A, 571, A12

Planck Collaboration XVI. 2014, A&A, 571, A16

Planck Collaboration XXIX. 2014, A&A, 571, A29

Planck Collaboration XXXII. 2015, A&A, 581, A14

Planck Collaboration I. 2016, A&A, 594, A1

Planck Collaboration IX. 2016, A&A, 594, A9

Planck Collaboration X. 2016, A&A, 594, A10

Planck Collaboration XXVII. 2016, A&A, 594, A27

Planck Collaboration Int. I. 2012, A&A, 543, A102

Planck Collaboration Int. IV. 2013, A&A, 550, A130

Planck Collaboration Int. XI. 2013, A&A, 557, A52

Planck Collaboration Int. XXVI. 2015, A&A, 582, A29

Postman, M., Coe, D., Benítez, N., et al. 2012, The Astrophysical Journal Supplement Series, 199, 25

Pratt, G. W., Arnaud, M., Biviano, A., et al. 2019, Space Sci. Rev., 215, 25

Pratt, G. W., Croston, J. H., Arnaud, M., & Böhringer, H. 2009, A&A, 498, 361

Pratt, G. W., Pointecouteau, E., Arnaud, M., & van der Burg, R. F. J. 2016, A&A, 590, L1

Press, W. H., & Schechter, P. 1974, ApJ, 187, 425

Press, W. H., Teukolsky, S. A., Vetterling, W. T., & Flannery, B. P. 1992, Numerical recipes in FORTRAN. The art of scientific computing

Rasia, E., Borgani, S., Murante, G., et al. 2015, ApJ, 813, L17

Refsdal, S. 1964, MNRAS, 128, 307

Reichardt, C. L., Stalder, B., Bleem, L. E., et al. 2013, ApJ, 763, 127

Remazeilles, M., Bolliet, B., Rotti, A., & Chluba, J. 2019, MNRAS, 483, 3459

Rephaeli, Y. 1995, Annual Review of Astronomy and Astrophysics, 33, 541

Riess, A. G., Filippenko, A. V., Challis, P., et al. 1998, AJ, 116, 1009

Rizza, E., Loken, C., Bliton, M., et al. 2000, AJ, 119, 21

Rubin, V. C., & Ford, W. Kent, J. 1970, ApJ, 159, 379

Ruel, J., Bazin, G., Bayliss, M., et al. 2014, ApJ, 792, 45

Salvati, L., Douspis, M., & Aghanim, N. 2018, A&A, 614, A13

Sarazin, C. L. 1988, X-ray emission from clusters of galaxies

Sarazin, C. L., & Bahcall, J. N. 1977, The Astrophysical Journal Supplement Series, 34, 451

Saro, A., Mohr, J. J., Bazin, G., & Dolag, K. 2013, ApJ, 772, 47

Sayers, J., Zemcov, M., Glenn, J., et al. 2016, ApJ, 820, 101

Sehgal, N., Bode, P., Das, S., et al. 2010, ApJ, 709, 920

Sembolini, F., Yepes, G., De Petris, M., et al. 2013, MNRAS, 434, 2718

Sereno, M., Covone, G., Izzo, L., et al. 2017, MNRAS, 472, 1946

Sereno, M., & Ettori, S. 2015, MNRAS, 450, 3633

Sereno, M., Giocoli, C., Izzo, L., et al. 2018, Nature Astronomy, 2, 744

Sifón, C., Battaglia, N., Hasselfield, M., et al. 2016, MNRAS, 461, 248

Smith, G. P., Mazzotta, P., Okabe, N., et al. 2016, MNRAS, 456, L74

Soucail, G., Fort, B., Mellier, Y., & Picat, J. P. 1987, A&A, 172, L14

Springel, V. 2005, MNRAS, 364, 1105

Springel, V., Di Matteo, T., & Hernquist, L. 2005, ApJ, 620, L79

Springel, V., Yoshida, N., & White, S. D. M. 2001a, New Astron., 6, 79

Springel, V., Yoshida, N., & White, S. D. M. 2001b, New Astron., 6, 79

Stanek, R., Rasia, E., Evrard, A. E., Pearce, F., & Gazzola, L. 2010, ApJ, 715, 1508

Steigman, G. 2008, arXiv e-prints, arXiv:0807.3004

Steinhardt, P. J. 1997, in Critical Problems in Physics, 123

Streblyanska, A., Aguado-Barahona, A., Ferragamo, A., et al. 2019, A&A, 628, A13

Strüder, L., Briel, U., Dennerl, K., et al. 2001, A&A, 365, L18

Subrahmanyan, R., Beasley, A. J., Goss, W. M., Golap, K., & Hunstead, R. W. 2003, AJ, 125, 1095

Sunyaev, R. A., & Zeldovich, I. B. 1980, Annual Review of Astronomy and Astrophysics, 18, 537

Sunyaev, R. A., & Zeldovich, Y. B. 1970, Ap&SS, 7, 3

—. 1972, Comments on Astrophysics and Space Physics, 4, 173

Szabo, T., Pierpaoli, E., Dong, F., Pipino, A., & Gunn, J. 2011, ApJ, 736, 21

Tinker, J., Kravtsov, A. V., Klypin, A., et al. 2008, ApJ, 688, 709

Tonry, J., & Davis, M. 1979, AJ, 84, 1511

Tukey, J. W. 1958, Annals of Mathematical Statistics, 29, 614

Turner, M. J. L., Abbey, A., Arnaud, M., et al. 2001, A&A, 365, L27

Tyson, J. A., Valdes, F., & Wenk, R. A. 1990, ApJ, 349, L1

Umetsu, K. 2010, arXiv e-prints, arXiv:1002.3952

van der Burg, R. F. J., Aussel, H., Pratt, G. W., et al. 2016, A&A, 587, A23

Vanderlinde, K., Crawford, T. M., de Haan, T., et al. 2010, ApJ, 722, 1180

Vikhlinin, A. 2006, ApJ, 640, 710

Vikhlinin, A., Burenin, R. A., Ebeling, H., et al. 2009, ApJ, 692, 1033

Voevodkin, A., Borozdin, K., Heitmann, K., et al. 2010, ApJ, 708, 1376

Voges, W., Aschenbach, B., Boller, T., et al. 1999a, A&A, 349, 389

—. 1999b, A&A, 349, 389

—. 2000, IAU Circ., 7432

von der Linden, A., Mantz, A., Allen, S. W., et al. 2014, MNRAS, 443, 1973

Wainer, H., & D., T. 1976, Psychometrika, 41, 9

Wambsganss, J. 1998, Living Reviews in Relativity, 1, 12

Weinberg, S. 1972, Gravitation and Cosmology: Principles and Applications of the General Theory of Relativity

Weisskopf, M. C., Brinkman, B., Canizares, C., et al. 2002, Publications of the Astronomical Society of the Pacific, 114, 1

Wellington, K. J., Miley, G. K., & van der Laan, H. 1973, Nature, 244, 502

Wen, Z. L., & Han, J. L. 2018, MNRAS, 481, 4158

Wen, Z. L., Han, J. L., & Liu, F. S. 2012, The Astrophysical Journal Supplement Series, 199, 34

Wen, Z. L., Han, J. L., & Yang, F. 2018, MNRAS, 475, 343

White, S. D. M. 1976, MNRAS, 177, 717

Wiersma, R. P. C., Schaye, J., & Smith, B. D. 2009, MNRAS, 393, 99

Williamson, R., Benson, B. A., High, F. W., et al. 2011, ApJ, 738, 139

Willson, M. A. G. 1970, MNRAS, 151, 1

Wojtak, R., Old, L., Mamon, G. A., et al. 2018, MNRAS, 481, 324

Wright, E. L., Eisenhardt, P. R. M., Mainzer, A. K., et al. 2010, AJ, 140, 1868

Yahil, A., & Vidal, N. V. 1977, ApJ, 214, 347

Yang, H. Y. K., Bhattacharya, S., & Ricker, P. M. 2010, ApJ, 725, 1124

Yano, T., Nagashima, M., & Gouda, N. 1996, ApJ, 466, 1

Yoo, J., & Watanabe, Y. 2012, International Journal of Modern Physics D, 21, 1230002

Zwicky, F. 1933, Helvetica Physica Acta, 6, 110

—. 1937a, Physical Review, 51, 290

—. 1937b, Physical Review, 51, 679

Zwicky, F., Herzog, E., Wild, P., Karpowicz, M., & Kowal, C. T. 1961, Catalogue of galaxies and of clusters of galaxies, Vol. I